

This electronic thesis or dissertation has been downloaded from the King's Research Portal at <https://kclpure.kcl.ac.uk/portal/>



Engineering Stem Cell-Derived Neuromuscular Circuits to Model Amyotrophic Lateral Sclerosis (ALS)

Harley, Pete

Awarding institution:
King's College London

The copyright of this thesis rests with the author and no quotation from it or information derived from it may be published without proper acknowledgement.

END USER LICENCE AGREEMENT



Unless another licence is stated on the immediately following page this work is licensed

under a Creative Commons Attribution-NonCommercial-NoDerivatives 4.0 International

licence. <https://creativecommons.org/licenses/by-nc-nd/4.0/>

You are free to copy, distribute and transmit the work

Under the following conditions:

- Attribution: You must attribute the work in the manner specified by the author (but not in any way that suggests that they endorse you or your use of the work).
- Non Commercial: You may not use this work for commercial purposes.
- No Derivative Works - You may not alter, transform, or build upon this work.

Any of these conditions can be waived if you receive permission from the author. Your fair dealings and other rights are in no way affected by the above.

Take down policy

If you believe that this document breaches copyright please contact librarypure@kcl.ac.uk providing details, and we will remove access to the work immediately and investigate your claim.

Engineering Stem Cell-Derived Neuromuscular Circuits
to Model Amyotrophic Lateral Sclerosis (ALS)



Peter Harley

Thesis submitted for the degree of Doctor of Philosophy

March 2022

Centre for Gene Therapy & Regenerative Medicine, MRC Centre for Developmental
Neurobiology

King's College London

Abstract:

Amyotrophic lateral sclerosis (ALS) is a neurodegenerative disease characterised by degeneration of motor neurons in the brain and spinal cord, leading to progressive paralysis and death. Currently no cure exists, and the only treatments available extend life by a matter of months. Cytoplasmic aggregation of TAR DNA-binding protein 43 (TDP-43) is a key pathological hallmark, seen in the vast majority of patients with ALS. The mechanisms by which TDP-43 contributes to motor neuron degeneration are not fully understood, although aberrant alternative splicing and perturbed RNA metabolism are thought to play pivotal roles. Emerging evidence suggests that some of the earliest pathological events in the progression of ALS occur peripherally. These include neuronal hyperexcitability, spontaneous muscle fasciculations (twitching), impaired neuromuscular transmission, neuromuscular synapse dismantling and axonal degeneration. To develop drugs that can target these early peripheral events, better *in vitro* disease models are required that accurately reflect these complex phenotypes.

This work describes the development of human induced pluripotent stem cell (hiPSC) derived neuromuscular circuits (Chapter 4), based on preliminary work using mouse embryonic stem cells (mESCs) and primary chick myoblasts (Chapter 3). CRISPR-Cas9 genome editing was used to correct a pathogenic ALS-related TDP-43^{G298S} mutation in patient derived hiPSCs. hiPSC lines were also engineered to express a MACS sortable motor neuron marker and the optogenetic actuator CHR2-YFP to enrich and control the activity of hiPSC-derived motor neurons. MACS enriched hiPSC-motor neurons were co-cultured with iPAX7 forward programmed hiPSC-myoblasts in compartmentalised microdevices, whereby motor axons were able to grow through micro-channels and form functional neuromuscular junctions (NMJs) with target muscle. Optogenetic stimulation of the motor neurons elicited robust myofiber contractions and daily optogenetic entrainment was found to enhance neuromuscular synapse formation, mirroring the activity-dependence of NMJ formation *in vivo*. Furthermore, it was found that the neuromuscular co-cultures containing TDP-43^{G298S} motor neurons displayed increased spontaneous myofiber contractions yet weaker optogenetically evoked maximal contractile output, which was linked to reduced axon

outgrowth and a lower number of neuromuscular synapses (Chapter 4). These phenotypes resemble the muscle fasciculations and muscle weakness observed in patients with ALS.

In conjunction with the compartmentalised co-culture format, a high-throughput 96-well hiPSC-neuromuscular co-culture platform was established (Chapter 5), whereby neuromuscular disease phenotypes could be imaged and quantified automatically using high content image analysis more rapidly and at a larger scale than has previously been possible. Using this approach, it was possible to model both ALS related phenotypes and Duchenne muscular dystrophy (DMD) related phenotypes – two contrasting neuromuscular diseases. Furthermore, it was possible to test candidate drugs and it was found the RIPK1 inhibitor necrostatin could partially rescue ALS-related neuromuscular phenotypes, while the TGFβ inhibitor SB431542 could rescue DMD-related phenotypes. Finally, by generating custom-built 96-well plates with suspended electrospun elastic nanofibers it was possible to stabilise contractile myofibers for longer-term neuromuscular culture stability and maturation in the 96-well plate format.

Finally, to uncover mechanistic insights into the hyperactivity of the ALS-TDP-43^{G298S} neuromuscular co-cultures, whole-cell patch clamp recordings were performed. These showed dysregulated neuronal excitability of TDP-43^{G298S} motor neurons, relative to wildtype and CRISPR-corrected controls. Interestingly, these changes were associated with structural abnormalities of the axon initial segment (AIS) – the primary site of action potential initiation, as well as perturbed functional plasticity of the AIS. Specifically, early (6-weeks) TDP-43^{G298S} motor neurons showed an increase in the length of the AIS and hyperexcitability, while late (10-weeks) TDP-43^{G298S} motor neurons showed shortening of the AIS and hypoexcitability. Furthermore, at all stages, activity-dependent plasticity of the AIS was impaired, further contributing to abnormal homeostatic regulation of neuronal excitability (Chapter 6). Taken together these results suggest for the first time that abnormal AIS structure and plasticity may contribute to dysregulated neuronal excitability in ALS-related TDP-43^{G298S} motor neurons.

Acknowledgments

Firstly, thank you to my PhD supervisors. Ivo, thanks for giving me the freedom to take my own path through the PhD, your creativity and passion for science made it a fantastic four years. Thanks for the evenings with cheese, meat, beers and cosmopolitans! Thank you Maddy, your friendliness and thoughtful discussions were always encouraging throughout. Thank you to my collaborators, Juan & Guilherme for introducing me to the world of patch clamping and electrophysiology. Juan, your encouragement, passion and knowledge was inspiring, it was very kind of you to welcome me to your lab. Guilherme, the time and patience you took teaching me how to patch was incredibly generous – my entire 6th chapter exists entirely thanks to you!

Thank you to all my lab mates over the years. Fede, whether it was a plasmid, a quick pint after work, or a night out at Troy-22 I could always rely on you! Aimee as well I couldn't have asked for anyone better to share the PhD journey with from start to finish! Carolina, your encouragement and collaboration were unsurpassed. And to everyone else in the Lieberam lab over the years: Steph, Ieva, Gaby, Victoria, Lea, Caoimhe, Sofia – Thanks! Also, thanks to everyone in the Burrone group – Rachel, Winnie, Marcio, Vincenzo, Lily and Sally. And thanks to Amaia in Yung-Yao's group – it was great working on your paper with you!

Thanks to my Wellcome trust cohort: Gaby, Ella, Emily, Teo, Luigi. Fay and Fiona – thanks for starting such a great programme and for all your encouragement over the years. Thanks to all my other friends and colleagues from King's. Chris, Geraldine and Matt thanks for being great friends over the years. Everyone from the CCRSM/CDN: Blaise, Victor, Alice, Matteo, Francesco, Eamonn, Fernandina, Mario, Ana-Maria, Christina, and everyone else – Cheers! The Leeds boys in London: Jim, Alex, Joe, Nathaniel, Zach, and my other long-suffering London friends: Jonno, Liv, Ana, Charlie, Jamie, Martin and the rest thanks for always being there!

To Alice, you've been my rock throughout and mean the world to me. Mum, the best days over the last four years have been the ones coming back to Leeds to see you. Dom, Phill, Josh, Sam and Alice thanks for the wild Christmas parties, Mum – Sorry. Dad, Ailith, Aiyana, and Thalia - Thanks for always being there.

Table of Contents

Abstract:	1
Acknowledgments	3
Table of Contents	4
Table of Figures	7
Table of Tables	10
List of abbreviations	11
1. Introduction	15
1.1 Motor neuron development	15
1.2 Astrocyte development.....	17
1.3 Skeletal muscle development	18
1.4 The neuromuscular junction	20
1.5 Amyotrophic Lateral Sclerosis (ALS) background.....	22
1.6 Genetics of ALS	24
1.7 Environmental risk factors for ALS	25
1.8 Histopathology of ALS	26
1.9 Superoxide dismutase 1 (SOD1).....	26
1.10 TAR DNA-binding protein 43 (TDP-43).....	27
1.11 The neuromuscular junction in ALS	30
1.12 Modelling the neuromuscular junction <i>in vitro</i>	33
1.13 Neuronal excitability in ALS	36
1.14 Neuronal plasticity	39
1.15 The axon initial segment (AIS).....	41
1.16 PhD Aims	45
2. Materials & methods	47
2.1 Experimental model details	47
2.1.1 mESC culture and differentiation into motor neurons and astrocytes	47
2.1.2 hiPSC culture and differentiation to motor neurons, astrocytes and myoblasts.....	48
2.1.3 Manufacturing compartmentalised PDMS microdevices	51
2.1.4 Neuromuscular co-cultures in compartmentalised microdevices	52
2.1.5 Manufacturing 96-well plates with suspended electrospun elastomer nanofibers	52
2.1.6 Neuromuscular co-cultures in 96-well plates	53
2.2 Method details.....	53
2.2.1 Genetic engineering hiPSC lines.....	53

2.2.2 Magnetic activated cell sorting (MACS)	55
2.3.3 Flow cytometry	56
2.2.4 Optogenetic entrainment and stimulation	56
2.2.5 Whole-cell patch clamp electrophysiology	56
2.2.6 Muscle contraction recordings	58
2.2.7 Immunofluorescence	58
2.2.8 Western blot	59
2.2.9 qRT-PCR.....	59
2.2.10 RNA-sequencing.....	60
2.2.11 Karyotyping	60
2.3 Quantification and statistical analysis:.....	60
2.3.1 MACS enrichment analysis (IF).....	60
2.3.2 Motor neuron survival analysis.....	60
2.3.3 Fourier analysis of myofiber alignment	61
2.3.4 Particle image velocimetry (PIV) analysis.....	61
2.3.5 Analysis of axon outgrowth and detection of NMJs	62
2.3.6 IF analysis of SOD1/UB41 inclusions	63
2.3.7 IF analysis of myogenic differentiation	63
2.3.8 Analysis of electrophysiology.....	64
2.3.9 Analysis of AIS morphology.....	65
2.3.10 Analysis of soma size and number of dendrites.....	66
2.3.11 Analysis of TDP-43.....	66
2.3.12 Bioinformatics analysis	66
2.3.13 High content image analysis of neuromuscular co-cultures	66
2.3.14 Calculation of myofiber contraction force on elastomer nanofibers.....	67
2.3.15 Diagrams and schematics.....	67
2.3.16 Statistics	67
2.3.17 Statement on biological, experimental, and technical replicates.....	67
3. Engineering mouse ESC-derived neuromuscular co-cultures to model ALS	69
3.1 Hypotheses and aims	69
3.2 Differentiation and MACS purification of mouse ESC derived motor neurons and astrocytes ..	69
3.3 Assembly of neuromuscular co-cultures in 3D-compartmentalized microdevices containing mESC-motor neurons, mESC-astrocytes and chick myoblasts.....	71
3.4 Formation of functional neuromuscular junctions in 3D-compartmentalized micro-devices ...	71
3.5 Optogenetic entrainment enhances NMJ formation	72
3.6 Optogenetic entrainment enhances myofiber contractility	73

3.7 mESC-derived SOD1 ^{G93A} astrocytes display ubiquitin positive inclusions and negatively impact motor neuron survival	74
3.8 The RIPK1 inhibitor necrostatin rescues axon outgrowth and NMJ phenotypes in SOD1 ^{G93A} neuromuscular co-cultures	75
3.9 The RIPK1 inhibitor necrostatin rescues myofiber contractions in SOD1 ^{G93A} neuromuscular co-cultures	76
3.10 BCR-Abl inhibition rescues SOD1 ^{G93A} related neuromuscular phenotypes in an automated high content 96 well neuromuscular co-culture assay	77
3.11 Discussion	93
4. Engineering human iPSC-derived neuromuscular co-cultures to model ALS.....	100
4.1 Hypotheses and aims	100
4.2 CRISPR–Cas9 mediated genome correction of ALS-related TDP-43 ^{G298S} mutation in a patient derived human iPSC line	101
4.3 Directed differentiation of human iPSCs into motor neuron progenitors	102
4.4 Stable integration of <i>HB9::CD14</i> construct into human iPSCs allows efficient magnetic activated cell sorting (MACS) enrichment of post-mitotic motor neurons.....	103
4.5 Stable integration of <i>CAG::CHR2-YFP</i> construct into human iPSCs facilitates optogenetic control of motor neurons	104
4.6 Stable integration of doxycycline-inducible <i>iPAX7</i> construct into human iPSC lines facilitates forward programming into myoblast progenitors	104
4.7 Generation of functional human iPSC-derived neuromuscular circuits in compartmentalized microdevices	105
4.8 Optogenetic entrainment enhances NMJ formation and myofiber contractility in human iPSC neuromuscular circuits	106
4.9 Human iPSC-derived neuromuscular circuits containing TDP-43 ^{G298S} motor neurons display increased spontaneous myofiber contractility, yet reduced optogenetically evoked maximal contractile output	107
4.10 Human iPSC-derived neuromuscular circuits containing TDP-43 ^{G298S} motor neurons display a reduction in axon outgrowth and neuromuscular synapses.....	108
4.11 Discussion	131
5. Engineering high-throughput 96-well human iPSC-derived neuromuscular co-cultures	138
5.1 Aims & hypotheses	138
5.2 Automated high content image analysis of hiPSC-neuromuscular co-cultures in high-throughput 96-well plates	139
5.3 Formation of functional neuromuscular junctions in 96-well plates	140
5.4 Automated HCI analysis of ALS-related phenotypes in high-throughput 96-well neuromuscular co-cultures	140
5.5 Automated HCI analysis of DMD-related phenotypes in high-throughput 96-well neuromuscular co-cultures	141

5.6 Manufacturing suspended biobased elastomer nanofiber scaffolds in 96-well imaging plates.	143
5.7 Electrospun suspended elastic nanofibers support long term stability, alignment and maturation of contractile myofibers in 96-well neuromuscular co-cultures	143
5.8 Necrostatin rescues ALS-related phenotypes in long-term neuromuscular co-cultures grown on 96-well nanofiber plates	144
5.8 Discussion	159
6. Pathogenic TDP-43^{G298S} disrupts neuronal excitability and axon initial segment structure and plasticity.....	164
6.1 Hypothesis and aims	164
6.2 TDP-43 ^{G298S} causes hyperexcitability in early (6 week) motor neurons	164
6.3 TDP-43 ^{G298S} causes increased AIS length in early (6 week) motor neurons	165
6.4 TDP-43 ^{G298S} impairs activity-dependent AIS plasticity and excitability homeostasis in early (6 week) motor neurons	166
6.5 TDP-43 ^{G298S} causes differential expression of AIS and synaptic genes in early (6 week) motor neurons	167
6.6 TDP-43 ^{G298S} causes AIS shortening, hypoexcitability and impaired plasticity in late (10 week) motor neurons	168
6.7 Changes in axon initial segment properties overtime	169
6.8 Changes in electrophysiological properties overtime.....	170
6.9 TDP-43 pathology in early (6-week) and late (10-week) motor neurons.....	171
6.10 Discussion	191
7. Conclusions and future perspectives	198
References:	203
Appendix.....	223
Publications.....	223
Small molecule screen – AstraZeneca compound list.....	228

Table of Figures

Figure 1.1. Development of spinal motor neurons.	17
Figure 1.2. Development of skeletal muscle.	19
Figure 1.3. Development of the neuromuscular junction	22
Figure 1.4. Summary of amyotrophic lateral sclerosis (ALS).	23
Figure 1.5. Overview of TDP-43 pathology in ALS.	29
Figure 1.6. The neuromuscular junction in ALS.....	33
Figure 1.7. Cytoskeletal organisation of the axon initial segment (AIS).....	42
Figure 2.1. PIV analysis of muscle contraction using PIV lab package in MATLAB	62

Figure 2.2. Automated SV2/AChR colocalisation analysis and uniform object thresholding to derive NMJ parameters in IMARIS 9.1.2	63
Figure 2.3. Schematic outlining single and repetitive action potential analysis for whole cell patch clamp electrophysiology recordings.....	65
Figure 3.1. Differentiation and MACS purification of mESC derived motor neurons and astrocytes. .	79
Figure 3.2. Assembly of neuromuscular co-cultures in 3D-compartmentalized microdevices containing mESC-motor neurons, mESC-astrocytes and chick myoblasts.	81
Figure 3.3. Formation of functional neuromuscular junctions in 3D-compartmentalized microdevices.	83
Figure 3.4. Optogenetic entrainment enhances neuromuscular junction formation.	85
Figure 3.5. Optogenetic entrainment enhances myofiber contractility.....	86
Figure 3.6. mESC-derived SOD1 ^{G93A} astrocytes display ubiquitin positive inclusions and negatively impact motor neuron survival.....	88
Figure 3.7. The RIPK1 inhibitor necrostatin rescues axon outgrowth and NMJ phenotypes in SOD1 ^{G93A} neuromuscular co-cultures.	89
Figure 3.8. The RIPK1 inhibitor necrostatin rescues myofiber contractions in SOD1 ^{G93A} neuromuscular co-cultures.....	90
Figure 3.9. BCR-Abl inhibition rescues SOD1 ^{G93A} related neuromuscular phenotypes in an automated high content 96-well neuromuscular co-culture assay.	92
Figure 4.1. CRISPR–Cas9 mediated genome correction of ALS-related TDP-43 ^{G298S} mutation in a patient derived human iPSC line.	110
Figure 4.2. Directed differentiation of human iPSCs into motor neuron progenitors.....	111
Figure 4.3. Stable integration of <i>HB9::CD14</i> construct into human iPSCs allows efficient magnetic activated cell sorting (MACS) enrichment of post-mitotic motor neurons.	113
Figure 4.4. Stable integration of <i>CAG::CHR2-YFP</i> construct into human iPSCs facilitates optogenetic control of motor neurons.....	115
Figure 4.5. Stable integration of doxycycline-inducible <i>iPAX7</i> construct into human iPSC lines facilitates forward proگرامing into myoblast progenitors.	117
Figure 4.6. Generation of functional human iPSC-derived neuromuscular circuits in compartmentalized microdevices.	119
Figure 4.7. Optogenetic entrainment enhances NMJ formation and myofiber contractility in human iPSC neuromuscular circuits.	121

Figure 4.8. Human iPSC-derived neuromuscular circuits containing TDP-43 ^{G298S} motor neurons display increased spontaneous myofiber contractility, yet reduced optogenetically evoked maximal contractile output.	123
Figure 4.9. Human iPSC-derived neuromuscular circuits containing TDP-43 ^{G298S} motor neurons display a reduction in axon outgrowth and neuromuscular synapses.	124
Supplementary Figure 4.10. TIDE analysis of sgRNA-9 and sgRNA-10.	125
Supplementary Figure 4.11. CRISPR-cas9 mediated knockdown of TDP-43 in wildtype hiPSCs.	126
Supplementary Figure 4.12. Impaired differentiation of TDP-43 ^{G298S} iPAX7 hiPSCs into myoblasts. .	127
Supplementary Figure 4.13. Generation and characterization of hiPSC-GDNF+ iAstrocytes.	129
Supplementary Figure 4.14. QR codes for supplementary movies.	130
Figure 5.1. Automated high content image analysis of hiPSC-neuromuscular co-cultures in high-throughput 96-well plates.	146
Figure 5.2. Formation of functional neuromuscular junctions in 96-well plates.	147
Figure 5.3. Automated HCl analysis of ALS-related phenotypes in high-throughput 96-well neuromuscular co-cultures.	148
Figure 5.4. Automated HCl analysis of DMD-related phenotypes in high-throughput 96-well neuromuscular co-cultures.	150
Figure 5.5. Manufacturing suspended biobased elastomer nanofiber scaffolds in 96-well imaging plates.	152
Figure 5.6. Electrospun suspended elastic nanofibers support long term stability, alignment and maturation of contractile myofibers in 96-well neuromuscular co-cultures.	154
Figure 5.7. Necrostatin rescues ALS-related phenotypes in long-term neuromuscular co-cultures grown on 96-well nanofiber plates.	156
Supplementary Figure 5.8. Example of filtering background noise in automated high content image analysis.	157
Supplementary Figure 5.9. The TGFβ inhibitor SB431542 partially rescues DMD-related neuromuscular phenotypes.	158
Supplementary Figure 5.10. QR codes for supplementary movies.	159
Figure 6.1. Pathogenic TDP-43 ^{G298S} causes hyperexcitability in early MNs.	173
Figure 6.2. Pathogenic TDP-43 ^{G298S} causes increased AIS length in early MNs.	175
Figure 6.3. Pathogenic TDP-43 ^{G298S} reduces activity-dependent plasticity of the AIS in early MNs. ...	177
Figure 6.4. TDP-43 ^{G298S} causes differential expression of AIS and synaptic genes in early (6 week) motor neurons.	179

Figure 6.5. Pathogenic TDP-43 ^{G298S} causes AIS shortening, impaired plasticity, and hypoexcitability in late MNs.	181
Figure 6.6. Changes in axon initial segment properties overtime.....	183
Figure 6.7. Changes in electrophysiological properties overtime.	185
Figure 6.8. TDP-43 pathology in early (6-week) and late (10-week) motor neurons.	187
Supplementary Figure 6.9. Additional bulk RNA-sequencing analysis.	190

Table of Tables

Table 1.1. Genetic architecture of ALS and ALS-FTD.	25
Table 2.1. Mouse embryonic stem cell maintenance and differentiation media compositions.	48
Table 2.2. Human induced pluripotent stem cell (hiPSC) maintenance and differentiation medias to derive motor neurons, myoblasts and astrocytes.....	51
Table 2.3. SgRNA and primer sequences used for genetic engineering of hiPSC lines.....	55
Table 2.4. Details of primary and secondary antibodies used for immunofluorescence	59
Table 2.5. qRT-PCR primer sequences used	60
Supplementary Table 6.1. Passive membrane properties and other electrophysiological parameters.	188
Supplementary Table 6.2. Passive membrane properties and other electrophysiological parameters.	189

List of abbreviations

2D	Two-dimensional
3D	Three-dimensional
AAVS1	Adeno-associated virus integration site 1
ACh	Acetylcholine
AChR	Acetylcholine receptor
ACs	Astrocytes
AD	autosomal dominant
ADP	Adenosine diphosphate
AIS	Axon initial segment
ALS	Amyotrophic lateral sclerosis alpha-amino-3-hydroxy-5-methyl-4-isoxazole-propionic acid
AMPA	acid
AP	action potential
AR	autosomal recessive
ASD	Autism spectrum disorder
ATP	Adenosine triphosphate
BCR-Abl	breakpoint cluster region gene - ableson proto-oncogene
bFGF/FGF2	Basic fibroblast growth factor
bHLH	Homeobox gene
BMP	Bone morphogenetic protein
bp	Base pair
BPD	Bi-polar disorder
BSA	Bovine serum albumin
Ca ²⁺	Calcium
CAG	Chicken beta-actin promoter
CAMK	Calcium/calmodulin dependent protein kinase
CAS9	CRISPR-associated protein 9
CD14	Cluster of differentiation 14
CHAT	Choline acetyltransferase
CHR2	Channel rhodopsin 2
CHR2-YFP	Channel rhodopsin 2 yellow fluorescent protein
CLYBL	Citramalyl CoA lysase
CNS	Central nervous system
CNTF	Ciliary neurotrophic factor
CRISPR	Clustered regularly spaced palindromic repeats
Ct	Threshold cycle
DAPI	4',6-diamidino-2-phenylindole
DMD	Duchenne muscular dystrophy
DMEM	Dulbeco's modified eagle serum
DMSO	Dimethylsulphoxide
DNA	Deoxyribonucleic acid

DOK7	Docking protein 7
Dox	Doxycycline
DTC	d-Tubocurarine
E6	Essential 6 medium
EB	Embryoid body
EB1/3	End-binding protein 1/3
EDTA	ethylenediaminetetraacetic acid
EGF	Ectodermal growth factor
EPP	Endplate potential
E/IPSP	Excitatory/inhibitory post synaptic potential
ESC	Embryonic stem cell
FACS	Fluorescent activated cell sorting
FF	Fast fatigable
FR	Fast resistant
FTD	Frontal temporal lobe dementia
GABAA	Y-Aminobutyric acid type A
GD (11)	Growth differentiation factor (11)
GDNF	Glial derived neurotrophic factor
GFAP	Glial fibrillary acidic protein
GFP	Green fluorescent protein
GO	Gene ontology
GWAS	Genome wide association study
HB9	
(MNX1)	Motor neuron and pancreas homeobox
HCI	High content imaging
hiPSC	human induced pluripotent stem cell
HMC	Hypaxial motor column
HOX	Homeobox
IGF	Insulin-like growth factor
Indel	insertion/deletion
ISL1	Insulin gene enhancer protein 1
K+	Potassium
KL4	Kruppel-like factor 4
Kv1	Voltage gated potassium channel subunit
LED	Light-emitting diode
LMC	Lateral motor column
LRP4	LDL receptor related protein 4
MACS	Magnetic activated cell sorting
mESC	mouse embryonic stem cell
MF	Myofiber
MM	mismatch
MMC	Median motor column
MNPs	Motor neuron progenitors

MNs	Motor neurons
mRNA	messenger RNA
MUSK	Muscle associated receptor tyrosine kinase
MYH	Myosin heavy chain
MYH2	Myosin
MYOD	Myoblast determination protein 1
MYOG	Myogenin
Na ⁺	Sodium
Nav1.X	Voltage gated sodium channel subunit
Ndel1	NudE neurodevelopmental protein 1
NEAA	Non-essential amino acids
NEPs	Neuroectodermal progenitors
NF1	Neurofibronin 1
NMDA	N-methyl-D-aspartate
NMJ	Neuromuscular junction
NRCAM	Neuronal adhesion molecule
O.OCT4	Octamer binding transcription factor 4
OLIG2	Oligodendrocyte transcription factor 2
PAX	Homeobox gene
PBS	Phosphate buffered saline
PC	Principle component
PCR	polymerase chain reaction
PDMS	Polydimethylsiloxane
PFA	Paraformaldehyde
PGC	Preganglionic column
PIV	Particle image velocimetry
PN	Phrenic nucleusLM
QR	Quick response
qRT-PCR	Quantitative reverse transcription polymerase chain reaction
RA	Retinoic acid
RIPK1	Receptor interacting serine/threonine kinase 1
RNA	ribonucleic acid
RNP	Ribonucleoprotein
RT	Room temperature
S	Slow
SAG	Sonic hedehog agonist
SEM	Standard error of the mean
sgRNA	Synthetic guide RNA
SHH	Sonic hedgehog
SNARE	SNAP recteptor
SOX2	Sex determining region Y-box 2
STORM	Stochastic optical reconstruction microscopy

SV2	Synaptic vesicle 2
TALENS	Transcription activator-like effector nucleases
TGF β	Homeobox gene
TIDE	Tracking of indels by decomposition
TRIM46	Tripartite motif containing protein 46
TTN	Titin
TTX	Tetrodotoxin
TUBB3	Tubulin beta 3 class III
VACHT	Vascular acetylcholine transporter
VEGFA	Vascular endothelial growth factor A
VGCC	Voltage gated calcium channel
VNC	Vinculin
Wnt	Wingless-related integration site
XD	X-linked dominant

1. Introduction

1.1 Motor neuron development

Motor neurons relay information from the brain to the body and govern voluntary movement of skeletal muscles, as well as autonomic control of cardiac/smooth muscle. Broadly they are categorised into two types: upper motor neurons, and lower motor neurons. The cell bodies of upper motor neurons reside in the primary motor cortex (M1) and brainstem and project axons into the spinal cord where they form glutamatergic synapses on other neurons. Conversely the cell bodies of lower motor neurons reside in the brainstem or the ventral horn of the spinal cord and project axons out of the spinal cord to form cholinergic synapses on target muscle (Stifani 2014). Lower motor neurons are further subdivided into three types: visceral, branchial and somatic. Visceral motor neurons form part of the autonomic nervous system and are responsible for sympathetic and parasympathetic control of cardiac and smooth muscle found in glands, organs and arteries. They are further divided into preganglionic (located in the CNS) and post ganglionic (located in the PNS). Branchial motor neurons innervate striated muscle in the face and neck and only differ from somatic motor neurons in their developmental origin from the branchial arches rather than the somites. Somatic motor neurons control voluntary movement of skeletal muscle for the rest of the body. Collectively these different types of spinal motor neurons are organised into coherent target-specific columnar arrangements within the ventral horn of the spinal cord termed motor pools. These include the phrenic nucleus (PN), lateral motor column (LMC), preganglionic column (PGC), hypaxial motor column (HMC) and median motor column (MMC). Somatic motor neurons are also further subdivided based on the type of muscle fiber they innervate. Alpha and beta motor neurons innervate extrafusal fibers responsible for movement and can be further divided into fast fatigable (FF), fast resistant (FR) and slow (S). beta and gamma motor neurons innervate intrafusal muscle fibers responsible for modulating stretch sensitivity. Alpha FF motor neurons are typically the largest neurons, while beta and gamma motor neurons the smallest (Kanning, Kaplan and Henderson 2010).

During development, signals including noggin, chordin, and follistatin are emitted from the dorsal lip of the blastopore – the Spemann-Mangold organiser – and act to inhibit bone morphogenetic protein 4 (BMP4) signalling, leading to the specification of the neuroectoderm

(Davis-Dusenbery et al. 2014). In higher organism's additional inductive signals including fibroblast growth factor (FGF), ectodermal growth factor (EGF) and Wnts are also required (Davis-Dusenbery et al. 2014). This process leads to the formation of the neural plate, which folds to become the neural tube. Morphogenetic signalling along the rostro-caudal/anterior-posterior axes of the neural tube by retinoic acid (RA) generated by Raldh2 in the somites specifies the spinal cord. In particular high levels of RA specifies the initial spinal cord/hindbrain boundary from the forebrain. Decreasing concentration of RA complemented by increasing opposing concentrations of FGF18 and GDF11 at the other end of the neural tube specifies caudal spinal cell types (Liu, Laufer and Jessell 2001). Activation of specific HOX genes along this axis acts to further specify MN subtypes. *HOX* genes are arranged in four chromosomal clusters (*HoxA*, *HoxB*, *HoxC*, *HoxD*), each of which is further divided into 13 paralogues (*Hox1-13*). Spatial and temporal expression of each *Hox* gene is concordant with chromosomal position, so *Hox1* genes are expressed rostrally and *Hox13* genes are expressed caudally. *Hox4-8* genes are expressed at brachial regions, *Hox8-9* at thoracic regions, and *Hox10-11* at lumbar regions. The dorso-ventral axis of the neural tube is specified by morphogenetic signalling of BMPs/TGFβs released from the dorsal roof plate (Lee, Mendelsohn and Jessell 1998) and sonic hedgehog (Shh) released from the floor plate/notochord (Lee, Dietrich and Jessell 2000). The action of these morphogens patterns the dorso-ventral axis of the neural tube into distinct progenitor domains: p0-p3, which give rise to V0-V3 interneurons as well as pMN which gives rise to motor neurons. This is achieved by specific activation of cross-repressive class I and class II homeodomain and basic helix-loop-helix (bHLH) transcription factors. Shh signalling activates class II transcription factors such as NKX6.1, OLIG2 and NKX2.2, which in turn repress expression of class I transcription factors such as PAX6, IRX3, DBX1 and DBX2. Specific activation of PAX6, OLIG2, NKX6.1, and NKX6.2 gives rise to the pMN domain, which gives rise to motor neurons (Jessell 2000). Cell cycle exit is driven by expression of HB9 and ISL1 to generate post-mitotic motor neurons. Mature motor neurons later begin to express choline acetyl transferase (CHAT), although this is not specific and also expressed by other cholinergic neurons in the central nervous system (Ahmed, Knowles and Dehorter 2019). Motor neurons are only created during embryonic neurogenesis and as such cannot regenerate during adulthood.

promote DNA methylation and increase GFAP expression, while NOTCH signalling induces expression of NFIA and NF1B, which activates promoters of other astrocyte specific genes such as *SOX9*, *S100b* and *GLAST* by displacing DNMT1 (Tiwari et al. 2018). Mature astrocytes in the spinal cord secrete trophic factors such as VEGF, GDNF, CNTF and IGF-1 that are important for motor neuron survival and are upregulated following spinal cord injury as a protective mechanism (Tovar-y-Romo et al. 2014). Mature astrocytes also promote neuronal survival by removing excess glutamate at synapses, preventing glutamate induced excitotoxicity (Rothstein et al. 1996). Astrocytes also support neurons by responding to changes in blood flow, maintaining ionic and pH homeostasis, modulating synaptic activity, and by regulating CNS energy and metabolism (Sofroniew and Vinters 2010). In response to pathological situations astrocytes can become reactive, whereby they undergo morphological, molecular and functional changes. Reactive astrocytes can vary considerably depending on the pathological situation and may confer protective as well as deleterious effects (Escartin et al. 2021).

1.3 Skeletal muscle development

Skeletal muscle develops from the paraxial mesoderm, with myogenesis occurring in the somites. Somites are formed from pre-somitic mesoderm through an oscillatory gene network that acts to produce pulses of morphogens (Notch, FGF and Wnt) which create new somites in a time-dependent manner during axis elongation (Chal and Pourquie 2017, Bentzinger, Wang and Rudnicki 2012). Retinoic acid and Wnt gradients specify the rostro-caudal identity of the developing somites. The dorso-ventral axis of each somite is patterned by morphogen gradients of Shh, Wnt and BMP. Shh released ventrally from the notochord induces formation of the mesenchymal sclerotome, which ultimately forms bone and cartilage. Conversely dorsal Wnt signalling from the neural tube specifies the dermomyotome, which goes on to form skeletal muscle. BMP signalling from the lateral plate mesoderm inhibits lateral somitogenesis.

Within the dermomyotome distinct transcriptional programmes control myogenesis, whereby skeletal myoblasts exit the cell cycle to form myocytes. These in turn fuse to form multinucleated myotubes, which then align and mature into contractile myofibers. Skeletal

myoblasts are defined by the expression of PAX3, PAX7, MYF5 and MYOD and are found in the myotome – a layer of cells sandwiched between the ventral sclerotome and the dorsal dermomyotome. The first cells to exit the cell cycle are the myocytes, defined by the expression of MYOD, MYOG, and MRF4, however a resident PAX7+ satellite stem cell population is maintained into adulthood in order to regenerate damaged muscle (Yin, Price and Rudnicki 2013). Following fusion into myotubes, maturation of myofibers is defined by expression of TTN (Titin), and myosin heavy chains: Embryonic myosin heavy chain (MYH3) and slow myosin heavy chain (MYH7).

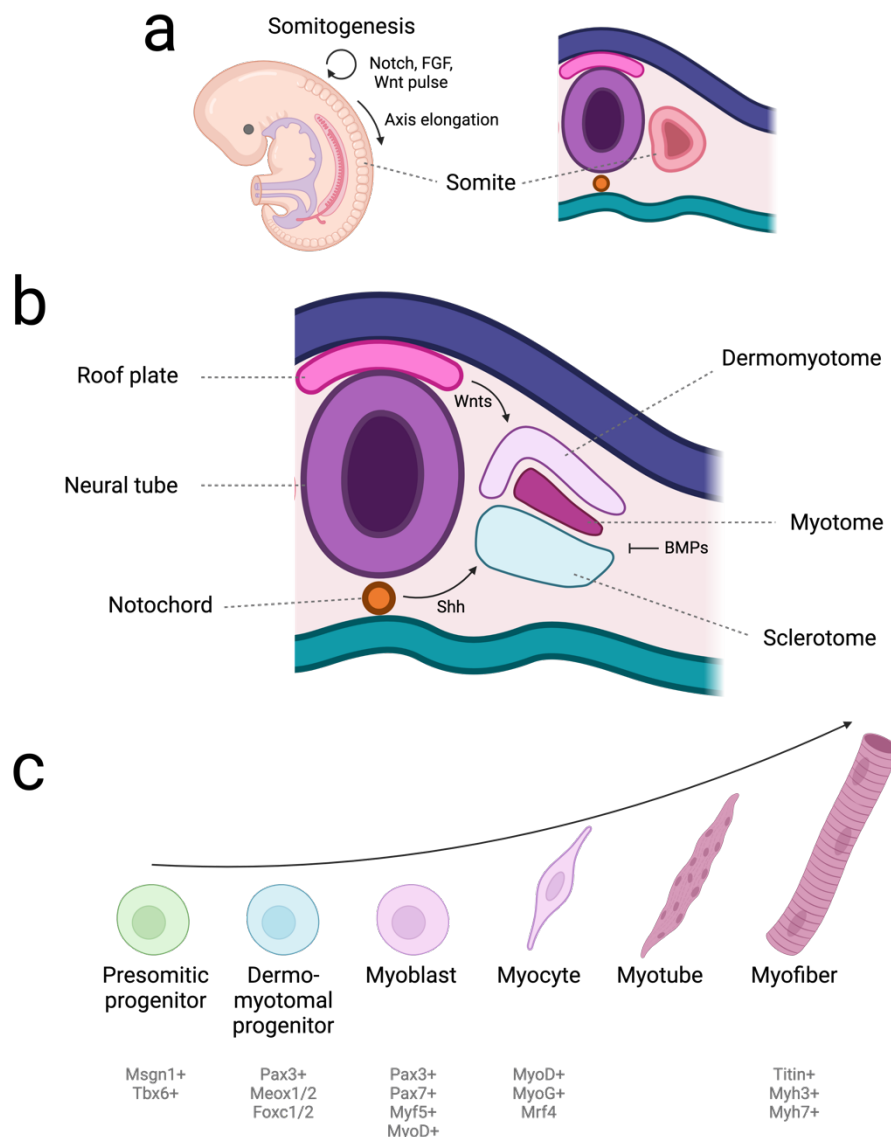


Figure 1.2. Development of skeletal muscle.

A, Somitogenesis via periodic Notch, FGF, Wnt signalling during axis elongation. **B**, Specification of the somites into dermomyotome, myotome and sclerotome by Wnt and Shh signalling. **C**, Hierarchy of myogenic transcription factors. Adapted from (Bentzinger et al. 2012).

1.4 The neuromuscular junction

The neuromuscular junction (NMJ) is a specialised tripartite synapse formed between motor neurons, myofibers and terminal Schwann cells. This synapse converts pre-synaptic action potentials into myofiber contractility via release of the chemical neurotransmitter, acetylcholine, across the synaptic cleft. NMJs are small structures (30um) and in mice form a classically described 'pretzel' shaped morphology, although human NMJs are typically smaller and more fragmented (Cruz et al. 2020, Sanes and Lichtman 1999, Jones et al. 2017). Acetylcholine is synthesised from acetyl coenzyme A (AcCoA) and choline by the enzyme choline acetyltransferase (ChAT) and packaged into vesicles via the vesicular acetylcholine transporter (VACHT). Pre-synaptic action potentials arrive at the nerve terminal and trigger the opening of voltage-gated calcium channels, leading to Ca²⁺ inflow, which triggers vesicle fusion and release via the SNARE proteins. ACh travels across the synaptic cleft and binds to the α , δ and ϵ -subunits of the ACh-receptor (AChR), inducing a conformational opening of the receptor. This facilitates influx of positively charged ions to generate an endplate potential (EPP), activating NAV1.4 voltage-gated sodium channels to open, which in turn generates an action potential that propagates along the myofiber. This depolarisation activates dihydropyridine (VGCCs) and ryanodine receptors leading to Ca²⁺ release from the sarcoplasmic reticulum. Ca²⁺ in turn binds to Troponin C to expose the myosin binding sites on actin. Hydrolysis of ATP then leaves ADP and an inorganic phosphate bound to the myosin head. The myosin head makes a weak contact on the actin filament releasing the inorganic phosphate, which reinforces the binding affinity of myosin and actin, triggering the 'power stroke' whereby actin and myosin filaments slide in opposing directions and release ADP, generating contractile force. A new ATP molecule can then bind to the myosin head domain causing it to release the actin filament by reducing its affinity for actin and causing a large conformational shift in the myosin head, bending it to a position further along the actin filament, facilitating crossbridge recycling (Cooke 2004).

During development motor axons innervate pre-patterned AChR clusters on the myofibers (Kim and Burden 2008). The presynaptic terminal of the developing axon secretes a unique form of neuronal agrin, which binds to LRP4 on the muscle and activates MuSK leading to the formation of a tetrameric complex (Zong and Jin 2013). MuSK activation then leads to further clustering of AChRs via the scaffolding protein rapsyn and the docking protein DOK7. Subsequently aneural AChR clusters are dispersed by a negative cue thought to be driven by synaptic release of ACh. Furthermore, LRP4 acts as a retrograde trophic signal responsible for presynaptic organisation and differentiation. Terminal Schwann cells also play a critical role in AChR clustering during development and ablation of them leads to reduced number and size of clusters as well as reduced miniature endplate potential amplitude (Barik et al. 2016). Initially myofibers are poly-innervated by multiple motor axons, however during NMJ maturation motor axons are eliminated in an activity dependent manner until one myofiber is innervated by a single motor axon (Barber and Lichtman 1999, Sanes and Lichtman 1999). Conversely one motor neuron can innervate many individual myofibers – and this is termed a motor unit.

Neuronal activity is crucial for the development and maintenance of functional motor units. While synaptogenesis can occur initially in the absence of neuronal activity (Varoqueaux et al. 2002, Verhage et al. 2000, Sando et al. 2017, Sigler et al. 2017), mice lacking the capacity to generate acetylcholine at the NMJ, and thus completely lacking any neuromuscular transmission, exhibit a reduction in the number and size of motor units, suggesting that activity may in fact be important for initial synaptogenesis at the NMJ (Brandon et al. 2003). Neuronal activity is also crucial for synaptic elimination, refinement, maintenance, and plasticity during development and in mature synapses. Indeed, activity dependent synaptic elimination is a crucial process allowing immature poly-innervated myofibers to become mono-innervated (Sanes and Lichtman 1999). Numerous studies have shown that early in development higher frequency axons have a competitive advantage over lower frequency axons, however this trend is reversed later in development in order to favour the higher efficacy of lower firing axons (Barber and Lichtman 1999). More recent work has found that precise spike timing is crucial for this process, since synchronous spiking of two axons innervating the same myofiber did not lead to elimination of either synapse, while asynchronous spiking promoted elimination (Favero, Busetto and Cangiano 2012).

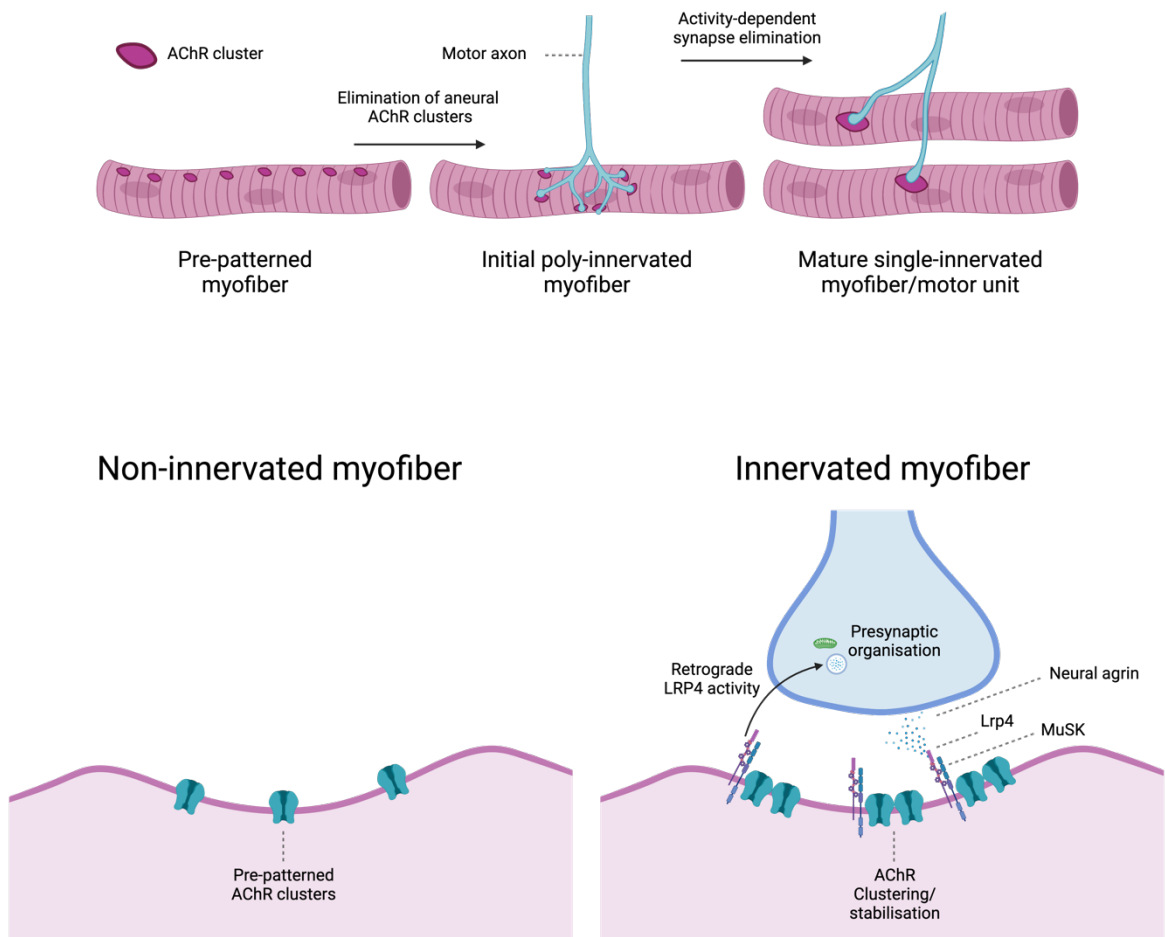


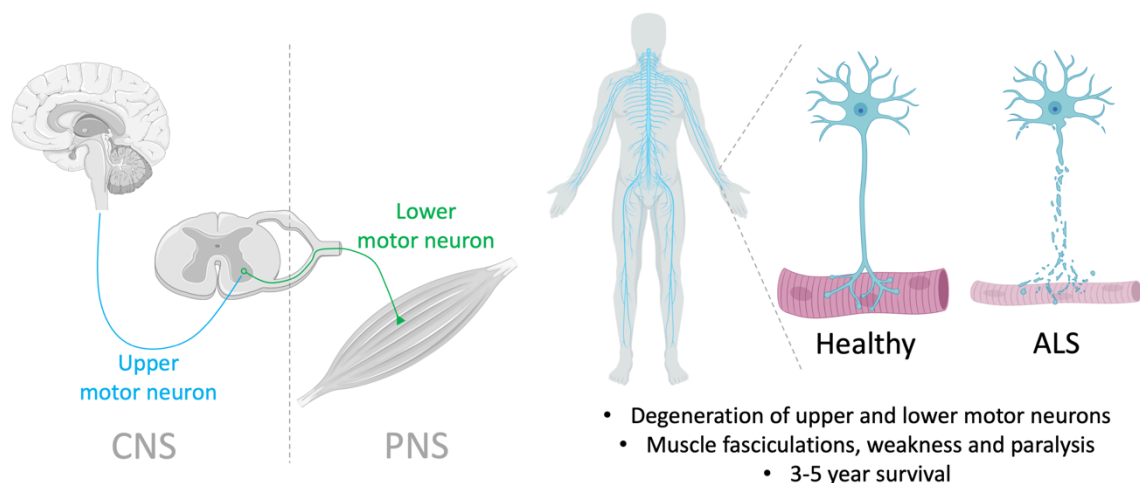
Figure 1.3. Development of the neuromuscular junction

Initially myofibers with pre-patterned AChR clusters become poly-innervated by motor axons. Post-natal activity dependent synapse elimination leads to the formation of mature motor units where a myofiber is innervated by a single motor axon. NMJ formation requires the concerted activity of neural agrin, and post-synaptic LRP4 and MUSK to stabilise AChR clusters.

1.5 Amyotrophic Lateral Sclerosis (ALS) background

Amyotrophic lateral sclerosis (ALS) is a fatal neuromuscular disease characterised by degeneration of both upper and lower motor neurons in the brain and spinal cord, leading to progressive paralysis and death within around 3-5 years of initial diagnosis (Figure 1). The disease carries a cumulative life-time risk of 1:300 and usually occurs between the ages of 50-65 (Johnston et al. 2006, Mehta et al. 2019). Initial clinical presentation typically falls into

three categories. 1, spinal onset – seen in approximately 65% of cases is characterised by asymmetric limb symptoms, including muscle fasciculations (spontaneous contractions), cramping and weakness. 2, bulbar onset – seen in around 30% of cases is characterised by dysphagia (difficulty in swallowing) and dysarthria (difficulty with speech). 3, respiratory onset – only seen in <5% of cases is characterised by early respiratory dysfunction such as dyspnea (shortness of breath) and poor vocal projection (Hardiman, van den Berg and Kiernan 2011, Logroscino et al. 2010). Although primarily a disease affecting motor function, nearly 50% of patients also develop cognitive and behavioural impairments (Phukan et al. 2012). Approximately 14% of patients are also given a formal diagnosis of frontal temporal lobe dementia (FTD) and conversely a similar proportion of FTD patients also develop ALS (Phukan et al. 2012). Combined with the fact that several genetic factors have been linked to the two diseases – most notably hexanucleotide repeat expansions in *C9orf72* – has led many to consider ALS and FTD as a spectrum neurodegenerative disorder (Table 1) (Hardiman et al. 2017).



- Degeneration of upper and lower motor neurons
- Muscle fasciculations, weakness and paralysis
- 3-5 year survival

Figure 1.4. Summary of amyotrophic lateral sclerosis (ALS).

ALS is characterised by degeneration of upper and lower motor neurons in the brain and spinal cord, leading to muscle wasting, paralysis and death within 3-5 years following initial diagnosis.

1.6 Genetics of ALS

Approximately 90% of ALS cases occur sporadically, while the remaining 10% of patients are found to have first and second degree affected relatives – often termed familial ALS (Taylor, Brown and Cleveland 2016). This characterisation however is an oversimplification and largely based on studies in ancestral European and east Asian populations (Hardiman et al. 2017). Sometimes sporadic ALS is mistakenly described as having no genetic basis, however DNA sequencing of individuals with sporadic ALS often reveals the occurrence of mutations in the same genes associated with familial ALS with evidence of complex oligogenic and polygenic inheritance patterns. Furthermore, of the >30 genes that confer a major risk of ALS and follow known mendelian-inheritance patterns, there is strong evidence of low (<50%) phenotypic penetrance and genetic pleiotropy (Table 1). Four genes: *C9orf72*, *TARDBP*, *SOD1*, and *FUS* account for up to 60-70% of cases with known family history. With *C9orf72* expansions being the most common in European familial ALS (33.7%), followed by *SOD1* mutations (14.8%), then *TARDBP* mutations (4.2%) and finally *FUS* (2.8%) (Mejzini et al. 2019). In contrast, there remains a considerable gap in our understanding of the genetics in seemingly sporadic cases of ALS. Large GWAS studies suggest this complex genetic architecture is based primarily on many rare individual variants specific to individuals, families and populations, rather than large numbers of common variants. In an effort to bridge this gap in understanding a recent study published by the Project MinE Consortium performed ancestral GWAS across 29,612 patients with ALS and 122,656 controls and identified 15 additional risk loci (van Rheenen et al. 2021).

Locus	Gene (protein)	Inheritance	Mechanisms
ALS1	<i>SOD1</i> (Superoxide dismutase)	AD/AR	Oxidative stress
ALS2	<i>ALS2</i> (Alsin)	AR	Endosomal trafficking
ALS3	Unknown	AD	Unknown
ALS4	<i>SETX</i> (Senataxin)	AD	RNA metabolism
ALS5	Unknown	AR	DNA repair, axon growth
ALS6	<i>FUS</i> (RNA-binding protein FUS)	AD/AR	RNA metabolism
ALS7	Unknown	AD	Unknown
ALS8	<i>VAPB</i> (VAMP-associated protein B/C)	AD	ER stress
ALS9	<i>ANG</i> (Angiogenin)	AD	RNA metabolism
ALS10	<i>TARDBP</i> (TAR DNA-binding protein 43)	AD	RNA metabolism
ALS11	<i>FIG4</i> (polyphosphoinositide phosphatase)	AD	Endosomal trafficking
ALS12	<i>OPTN</i> (Optineurin)	AD/AR	Autophagy

ALS13	<i>ATXN2</i> (Ataxin 2)	AD	RNA metabolism
ALS14	<i>VCP</i> (Valso-containing protein)	AD	Autophagy
ALS15	<i>UBQLN2</i> (Ubiquilin 2)	XD	UPS and autophagy
ALS16	<i>SIGMAR1</i> (Sigma non-opioid intracellular receptor 1)	AD	UPS and autophagy
ALS17	<i>CHMP2B</i> (Charged multivesicular body protein 2B)	AD	Endosomal trafficking
ALS18	<i>PFN1</i> (Profilin 1)	AD	Cytoskeleton
ALS19	<i>ERBB4</i> (receptor tyrosine-protein kinase erbB 4)	AD	Neuronal development
ALS20	<i>HNRNPA1</i> (Heterogeneous nuclear ribonucleoprotein A1)	AD	RNA metabolism
ALS21	<i>MATR3</i> (Matrin 3)	AD	RNA metabolism
ALS22	<i>TUBA4A</i> (Tubulin a4A)	AD	Cytoskeleton
ALS23	<i>ANXA11</i> (Annexin A11)	AD	Cell cycle
ALS24	<i>NEK1</i> (NIMA related kinase 1)	AD	Cell cycle
ALS25	<i>KIF5A</i> (Kinesin family member 5A)	AD	Axon transport
ALS26	<i>TIA1</i> (TIA1 cytotoxic granule associated RNA binding protein)	AD/AR	RNA metabolism
FTDALS1	<i>C9orf72</i> (Guanine nucleotide exchange C9orf72)	AD	RNA metabolism and autophagy
FTDALS2	<i>CHCHD10</i> (Coiled-coil-helix-coiled-coil-helix domain-containing 10)	AD	Mitochondrial maintenance
FTDALS3	<i>SQSTM1</i> (Sequestosome 1)	AD	Autophagy
FTDALS4	<i>TBK1</i> (Serine/threonine-protein kinase TBK1)	Unknown	Autophagy
FTDALS5	<i>CCNF</i> (Cyclin F)	Unknown	Cell cycle
FTDALS6	<i>VCP</i> (Valso-containing protein)	AD	Autophagy
FTDALS7	<i>CHMP2B</i> (Charged multivesicular body protein 2B)	AD	Endosomal trafficking
FTDALS8	<i>CYLD</i> (CYLD lysine 63 deubiquitinase)	AD	UPS and autophagy

Table 1.1. Genetic architecture of ALS and ALS-FTD.

AD = autosomal dominant, AR = autosomal recessive, XD = X-linked dominant. Adapted from (Hardiman et al. 2017), and omim.org.

1.7 Environmental risk factors for ALS

Mathematical disease occurrence models indicate that a combination of 6 genetic and environmental risk factors are required to initiate the onset of ALS. Indeed, a diverse array of environmental risk factors have been proposed to contribute to ALS, all with varying degrees of supporting evidence. These include age (risk increases proportionally with age), gender (1.5x more common in men), cigarette smoke (44% increased risk), lead, formaldehyde, agricultural pesticides, beta-methylamino-L-alanine, physical activity, trauma, electromagnetic radiation, cancer and the use of statins (Oskarsson, Horton and Mitsumoto 2015). Recent studies have shown that intense physical exercise is associated with earlier onset of ALS in patients with existing genetic risk factors (Julian et al. 2021), supporting the

notion of a complex interplay of genetic and environmental risk factors contributing to disease onset. Further to this, the Project MinE consortium found through mendelian randomisation analysis a potential causal role for high cholesterol in the pathogenesis of ALS (van Rheenen et al. 2021).

1.8 Histopathology of ALS

Mis-localised, misfolded, hyperphosphorylated and ubiquitinated pathological protein inclusions within motor neurons are one of the clearest histopathological hallmarks of ALS - similar to those seen in other neurodegenerative diseases, such as Lewy bodies containing alpha-synuclein in Parkinson's disease, and Amyloid plaques in Alzheimer's disease. In the vast majority of patients with ALS, TAR DNA-binding protein 43 (TDP-43) is found to be the predominant component of these inclusions, despite the fact that mutations to *TARDBP* are a rare cause of ALS (Figure. 2) (Neumann et al. 2006, Sreedharan et al. 2008). Superoxide dismutase (SOD1) inclusions on the other hand are widely observed in patients with familial SOD1 mutations; however, these same patients do not exhibit pathological TDP-43 inclusions. As such TDP-43 and SOD1 likely represent two very distinct subtypes of ALS. Furthermore abnormal accumulation of neurofilaments has been seen across divergent subtypes of ALS and can even be used as a reliable biomarker of neurodegeneration (Poesen and Van Damme 2019).

1.9 Superoxide dismutase 1 (SOD1)

Dominant mutations in the *SOD1* gene were the first identified genetic cause for ALS (Rosen et al. 1993), and as such have become the most widely studied ALS gene, with 4,378 papers published (Pubmed search, date: 01.02.22, search terms: "*SOD1*" + "ALS") vs. 2,502 for TDP-43 and 1,755 for *C9orf72*. The *SOD1* gene encodes the superoxide dismutase protein, which catalyses the conversion of highly reactive oxygen species (ROS) to hydrogen peroxide or oxygen (Barber and Shaw 2010). Indeed, oxidative stress is thought to play a pivotal role in ALS by driving apoptosis and necroptosis of motor neurons (Valko et al. 2006, Re et al. 2014). The combination of loss of SOD1 function and toxic gain of pathological SOD1 aggregates is thought to drive cell autonomous mechanisms of neuronal dysfunction. These include oxidative/ER stress, impaired autophagy, disorganised axonal transport, disturbed RNA

metabolism, and mitochondrial dysfunction. Interestingly non-cell autonomous mechanisms mediated by *SOD1* mutations have also been reported. In these cases, dysfunction of non-neuronal cell types such as microglia, oligodendrocytes, and astrocytes contributes to motor neuron dysfunction. It is thought that currently un-identified toxic species, possibly including TGF β 1, are transmitted from both micro-glia and astrocytes to motor neurons (Endo et al. 2015). Furthermore, altered expression of the glutamate transporters GLT1 and EAAT2 in *SOD1* astrocytes has been shown to reduce glutamate clearance (Pardo et al. 2006, Gibb et al. 2007). Combined with motor neurons intrinsically poor Ca²⁺ buffering capabilities this is thought to contribute to excitotoxicity and subsequent motor-neuron death (Taylor et al. 2016).

1.10 TAR DNA-binding protein 43 (TDP-43)

TDP-43 is a widely expressed 43kDa RNA/DNA binding protein, encoded by the *TARDBP* gene. It predominantly resides in the nucleus, where it plays a crucial role in microRNA biogenesis and regulates alternative splicing for numerous genes (Gregory et al. 2004, Arnold et al. 2013). In the cytoplasm TDP-43 plays a crucial role in stress granule formation, whereby redundant mRNAs are sequestered for degradation during periods of transient cellular stress (Colombrita et al. 2009). TDP-43 also plays an important role in axonal transport of RNA and localised RNA translation at synapses (Figure. 2) (Alami et al. 2014, Altman et al. 2021, Chand et al. 2018).

In ALS, TDP-43 becomes mis-localised to the cytoplasm, where it forms pathological aggregates with other proteins and RNAs via its highly disordered, low-complexity, C-terminal domain (Babinchak et al. 2019). Interestingly the majority of ALS-related *TARDBP* mutations cluster at this domain, encoded by exon 6 of the *TARDBP* gene, highlighting its importance in the pathogenesis of ALS (Figure. 2) (Prasad et al. 2019). Normally the low-complexity glycine rich and uncharged glutamine/asparagine rich sequences within this domain facilitate liquid-phase separation of TDP-43 into droplets, which is thought to be important for the transient formation of RNA stress granules (Gasset-Rosa et al. 2019). In ALS, mutations to this region as well as genetic and environmental factors that prolong cellular stress and impair autophagy are thought to contribute to chronic cytoplasmic aggregation of TDP-43. Indeed, other

causative ALS mutations affect proteins involved in autophagy and the ubiquitin proteasome system (UPS), such as *VCP*, *UBQLN2* and *OPTN*, *SQSTM1*, and *TBK1*. This is likely to contribute to pathological TDP-43 aggregation, since both autophagy and the ubiquitin proteasome system (UPS) are crucial for TDP-43 clearance (Scotter et al. 2014).

Pathological TDP-43 aggregates become hyperphosphorylated, ubiquitinated and insoluble and can be used to accurately stage the progression of ALS (Hasegawa et al. 2008). Interestingly, the c-terminal domain of TDP-43 shares many structural similarities to prion proteins in yeast, as well as other DNA/RNA-binding proteins implicated in ALS, including: *C9orf72*, *FUS*, *hnRNPA1*, and *MATR3* (Prasad et al. 2019). Indeed, it has been demonstrated that TDP-43 aggregates can spread in a prion-like fashion whereby misfolded TDP-43 can trigger misfolding of the naïve protein and thus seed the formation of new pathological aggregates. This process can occur along axons, between synapses and between supporting glial cell types. It is thought that this mechanism may contribute to the focal spreading of ALS pathology (Figure. 2) (Nonaka et al. 2013, Smethurst et al. 2016, Feiler et al. 2015).

The effect of TDP-43 aggregation is twofold; first TDP-43 is sequestered from performing its usual role within the cell, and as such there is a loss of function in alternative splicing, microRNA biogenesis, transient stress granule formation, axonal transport of mRNA/structural proteins, and localised protein synthesis at synapses. Secondly TDP-43 aggregates and cleaved peptides from the C-terminal region have a toxic gain of function effect, most notably in the prion like spreading of misfolded TDP-43, the production of abnormal mRNA splice variants, production of neurofilament accumulations that along with TDP-43 aggregates can physically damage/obstruction of axons and synapses, and activation of: ER-stress, oxidative stress, apoptotic and necroptotic signalling pathways that lead to cell death (Figure. 2) (Scotter, Chen and Shaw 2015).

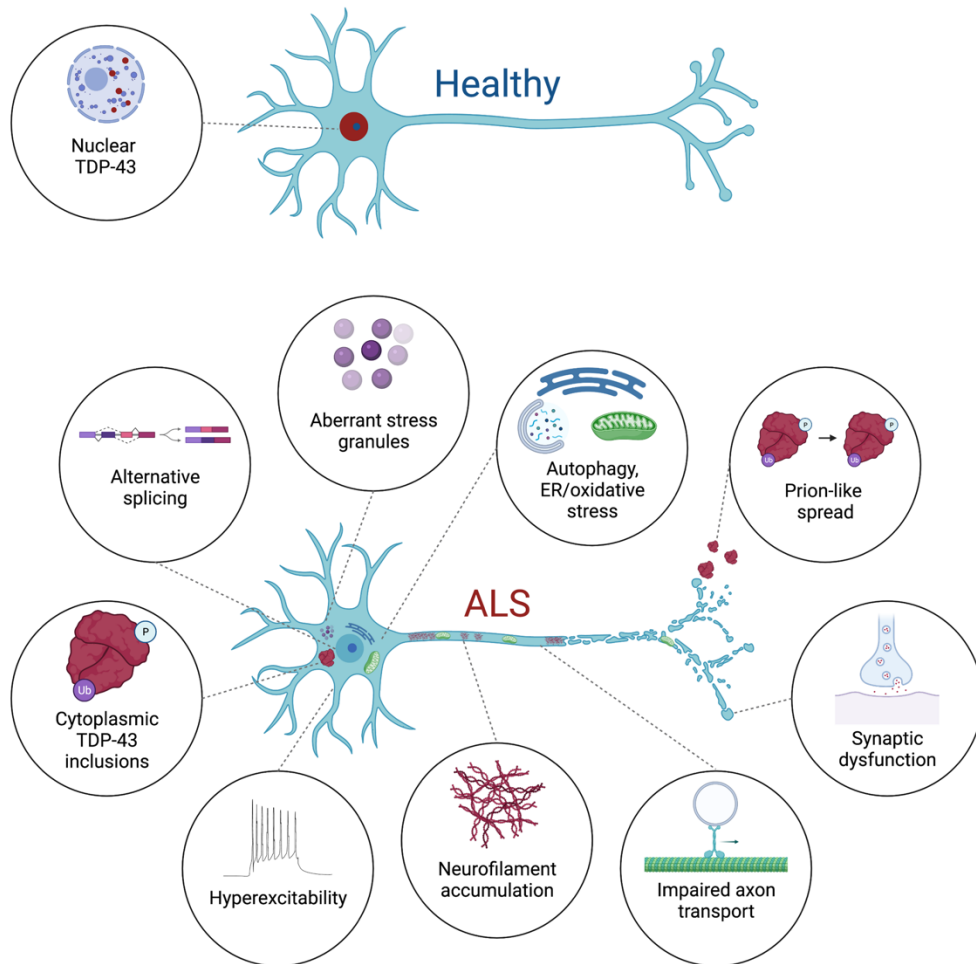
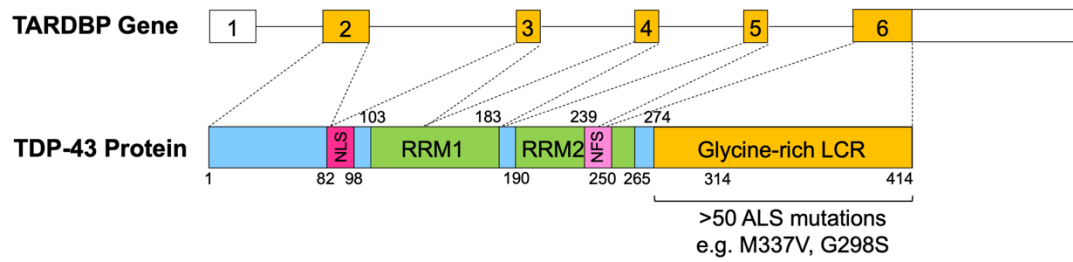


Figure 1.5. Overview of TDP-43 pathology in ALS.

Schematic of the *TARDBP* gene and TAR DNA-binding protein 43 (TDP-43) structure. Schematic outlining key pathological features associated with neuronal dysfunction and TDP-43 protein pathology.

1.11 The neuromuscular junction in ALS

There is strong debate as to where motor neuron degeneration is initiated in ALS. Whether neurodegeneration is initiated centrally and focally spreads in an anterograde fashion, termed the 'dying forward' hypothesis, or, whether neurodegeneration is initiated peripherally and spreads in a retrograde fashion, termed the 'dying back' hypothesis (Fischer et al. 2004). Often there is a lack of clarity as to whether these terms refer strictly to motor neuron subsystems i.e. do lower motor neurons degenerate before upper motor neurons? Or refer more specifically to domains within a single motor neuron, i.e. does the synapse degenerate prior to the cell body. Indeed, it would be possible that both could occur independently from one another or in conjunction with one another. While mounting genetic evidence certainly suggests that ALS has considerable overlap with frontal temporal lobe dementia – a CNS neurodegenerative disease, extensive evidence from patient and animal studies also suggests ALS is a distal axonopathy, implicating neuromuscular junction dismantling and axon degeneration as some of the earliest events in the disease. Ultimately, given the complex genetic and environmental landscape of ALS, it is possible that the site of disease initiation is equally diverse and complex and both 'dying forward' and 'dying back' mechanisms contribute to disease progression.

While it is hard to assess neuromuscular junction and axonal degeneration in patients with ALS, several studies have found evidence of axonal denervation (Hanyu et al. 1982), synapse loss (Sasaki and Maruyama 1994), abnormal calcium levels and mitochondrial function at neuromuscular synapses (Siklos et al. 1996, Borthwick et al. 1999). Other studies have demonstrated that changes in the estimated size and activity of motor units precedes the onset of clinical symptoms in patients (Felice 1997, Piotrkiewicz et al. 2008). Furthermore, in a single case study, post-mortem examination of a patient with mid-stage ALS who died of unrelated causes, found motor neuron degeneration only in the innervating muscle. Motor components in the spinal cord and motor cortex of the brain were completely normal (Fischer et al. 2004). Another study analysing muscle biopsies from patients with ALS showed that NMJ reinnervation was associated with extended survival time (Bruneteau et al. 2013), indicating not only NMJ involvement in the disease but also highlighting NMJ dysfunction as a potential target in extending life-span in patients with ALS.

More in-depth evidence for ALS as a distal axonopathy comes from transgenic animal models of the disease. Most notably the SOD1 mouse model shows clear evidence of synaptic weakening and impaired axonal transport before the first symptoms of the disease (Parkhouse et al. 2008). In this model, denervation at the NMJ occurs at day 47, followed by axonal degeneration in the ventral root between day 47 and 80, and finally loss of motor neuron cell bodies in the brain and spinal cord after day 80 (Fischer et al. 2004). Impaired axon transport of mitochondria and synaptic proteins to the NMJ is thought to contribute to ROS-induced ROS release, perturbed Ca²⁺ buffering and a diminished neurotransmitter pool at the NMJ (Pollari et al. 2014). It has also been shown that RIPK1 dependent necroptosis of oligodendrocytes may mediate axonal degeneration in the SOD1^{G93A} and OPTN mouse models of ALS (Ito et al. 2016).

While the precise causes of axonal degeneration in these models is not fully understood and is gradual and heterogeneous, there are a number of similarities to classical Wallerian degeneration that is caused by temporally and spatially precise axonal injury (Conforti, Gilley and Coleman 2014). This includes morphological similarities such as blebbing, fragmentation and swelling. This has led many to describe axonal degeneration in neurological disorders like ALS as “Wallerian-like degeneration”. However, while morphological similarities do not imply shared molecular cause, several lines of evidence would suggest some shared mechanistic overlap. For example overexpression of WLDs, a gene encoding a nicotinamide mononucleotide adenylyltransferase (NMNATs) that delays Wallerian degeneration (Mack et al. 2001), modestly extended lifespan in the SOD1 mouse model of ALS (Fischer et al. 2005). Furthermore, TDP-43 mediated loss of STMN2 via alternative splicing in models of ALS leads to axonal degeneration (Klim et al. 2019). Interestingly loss of STMN2 also occurs early in the latent phase of Wallerian degeneration (Shin et al. 2012).

With regards to TDP-43, studies have shown impaired axon transport (Alami et al. 2014), defective neuromuscular transmission (vesicle fusion and release) (Chand et al. 2018) and impaired localised synthesis of mitochondrial proteins (Altman et al. 2021) in various models of TDP-43 associated ALS. Furthermore, since TDP-43 regulates the splicing of a considerable number of axonal and synaptic proteins, loss of splicing or aberrant synaptic splice variants may also contribute to extensive synaptic dysfunction in ALS. For instance, it was recently

reported that knockdown of TDP-43 mediated inclusion of a cryptic exon in *UNC13A*, a critical synaptic protein, leading to reduced levels of expression. Indeed, *UNC13A* is emerging as an important synaptic target of TDP-43 and has also been shown to be a novel risk modifier allele for ALS (van Rheenen et al. 2021, Brown et al. 2022).

Since the NMJ is a tripartite synapse, comprising the pre-synaptic motor terminal, post-synaptic myofibers and terminal Schwann cells, signalling between all three of these components is essential for normal NMJ maintenance and stability. As such, both cell autonomous and non-cell autonomous mechanisms and the trophic support between these three components is crucial when considering dysfunction of neuromuscular junction in ALS (Moloney, de Winter and Verhaagen 2014). Indeed muscle specific expression of HDAC4 and its regulator microRNA-206 was shown to be crucial for NMJ reinnervation and extended lifespan in patients with ALS (Bruneteau et al. 2013). Increased release of NOGOA by muscle and semaphorin3A by terminal Schwann cells has also been shown to destabilise the NMJ in mouse models of ALS (Lin et al. 2019, De Winter et al. 2006). Further to this, a recent study showed that treatment using muscle specific MUSK antibodies could stabilise neuromuscular synapses and delay disease progression in SOD1 mice (Cantor et al. 2018). Interestingly it has recently been found that TDP-43 aggregates are also found in the skeletal muscle of patients with ALS (Mori et al. 2019), and other studies have shown that TDP-43 granules form in regenerating muscle (Vogler et al. 2018). These findings may suggest a muscle specific origin/contribution of TDP-43 pathology and synaptic dysfunction in ALS.

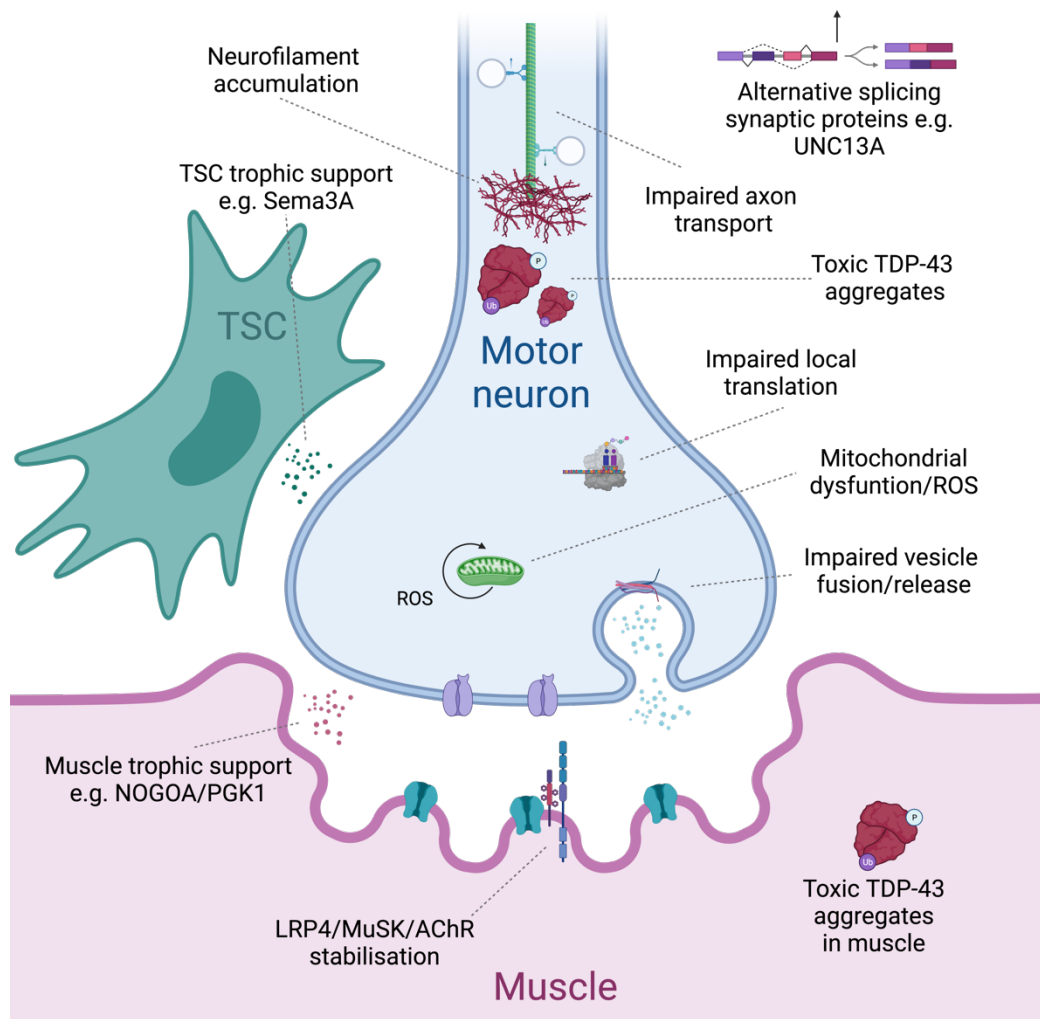


Figure 1.6. The neuromuscular junction in ALS.

Schematic outlining examples of pathological processes affecting the neuromuscular junction in ALS.

1.12 Modelling the neuromuscular junction *in vitro*

Studying neuromuscular synapses *in vitro* poses several key advantages, including easier manipulation and the possibility to scale studies beyond what would be possible using animal models – making them more amenable to early-stage drug discovery. Furthermore, with the development of human induced pluripotent stem cell (hiPSC) technologies it has become possible to generate and study human neuromuscular junctions, which have been shown to pose highly distinct morphological and molecular profiles compared to murine NMJs (Jones et al. 2017). Human iPSCs also allow patient derived cell types to be modelled with disease

specific backgrounds, facilitating the study of numerous genetic neuromuscular disorders in *in vitro* humanised model systems.

Shinya Yamanaka's seminal Nobel prize winning work describing the reprogramming of adult cells into embryonic like pluripotent stem cells by defined genetic "Yamanaka" factors – *OCT4*, *SOX2*, *KLF4* and *C-MYC*, opened the doors to a new age of *in vitro* human disease modelling (Takahashi and Yamanaka 2006, Takahashi et al. 2007). Indeed, the first hiPSCs derived from patients with a known genetic disease background were in fact from patients with ALS (Dimos et al. 2008). Techniques to differentiate pluripotent stem cells towards motor neuron and myoblast cell types were first crucial in the development of *in vitro* human neuromuscular circuits. One of the first methods to differentiate mouse embryonic stem cells (mESCs) into motor neurons utilised developmental principles in its approach by applying specific concentrations of the morphogens retinoic acid (RA) and Sonic hedgehog (Shh) that pattern the rostro-caudal and dorso-ventral identity of spinal motor neurons (Wichterle et al. 2002). More recent adaptations of this protocol allow the derivation of hiPSC-derived motor neuron progenitors that can be frozen and expanded before being differentiated into terminal motor neurons that could form neuromuscular synapses (Du et al. 2015). A criticism of these small-molecule approaches is the variability in efficiency between experiments and cell lines, and the possible contamination of immature or unrelated cell types. Forward programming techniques have been shown to overcome some of these limitations. In this approach, forced expression of specific transcription factors induces genetic programmes to drive cell fate acquisition. For motor neurons it was recently shown that by over-expressing *ISL1*, *LHX3* and *NGN2* motor neurons expressing HB9 could be generated at high efficiency. However, detailed functional characterisation of these cells – including the ability to fire action potentials and form functional neuromuscular junctions has not been demonstrated. With regards to derivation of myoblasts from hiPSCs, many of the first approaches also utilised small molecules to mimic morphogen signalling during development (Chal et al. 2016). As with similar approaches to derive motor neurons, variability in efficiency between experiments and cell lines is still a concern. Forward programming techniques have yielded more reproducible results, with forced expression of MYOD being used to generate terminally differentiated myocytes (Pawlowski et al. 2017), while forced expression of the earlier PAX7 marker being used to generate myoblast progenitors that can be expanded (Rao et al. 2018).

Furthermore, the establishment of optogenetic techniques whereby light-sensitive ion channels can be used to control neural activity has opened the possibility of precisely controlling the activity of *in vitro* neuromuscular circuits. One of the most widely adopted optogenetic actuators, channel rhodopsin-2 (CHR2) is a blue light-activated cation channel originally cloned from the alga *Chlamydomonas reinhardtii*. Incorporation of the engineered CHR2-YFP transgene into isolated neurons has been shown to facilitate sustained trains of light triggered activity at single action potential resolution (Zhang et al. 2006, Deisseroth et al. 2006).

Generating *in vitro* neuromuscular junctions from motor neurons and/or muscle derived from human PSCs in order to model human disease was first achieved by (Yoshida et al. 2015), where NMJs, characterised based on immunocytochemistry of pre- and post-synaptic structures, were found to be abnormal in co-cultures containing motor neurons from patients with spinal muscular atrophy (SMA). However functional neurotransmission at the neuromuscular junction was not assessed. Indeed (Abd Al Samid et al. 2018) showed that functional contractions of myofibers in 2D neuromuscular co-cultures led to detachment of the myofibers from the tissue-culture substrate, highlighting a major challenge in culturing contractile myofibers. To overcome these challenges (Uzel et al. 2016) developed a microfluidic co-culture system where myofibers were suspended between compliant micropillars. By optogenetically stimulating the motor neurons they were able to measure contractile force based on deflection of the pillars. Other teams have also developed similar micro-pillar approaches (Bakooshi et al. 2019). In more recent work Kamm and colleagues showed this approach could be used to model ALS by co-culturing ALS hiPSC-MNs (Osaki, Uzel and Kamm 2018). In this study it was shown that contractile force and reliability of neurotransmission was reduced in the TDP-43 ALS motor neuron containing co-cultures. However, it was unclear whether this may have been a result of the lower proportion of ISL1 positive MNs in the co-cultures – ~85% in wildtype cultures vs ~60% in the ALS cultures rather than a consequence of the ALS genotype. This highlights not only the importance of stabilising myofibers in a 3D scaffold, but also generating highly enriched and comparable cultures of motor neurons, an issue also raised by (Yoshida et al. 2015) who showed low yields (20-30%) of HB9 positive motor neurons. Another recent approach to model human neuromuscular

junctions *in vitro* was demonstrated through the generation of 3D neuromuscular organoids (Martins et al. 2020). However, like before, a drawback to this approach is the high proportion of undefined cell types in the culture and reproducibility between cell lines.

1.13 Neuronal excitability in ALS

Neuronal excitability is an intrinsic property of a neuron, referring to the propensity to which an output – a change in membrane potential, usually an action potential, is generated in response to a given input. Excitability can be modulated by numerous factors, such as the biophysical properties of a neuron, ion channel (e.g., Na⁺, K⁺, Ca²⁺) quantity and composition, and the affinity, quantity and composition of different post-synaptic neurotransmitter receptors (e.g., GABA_A, AMPA, NMDA, nAChR). Neural activity on the other hand is an emergent property of neuronal networks, determined by numerous factors, including the excitability of individual neurons, synapse number and strength, and excitation-inhibition (E/I) balance): driven by post-synaptic receptor composition and the relative numbers of excitatory and inhibitory neurons within the network (Gunes et al. 2020). Changes in neuronal excitability are not always reflected in overall changes in network activity – for instance lower levels of network activity may lead to homeostatic increases in neuronal excitability (Jamann et al. 2021, Galliano et al. 2021) and in pathological conditions such as epilepsy, reduced intrinsic excitability of inhibitory neurons can lead to network hyperactivity (Ogiwara et al. 2007).

Muscle fasciculations (spontaneous contractions) driven by altered neuronal excitability/activity are a common feature in the majority of patients with ALS (Liu et al. 2021, Mills 2010) and form a major diagnostic criteria for the disease (de Carvalho, Kiernan and Swash 2017, Hardiman et al. 2017). Fasciculations have been shown to peak early in the disease at the onset of muscle weakness and initial loss of motor units, then decline in conjunction with further loss of motor units as the rate of denervation exceeds that of reinnervation (Bashford et al. 2020). The severity of fasciculations also correlates with increased disease severity and reduced survival time in patients with ALS, suggesting that this phenomenon may play an active role in the progression of the disease (Shimizu et al. 2014). The exact cause of fasciculations is unclear, whether caused by increased drive from

hyperactive/excitable upper motor neurons in the cortex, loss of inhibitory function in the brain and spinal cord or increased intrinsic excitability of lower motor neurons.

Threshold-tracking transcranial magnetic stimulation (TMS) studies have revealed the occurrence of motor cortex hyperexcitability and hyperactivity in patients with ALS. This technique works by applying increasing intensities of magnetic stimulation and measuring the threshold intensity required to elicit neuronal firing (Barker and Jalinous 1985). By measuring associated motor evoked potentials (MEPs) in corresponding muscle groups other studies have been able to demonstrate that this cortical hyperexcitability/hyperactivity drives activation of lower motor neurons (Park, Kiernan and Vucic 2017). By varying TMS protocols to probe short interval intracortical inhibition (SICI) - a property of inhibitory network function, as well as intracortical facilitation (ICF) – a property of excitatory network function (Oliveri et al. 2000) various studies have demonstrated that cortical hyperactivity in patients with ALS arises from both increased intrinsic excitability (Vucic, Nicholson and Kiernan 2008) and loss of inhibition (Van den Bos et al. 2018).

Changes to the excitability/activity of lower motor neurons has also been extensively investigated in patients with ALS, through indirect nerve conductance (NCS) and electromyography (EMG) studies. These studies have demonstrated hyperexcitability/activity of lower motor neurons, evidenced by increased fasciculation potentials, and abnormal motor unit firing (Piotrkiewicz et al. 2008, Nakata et al. 2006, Vucic and Kiernan 2006). This increased excitability is likely due to imbalance in Na⁺ and K⁺ conductances (Kanai et al. 2006, Vucic and Kiernan 2010), possibly as a result of reduced ion channel expression (Howells et al. 2018).

While TMS and NCS studies provide invaluable indications of abnormal electrical activity in the brain and peripheral nerves of patients with ALS they cannot resolve intrinsic properties of individual neurons or the molecular and structural mechanisms that contribute to these changes. Furthermore, the precise mechanisms of TMS are poorly understood owing to magnetic interferences that prevent direct electrode-based recordings within a 100ms interval following application of the stimulation (Li et al. 2017). As such these studies need to be complemented by direct electrophysiological approaches in animal and cell culture models

(Scanziani and Hausser 2009). In particular, whole-cell patch clamp recordings provide unprecedented detail on the electrical properties of individual neurons with high signal to noise sensitivity. Voltage clamp recordings allow measurement of ionic currents and when paired with pharmacological inhibitors can be used to isolate specific currents, most notably fast inward Na⁺ and steady state outward K⁺ currents. Current clamp recordings on the other hand provide precise detail on the properties of single action potentials and crucially can measure the excitability of a neuron through measurement of the voltage threshold (inflection point) as well as current threshold (injected current required to elicit a single AP) and rheobase (minimum current required to elicit a single AP given an infinite duration of stimulation). Longer current clamp stimulation protocols can be used to stimulate trains of action potentials, providing input-output relationships of injected current to spike frequency – a crucial measure of intrinsic neuronal excitability. Pairing patient data from TMS and NCS studies with detailed electrophysiological measurements from animal and cell culture models is crucial to understanding how neuronal excitability is modulated in ALS.

To this end, hyperexcitability of lower motor neurons has been extensively demonstrated in the SOD1 mouse model of ALS using whole-cell patch clamp recordings. These studies found evidence of increased persistent Na⁺ currents, reduced voltage and current thresholds for AP firing, increased firing frequency in response to injected current, and increased maximum firing rate (Kuo et al. 2004, Kuo et al. 2005). Furthermore a mouse model of TDP-43 mislocalisation showed extensive hyperexcitability in cortical motor neurons, characterised by a shift in the relationship between injected current and AP spiking as well as reduced rheobase current threshold (Dyer et al. 2021). This model also showed simultaneous occurrence of reduced synaptic activity.

Several studies have also reported altered excitability in ALS patient-derived human induced pluripotent stem cell (hiPSC) motor neurons with a range of ALS-related mutations. Some studies report hyperexcitability (Wainger et al. 2014, Devlin et al. 2015), while others hypoexcitability (Sareen et al. 2013, Naujock et al. 2016). Interestingly, (Devlin et al. 2015) found that early motor neuron cultures (2-6 weeks) were hyperexcitable evidenced by a shift in the relationship of injected current to AP spiking, while later cultures (7-10 weeks) transitioned to a hypoexcitable state, evidenced by a reduction in Na⁺ and K⁺ currents.

Indeed, a transition to hypoexcitability has also been reported in mouse models and patient studies and probably reflects a decline in motor neuron function prior to cell death. It is also possible that the selective vulnerability of fast-fatiguable (FF) motor units to degeneration is responsible for this decline in function.

Neuronal hyperexcitability has long been suspected of contributing to excitotoxicity and MN vulnerability in ALS. Indeed, one of the few approved drugs to extend survival in ALS, Riluzole, primarily acts to dampen neuronal excitability by inhibiting persistent inward Na^+ currents as well as dampening glutamate induced excitotoxicity (Doble 1996, Song et al. 1997). Furthermore, the incidence of peripheral axonal and motor unit hyperexcitability leading to complex muscle fasciculations has been shown to correlate with increased disease severity and reduced survival time in patients with ALS, suggesting that this process influences progression of the disease.

1.14 Neuronal plasticity

Neuronal plasticity plays a crucial role in the adaptive control of neuronal networks and is achieved primarily through functional changes in synaptic strength and intrinsic changes to neuronal excitability (Zhang and Linden 2003). Two key forms of plasticity exist that play opposing roles in controlling network activity and connectivity. Homeostatic plasticity involves compensatory changes that are modulated around a set point via negative feedback to maintain a steady state and network stability (Fox and Stryker 2017). In contrast, Hebbian plasticity operates via positive feedback and leads to synaptic strengthening or weakening following changes in activity and is thought to be a key process for learning and memory in the brain (Hebb, Martinez and Glickman 1994, Galanis and Vlachos 2020, Fox and Stryker 2017). Within Hebbian plasticity, long-term potentiation (LTP) and long-term depression (LTD) are the two most well characterised. Long-term potentiation is a process whereby synaptic efficacy is increased following repeated stimulation (Lomo 2003), whereas long-term depression is where synaptic efficacy is reduced following patterned stimulus (Dudek and Bear 1992). Furthermore numerous forms of short-term synaptic plasticity have also been described (Zucker and Regehr 2002).

A huge range of cellular and molecular mechanisms are responsible for driving these different forms of neuronal plasticity. Changes in pre-synaptic function typically modify release probability and frequency dependent information (Costa et al. 2017). This is achieved through multiple mechanisms, including; cAMP/PKA signalling, structural changes to active zone (AZ) organisation, altered local protein synthesis, associative changes in retrograde signalling via GPCR and preNMDARs, and changes in release probability mediated through effectors such as Rab3, RIM1a, Munc13-1 and VGCCs (Sudhof 2012, Banerjee et al. 2016, Fourcaudot et al. 2008, Rosenberg et al. 2014). Conversely changes in post-synaptic function typically modify synaptic gain, or quantal amplitude (Costa et al. 2017). Numerous molecular mechanisms contribute to post-synaptic plasticity, including; signalling through NMDARs, mGLUR, PKC/CAMK2A, BDNF and MTOR, which typically act to alter the expression, phosphorylation and activity of post-synaptic neurotransmitter AMPA, NMDA and GABA receptors that account for cell intrinsic excitation/inhibition balance, and altered cytoskeletal organisation of actin and PSDs in the spine head (Caroni, Donato and Muller 2012). In addition to synaptic mechanisms driving Hebbian forms of plasticity, intrinsic changes to neuronal excitability can also produce large scale changes to neuronal output that simultaneously affects large ensembles of synapses (Zhang and Linden 2003). An elegant example of this is persistent firing following brief excitation in entorhinal cortical neurons (Egorov et al. 2002), thought to be driven by calcium dependent afterdepolarisation through CAN or ERG channels that leads to sustained Na⁺ influx (Debanne, Inglebert and Russier 2019). Other mechanisms that contribute to intrinsic plasticity include localised EPSP amplification in dendritic arbours and global changes in spike threshold and membrane potential mediated via ion channel expression and activation (Debanne et al. 2019).

Homeostatic forms of neuronal plasticity are required to maintain stable network activity; helping to keep Hebbian forms of plasticity under control and prevent extreme levels of activity that could lead to seizures, excitotoxicity and other pathological phenomenon (Keck et al. 2017). These homeostatic forms of plasticity are compensatory and act via negative feedback to keep activity around a set point. Synaptic forms of homeostatic plasticity have been widely documented, and found to be regulated spatially, developmentally and in a connection specific manner (Pozo and Goda 2010). For example in hippocampal neurons it was found that activity blockade resulted in both pre-and post-synaptic homeostatic

plasticity, characterised by increased mEPSC amplitude and release efficacy mediated by CAMK2A and CAMK2B (Thiagarajan, Piedras-Renteria and Tsien 2002). Activity-dependent gene expression and localised protein synthesis are thought to play a major role in homeostatic synaptic plasticity; key examples include Arc/Arg3.1 and eEF2 (Shepherd et al. 2006, Zhang et al. 2009). Other molecular mechanisms thought to contribute to homeostatic synaptic plasticity include neurotrophic signalling, interactions of cell adhesion molecules, post synaptic PSD-95, GluA1 and GluA2 levels and Ca²⁺ signalling via CAMK2, PLK2, CDK5 (Pozo and Goda 2010). Homeostatic regulation of intrinsic neuronal excitability may be even more influential on setting network excitability than more commonly studied forms of synaptic plasticity (Wilhelm, Rich and Wenner 2009). Homeostatic intrinsic plasticity can be achieved by dynamic regulation of voltage gated Na⁺ and K⁺ ion channel expression, phosphorylation, and localisation, with altered levels of activity thought to be primarily detected via alterations in calcium signalling through VGCC's (O'Leary, van Rossum and Wyllie 2010, Bulow et al. 2019, Morgan et al. 2019). Recent work has uncovered a pivotal role of the axon initial segment (AIS), the site of action potential generation in neurons, in modulating homeostatic regulation of neuronal excitability.

1.15 The axon initial segment (AIS)

The axon initial segment (AIS) is a specialised 20-60 μ m region of the proximal axon characterised by a unique cytoskeletal arrangement of scaffolding proteins that anchor receptors, ion channels and signalling molecules to the membrane. The axon initial segment serves two crucial functions: it specifies dendritic/axonal polarity and serves as the site for action potential (AP) initiation owing to its high density of voltage-gated Na⁺ and K⁺ channels, and as such plays a crucial role in regulating neuronal excitability.

Periodic spacing of actin rings occurs along the AIS at 190nm intervals, which are interconnected by AIS specific alpha-2 and beta-4 spectrin tetramers. Conversely alpha-2 and beta-2 spectrin tetramers are seen in the distal portion of the axon. The 480kDa isoform of Ankyrin-G then binds to the centre of the α 2/ β 4 spectrin tetramer and acts to anchor voltage-gated sodium and potassium channels to the membrane in a periodic manner (Figure 1.7). Furthermore Ankyrin-G anchors two cell adhesion molecules (CAMs): Neurofascin-186 and

NRCAM to the membrane. The intracellular c-terminal of Ankyrin-G also binds microtubules via interactions with microtubule proteins EB1/3 and Ndel1 (Leterrier 2018). The specific subtypes of sodium channels found at the AIS include Nav1.1, Nav1.2 and Nav1.6, while specific subtypes of potassium channels include Kv1.1, Kv1.2 and at the distal part of the AIS KCNQ2 and KCNQ3 that modulate excitability via M-type potassium currents (Fujitani, Otani and Miyajima 2021, Leterrier 2018).

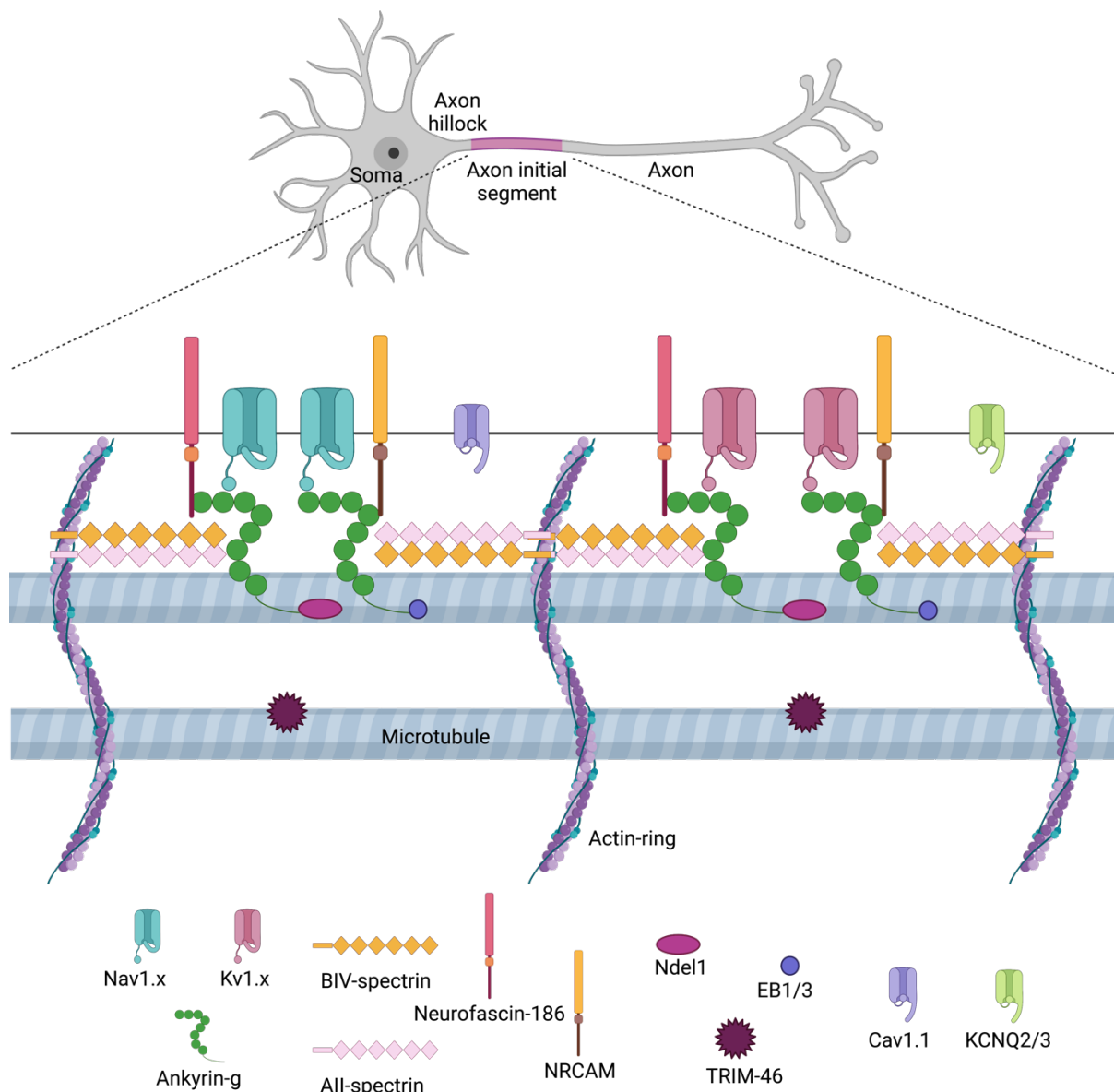


Figure 1.7. Cytoskeletal organisation of the axon initial segment (AIS)

Early studies demonstrated that the high density of voltage-gated Na⁺ channels found at the AIS was crucial for generating and shaping action potentials (Kole et al. 2008) and as such the

AIS was shown to be the primary site of AP initiation, rather than the soma. Indeed more recent studies in hiPSC-neurons show that AP and AIS maturation occur concurrently in a stage specific manner during neuronal polarisation (Lindhout et al. 2020). Remarkably, a growing body of research has shown that the structure of the AIS is able to undergo different forms of homeostatic activity-dependent plasticity. (Kuba, Oichi and Ohmori 2010) showed that in response to auditory deprivation the AIS of avian auditory brain stem neurons increased in length. This increase was associated with a homeostatic increase in excitability, characterised by reduced current and voltage thresholds, increased spontaneous AP firing and altered AP properties, including increased AP amplitude. (Grubb and Burrone 2010a) also showed that the AIS was able to distally relocate in response to increased levels of activity. This distal relocation was associated with a homeostatic reduction in excitability characterised by a downward shift in the input-output relationship of injected current to AP firing and increased current threshold. Further experimental studies have confirmed both changes in AIS length (Evans et al. 2015, Galliano et al. 2021, Jamann et al. 2021, Pan-Vazquez et al. 2020, Sohn et al. 2019) and position (Hatch et al. 2017, Lezmy et al. 2017, Wefelmeyer, Cattaert and Burrone 2015) are associated with corresponding changes in neuronal excitability. Computational modelling studies have also confirmed that increasing AIS length is predicted to increase neuronal excitability via increasing sodium conductance density. In these models both current and voltage thresholds are predicted to decrease with increasing AIS length, although current threshold was also shown to also be dependent on other biophysical properties of the neuron (Gulledge and Bravo 2016, Goethals and Brette 2020). These same computational studies relating AIS position to neuronal excitability throw up a more complicated picture, whereby distal relocation of the AIS increases resistive de-coupling from the soma, which is predicted to increase neuronal excitability – in contrast to many experimental findings (Gulledge and Bravo 2016). However, if hyperpolarising currents are present at the AIS then this trend is predicted to reverse. Indeed studies looking at inhibitory axo-axonic synapses at the AIS confirm this relationship (Wefelmeyer et al. 2015). Calcium signalling via L-type voltage gated Ca^{2+} channels (Cav1.1) calcineurin and CAMK2 has been shown to be crucial for AIS plasticity (Evans et al. 2013). Furthermore, phosphorylation of myosin light chain kinase (pMLC) and localised myosin 2 activity has also been shown to be crucial for this process (Berger et al. 2018).

The AIS has been implicated in an increasing number of pathophysiological conditions, including autism spectrum disorder (ASD), bi-polar disorder (BPD), Schizophrenia, epilepsy, diabetes, traumatic brain injury, stroke, neuroinflammation, hereditary motor neuropathy, and Alzheimer's disease (Fujitani et al. 2021). Indeed, direct pathogenic mutations to AIS genes have been found in several conditions. Mutations to *ANK3* (encoding ankyrin-G) have been found in patients with ASD, and BPD. Mutations to *SCN1A* (encoding Nav1.1) have been found in patients with epilepsy – most notably in Dravet Syndrome. Mutations to *SPTAN1* (encoding α 2-spectrin) have been found in patients with epilepsy, spastic quadriplegia and hereditary motor neuropathy. Mutations to *SPTBN4* (encoding β 4-spectrin) have been found in patients with congenital neuropathy and motor axonal neuropathy. Mutations in *KCNQ2* are also seen in numerous forms of childhood epilepsy (Lee et al. 2019). There is also direct evidence of altered AIS characteristics in numerous pathophysiological conditions. Decreased AIS length was seen in animal models of stroke (Hinman, Rasband and Carmichael 2013) traumatic brain injury (Vascak et al. 2017) and diabetic neuropathy (Yermakov et al. 2018), while altered AIS plasticity has been seen in models of microglia dependent neuroinflammation (Benusa et al. 2017), epilepsy (Harty et al. 2013) and Tau-FTD Alzheimer's disease (Sohn et al. 2019). In this latter study it was found that pathogenic Tau aberrantly bound to the ankyrin-g adaptor protein EB3 and prevented structural shortening of the AIS in response to elevated activity. This was found to impair homeostatic regulation of network activity in hiPSC-cultured cortical neurons.

A small number of studies have hinted towards possible abnormalities of the AIS in ALS. First mutations to AIS genes are found in diseases with similar clinical features to ALS. For example mutations in *SPTAN1* can cause hereditary motor neuropathy (Dong, Chen and Wu 2021), a disease with highly similar clinical presentation to juvenile forms of ALS, characterised by distal axonopathy and progressive muscle wasting (Rossor et al. 2012). Direct evidence of altered AIS properties in ALS came from (Sasaki and Maruyama 1992) who found significant swelling of the AIS in spinal motor neurons from post-mortem ALS samples. This swelling was restricted to the AIS and was not present in the internodes or at the axon hillock. Follow-up work found evidence of impaired axon transport and neurofilament accumulation at the AIS in the *SOD1* mouse model of ALS (Sasaki et al. 2005, Ackerley et al. 2004). More recent work found evidence for dynamic changes in AIS length in pre-symptomatic and symptomatic

stages of the disease in the SOD1 mouse model (Jorgensen et al. 2021, Bonnevie et al. 2020), the latter of which also found increased Na⁺ currents associated with increased AIS length at symptom onset. Despite this work, mechanistic links between TDP-43 pathology seen in the vast majority of patients with ALS, altered AIS structure and plasticity, altered neuronal excitability and motor unit function have not been investigated. Interestingly however it is known that TDP-43 can bind and regulate the splicing of several important AIS genes, including *ANK3* and *SCN1A* (Narayanan et al. 2013, Lagier-Tourenne et al. 2012, Brown et al. 2022, Ma et al. 2022). Moreover, alternative splicing is emerging as an important mechanism in regulating AIS functionality (Iijima and Yoshimura 2019).

1.16 PhD Aims

The primary aim of this work was to develop new *in vitro* approaches to model peripheral pathological events in ALS. In particular, to develop an *in vitro* stem-cell derived model of functional neuromuscular circuits to model axonal and neuromuscular synapse phenotypes, and changes to motor unit function, such as muscle weakness and spontaneous muscle contractions (fasciculations) seen in patients with ALS. Initially the following aims were set out:

1. Engineer functional optogenetic neuromuscular circuits from mouse ESCs (lines previously generated in the lab) using compartmentalised microdevices.
2. Generate new stable human iPSC lines: CRISPR correction of TDP-43^{G298S} mutation, stable expression of MACS sortable HB9::CD14 construct and CHR2-YFP, inducible iPAX7 expression.
3. Engineer functional optogenetic compartmentalised neuromuscular circuits from ALS-patient derived human iPSCs and CRISPR-corrected controls
4. Understand the effects of ALS-related mutations on peripheral phenotypes, such as: NMJ innervation, muscle contraction strength, and spontaneous activity.
5. Develop a scalable version of these neuromuscular co-cultures in 96-well assay plates and employ automated HCI analysis to quantify neuromuscular disease phenotypes.

Based on the results obtained from these initial aims, particularly relating to the increased spontaneous motor unit activity observed in the ALS-related TDP-43^{G298S} neuromuscular co-cultures some additional aims/hypotheses were set:

6. Are TDP-43^{G298S} motor neurons hyperexcitable relative to isogenic controls?
7. Could structural changes to the axon initial segment and altered homeostatic plasticity contribute to abnormal regulation of neuronal excitability?

2. Materials & methods

2.1 Experimental model details

2.1.1 mESC culture and differentiation into motor neurons and astrocytes

Mouse embryonic stem cells (mESCs) were maintained on laminin-521 (LN521, BioLamina) coated tissue culture treated plates, coated for 3 hours at 37°C or overnight at 4°C 0.08µg/cm². Cells were cultured in 2i inhibitor/leukemia inhibitory factor (2i/LIF) media (Table 2.1) and passaged at a 1:3-1:10 ratio when 70-80% confluent. Cells were incubated at 37°C, 5% CO₂. Motor neuron and astrocyte differentiation was carried out according to (Machado et al. 2019) using a channelrhodopsin-YFP *HB9::hCD14* mESC clone (CCRY) to derive optogenetic motor neurons, a *CAG::GDNF*, *GFAP::hCD14* clone (G6) to derive GDNF+ astrocytes, a *GFAP::hCD14* WTSOD1 clone (H6) to derive wildtype astrocytes and a *GFAP::hCD14* SOD1^{G93A} clone (S3) to derive SOD1^{G93A} astrocytes. Briefly mESCs were cultured to 80% confluency then dissociated at day 0 into single cells using 0.25% Trypsin/EDTA (ThermoFisher) and 2x10⁶ cells seeded into 10cm² non-TC treated suspension plates (Corning) in ADFNB media (Table 2.1) to form embryoid bodies (EBs). At day 2 EBs were split 1:4-1:6 and neural induction was achieved using 0.5µM SAG (smoothed agonist) (Merck) and 1µM RA (retinoic acid) (Sigma). At d5 CCRY EBs were MACS sorted into motor neurons. Conversely at day 5 G6 EBs were plated onto 1:100 Matrigel (Corning) coated 175cm² flasks (4x 10cm² plates of EBs > 1 flask) and grown in ADFNB for a further week before being MACS sorted into astrocytes. To form neural aggregates 15k MACS enriched motor neurons and 5k MACS enriched astrocytes were plated into lipidure (amsbio) coated (0.05%) non-adherent U-bottom 96-well plates.

Media	Component	Manufacturer	
2i/LIF medium (mESC maintenance)	DMEM/F-12 (1 part)	Gibco	
	Neurobasal (1 part)	Gibco	
	N2 supplement (1x)	Gibco	
	NeuroBrew21 w/o vitamin A supplement (1x)	Miltenyi Biotec	
	L-glutamine (2mM)	Gibco	
	Penicillin/streptomycin (1x)	Gibco	
	B-Mercaptoethanol (55 mM)	Gibco	
	Bovine Serum Albumin Fraction V (0.1% in PBS)	Roche	
	PD0325901 (1 µM)	Bio-Techne	
	CHIR99021 (3 µM)	Bio-Techne	
	Leukaemia inhibitory factor (LIF) supernatant (1:500)	COS7 cells transfected with pCAGGS::LIF (Bryson <i>et al.</i> , 2014a)	

ADFNB medium (mESC differentiation)	Advanced DMEM/F-12 (1 part)	Gibco
	Neurobasal (1 part)	Gibco
	N2 supplement (1x)	Gibco
	NeuroBrew21 (1x)	Miltenyi Biotec
	L-glutamine (2mM)	Gibco
	Penicillin/streptomycin (1x)	Gibco
	B-Mercaptoethanol (0.1%)	Sigma
	Bovine Serum Albumin Fraction V (0.1% in PBS)	Roche

Table 2.1. Mouse embryonic stem cell maintenance and differentiation media compositions.

2.1.2 hiPSC culture and differentiation to motor neurons, astrocytes and myoblasts

Patient-derived hiPSC line harbouring the pathogenic TDP-43^{G298S} mutation was provided by Christopher Shaw (King's College London) and Siddharthan Chandran (The University of Edinburgh). The Line was originally published in: (Barton et al. 2021). Wildtype hESC H9 line was acquired from WiCell (Madison, Wisconsin, USA) under a license from the steering committee for the UK Stem Cell Bank (No. SCS11-06). HipSci Lines samples were collected from consented research volunteer recruited from the NIHR Cambridge BioResource through (<http://www.cambridgebioresource.org.uk>). Initially, 250 normal samples were collected under ethics for iPSC derivation (REC Ref: 09/H0304/77, V2 04/01/2013), which require managed data access for all genetically identifying data, including genotypes, sequence and microarray data ('managed access samples'). In parallel the HipSci consortium obtained new ethics approval for a revised consent (REC Ref: 09/H0304/77, V3 15/03/2013), under which all data, except from the Y chromosome from males, can be made openly available (Y chromosome data can be used to de-identify men by surname matching), and samples since October 2013 have been collected with this revised consent ('open access samples').

Human iPSCs/ESCs were maintained on 0.4µg/cm² LN521 basement matrix (BioLamina) in StemMACS iPS-brew XF with iPSbrew supplement (1X) (Miltenyi Biotec) plus Penicillin/streptomycin (1x) (Gibco). Cells were passaged at 70% confluency as single cells by incubating cells with TrypLE express (Invitrogen) for 5 min at 37°C and replating in 10µM ROCK inhibitor Y-27632 (Tocris) for 24h. Typically 1x10⁶ hiPSCs were frozen in cell recovery medium (ThermoFisher)

MN differentiation was based on (Du et al. 2015) with minor modifications. hiPSCs were grown until 100% confluent on 0.4µg/cm² LN521 basement matrix (BioLamina) in StemMACS

iPS-brew XF with iPSbrew supplement (1X) (Miltenyi Biotec). Cells were then passaged 1:3 as clumps using 15 min 37°C incubation with 1mg/ml collagenase IV (Invitrogen) onto plates coated with 1:50 GFR-Matrigel (Corning) in iPS-brew XF containing 10µM ROCK inhibitor. After 2-3 days once colonies started to merge media was switched to NEP media (d0), comprising basal media: 1- part DMEM/F-12 (Gibco), 1-part Neurobasal (Gibco), N2 supplement (0.5x) (Gibco), Neurobrew-21 (0.5x) (Miltenyi Biotec), L-Glutamine (2mM) (Gibco), Penicillin/streptomycin (1x) (Gibco), plus 3µM CHIR99021 (Tocris), 2µM SB431542 (Tocris) and 0.2µM LDN193189 (Stemgent) for 6 days. After 6 days cells were again split 1:3 with collagenase IV onto 1:50 matrigel coated plates and media changed to MNP media, comprising basal media plus 0.1µM RA (Sigma), 0.5µM purmorphamine (Tocris), 1µM CHIR99021, 2µM SB431542, 0.2µM LDN193189. After a further 6 days cells were either frozen or split 1:3 using collagenase IV and switched to MNP expansion media, comprising basal media plus 0.1µM RA, 0.5µM purmorphamine, 3µM CHIR99021, 2µM SB431542, 0.2µM LDN193189, 0.5mM valproic acid (Stemgent). Cells were passaged up to 2 times in expansion conditions before freezing. Typically, 10-20x10⁶ MNPs were frozen in cell recovery medium (ThermoFisher). Subsequently a single vial would be thawed into 4x wells of a 6-well plate in MNP basal +10µM ROCK inhibitor Y-27632 +0.5µM RA, 0.1µM PurM and grown for 1-week prior to MACS enrichment.

Myoblast differentiation was based on (Rao et al. 2018) with minor modifications, using a custom built *iPAX7* knock-in hiPSC line rather than lentiviral transduction. At 70% confluency hiPSCs were split onto 1:50 Matrigel coated plates at a density of 33k/cm² in iPS-brew XF plus 10µM ROCK inhibitor Y-27632. The following day media was replaced with E6 media (Gibco) plus L-Glutamine (2mM) and Penicillin/streptomycin and 10µM CHIR99021 for 2 days, after which CHIR99021 was removed and replaced with 1µg/mL Doxycycline (Sigma) for 18 days with 10ng/ml bFGF (R&D) added from day 5. Myoblast progenitors were cultured on 1:50 matrigel coated flasks in expansion media, comprising low glucose DMEM (ThermoFisher), with 10% FBS (Gibco), 1x NEAA (Gibco), L-Glutamine (2mM), Penicillin/streptomycin, 1x β-Mercaptoethanol (Gibco) and expanded up to 4 passages. To differentiate the myoblasts into myotubes cells were seeded on 1:50 Matrigel coated plates at a density of 100k/cm² into myogenic differentiation media, comprising low glucose DMEM, 0.5x N2 supplement, 10% horse serum (Gibco), L-Glutamine (2mM), 1x Penicillin/streptomycin.

Astrocyte differentiation was based on (Li et al. 2018, Canals et al. 2018) with minor modifications using a custom built iAstro line generated by Federica Riccio. At day 0, 70% confluent hiPSCs were dissociated using Accutase (Gibco) into single cells at a density of 20k/cm² in iPS-brew + 10µM ROCK inhibitor Y-27632 + 2.5µg/mL Doxycycline (Sigma). At day 1 cultures were washed 2x in PBS and media changed to expansion medium (Table 2.1) + 2.5µg/mL Doxycycline. At day 3 media was changed to ¾ expansion medium, ¼ FGF medium + 2.5µg/mL Doxycycline. At day 4 media was changed to ½ expansion medium, ½ FGF medium + 2.5µg/mL Doxycycline. At day 5 media was changed to ¼ expansion medium, ¾ FGF medium + 2.5µg/mL Doxycycline. At day 6 media was changed to FGF medium + 2.5µg/mL Doxycycline. At day 7 cells were split using accutase and either frozen or replated onto Matrigel coated dishes in FGF medium + 2.5µg/mL Doxycycline. At day 8 media was changed to fresh FGF medium + 2.5µg/mL Doxycycline. + 5µM Ara-C (Sigma). At day 10 media was changed to maturation medium + 2.5µg/mL Doxycycline and refreshed every 2-3 days.

Media	Component	Manufacturer
iPS-brew medium (hiPSC-maintenance)	StemMACS IPS-brew XF	Miltenyi Biotec
	StemMACS IPS-brew XF supplement (0.5x)	Miltenyi Biotec
	Penicillin/streptomycin (1x)	Gibco
Motor neuron progenitor (MNP) basal medium (motor neuron differentiation)	DMEM/F-12 (1 part)	Gibco
	Neurobasal (1 part)	Gibco
	N2 supplement (0.5x)	Gibco
	NeuroBrew21 (0.5x)	Miltenyi Biotec
	L-glutamine (2mM)	Gibco
	Penicillin/streptomycin (1x)	Gibco
iPAX7 basal differentiation medium (myoblast differentiation)	Essential 6 medium	ThermoFisher
	L-glutamine (2mM)	Gibco
	Penicillin/streptomycin (1x)	Gibco
iPAX7 progenitor medium (myoblast expansion)	Low glucose DMEM	Gibco
	Fetal bovine serum (FBS) (10%)	Gibco
	Non-essential amino acids (NEAA) (1x)	Gibco
	L-glutamine (2mM)	Gibco
	Penicillin/streptomycin (1x)	Gibco
iPAX7 Myogenic medium (Myoblast maturation)	Low glucose DMEM	Gibco
	N2 supplement (0.5x)	Gibco
	Horse serum (HS) (10%)	Gibco
	L-glutamine (2mM)	Gibco
	Penicillin/streptomycin (1x)	Gibco
iAstro Expansion medium (astrocyte differentiation)	DMEM/F-12	Gibco
	Fetal bovine serum (FBS) (10%)	Gibco

	N2 supplement (0.5x)	Gibco
	Glutamax (1x)	ThermoFisher
iAstro FGF medium (astrocyte differentiation)	Neurobasal	
	B27 supplement (0.5x)	ThermoFisher
	Non-essential amino acids (NEAA) (1x)	Gibco
	Fetal bovine serum (FBS) (1%)	Gibco
	Glutamax (1x)	ThermoFisher
	FGF (8ng/ml)	Peprotech
	CNTF (ng/ml)	Peprotech
	BMP4 (10ng/ml)	Peprotech
iAstro Maturation medium (Astrocyte maturation)	DMEM/F-12 (1 part)	Gibco
	Neurobasal (1 part)	Gibco
	N2 supplement (0.5x)	Gibco
	Glutamax (1x)	ThermoFisher
	Sodium pyruvate (1x)	ThermoFisher
	N-acetylcysteine (5µg/ml)	Sigma
	Heparin-binding EGF-like growth factor (5ng/ml)	Peprotech
	CNTF (10ng/ml)	Peprotech
	BMP4 (10ng/ml)	Peprotech
	dbcAMP (500µg/ml)	Sigma

Table 2.2. Human induced pluripotent stem cell (hiPSC) maintenance and differentiation medias to derive motor neurons, myoblasts and astrocytes

2.1.3 Manufacturing compartmentalised PDMS microdevices

Compartmentalised microdevices were manufactured according to (Machado et al. 2019) using soft lithography. 2g Polydimethylsiloxane (PDMS) (Dow Corning, Sylgard-184) was cast on a silicon mould (produced using photolithography), degassed in a vacuum chamber for 20 minutes and cured for 2 hours at 80°C. 3x2 arrays were then cut out and either attached to glass bottom culture dishes (ibidi) by plasma bonding for 30s and single drops of NOA-73 (Norland products) applied as myofiber anchor points in the central compartment. Or alternatively a thin layer of NOA-73 was applied to plastic bottom 35mm dishes (ibidi) with a cell scraper and partially UV-cured for 10 s at 55 J/cm². Then, the PDMS arrays were placed on the resin and fully UV-cured for 1 min. Microdevices were then UV sterilised for 20 minutes. Subsequently they were coated with 1:50 matrigel. To achieve uniform coating in the chambers and microchannels, air bubbles were manually removed from the chambers using a pipette, then the devices were de-gassed using a vacuum at 800psi for 2 hours to remove air bubbles from the microchannels.

2.1.4 Neuromuscular co-cultures in compartmentalised microdevices

Neural aggregates comprising 15k MACS enriched motor neurons and 5k MACS enriched astrocytes were formed in 0.05% lipidure (amsbio) coated U-bottom 96-well plates. Neural aggregates were plated in a 160 μ l 24mg/ml fibrin + 40 μ l matrigel hydrogel solution and ~1 μ l 50U/ml thrombin (Sigma) was used to polymerise the hydrogel. The next day 1 μ l myoblasts were plated in the same solution at a concentration of 20k/ μ l. Mouse co-cultures were grown in ADFNB medium. Human co-cultures were cultured in 50:50 ADFNB/MNP maturation medium and myogenic maturation medium. Media was refreshed every 2-3 days.

2.1.5 Manufacturing 96-well plates with suspended electrospun elastomer nanofibers

Custom-built 96-well plates were prepared by Aimee Cheesbrough. The P(EDS-UU)-POSS polymer was prepared according to (Cheesbrough et al.). Elastomer nanofibers were incorporated into a 96-well format for high-throughput automated screening of neuromuscular co-cultures. To do this, black bottomless 96 well imaging plates (Greiner Bio-One, 6550000-06) were inverted and placed between two charged electrodes inside the electrospinning system previously described. The spinneret needle was connected to a motorised arm, which constantly displaced in the x direction (along the longer dimension of the microplate). This enabled even distribution of the nanofibers across the base of the plate. All other parameters of the electrospinning set-up were used as previously described. Nanofibers were electrospun for 30 minutes. A glass coverslip base 110x74mm (NEXTERION, 1535661) was attached beneath the nanofibers to render the plates watertight. To do this, a custom-made acrylic stamp was used to apply glue to the base of the plate. The stamp comprised a rectangle with 96 holes, fabricated from laser-cut acrylic sheet. A thin layer of glue was applied to the stamp using a cell scraper. The holes in the stamp prevented the glue from contacting the nanofibers. The plate was aligned and placed on top of the stamp, transferring the glue from the stamp to the plate. The stamp was then peeled off, and a glass coverslip placed on top. Plates were cured at 60°C overnight. The following day, the plates were air plasma treated (0.4 mBar, 20% power, 2mins) and UV sterilised under a benchtop UV lamp for 20 minutes. Sterile assembled plates could be stored at room temperature for further downstream use. The day before cell seeding, plates were coated with 1:50 GFR-Matrigel and incubated overnight at 4°C.

2.1.6 Neuromuscular co-cultures in 96-well plates

40k myoblasts were plated on 1:50 matrigel coated 96-well μ Clear high content imaging plates (Grenier) or custom built 96-well plates. The following day neural aggregates comprising 15k MACS enriched motor neurons and 5k MACS enriched aggregates were plated in the centre of the well. Mouse co-cultures were grown in ADFNB medium. Human co-cultures were cultured in 50:50 ADFNB/MNP maturation medium and myogenic maturation medium. Media was refreshed every 2-3 days. The commercially available BCR-Abl inhibitor Nitolinib (Sigma) was used at 3, 1, 0.3 and 0.1 μ M.

2.2 Method details

2.2.1 Genetic engineering hiPSC lines

Targeted gene editing in hiPSCs was achieved using CRISPR-Cas9 mediated homology directed repair to correct the endogenous TDP-43^{G298S} mutation. 3 μ g TrueCut CAS9 v2 (ThermoFisher) was combined with 90 μ M sygRNA (sgRNA-9, CRISPR ID: 901697809, sequence: 5' - GGATTTGGTAATAGCAGAGGGGG - 3'; sgRNA-10, CRISPR ID: 901697810, sequence: 5' - TTTGGTAATAGCAGAGGGGGTGG - 3') (Table 2.3) (Merck) at RT for 15 minutes to form an RNP complex. This complex was then electroporated using a NEPA- 21 electroporator (Nepagene) into 1x10⁶ hiPSCs along with 50 μ M ddOligo template DNA (ThermoFisher). The donor template was engineered with the GGT codon to correct the AGT codon responsible for the TDP-43^{G298S} mutation and with a silent Xho1 restriction site in the seed region of the sgRNA. Cells were then plated at a low density of 3-5k/10cm² and single clones were manually passaged into 24 well plates. Genomic DNA was then extracted using QuickExtract solution (Epicenter) and clones were screened for the presence of the Xho1 restriction site by PCR amplification using the X6 forward and reverse primers (Table 2.3) and a Q5 high-fidelity master mix (NEB). Initial denaturation 98°C 30s, 35x: 98°C 10s, 69°C 30s 72°C 30s, final extension 72°C 2min, hold at 4°C. And Xho1 (NEB) restriction digest was performed according to manufacturer's instructions. Positive clones were then sequenced using sanger sequencing (SourceBioscience). Subsequently ~1000bp upstream and downstream of exon 6 of *TARDBP* was sequenced as well as the top 5 predicted off-target sgRNA binding sites to confirm no off-

target genome editing (Table 2.3). We then carried out g-banding to confirm a normal karyotype (CellGuidanceSystems) and Western blot analysis of TDP-43 using an n-terminal TDP-43 antibody (MAB7778 - Biotechne) to confirm normal protein expression (SFigure. 1c).

hiPSC cell clones intended for MN differentiation and enrichment were engineered to express the *HB9::hCD14* MACS sortable construct (generated by Carolina Barcellos-Machado) using TALENS based insertion into the AAVS1 safe- harbour locus using a NEPA-21 electroporator (Sonidel). Genomic DNA was isolated from single cell clones (as previously described). A1/A2 primers were used to detect wildtype alleles, while A2/A3 primer pairs were used to detect integrated alleles using PCR amplification (Table 2.3). PCR amplification was achieved using Taq polymerase master mix (NEB): Initial denaturation 95°C 3min, 35x: 95°C 30s, 57.1°C 30s 72°C 90s, final extension 72°C 5min, hold at 4°C. Cell lines were also engineered to express the optogenetic actuator transgene CAG::CHR2-YFP using a PiggyBAC- mediated integration system via electroporation. Fluorescence activated cell-sorting (FACS) was carried out using a BD FACSAria™ 3 (BDBiosciences) to select CHR2-YFP positive cells to generate polyclonal cell lines with comparable YFP expression.

Inducible *iPAX7* hiPSC-lines to forward program hiPSCs into myoblast progenitors were generated by TALENS based integration the Doxycycline-inducible *PAX7* construct (generated by Federica Riccio) into the CLYBL safe-harbour locus of the publicly available HiPSCi lines PAMV1 and KUTE4 (www.hiPSCi.org), via electroporation. Genomic DNA was isolated from single cell clones (as previously described). C1/C2 primer pairs were used to detect wildtype alleles, while C3/C4 primer pairs were used to detect integrated alleles (Table 3.2) using PCR amplification with the Q5 high-fidelity polymerase (NEB), initial denaturation 98°C 30s, 35x: 98°C 10s, 67°C 30s 72°C 30s, final extension 72°C 2min, hold at 4°C.

The CAG::GDNF construct (Generated by Carolina Barcellos-Machado) was stably integrated into the background iAstro PAMV1 line (generated by Federica Riccio) using a piggyBAC mediated integration system via electroporation. Single cell clones were then treated with 10µM Brefeldin A (Sigma) then fixed and stained for GDNF. Positive clones were then expanded and frozen for future use.

sgRNA/primer:	Sequence 5'-3':
CRISPR-Cas9 guide RNAs:	

sgRNA-9	GGATTTGGTAATAGCAGAGGGGG
sgRNA-10	TTTGGTAATAGCAGAGGGGGTGG
TDP-43^{G298S} exon 6 PCR/sequencing primers:	
X6 F-primer	ATTGCGCAGTCTCTTTGTGGAGAGG
X6 R-primer	TACATTCCCCAGCCAGAAGACTTAG
US1000 X6 F-primer	GCTCACTACACCCTAGAACTCC
US1000 X6 R-primer	ACCCTGATTCCCAAAGCCAC
DS1000 X6 F-primer	GGATCAGCATCCAATGCAG
DS1000 X6 R-primer	ACTCTCTACCAAAGCCAC
CRISPR Off-target screening:	
OT1 F-primer	CAGCAGTGAAAGTGAAAAGACC
OT1 R-primer	CCAGCCAGAAGACTTAGAATCC
OT2 F-primer	CCTCAAAACAACACGAAGCC
OT2 R-primer	GACCAGAAGCCTAAACACC
OT3 F-primer	ATCTAACACAGAGTTGAACAGGG
OT3 R-primer	TAACAATAAGGGACCCTACTGG
OT4 F-primer	TGGGTACAACACTGAAATCTGG
OT4 R-primer	CACCGCCACTAATGTTAATATGG
OT5 F-primer	GGCAAATGAAGTCACAAATGGG
OT5 R-primer	TTATTTCCATAGCTGTGCTTGGG
AAVS1 screening primers:	
A1	GGAATCTGCCTAACAGGAGGT
A2	CGGTTAATGTGGCTCTGGTT
A3	CCCCAGAATAGAATGACACC
CLYBL screening primers:	
C1	TGACTAAACACTGTGCCCA
C2	AGGCAGGATGAATTGGTGGA
C3	CAGACAAGTCAGTAGGGCCA
C4	AGAAGACTTCTCTGCCCTC

Table 2.3. SgRNA and primer sequences used for genetic engineering of hiPSC lines

2.2.2 Magnetic activated cell sorting (MACS)

hiPSC-motor neuron progenitors (MNPs) (see 2.1.2) were thawed in MNP differentiation medium, comprising basal medium plus 0.5 μ M RA, 0.1 μ M purmorphamine and ROCK inhibitor Y-27632 for 24h at density of 600k/cm² onto Matrigel coated plates. Cells were grown in these conditions for 1 week prior to MACS sorting. Cells were then dissociated in TrypLE +10U/ml DNase (Roche) for 5-7 mins at 37°C into a single cell solution. mESC-astrocytes were dissociated in Trypsin-EDTA for 20mins at 37°C, while mESC-motor neurons were dissociated in Trypsin-EDTA for 10mins at 37°C. Following dissociation cells were washed 3x in DMEM +10U/ml DNase, filtered using a 40 μ m nylon strainer (BD Falcon) and re-suspended in MACS buffer comprising PBS (Gibco), 10% BSA (ThermoFisher), +10U/ml DNase and 3 μ g/ml anti-CD14 antibody (clone 26ic, DSHB), and transferred to a MACSmix tube rotator (Miltenyi Biotec) at 4°C for 20 min. Cells were then washed and resuspended in MACS buffer plus 1:5 anti-mouse igG microbeads (Miltenyi Biotec) and rotated at 4°C for a further 20 min. Cells were then resuspended in 1ml MACS buffer and applied to a MS magnetic

column mounted to an OctoMACS magnet (Miltenyi Biotec). Cells were washed 3x with 500 μ l MACS buffer then the positive fraction eluted in 1ml MACS buffer.

2.3.3 Flow cytometry

To confirm MACS enrichment flow cytometry was used. Pre-sort, flow-through and eluate populations were incubated with DAPI (ThermoFisher) and APC-CD14 (ThermoFisher) for 20mins on the MACSmix tube rotator at 4°C (Miltenyi Biotec). Samples were then washed in RT PBS and incubated in 2% PFA on the rotator at 4°C. Cells were then washed in ice cold PBS then analysed on a BD Fortessa 1 at the BRC Flow Cytometry Core, Guy's Hospital, with 50k events recorded per sample. Unstained control samples were used to set up appropriate gating.

2.2.4 Optogenetic entrainment and stimulation

To analyse changes to the AIS and electrophysiological parameters in response to short term activity we optogenetically stimulated cultures using a custom-built heat sink and LED assembly (Machado et al. 2019). Custom written software controlled the timing of LED emission. LEDs emitted pulses of 450nm blue light at a frequency of 5Hz with a 20ms epoch set at an LED intensity of 40%. Cultures were supplemented with 1x antioxidant supplement (Sigma) to mitigate the effects of phototoxicity. For optogenetic entrainment of neuromuscular co-cultures the same custom-built system was used. Cultures were stimulated with 450nm blue light at a frequency of 5Hz with a 20ms epoch set at an LED intensity of 40% for 1hr a day for five days. Cultures were supplemented with 1x antioxidant supplement (Sigma) to mitigate the effects of phototoxicity.

2.2.5 Whole-cell patch clamp electrophysiology

For patch clamp recordings 50k MACS sorted motor neurons and 50k MACS sorted mESC-GDNF astrocytes were seeded onto 1:50 Matrigel coated 18mm glass coverslips and cultured in MN maturation medium, comprising basal medium plus 0.1 μ M RA, 0.1 μ M purmorphamine and ROCK inhibitor Y-27632. Coverslips were transferred to an open bath chamber (RC-41LP Warner Instruments) containing extracellular solution: NaCl 136 mM, KCl 2.5 mM, HEPES 10 mM, MgCl₂ 1.3 mM, CaCl₂ 2 mM, Glucose 10 mM, pH adjusted to 7.3 and osmolarity adjusted

to 300 mOsm. The chamber was mounted on an inverted epifluorescence microscope (Olympus IX71) and visualised using a 60x oil objective. Pipettes were pulled from borosilicate glass (O.D. 1.5mm, I.D. 0.86mm, Sutter instruments) to a resistance of between 3-5M Ω . Intracellular solution contained the following: 125 mM KMeSO₄, 5 mM MgCl₂, 10 mM EGTA, 10 mM HEPES, 0.5 mM NaGTP, 5 mM Na₂ATP, pH = 7.4, osmolarity = 290mOsm. Whole-cell patch clamp recordings were then made at the soma of CHR2-YFP+ motor neurons using a Multiclamp 700B amplifier (Molecular Devices) and the data acquired using a Digidata 1440A digitizer (Molecular Devices). All recordings were carried out at room temperature. Data was acquired with Clampex software (Molecular Devices) and Axon Multiclamp Commander Software (Molecular Devices). Current-clamp data was sampled at a rate of 50kHz and filtered at 10kHz and Voltage-clamp data was sampled at 20 kHz and filtered at 10 kHz. Passive membrane properties (RM, CM) and series resistance (RS) were measured by applying a subthreshold voltage step. RS was calculated as proportional to the current response amplitude, CM was estimated from the transient time constant by fitting the current transients to exponential functions and RM was estimated from the steady state response following the current transients. Passive membrane properties and series resistance were measured at the beginning and at the end of all recordings to ensure proper access (RS >20m Ω) had been maintained. Whole-cell currents used to estimate Na⁺ and K⁺ conductances were recorded in voltage clamp using 50 ms voltage steps from -80mV to +50mV. Resting membrane potentials and spontaneous AP spiking were recorded for 1 minute in current clamp mode without current injection, within the first 2 minutes after break-in. Intrinsic excitability measurements and AP properties were recorded in current clamp mode, while using a steady current injection to maintain membrane potential at -60 mV \pm 2mV (values for injected current and membrane voltage were indistinguishable across genotypes and are reported on Supplementary Figure 4). Using either 100 ms current injections from -20pA – 170pA (for measurements of AP properties) or 500ms current injections from -50pA to 300pA (for measurements of Input-output characteristics). Although typically shorter current steps are used for establishing AP properties (eg - current threshold), these were unreliable at eliciting APs in younger MNs (6-week cultures). We therefore used 100ms current steps instead, which allowed us to compare AP properties across all stages. Assessment of optogenetic stimulation was carried out by delivering 500 ms pulses of 488 nm light were

applied using a CoolLED pE-100 illumination system and AP traces recorded in current clamp with membrane potential set to -60 mV.

2.2.6 Muscle contraction recordings

Brightfield muscle contraction recordings were acquired on an inverted Olympus IX71 epifluorescence microscope. Videos were taken at 10Hz with a 100ms exposure using an ORCA Flash4.0 V2 C11440-22CU scientific CMOS camera (Hamamatsu). Images were captured using HClmage software (Hamamatsu) at 2048x2048 resolution. Optogenetic stimulation of the CHR2-YFP motor neurons was achieved using a 500ms pulse of 470nm light at 1.32/mW/cm². LED timing and camera acquisition was triggered externally using Clampex software (pClamp 10, Molecular Devices).

2.2.7 Immunofluorescence

For imaging individual neurons 5k MACS sorted MNs were seeded onto 20k MACS sorted GDNF+ mESC-derived astrocytes in 96-well high content imaging plates (Greiner 655090) and grown in MN maturation medium, comprising basal medium plus 0.1µM RA, 0.1µM purmorphamine and ROCK inhibitor Y-27632. Cells were then fixed in 4% PFA for 15 min at RT and washed 3x in PBS. Subsequently cells were blocked in 3% BSA and 0.1% Triton X-100 in PBS for 1hr at RT. Neuromuscular co-cultures in compartmentalised microdevices were additionally permeabilised using 10% DMSO. Cells were incubated overnight with primary antibodies in blocking buffer at 4°C (Table 2.4). Cells were then washed 3x in 0.1% Triton X-100 in PBS and incubated with the secondary antibodies/DAPI (Sigma) either at RT for 2hr or overnight at 4°C. Cells were finally washed 3x in PBS (Table 2.4). Cells were then imaged using a Leica TCS SP8 confocal inverted laser scanning microscope at a 63x oil objective, or a Zeiss Axio Examiner.Z1 LSM 800 upright confocal with airyscan with a 63x oil objective, or an Operetta CLS high content image analysis system.

Target	Species/epitope/WL	Dilution	Manufacturer (ID)
Primary antibodies:			
AChR	Rat IgG	1:200	DSHB (MAB35)
Ankyrin-g	Mouse IgG2a	1:200	MerckMillipore (MABN466)
GDNF	Goat IgG	1:500	R&D Systems (AF-212-NA)
GFAP	Rat IgG	1:500	Invitrogen (13-0300)
GFP	Rabbit IgG	1:500	Invitrogen (A11122)
ISL1	Rabbit IgG	1:1000	Abcam (mf20)
MYOD	Mouse IgG1	1:500	BD Pharmingen (554130)
Myogenin	Mouse IgG1	1:200	DSHB (F5D)

Myosin	Mouse IgG2b	1:200	DSHB (MF20)
OCT4	Mouse IgG2b	1:50	Santa Cruz (sc-5279)
OLIG2	Rabbit IgG	1:500	Abcam (ab109186)
PAX7	Mouse IgG1	1:200	Santa Cruz (sc-81648)
S100b	Rabbit IgG	1:500	Abcam (ab52642)
SOD1	Mouse IgG2b	1:500	Santa Cruz (sc-17767)
SOX2	Rabbit IgG	1:500	Stemgent (09-0024)
SSEA4	Mouse IgG	1:500	Abcam (ab16287)
SV2	Mouse IgG1	1:200	DSHB
TDP-43	Rabbit IgG	1:200	Proteintech (10782-2-2AP)
Titin	Mouse IgM	1:20	DSHB (9D10)
TUBB3	Mouse IgG2a	1:1000	R&D Systems (MAB1195 – Tuj1)
UBQTN	Mouse IgG1	1:100	Santa Cruz (sc8017)
Secondary antibodies:			
Mouse IgM	405	1:1000	AlexaFluor
Mouse IgG2a	488, 647	1:1000	AlexaFluor
Mouse IgG1	647	1:1000	AlexaFluor
Mouse IgG	488, 555, 647	1:1000	AlexaFluor
Rat IgG	488, 555, 647	1:1000	AlexaFluor
Rabbit IgG	488, 555, 647	1:1000	AlexaFluor
Goat	555	1:1000	AlexaFluor

Table 2.4. Details of primary and secondary antibodies used for immunofluorescence

2.2.8 Western blot

Cell pellets were generated by centrifugation at 2500rpm for 5mins and washed 1x in cold PBS. Subsequently cells were lysed in NP40 lysis buffer supplemented with 1mM PMSF, 100mM NaVO₄, 1MNaF and 1:100 protease inhibitors and protein content quantified using 5x biorad reagent and a BSA standard curve (concentrations: 2,1,0.5,0.25,0.125mg/ml) and 40µg of protein was mixed with 4x laemmli buffer and boiled for 10min. Samples were then loaded into precast 10% polyacrylamide gels (Bio-rad) and run at 100V for 15 mins then 120V until complete. Samples were then transferred using the Biorad blotting system. Samples were blocked for 1hr at RT in blocking buffer: 1xTTBS, 5% dry milk, 0.1% Sodium Azide, washed 1x with TTBS then incubated with primary antibody overnight at 4°C in blocking buffer – TDP-43 (Proteintech), and vinculin (Proteintech) used at 1:1000. Samples were then washed 3x in TTBS then incubated with HRP-conjugated secondary antibodies (BioRad) in blocking buffer (without Sodium Azide) for 1.5hr at RT. Samples were then washed 3x in TTBS and developed using ECL substrate (Promega) and visualised using a BioRad ChemiDoc Touch.

2.2.9 qRT-PCR

RNA extraction and purification was carried out according to manufacturer's instructions using an Invitrogen RNA Mini/Micro-kit (Invitrogen). Reverse transcription to generate cDNA was carried out according to manufacturer's instructions using a GoScript Reverse

Transcription System (Promega). Primers (Table 2.5) were combined with fast SYBR (ThermoFisher) according to manufacturer's instructions and a Biorad SYBR 384X real-time PCR system was used to quantify transcript levels. Gene expression was normalised to the average of GAPDH.

Primer name	Sequence 5'-3'
TDP-43 F-primer	TCATCCCAAGCCATTGAGG
TDP-43 R-primer	TGCTTAGGTTTCGGCATTGGA
TDP-43 Exon 5 F-primer	TCATCCCAAGCCATTGAGG
TDP-43 Intron 5 F-primer	GTTTCACTGTTTTGATCTGGC
TDP-43 Exon 6 R-primer	GTGCTTAGGTTTCGGCATTG
GAPDH F-primer	GAAGGTGAAGGTCGGAGTC
GAPDH R-primer	GAAGATGGTGATGGGATTC

Table 2.5. qRT-PCR primer sequences used

2.2.10 RNA-sequencing

300k MACS enriched motor neurons were plated on 50k MACS enriched astrocytes and grown for 2 weeks. RNA extraction and purification was carried out according to manufacturer's instructions using an Invitrogen RNA Mini/Micro-kit (Invitrogen). Illumina NovaSeq 2x150bp paired-end read (350M read pairs) sequencing was then carried out at a depth of 100 million reads per sample with polyA selection on total RNA using GeneWiz.

2.2.11 Karyotyping

G-banding and karyotype analysis was carried out by Cambridge Biosciences.

2.3 Quantification and statistical analysis:

2.3.1 MACS enrichment analysis (IF)

IF images of pre-sort, flow-through and eluate populations were analysed manually using FIJI software. HB9, GFAP and ISL1 positive cells were manually counted using the cell counter plug-in in FIJI and expressed as a percentage of total cell counts as determined by DAPI staining.

2.3.2 Motor neuron survival analysis

Survival of motor neurons grown on different astrocyte populations was automatically analysed using an Operetta CLS HCI analysis system and Harmony 4.9 software. Plates were imaged in non-confocal mode using a 20x water objective. 69 fields were taken with a 20%

overlap and 2 Z-planes at 2 μ m intervals with a binning of 2. A pipeline was written to automatically count TUBB3/ISL1 positive cells as a proportion of total DAPI positive cells. Separate plates were imaged at different timepoints and normalised to the 24-hour timepoint.

2.3.3 Fourier analysis of myofiber alignment

Myofiber alignment was analysed using Fourier analysis in FIJI. The threshold function was used to create binary images. Then the directionality analysis plugin V2.3.0 was used with the Fourier components method set to a binning of 90 and histogram start of -180°C and end of 180°C.

2.3.4 Particle image velocimetry (PIV) analysis

Video recordings of spontaneous and optogenetically evoked myofiber contractions were analysed by Particle Image Velocimetry using the PIVlab package in Matlab. Images were loaded in a 'time resolved A+B, B+C' format. Three iterations of interrogation windows of 64/32/16 pixels, each with 50% overlap were used and frames calibrated to a known reference distance. Vectors were then validated by filtering out velocity values higher than 7 times the standard deviation. Mean velocity values for the myofiber compartment area were exported to derive peak velocity magnitude values and contraction frequency values. Spontaneous contractions were defined as peaks with a velocity value of at least 2.5 μ m/s. To show that contractions were dependent on synaptic transmission at NMJs, 50 μ M of the AChR agonist d-Tubocurarine (DTC) (Sigma) or 10 μ M of the Na⁺ channel agonist TTX was added to the co-cultures.

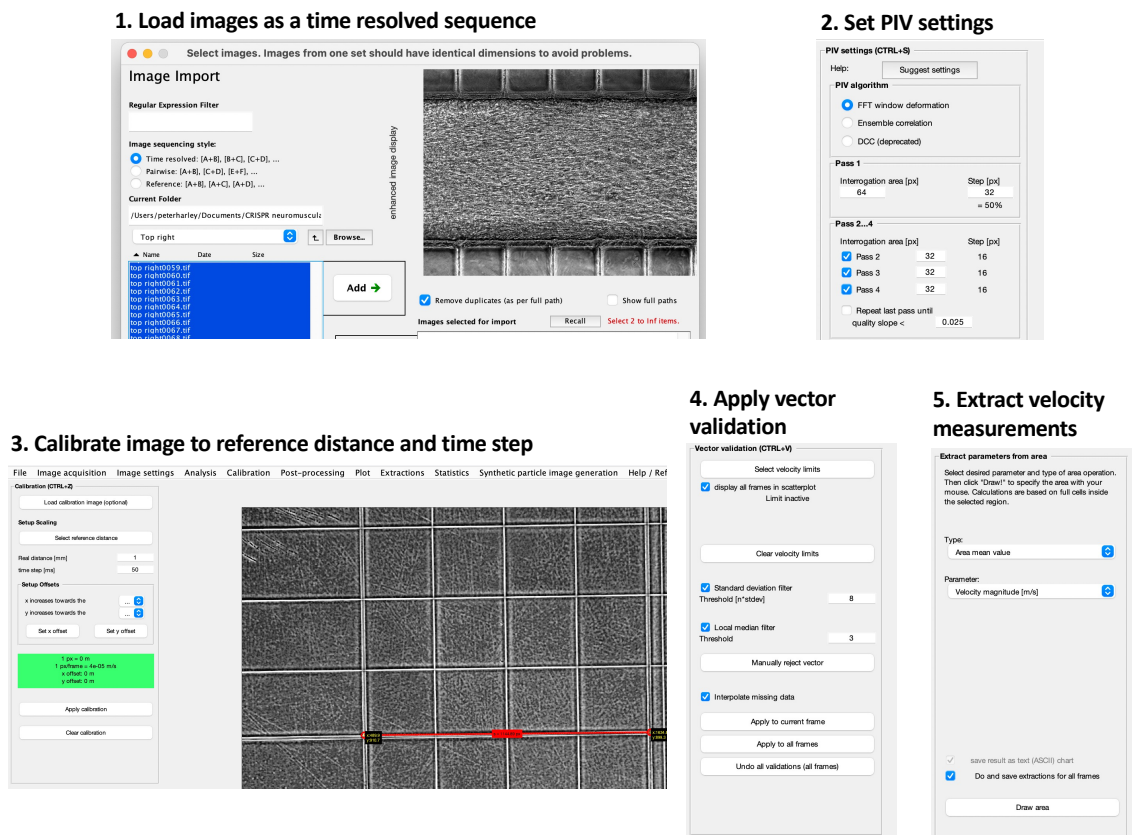


Figure 2.1. PIV analysis of muscle contraction using PIV lab package in MATLAB

2.3.5 Analysis of axon outgrowth and detection of NMJs

Axon outgrowth and neuromuscular junctions were analysed using IMARIS 9.1.2 software. For axon outgrowth, 3D surface maps were generated based on TUBB3 immunofluorescence using uniform and consistent gating thresholds. From these reconstructions the total axon volume and surface area per field of view were calculated. For analysis of neuromuscular junctions, the IMARIS colocalisation plug-in was used to automatically calculate and generate a colocalisation result and channel for the pre-synaptic SV2 immunofluorescence channel and the post-synaptic AChR channel. 3D surface maps were then generated based on this coloc channel using uniform and consistent gating thresholds. Blinding was deemed unnecessary for this analysis since the software was automatically calculating and setting the colocalization thresholds based on pixel intensities. From this surface map the total number of colocalised objects as well as the volume and surface area of these objects could be calculated.

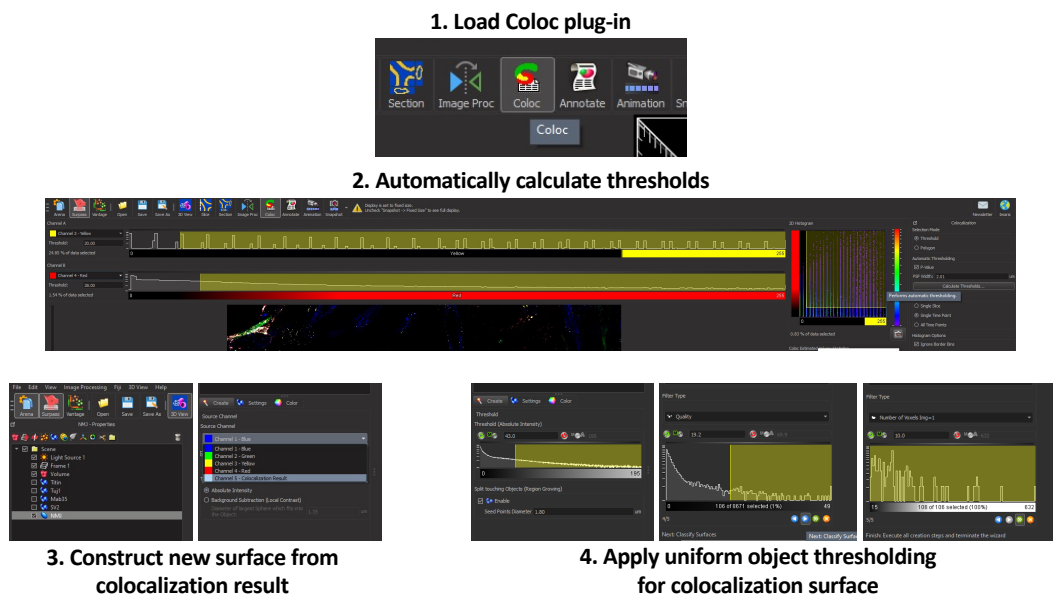


Figure 2.2. Automated SV2/ACHR colocalisation analysis and uniform object thresholding to derive NMJ parameters in IMARIS 9.1.2

2.3.6 IF analysis of SOD1/UB41 inclusions

IF images of UB41 and SOD1 stained wildtype and SOD1^{G93A} astrocytes were taken using the Operetta HCI analysis system and analysed using Harmony 4.9 software. A pipeline was developed to detect punctate UB41 and SOD1 inclusions as a percentage of total DAPI positive cells. The pipeline was able to detect the number and size of inclusions and whether they were UB41 positive, SOD1 positive or both UB41 and SOD1 positive.

2.3.7 IF analysis of myogenic differentiation

IF images of PAX7, MYOD, MYOG, MYH2 and TTN staining were analysed manually using the cell counter plug-in in FIJI software. Cells expressing these markers were expressed as a percentage of total DAPI positive cell counts per field of view.

2.3.8 Analysis of electrophysiology

Electrophysiological measurements were analysed with custom MatLab scripts written by Guilherme Neves. Inward currents in voltage clamp were measured by taking the minimum value of a current trace, whereas steady state outward currents were measured by averaging over a 15ms window taken 25 ms after the voltage step. Values were corrected for baseline current offset before stimulation. Individual AP properties in current clamp were obtained using sequential injection of 100 ms current steps of increasing amplitude (10 pA increments) (Figure 2.1). Only the first AP at the current threshold (first step to elicit an AP) was measured. AP waveforms were extracted using the MATLAB's findpeaks function with minimum peak Amplitude 0 mV). Extracted parameters were: Amplitude (Max amplitude – average Vm at the end of stimulus 50 ms window excluding APs), Voltage Threshold (Voltage at the time the speed of Vm rise is above 0.15 mV/ms), Width at half height. Input-Output parameters were obtained using sequential injection of 500ms current steps of increasing amplitude (50 pA increments). Location of AP were extracted using MATLAB's findpeaks function with minimum peak Amplitude 0 mV. For analysis described in Supplementary Fig.2, firing patterns were classified as: **no AP** (No AP detected at any current injection), **single AP** (maximum 1 AP detected at any stimulation intensity), **adaptive trains of APs** (multiple APs detected at at least one stimulation intensity, but frequency decrease with increasing stimulation) and **mature repetitive AP firing** (AP frequency increases monotonically with increasing stimulation strength, without frequency adaptation). AP frequency (Hz) was calculated by dividing the number of APs in the 500ms window by 0.5 to derive the number of APs per second. Cells with a series resistance greater than 30M Ω or a holding current lower than -100pA were rejected.

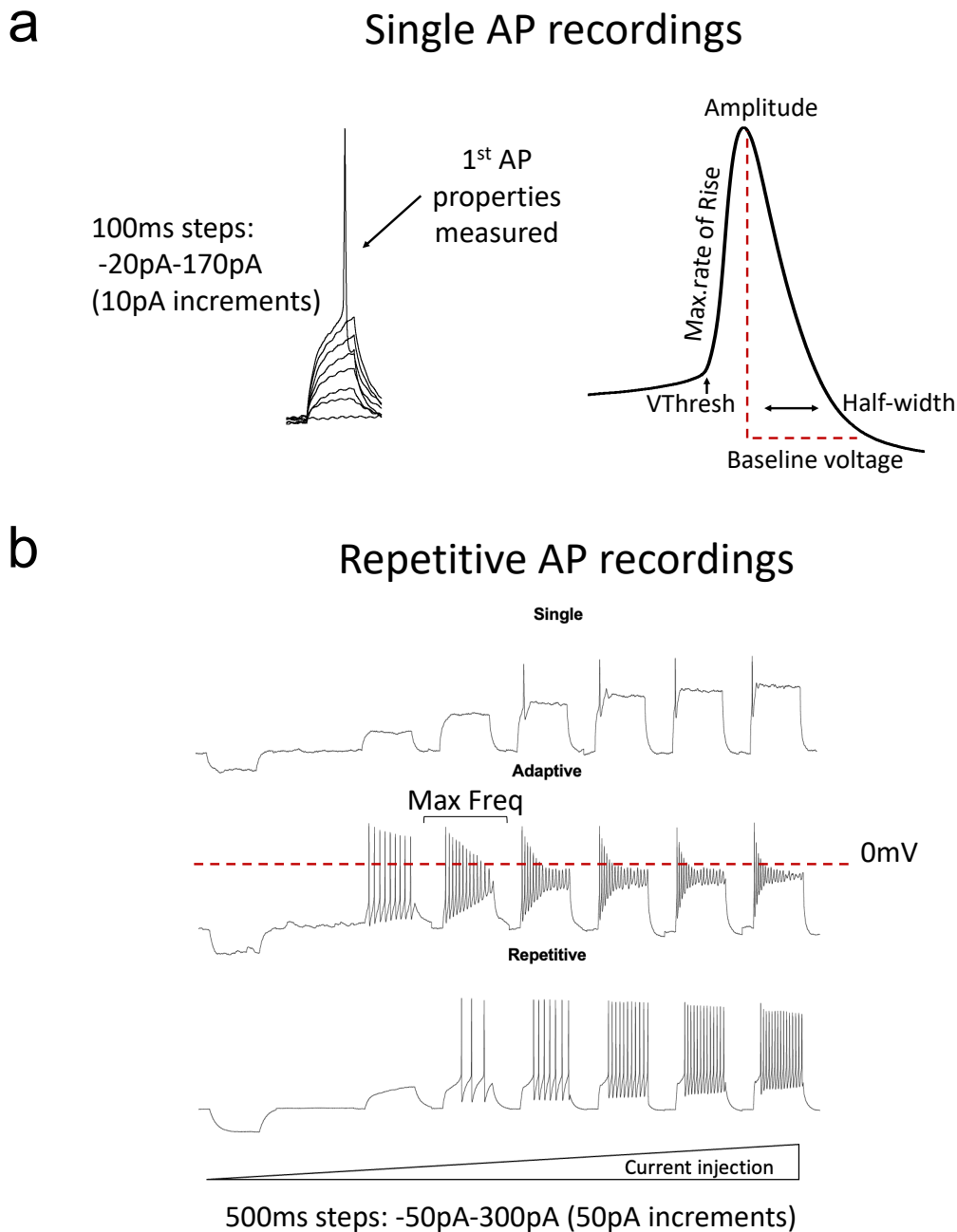


Figure 2.3. Schematic outlining single and repetitive action potential analysis for whole cell patch clamp electrophysiology recordings.

2.3.9 Analysis of AIS morphology

AIS length, diameter and start position were analysed using FIJI. Ankyrin-G fluorescence was uniformly thresholded and the AIS length and position relative to the soma, as determined by the CHR2-YFP counter stain, were manually traced. AIS diameter was measured at the mid-point of the AIS. 3D-reconstructions of the AIS to derive volume/surface area measurements were carried out using IMARIS 9.1.2 software by generating a surface map based on the

ankyrin-g fluorescence. Gating thresholds for this were kept constant between samples. To confirm the reliability of the manual tracing method and any bias introduced by the lack of blinding, a subset of AIS data (6-week) was analysed again in a blinded manner and compared to the original measurements. Length measurements were highly consistent between the original and the blinded analyses (Corrected length: difference mean 3.904 ± 3.891 , $p=0.32$, $r^2=0.76$. G298S length: difference mean 2.959 ± 5.299 , $p=0.56$, $r^2=0.76$).

2.3.10 Analysis of soma size and number of dendrites

Soma size and dendrite number were analysed manually using FIJI software based on CHR2-YFP staining. The soma was manually traced to derive the soma size. Simultaneously the number of dendritic branches directly emanating from the soma border was counted using the cell counter plug-in in FIJI.

2.3.11 Analysis of TDP-43

FIJI was used to analyse TDP-43 fluorescence intensity. DAPI was used as a reference to trace the nucleus to determine nuclear levels of TDP-43, while CHR2-YFP was used as a reference to trace the soma to determine cytoplasmic levels of TDP-43. Integrated density was used to measure fluorescence intensity.

2.3.12 Bioinformatics analysis

Quality control of the RNA sequencing data was carried out using fastQC and passed all QC measures. Further bioinformatics analysis was carried out by Fursham Hamid in R. Briefly Nextflow RNAseq pipeline was used to generate STAR alignment to the hg19 reference genome. Gene quantification was subsequently performed using Salmon.

2.3.13 High content image analysis of neuromuscular co-cultures

96-well neuromuscular co-cultures were imaged using an Operetta CLS high content image analysis system using Harmony 4.9 software. Plates were imaged in non-confocal mode using a 20x water objective. 69 fields were taken with a 20% overlap and 5 Z-planes at $2\mu\text{m}$ intervals with a binning of 2. For analysis using Harmony 4.9, advanced flatfield and brightfield correction was applied and stack processing was carried out using 3D analysis. Find nuclei

functions were used to generate initial masks for Titin, TUBB3, SV2 and AChR immunofluorescence. Threshold and splitting sensitivities were adjusted for each experiment depending on fluorescence intensity and background noise. The morphology and intensity calculator functions were used to derive morphological and fluorescence intensity parameters for all objects, which were then used to filter out background and non-specific staining. Mask filters were applied to SV2/AChR objects to derive objects that were co-localised in order to derive NMJ object values.

2.3.14 Calculation of myofiber contraction force on elastomer nanofibers

The velocity (\mathbf{v}) vectors (\mathbf{v}_x and \mathbf{v}_y) were exported from PIVLab and used to calculate an estimate for specific force at peak contraction velocity, using Hooke's laws. Displacement (\mathbf{d}) vectors (\mathbf{d}_x and \mathbf{d}_y) were calculated using $|\mathbf{v}|=|\mathbf{d}|/t$, and subsequently strain (ϵ_x and ϵ_y). Stress ($\boldsymbol{\sigma}$) vectors were calculated using $\sigma_x=\epsilon_x E$ and $\sigma_y=\epsilon_y E$ where $E= 30.5$ kPa (average elastic modulus for cultured skeletal muscle reported in the literature). Force (\mathbf{F}) vectors were estimated using $F_x=\sigma_x A_{yz}$ and $F_y=\sigma_y A_{xz}$, where A was cross sectional-area. Specific force (kN m^{-2}) = stress (kPa).

2.3.15 Diagrams and schematics

All diagrams and schematics were made using BioRender online software.

2.3.16 Statistics

Statistical analysis was performed using Prism 9 (GraphPad) and MATLAB. One-Way-ANOVA with Dunnet's test for comparisons, Two-Way-ANOVA, unpaired, non-parametric t-tests and Mann Whitney tests were all used to infer statistically significant differences between samples and groups of samples and are specified for each figure. P-values <0.05 were deemed to be statistically significant and are denoted by*. ** $p<0.01$, *** $p<0.001$, **** $p<0.0001$. All values are represented as the mean \pm SEM.

2.3.17 Statement on biological, experimental, and technical replicates

Initially it had been the intention to generate three TDP-43 lines and three control lines. This would comprise the patient-derived TDP-43^{G298S} line and a CRISPR corrected isogenic control

line, a wildtype line with the TDP-43^{G298S} mutation introduced by CRISPR and a separate TDP-43^{M337V} line. Multiple attempts were made to introduce the TDP-43^{G298S} mutation into the wildtype line without success, and we learnt that the TDP-43^{M337V} line had an abnormal karyotype so discontinued its use. Successfully engineering the remaining lines (wildtype, TDP-43^{G298S}, and TDP-43^{G298S} Corrected) with the HB9::CD14, CHR2-YFP, and iPAX7 constructs took a significant amount of time (~1-2 years) so it would have taken longer than the duration of the PhD to generate and perform the same experiments on additional cell lines. As such indicative statistics have been performed on the lines that were used, despite the true biological replicates being N=2 for control and N=1 for TDP-43. This is in line with similar published studies carrying out electrophysiology and neuromuscular co-cultures of ALS-related hiPSC neurons using single TDP-43 patient hiPSC lines (Osaki et al. 2018, Devlin et al. 2015).

In every figure biological replicates are denoted as (N) and are defined as individual cell lines derived from individual donors. Induction replicates are denoted as (iN) and are defined as how many times the experiment was repeated with separate inductions (Complete differentiations from PSCs to mature cell types). Technical replicates are denoted as (n) and include individual neurons for AIS and electrophysiology data, individual micro-device co-cultures for the neuromuscular co-cultures, and individual wells of a 96-well imaging plate /coverslips for HCI data and other types of imaging data. In text, the replicate number is provided on which the indicative statistics were performed. Indeed, for many published electrophysiology studies, statistics are often performed with individual neurons being the biological unit (n) pooled from several animals (N). Here we have tried to replicate this convention by performing statistics on individual neurons pooled from multiple inductions (iN). It is clearly an important point to make that this data is still from a true biological N=1 and future work with additional cell lines will be required to further validate the statistical conclusions reached from this work.

3. Engineering mouse ESC-derived neuromuscular co-cultures to model ALS

3.1 Hypotheses and aims

This chapter describes the establishment of two neuromuscular co-culture platforms using mouse embryonic stem cell (mESC) derived motor neurons and astrocytes cultured with primary chick myoblasts in custom built, compartmentalised microdevices. Using this platform, it was then possible address several questions relating to *in vitro* neuromuscular circuit formation and ALS-related phenotypes:

1. Is neuromuscular synapse formation activity-dependent?
2. Do ALS-linked SOD1^{G93A} astrocyte mutations cause ALS-related neuromuscular phenotypes?
3. Can this co-culture platform be used to test candidate ALS drugs?

Since the scalability and amenability to automation of this microdevice co-culture format was limited, another co-culture format that overcame these limitations was established (This format is further developed in chapter 5 using human iPSCs). This led to an additional aim being set:

4. Can neuromuscular co-cultures be scaled into a 96-well format, allowing automated HCl analysis of ALS-related phenotypes and candidate drug responses?

3.2 Differentiation and MACS purification of mouse ESC derived motor neurons and astrocytes

Mouse ESCs were differentiated into functional motor neurons and astrocytes using a small molecule directed differentiation approach and magnetic activated cell sorting (MACS) was used to generate highly enriched cell populations (Cell lines and protocols were originally developed by Carolina Barcellos-Machado). Mouse ESCs that were differentiated into motor neurons were genetically engineered to stably express the human cell surface antigen hCD14 under the control of the motor neuron specific *HB9* promoter. In addition, they were also

engineered to stably express the optogenetic actuator channel rhodopsin-2-YFP (CHR2-YFP) under the control of the CAG promoter. Mouse ESCs that were differentiated into astrocytes were engineered to stably express the human cell surface antigen hCD14 under the control of the astrocyte specific *GFAP* promoter as well as GDNF under the control of the constitutive CAG promoter.

Following well established differentiation protocols, mouse ESCs were made to form embryoid bodies (EBs) through culture in suspension dishes. Subsequent treatment with retinoic acid (RA) and sonic agonist (SAG) induced neuronal differentiation and an additional expansion stage on matrigel facilitated astrocyte differentiation (Figure 3.1a). MACS was then used to enrich motor neuron and astrocyte populations from the separate cultures. Briefly, a mouse monoclonal primary antibody was directed to the hCD14 antigen under the expression of the *HB9* and *GFAP* promoters and a secondary antibody against mouse IgG, conjugated to a magnetic microbead was used to allow magnetic activated positive cell enrichment. Pre-sort, flow through (FT) and eluate populations were then fixed and stained for GFAP and neuronal TUBB3 and imaged using confocal microscopy (Figure 3.1b). GFAP and β 3-tubulin (TUBB3) positive cells were quantified relative to total cell number based on DAPI. TUBB3 populations were found to be enriched from 35% (SE \pm 4.3) to 90% (SE \pm 3.6, T-test $p=0.0006$, $n=3$), while GFAP populations were enriched from 26% (SE \pm 4) to 91% (SE \pm 0.83, T-test $p<0.0001$, $n=3$), (Figure 3.1c).

Subsequently post-mitotic motor neurons and astrocytes were co-cultured at defined ratios (5k motor neurons, 20k astrocytes) in 96-well imaging plates (Figure 3.1d). We then assessed the ability of astrocytes stably expressing GDNF to support motor neuron survival by automatically quantifying motor neuron cell numbers at defined intervals using an operetta CLS high content imaging system and normalising to the original starting population. It was found that in as little as 72h, GDNF expressing astrocytes had a remarkable effect on preserving motor neuron survival from 52% (SE \pm 2.7) to 93% (SE \pm 5.1, T-test $p=0.0022$, $n=3$), (Fig 3.1d).

3.3 Assembly of neuromuscular co-cultures in 3D-compartmentalized microdevices containing mESC-motor neurons, mESC-astrocytes and chick myoblasts

Compartmentalised microdevices were manufactured by pouring uncured PDMS onto a silicon master-mould (Machado et al. 2019). The PDMS was then cured and peeled from the mould. Subsequently the PDMS casts were plasma bonded to 35mm tissue-culture dishes and NOA-73 anchor points were manually pipetted into the central myofiber compartment (Figure. 2a). Micro-devices were usually assembled in the 35mm dishes as a 2x3 array. Subsequently three neural aggregates containing 5k GDNF expressing mESC-astrocytes and 15k mESC-motor neurons were plated into each outer compartment in a fibrin/Matrigel hydrogel mix, which was polymerised by the addition of thrombin. One day later 20k primary chick myoblasts were plated into the central compartment in the same hydrogel mix. Axons were able to grow down the micro-channels and innervate myoblasts in the central compartment (Figure 3.2c,d,e). Fourier analysis showed that myoblasts grew in an aligned manner along the axis of the central compartment (Figure 3.2e).

3.4 Formation of functional neuromuscular junctions in 3D-compartmentalized micro-devices

The next step was to assess whether functional neuromuscular junctions could be formed in the neuromuscular co-cultures. Following co-culture for 9 days, cultures were fixed and stained for neuronal TUBB3, the pre-synaptic marker SV2 and the post synaptic marker AChR. Confocal microscopy then allowed co-localisation analysis of pre and post synaptic markers. Using IMARIS image analysis software it was possible to generate 3D reconstructions of neuromuscular synapses. Distinct bouton and pretzel shaped NMJ morphologies, resembling those of early neuromuscular synapses during development were observed (Figure 3.3a). In conjunction with this, while SV2 staining was enriched at the neuromuscular synapses, it was also widely observed along axons indicating a relatively early maturation stage, since in postnatal neuromuscular junctions SV2 is solely restricted to the neuromuscular junction itself.

To assess the functionality of these neuromuscular synapses, optogenetic stimulation using the optogenetic actuator CHR2-YFP was used to induce action potential firing in the motor

neurons, and particle image velocimetry (PIV) analysis was used to measure associated myofiber contraction velocities in recorded videos. A range of LED intensities were tested using whole-cell patch clamp electrophysiology to determine an optimum range that reliably triggered neuronal firing. It was found there was very little difference between 1% and 100% LED intensity and all could elicit robust firing. As such a mid-level of 40% LED intensity was chosen to mitigate phototoxicity, yet ensure robust firing even in low CHR2-YFP neurons. Briefly PIV analysis is an optical method of flow visualisations that tracks displacement vectors across many interrogation areas between frames of a video recording, allowing vector velocity and direction to be calculated. It was found that 500ms, 470nm (blue light) optogenetic stimulation induced robust and specific myofiber contractions with an average peak velocity magnitude of $24.8\mu\text{m/s}$ ($\text{SE} \pm 7.106$). These contractions were abolished through addition of the voltage gated Na^+ channel antagonist tetrodotoxin (TTX) from $24.8\mu\text{m/s}$ ($\text{SE} \pm 7.106$) to $0.33\mu\text{m/s}$ ($\text{SE} \pm 0.07$, T-test $p=0.038$, $n=6$) and through addition of the AChR antagonist tubacurarine (DTC) $24.8\mu\text{m/s}$ ($\text{SE} \pm 7.106$) to $1.19\mu\text{m/s}$ ($\text{SE} \pm 0.40$, T-test $p=0.04$, $n=6$) (Figure 3.3b,c) (DTC experiments were carried out by Carolina Barcellos-Machado). Taken together this data indicates that myofiber contractions are dependent on motor neuron action potential firing and acetylcholine release at functional neuromuscular synapses.

3.5 Optogenetic entrainment enhances NMJ formation

Synapse formation in the central and peripheral nervous system is activity dependent. Since the motor neuron populations in these cultures were highly enriched using MACS, spontaneous network activity primarily driven by inter-neuron activity was likely to be much lower than in mixed cultures. To this end, the role of motor neuron activity in neuromuscular synapse formation was investigated in these neuromuscular co-cultures. To do this, neuromuscular co-cultures were 'entrained' for 1 hour a day with 5Hz 470nm optogenetic stimulation at an LED intensity of 60% and an epoch of 20ms for 5 days (Figure 3.4a). Brief periods of entrainment were chosen to mitigate the effects of phototoxicity. Antioxidant supplement was also applied to the cultures during the entrainment periods to further mitigate this effect.

When compared to non-entrained cultures, 5 days of optogenetic entrainment significantly increased neuromuscular synapse formation by roughly two-fold (Figure. 3.4b,c). Non-entrained cultures had an average of 64.17 (SE \pm 10.6) colocalised SV2/AChR objects per field of view (henceforth defined as NMJs), while entrained cultures had an average of 124.5 (SE \pm 20.5) NMJs per field of view (T-test $p=0.026$, $n=6$) (Figure 3.4b,c). Optogenetic entrainment appeared to enhance the formation of both pre- and post-synaptic structures. The number of pre-synaptic SV2 objects increased from 513.3 (SE \pm 67.3) to 951 (SE \pm 103.1) per field of view (T-test $p=0.0052$, $n=6$), while the number of post-synaptic AChR objects increased in a similar fashion from 106.3 (SE \pm 20.1) to 256.3 (SE \pm 38.9) objects per field of view (T-test $p=0.0065$, $n=6$) (Figure 3.4b,c). Furthermore, total axon outgrowth also seemed to be improved following optogenetic stimulation from an average TUBB3 coverage of $33064\mu\text{m}^2$ (SE \pm 3152) per field of view to $55435\mu\text{m}^2$ (SE \pm 5924) per field of view (T-test $p=0.0087$, $n=3$) (Figure 3.4b,c). Taken together these results show that neuromuscular synapse formation is activity dependent and that activity influences formation of both pre- and post-synaptic structures.

3.6 Optogenetic entrainment enhances myofiber contractility

Since a strong effect of optogenetic entrainment had been seen on neuromuscular synapse formation the next goal was to ascertain whether this enhanced optogenetically evoked myofiber contractility. To do this PIV analysis was used to compare optogenetically evoked myofiber contraction velocities in entrained vs. non-entrained cultures. In addition to this, myofiber contraction velocities were also compared in entrained vs. non-entrained cultures that had been treated with TTX for the entire culture period to completely block any form of activity (Figure 3.5a). TTX was removed from these cultures 24hours prior to video recordings so that action potentials could be optogenetically evoked for the contraction recordings.

Optogenetic entrainment significantly enhanced evoked myofiber contractility from $2.72\mu\text{m/s}$ (SE \pm 0.59, $n=6$) to $5.28\mu\text{m/s}$ (SE \pm 0.79, $n=4$, T-test $p=0.029$) (Figure 3.5b,c). Completely blocking activity throughout the culture period using TTX significantly decreased evoked myofiber contractions down to $0.36\mu\text{m/s}$ (SE \pm 0.06) in non-entrained plus TTX conditions (T-test $p=0.0025$, $n=6$) and $0.34\mu\text{m/s}$ (SE \pm 0.02) in entrained plus TTX conditions (T-test $P<0.0001$, $n=6$) (Figure 3.5b,c). Taken together this data in conjunction with synaptic

staining data in figure 3.4 suggests that neuromuscular synapse formation in these neuromuscular co-cultures is highly dependent on neuronal activity.

3.7 mESC-derived SOD1^{G93A} astrocytes display ubiquitin positive inclusions and negatively impact motor neuron survival

The next objective was to use this neuromuscular co-culture platform to model neuromuscular disease phenotypes. In amyotrophic lateral sclerosis (ALS) neuromuscular synapse and axonal degeneration are key pathological events that occur in the disease progression (Fischer et al. 2004). Mutations to the superoxide dismutase 1 (*SOD1*) gene were the first identified genetic component of ALS and have become a standardized model of the disease in mice and cell culture models since. Furthermore, it has been demonstrated that *SOD1* mutations in astrocytes can have a non-cell autonomous deleterious effect on motor neuron survival (Nagai et al. 2007). To this end, mESCs harbouring a SOD1^{G93A} transgene were differentiated into astrocytes to see if they would induce pathological features of ALS such as ubiquitin positive inclusions and whether they would negatively impact motor neuron survival.

Mouse ESCs expressing the ALS-related human SOD1^{G93A} gene were differentiated into astrocytes, stained for ubiquitin and a CLS operetta high content imaging system used to automatically quantify the size and number of ubiquitin positive inclusions per astrocyte (Figure 3.6a). SOD1^{G93A} significantly increased the number of ubiquitin positive inclusions per cell from 3.2 (SE ± 0.1) to 4.0 (SE ± 0.3, T-test p<0.0001, n=3), while ubiquitin inclusion size also significantly increased from 40.1µm² (SE ± 0.5) to 41.5µm² (SE ± 0.4, T-test p=0.04, n=3) (Figure 3.6b). To assess the impact of SOD1^{G93A} astrocytes on motor neuron survival a longitudinal imaging assay was carried out using an Operetta CLS high content image analysis system to automatically quantify motor neuron survival at different time points. By normalising to 24h the percentage of wildtype motor neuron survival on wildtype and SOD1^{G93A} astrocytes at different timepoints was calculated. It was found that SOD1^{G93A} astrocytes negatively impacted motor neuron survival within 96 hours of co-culture. Wildtype motor neurons grown on wildtype astrocytes had 68.5% (SE ± 7.3, n=5) survival at this timepoint, compared to 34.7% (SE ± 5.7, n= 3, T-test p=0.019) for wildtype motor neurons

grown on SOD1^{G93A} astrocytes (Figure 3.6c). Finally, to confirm previous studies showing that mutant SOD1 astrocytes express higher levels of the reactive astrocyte markers: *GFAP* and *TGFβ1* qRT-PCR analysis was performed on differentiated wildtype and SOD1^{G93A} astrocytes and normalised expression to GAPDH. Despite previous findings in the literature, it was found that SOD1^{G93A} astrocytes expressed moderately lower levels of TGFβ1 0.035 (SE ± 0.004) compared to 0.047 (SE ± 0.002, T-test p=0.03, n=6) in wildtype astrocytes. Similarly, *GFAP* expression was slightly lower in SOD1^{G93A} astrocytes 0.19 (SE ± 0.03) compared to 0.32 (SE ± 0.08, T-test p=0.18, n=6) in wildtype astrocytes (Figure 3.6d). Taken together these results show that mESC-derived SOD1^{G93A} astrocytes exhibit ubiquitin positive inclusions similar to those seen in ALS patients and also negatively impact motor neuron survival. Despite this, previous studies showing that *TGFβ1* and *GFAP* upregulation contribute to these effects were not replicated here.

3.8 The RIPK1 inhibitor necrostatin rescues axon outgrowth and NMJ phenotypes in SOD1^{G93A} neuromuscular co-cultures

Since ALS related phenotypes had been observed in the SOD1^{G93A} astrocytes, the next goal was to assess how they would impact neuromuscular related phenotypes and whether targeting ALS-related pathways could rescue these phenotypes. In ALS some of the earliest pathological events include muscle weakness, axon denervation and neuromuscular synapse degeneration. Furthermore, RIPK1 has been shown to play an important role in necroptosis of axons in mouse models of the disease and as such RIPK1 inhibitors have been proposed as a potential treatment strategy for ALS (Ito et al. 2016, Re et al. 2014). Neuromuscular co-cultures with both wildtype and SOD1^{G93A} astrocytes were generated and stained for the pre-synaptic marker TUBB3 and post synaptic marker AChR and IMARIS used to generate 3D reconstructions of neuromuscular synapses.

In the SOD1^{G93A} neuromuscular co-cultures there was a strong reduction in axon outgrowth from $31 \times 10^5 \mu\text{m}^2$ (SE ± 69×10^4) to $88 \times 10^4 \mu\text{m}^2$ (SE ± 18×10^4 , T-test p=0.036, n=3), which was rescued by the RIPK1 inhibitor necrostatin back to $54 \times 10^5 \mu\text{m}^2$ (SE ± 15×10^5 , T-test p=0.043, n=3) (Figure 3.7a,b). Furthermore, there was a modest reduction in the number of neuromuscular synapses in the SOD1^{G93A} co-cultures from 41.7 per field of view (SE ± 10.1) in

the wildtype cultures to 31 (SE \pm 4.9, T-test $p=0.39$, $n=3$) in the SOD1^{G93A} cultures (Fig.7a,b). This was significantly improved by 10 μ M treatment of the RIPK1 inhibitor necrostatin up to 88.7 (SE \pm 12.1) neuromuscular synapses per field of view (T-test $p=0.011$, $n=3$) (Figure 3.7a,b). Finally, there was a significant reduction in NMJ size in SOD1^{G93A} co-cultures, with an average NMJ surface area of 29.8 μ m² (SE \pm 5.8) compared to 60.5 μ m² (SE \pm 8.6, T-test $p=0.041$, $n=3$) in wildtype cultures (Figure 3.7a,b). Necrostatin had no significant effect on restoring this phenotype (Figure 3.7b). Taken together these results show that ALS-linked SOD1^{G93A} astrocytes have a significant impact on axon outgrowth and neuromuscular synapse formation and that the RIPK1 inhibitor can partially rescue these phenotypes.

3.9 The RIPK1 inhibitor necrostatin rescues myofiber contractions in SOD1^{G93A} neuromuscular co-cultures

Having observed that SOD1^{G93A} astrocytes significantly impair axon outgrowth and alter neuromuscular synapse formation, the next goal was to assess whether there was a concomitant decrease in optogenetically evoked myofiber contractions. To do this neuromuscular co-cultures were generated with both wildtype and SOD1^{G93A} astrocytes and optogenetic stimulation of the motor neurons used to induce myofiber contractions that were analysed using PIV analysis.

It was found that SOD1^{G93A} co-cultures had significantly weaker optogenetically evoked myofiber contractions compared to wildtype co-cultures with an average peak contraction velocity of 3.3 μ m/s (SE \pm 0.4) vs 5.5 μ m/s (SE \pm 0.6, t-test $p=0.02$, $n=4$) (Figure 3.8a,b). It was also found that 10 μ M necrostatin treatment significantly improved optogenetically evoked myofiber contraction velocities from 3.3 μ m/s (SE \pm 0.4) to 9.3 μ m/s (SE \pm 2.2, T-test $p=0.03$, $n=4$) (Figure 3.8a,c). Taken together this data shows that ALS-linked SOD1^{G93A} astrocytes caused weaker optogenetically evoked myofiber contractions, mirroring symptoms in ALS patients. Furthermore, treatment with the RIPK1 inhibitor, necrostatin, effectively rescued this phenotype, validating RIPK1 as a potential therapeutic target for the treatment of ALS.

3.10 BCR-Abl inhibition rescues SOD1^{G93A} related neuromuscular phenotypes in an automated high content 96 well neuromuscular co-culture assay

Two major limitations were encountered in scaling up the neuromuscular co-cultures in the compartmentalized microdevice format. First, initial plating of the cells was very time-consuming and technically challenging, limiting the scale at which cultures could be produced. Secondly, the 35mm dish format of the cultures meant they were not amenable to high throughput automated imaging and analysis. As such imaging and analysing multiple conditions proved time-consuming. In order to make such a co-culture assay suitable for carrying out larger scale small-molecule screens an alternative assay was developed that could overcome these limitations.

To this end, neuromuscular co-cultures in 96-well imaging plates were developed, whereby mESC-MN/AC aggregates were plated on top of a sheet of primary chick myofibers. This format allowed faster plating of the cells, allowing far more conditions to be set up simultaneously. It also allowed automated imaging and analysis of the cultures using an operetta CLS high content imaging system (Figure 3.9a). Using the same immunofluorescence panel as in the microdevice cultures (Titin = myofibers, TUBB3 = motor axons, SV2 = pre-synaptic and AChR = post-synaptic) an automated image segmentation pipeline was developed using Harmony 4.8 to generate masks of each structure, allowing quantification of myofiber number and morphology, total axonal outgrowth and the number and morphology of pre- and post-synaptic structures. The pipeline also analysed co-localisation of pre- and post-synaptic structures, which was used to infer neuromuscular synapse number and morphology (Figure 3.9b). While developing this assay several lead molecular targets were tested in the 96 well neuromuscular co-culture assay. The resulting data is shown for the lead compound, a BCR-Abl inhibitor, similar to the commercially available Nilotinib (Sigma).

Firstly, similar SOD1^{G93A} astrocyte dependent phenotypes were observed in the 96 well neuromuscular assay as in the microdevice co-cultures. Axon outgrowth was reduced in the SOD1^{G93A} co-cultures from $36.5 \times 10^6 \mu\text{m}^3$ (SE $\pm 2.9 \times 10^6$) to $26.7 \times 10^6 \mu\text{m}^3$ (SE $\pm 2.5 \times 10^6$, T-test $p=0.023$, $n=8$), (Figure 3.9c,d). Similarly, the number of NMJs was moderately reduced from 8752 (SE ± 1089) per well to 6441 per well (SE ± 784 , T-test $p=0.1$, $n=8$) although this was not statistically

significant. Furthermore, NMJ surface area was also reduced from $77.7\mu\text{m}^2$ (SE \pm 7.6) to $55\mu\text{m}^2$ (SE \pm 2.7), T-test $p=0.064$, $n=8$). A dose response of the BCR-Abl inhibitor in the SOD1^{G93A} co-cultures was carried out. It was found that lower doses were particularly effective in restoring or even improving various parameters of the neuromuscular co-culture. Treatment with $0.1\mu\text{M}$ BCR-Abl inhibitor improved axon outgrowth from $26.7 \times 10^6 \mu\text{m}^3$ (SE \pm 2.5×10^6) to $56.1 \times 10^6 \mu\text{m}^3$ (SE \pm 2.4×10^6 , T-test $p < 0.0001$, $n=8$). in a similar fashion $0.1\mu\text{M}$ BCR-Abl inhibitor increased the number of pre-synaptic SV2 objects from 18494 (SE \pm 1638) to 43948 (SE \pm 3603, T-test $p < 0.0001$, $n=8$). The total number of NMJs also increased following $0.1\mu\text{M}$ BCR-Abl inhibition from 6441 (SE \pm 781) to 16888 (SE \pm 1386, T-test $p < 0.0001$, $n=8$). Finally, $0.1\mu\text{M}$ BCR-Abl inhibitor significantly increased NMJ surface area from $55\mu\text{m}^2$ (SE \pm 2.7) to $112\mu\text{m}^2$ (SE \pm 9.4, T-test $p=0.0002$, $n=8$).

Taken together these data shows the feasibility of using 96-well neuromuscular co-cultures to automatically quantify neuromuscular phenotypes in a rapid and unbiased manner. This approach replicates the same SOD1^{G93A} dependent phenotypes previously observed in the microdevice neuromuscular co-cultures. Finally, the feasibility of this approach to screen ALS relevant drugs was demonstrated, showing that BCR-Abl inhibition can rescue ALS related neuromuscular phenotypes. However, an evident caveat of this data is that the effect of the BCR-Abl inhibitor was not titrated out.

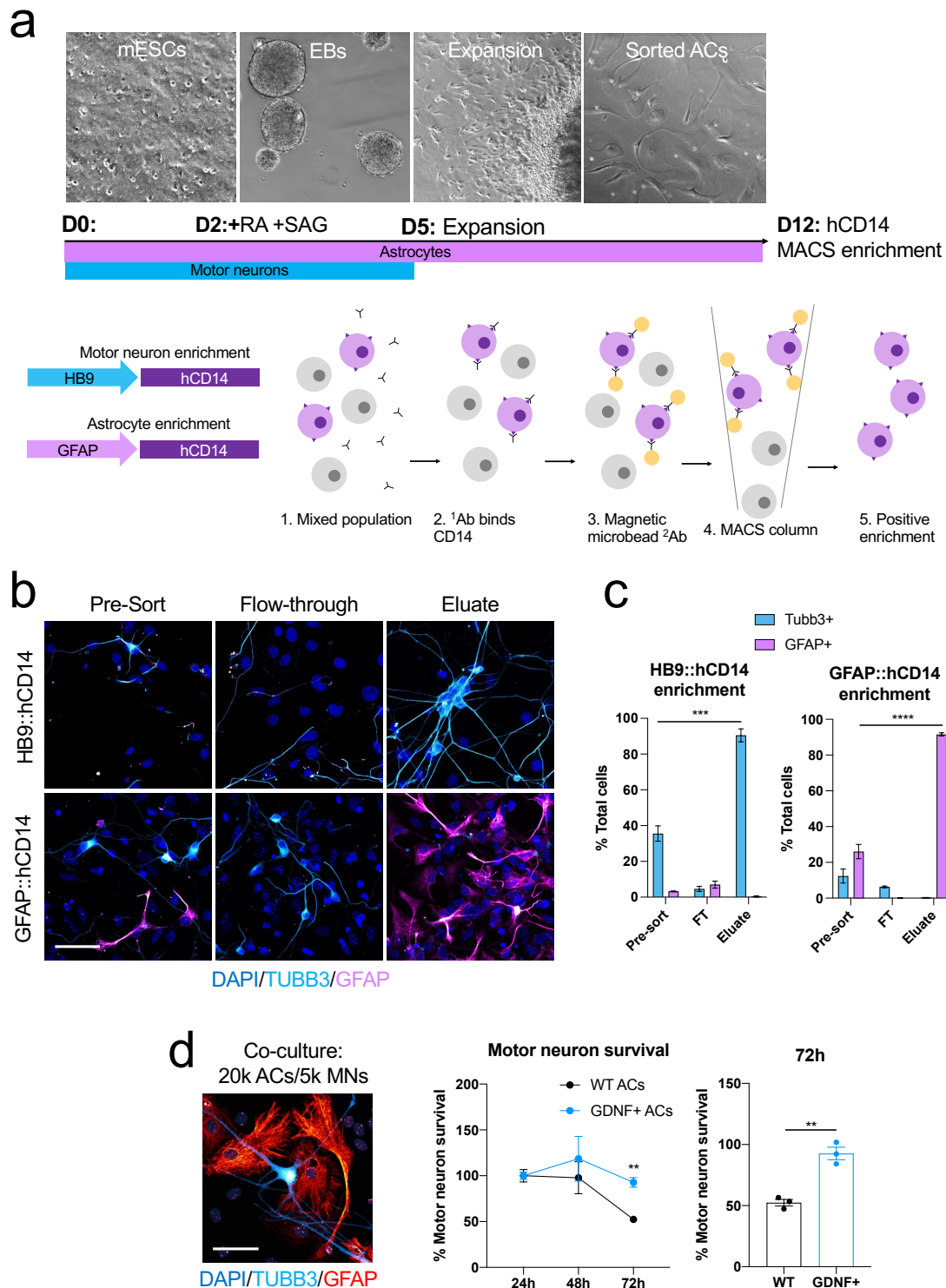


Figure 3.1. Differentiation and MACS purification of mESC derived motor neurons and astrocytes.

A, Schematic showing the differentiation and MACS protocols used to derive motor neurons and astrocytes from mouse ESCs. **B**, Immunofluorescence images showing pre-sort, flow through and enriched motor neuron (TUBB3) and astrocyte (GFAP) cell populations following MACS (Scale bar = 50µm). **C**, Quantification of motor

neuron/astrocyte enrichment following MACS relative to total cell number (DAPI) (N=1, iN=1, n=3). **D**, 5k motor neurons were co-cultured with 30k wildtype or GDNF expressing astrocytes and stained for DAPI, TUBB3 and GFAP (Scale bar = 50 μ m). Motor neuron survival was quantified using a longitudinal high content imaging operetta CLS pipeline and cell survival expressed relative to 24h cell counts (N=1, iN=1, n=3). Unpaired, two-tailed T-test used to infer statistical significance **p<0.01, ***p<0.001, ****p<0.0001. Error bars represent SEM.

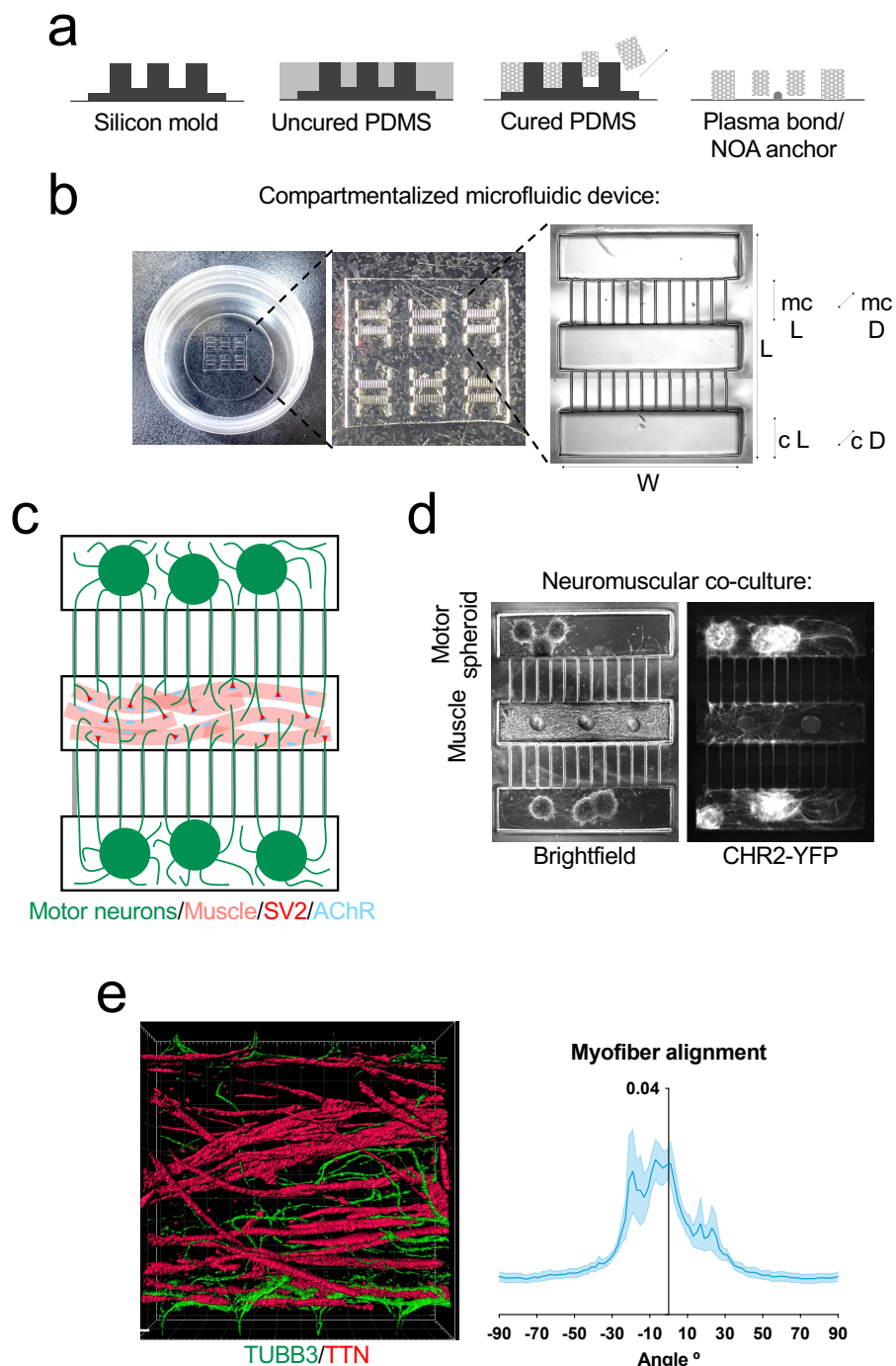


Figure 3.2. Assembly of neuromuscular co-cultures in 3D-compartmentalized microdevices containing mESC-motor neurons, mESC-astrocytes and chick myoblasts.

A, Schematic showing fabrication of compartmentalized microfluidic devices by PDMS casting on silicon master molds and plasma bonding cured PDMS to tissue-culture plastic dishes. **B**, Images of final manufactured compartmentalized microfluidic devices arranged in a 2x3 array. Device width = 2000 μ m, length = 2350 μ m, chamber length 450 μ m, micro-

channel length 500 μ m, chamber depth 500 μ m, micro-channel depth 10 μ m. **C**, Schematic showing 3D compartmentalized neuromuscular co-culture. mESC-motor neuron/astrocyte spheroids are plated into outer chambers and project axons into the central chamber to innervate primary chick myofibers. **D**, Brightfield and CHR2-YFP images of mouse/chick neuromuscular co-cultures. **E**, Immunofluorescence 3D reconstruction of Titin/TUBB3 labelling in the central compartment. Fourier analysis of myofiber alignment along the axis of the central compartment (N=1, iN=1, n=6). Error bars represent SEM.

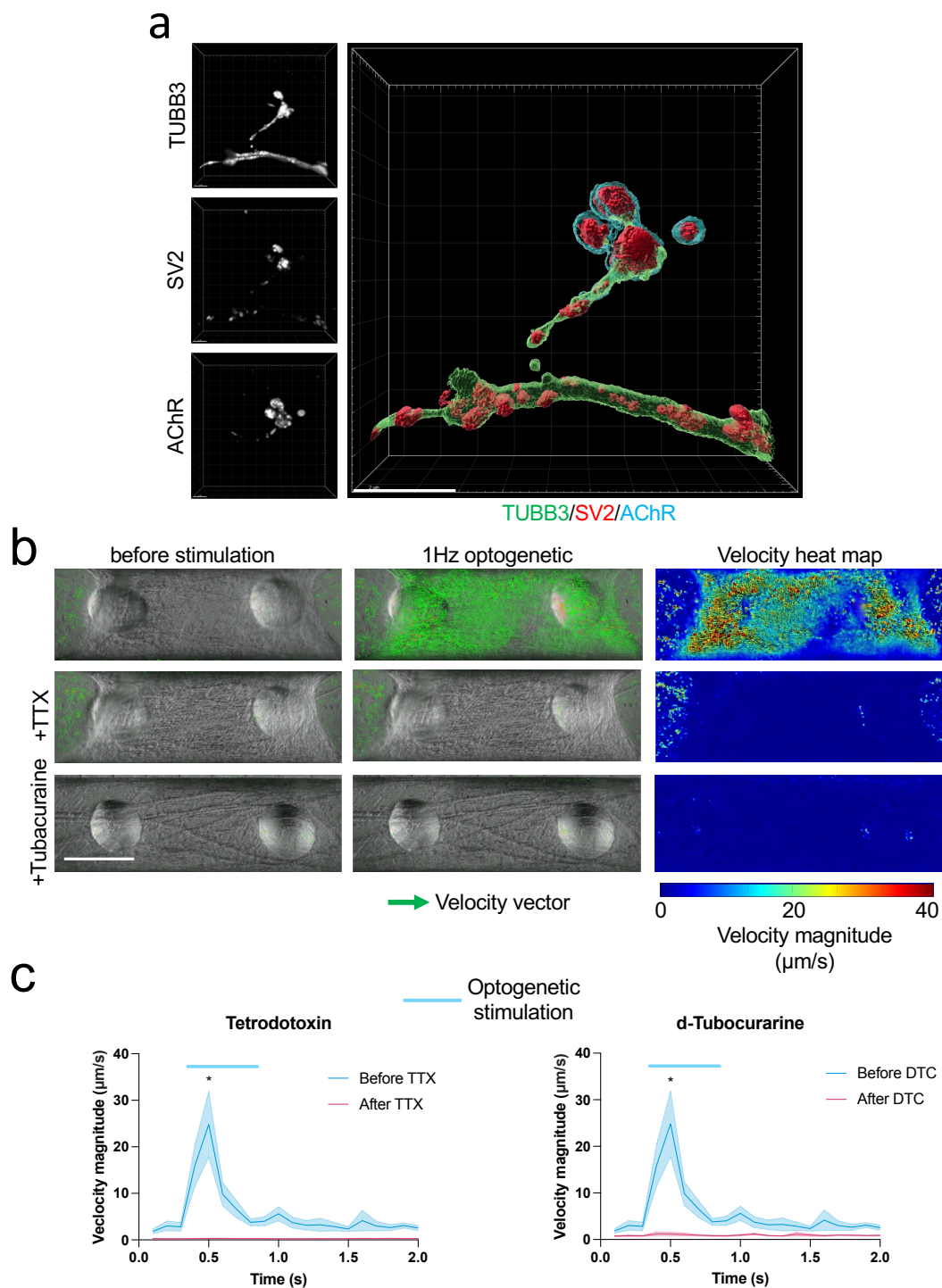


Figure 3.3. Formation of functional neuromuscular junctions in 3D-compartmentalized microdevices.

A, Immunofluorescence labelling of TUBB3, SV2 and AChR and 3D reconstruction of a neuromuscular junction (Scale bar = 5µm). **B**, PIV analysis of optogenetically evoked myofiber contractions showing start and peak frames with velocity vectors in green as well

as a velocity heatmap for the frame of peak contraction. Images shown for untreated, TTX treated and tubocurarine treated cultures (N=1, iN=1 n=6) (Scale bar = 500 μ m). **C**, PIV quantification of optogenetically evoked myofiber contraction velocity in untreated, TTX treated and tubocurarine treated cultures (N=1, iN=1, n=6). Unpaired, two-tailed T-test used to infer statistical significance * $p < 0.05$. Error bars represent the SEM.

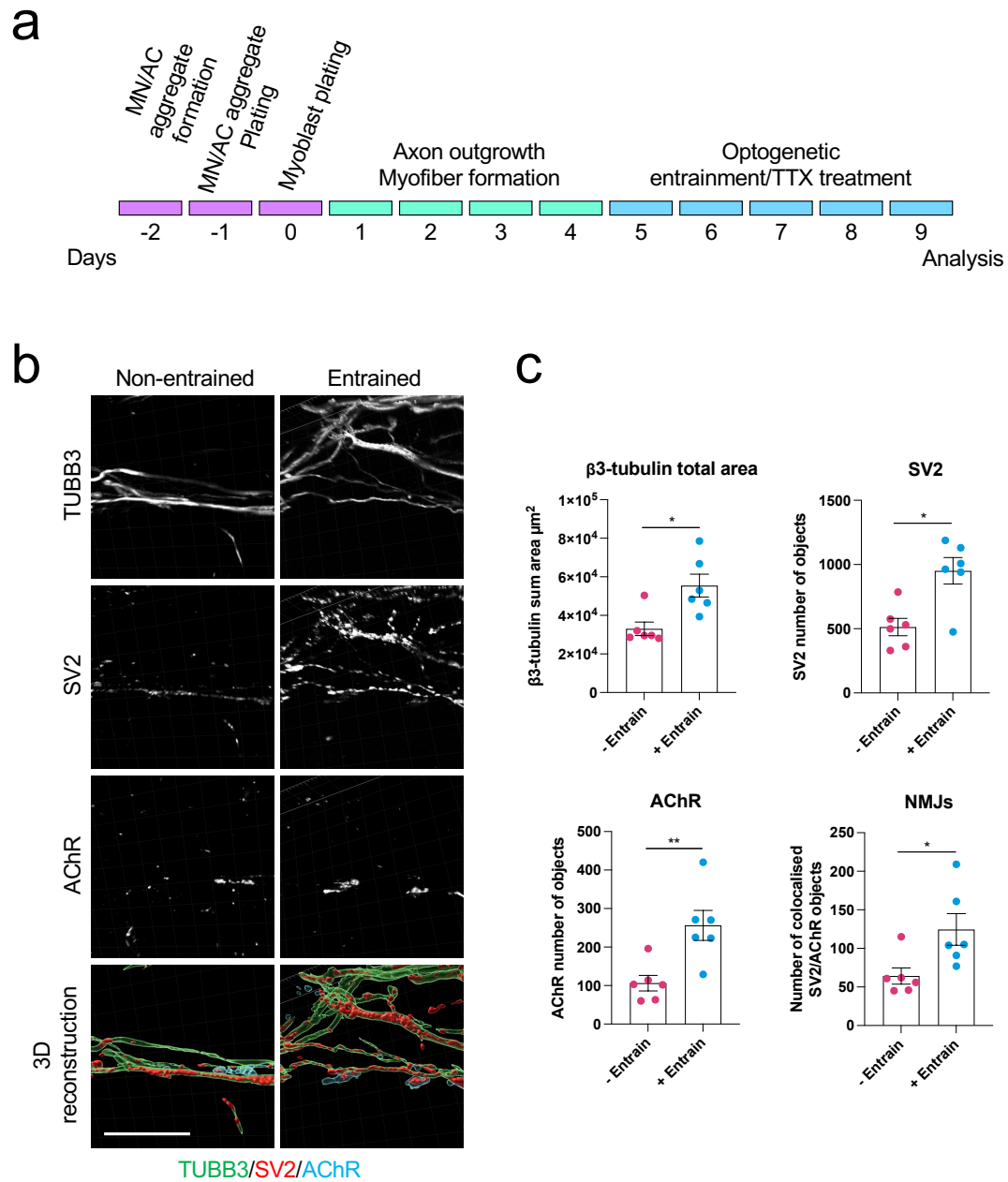


Figure 3.4. Optogenetic entrainment enhances neuromuscular junction formation.

A, Schematic showing neuromuscular co-culture and optogenetic entrainment timeline. Following cell plating 4 days were allowed for myofiber formation and axon outgrowth. After this 1hour of 5Hz optogenetic stimulation was applied to the co-cultures each day for 5 days. **B**, Immunofluorescence labelling and 3D reconstructions of TUBB3, SV2 and AChR in un-entrained and entrained conditions, $n=6$ (Scale bar = 100 μm). **C**, Quantification based on immunofluorescence labelling of axon outgrowth, pre and post synaptic object number and NMJ number in un-entrained and entrained conditions, ($N=1$, $iN=1$, $n=6$). Unpaired, two-tailed t-test used to infer statistical significance * $p<0.05$, ** $p<0.01$. Error bars represent the SEM.

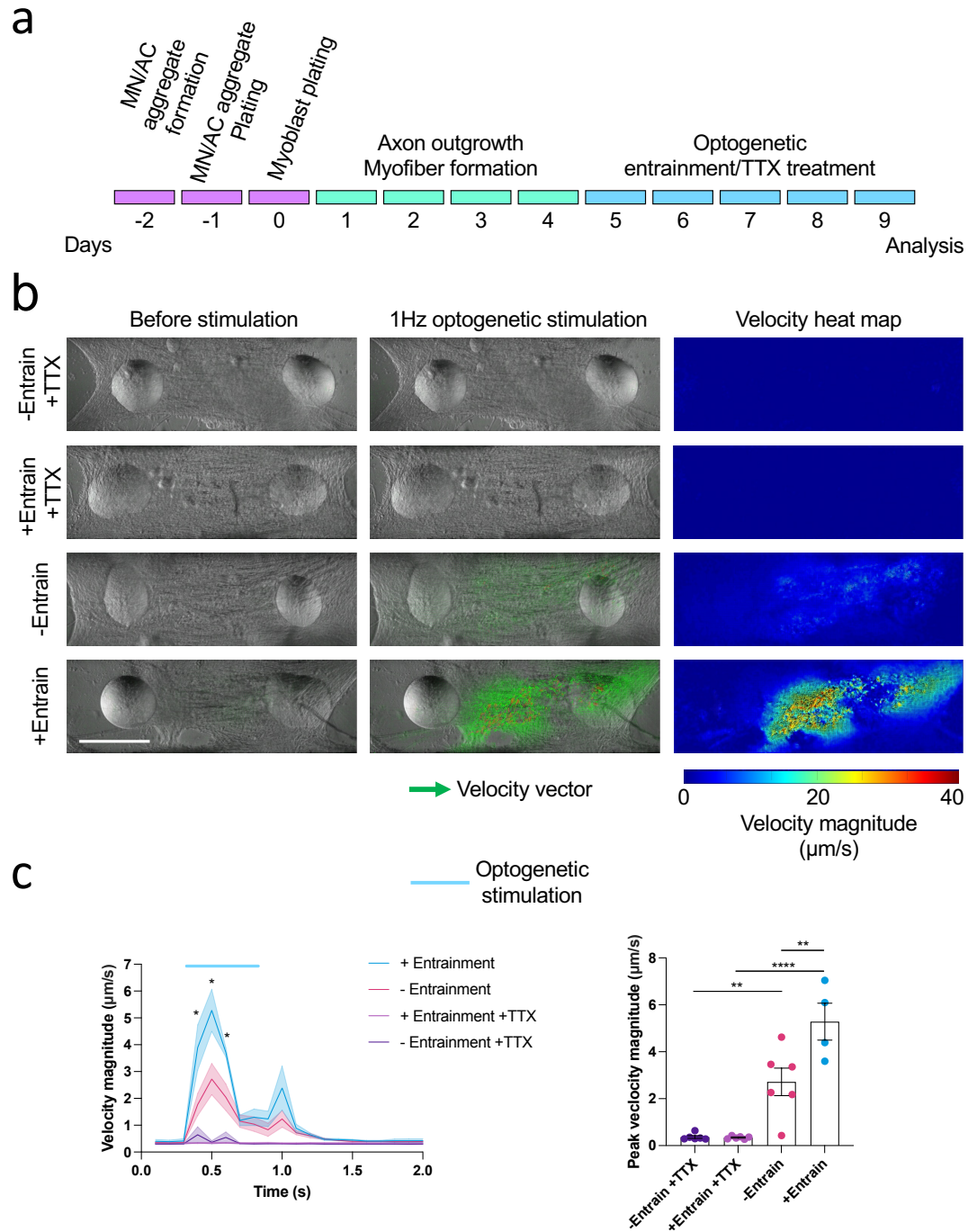


Figure 3.5. Optogenetic entrainment enhances myofiber contractility.

A, Schematic showing neuromuscular co-culture and optogenetic entrainment timeline. Following cell plating 4 days were allowed for myofiber formation and axon outgrowth. After this 1hour of 5Hz optogenetic stimulation was applied to the co-cultures every day for 5 days. **B**, PIV analysis of optogenetically evoked myofiber contractions in un-entrained and entrained cultures treated with and without TTX throughout the entrainment period,

n=6. Images show start and peak frames with velocity vectors in green as well as a velocity heatmap of the frame of peak contraction (Scale bar =500 μ m). **C**, PIV quantification of optogenetically evoked myofiber contractions in un-entrained and entrained cultures treated with and without TTX throughout the entrainment period (N=1, iN=1, n=6). Unpaired, two-tailed T-test used to infer statistical significance *p<0.05, **p<0.01, ****p<0.0001. Error bars represent SEM.

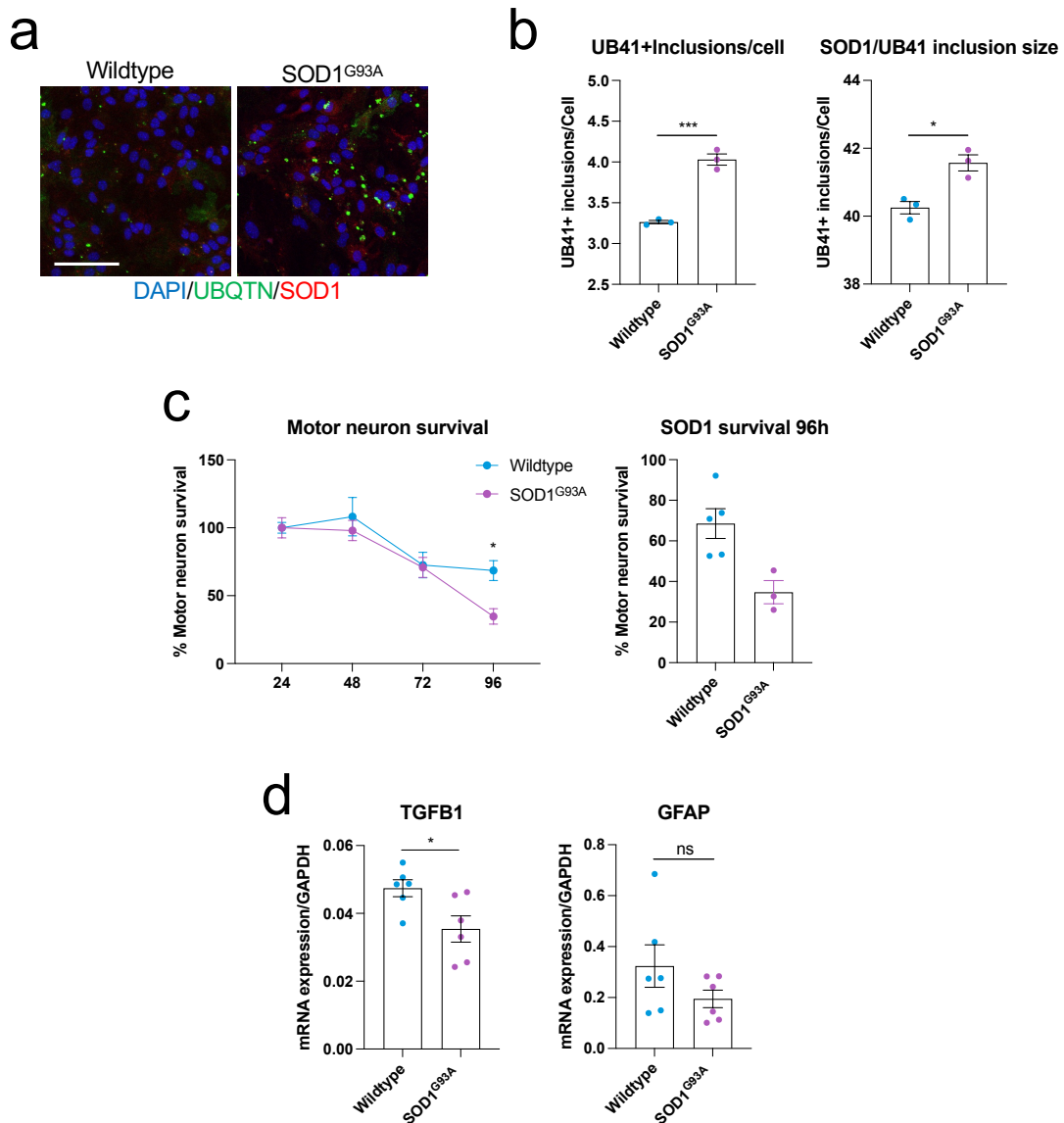


Figure 3.6. mESC-derived SOD1^{G93A} astrocytes display ubiquitin positive inclusions and negatively impact motor neuron survival.

A, Immunofluorescence labelling of UBQTN and SOD1 in mESC-derived astrocytes harbouring human wildtype SOD1 and ALS linked SOD1^{G93A} mutation, (N=1, iN=1, n=3) (Scale bar =100µm). **B**, Quantification of the number and size of ubiquitin+ inclusions per cell. **C**, Quantification of motor neuron survival on wildtype and SOD1^{G93A} astrocytes, (N=1, iN=1, n=3). **D**, qRT-PCR quantification of *TGFB1* and *GFAP* mRNA expression relative to GAPDH in wildtype and SOD1^{G93A} astrocytes, (N=1, iN=1, n=6). *p<0.05, ***p<0.001. Error bars represent SEM.

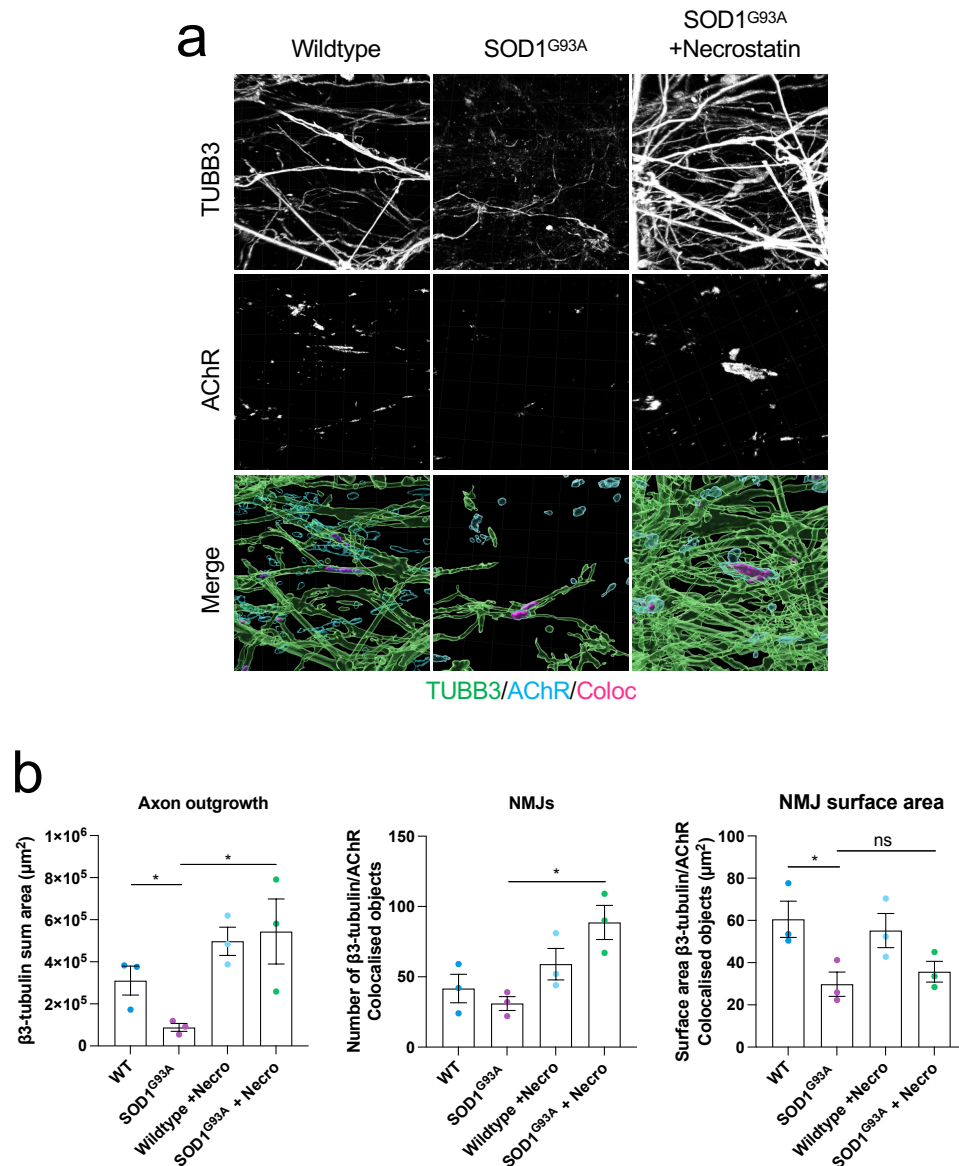


Figure 3.7. The RIPK1 inhibitor necrostatin rescues axon outgrowth and NMJ phenotypes in SOD1^{G93A} neuromuscular co-cultures.

A, Immunofluorescence labelling of TUBB3 and AChR alongside composite 3D NMJ reconstructions. Images shown for neuromuscular co-cultures containing wildtype astrocytes, SOD1^{G93A} astrocytes and SOD1^{G93A} astrocytes treated with the RIPK1 inhibitor necrostatin. (Scale bar = 100 μm). **B**, Quantification of axon outgrowth, NMJ number and NMJ size based on immunofluorescence labelling, (N=1, iN=1 n=3). Unpaired, two-tailed T-test used to infer statistical significance * $p < 0.05$. Error bars represent the SEM.

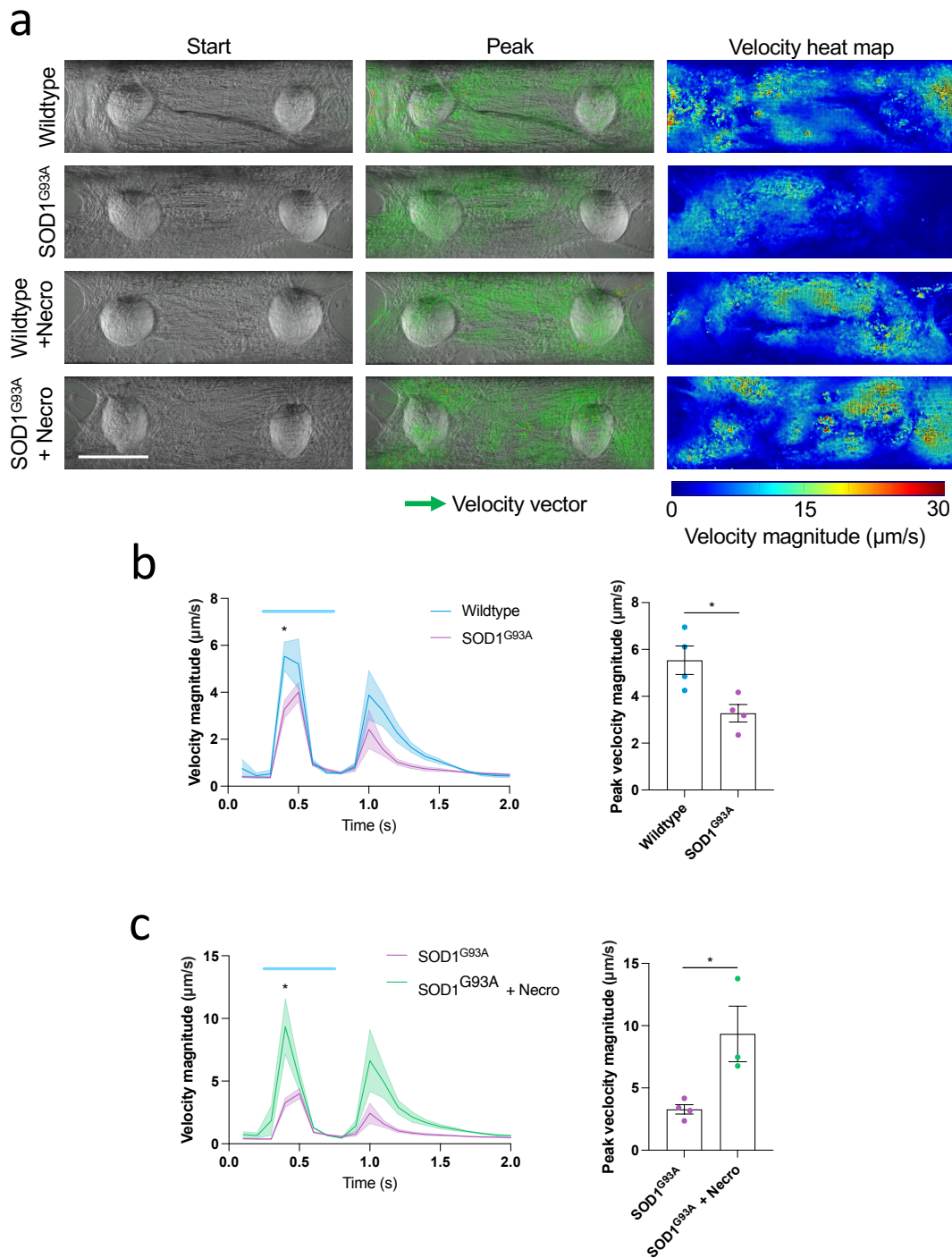


Figure 3.8. The RIPK1 inhibitor necrostatin rescues myofiber contractions in SOD1^{G93A} neuromuscular co-cultures.

A, PIV analysis of optogenetically evoked myofiber contractions in neuromuscular co-cultures containing wildtype and SOD1^{G93A} astrocytes treated with and without the RIPK1 inhibitor necrostatin. Images show start and peak frames with velocity vectors in green as well as a velocity heatmap of the peak contraction frame (N=1, iN=1, n=3) (Scale bar = 500μm). **B**, PIV quantification of optogenetically evoked myofiber contractions in wildtype and SOD1^{G93A} neuromuscular co-cultures. **C**, PIV quantification of optogenetically evoked

myofiber contractions in SOD1^{G93A} neuromuscular co-cultures treated with and without necrostatin (N=1, iN=1, n=3). Unpaired, two-tailed T-test used to infer statistical significance *p<0.05. Error bars represent SEM.

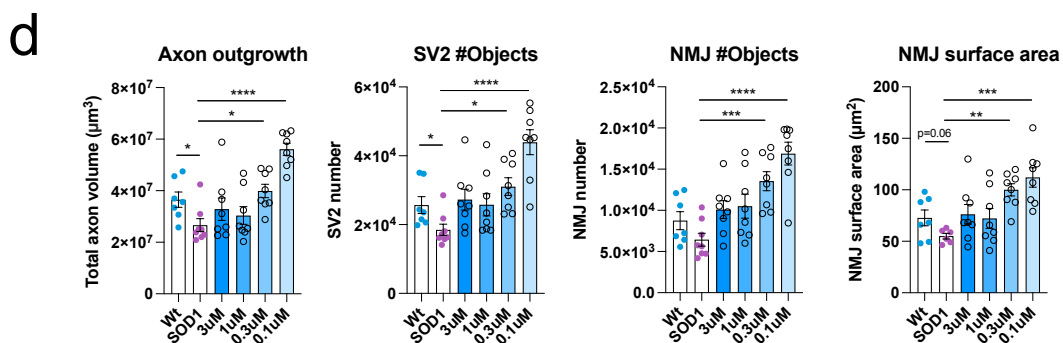
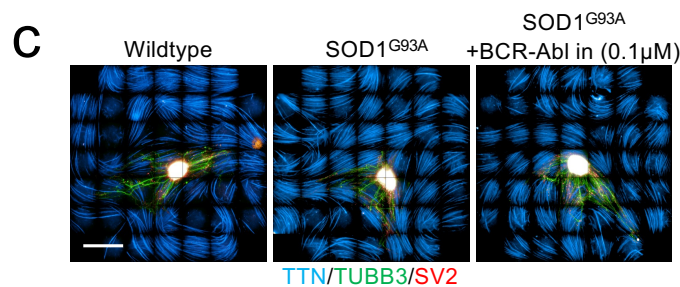
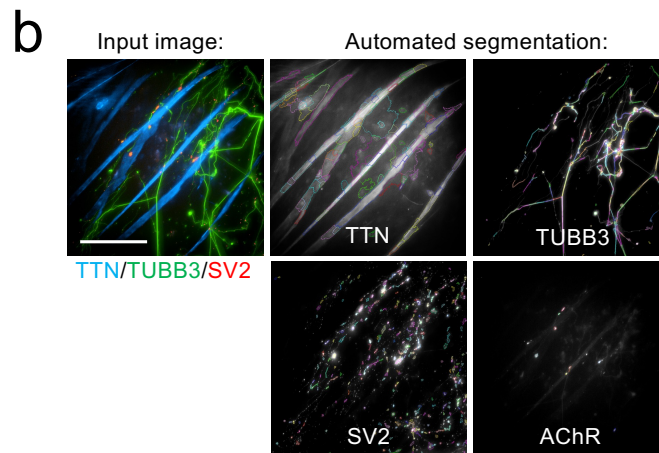
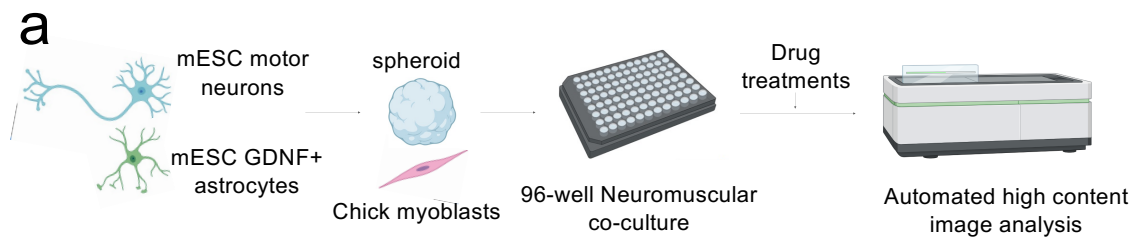


Figure 3.9. BCR-Abl inhibition rescues SOD1^{G93A} related neuromuscular phenotypes in an automated high content 96-well neuromuscular co-culture assay.

A, Schematic showing automated high content 96-well neuromuscular co-cultures assay. Motor neuron/astrocyte spheroids were plated on a sheet of chick myofibers in 96 well imaging plates. Following drug treatments and co-culture for 14 days, plates were imaged

and analysed automatically using an operetta CLS high content imaging system. **B**, Example of the automated image segmentation masks. Input image based on TUBB3, SV2, AChR and Titin staining. Subsequently masks were created for each channel and used to quantify axon outgrowth and neuromuscular junction phenotypes (Scale bar = 200 μ m). **C**, Whole well images of neuromuscular co-cultures containing wildtype astrocytes, SOD1^{G93A} astrocytes and SOD1^{G93A} astrocytes treated with a BCR-Abl inhibitor through an industry collaboration (Scale bar = 250 μ m) **D**, Automated quantification of axon outgrowth and neuromuscular junction phenotypes in wildtype and SOD1^{G93A} neuromuscular co-cultures treated with different concentrations of BCR-Abl inhibitor (N=1, iN=1, n=8). Unpaired, two-tailed T-tests used to infer statistical significance *p<0.05, **p<0.01, ***p<0.001, ****p<0.0001. Error bars represent the SEM.

3.11 Discussion

This chapter describes the development of a neuromuscular co-culture platform using mouse ESC-derived CHR2-YFP expressing motor neurons, mouse ESC-derived GDNF expressing astrocytes and primary chick myofibers (Figure 3.1, 3.2). These cells are co-cultured together in a compartmentalized PDMS microdevice, with neural aggregates plated in outer compartments that project axons through microchannels to innervate target muscle in a central compartment (Figure 3.2). This accurately reflects the CNS/PNS spatial separation of the different cell types that occurs *in vivo*. A published version of this work can be found here: (Machado et al. 2019). Using this co-culture platform, it was possible to grow functional neuromuscular junctions *in vitro*, despite interspecies differences of the different cell types. This was demonstrated through optogenetic stimulation of the motor neurons, which induced robust myofiber contractions that could be abolished by the Na⁺ channel blocker TTX and the ACh receptor blocker DTC (Figure. 3.3). Furthermore, it was shown that NMJ formation was activity dependent, since optogenetic entrainment improved myofiber contractility, axon outgrowth and the total number of NMJs (Figure. 3.4, 3.5). Finally, it was shown that ALS-related SOD1^{G93A} astrocytes induced neuromuscular phenotypes, including weaker optogenetically evoked myofiber contractions (Figure. 3.8), reduced NMJ size and axonal denervation, which could be partially rescued or improved by treatment with the RIPK1 inhibitor necrostatin (Figure. 3.9). Taken together, the data in this chapter shows the establishment of a robust neuromuscular co-culture platform that can be used to model both developmental and neurodegenerative processes relating to neuromuscular function.

The design of the microdevices described in this chapter offers several unique features compared to other similar co-culture platforms previously developed (Uzel et al. 2016, Yoshida et al. 2015, Abd Al Samid et al. 2018). First the manufacture of the devices is a simple and scalable design comprising a one-part PDMS construct (Figure. 3.2). While not fully suited to larger scale screening studies, the design easily allows an equivalent number of replicates to be carried out in a single experiment as those that would be used in basic research studies using animal models. Secondly the microdevices are open, rather than microfluidic, so compartments can easily be loaded with cells and there is less risk of hypoxia induced cell death. Furthermore, cell types are located close to the glass bottom of the tissue-culture dish, allowing the cultures to be directly imaged at high magnification without the need for additional tissue sectioning and processing (Figure. 3.3). Finally, the compartmentalized nature of the design recapitulates the spatial separation of the different cell types that occurs *in vivo* into CNS and PNS regions. In future this feature would make it possible to carry out additional regional specific assays, such as axonal transport assays, or RNA sequencing from central, axonal or NMJ regions to look at regional specific differences in gene expression and alternative splicing. This is particularly relevant to ALS-research, since there is extensive debate into the central/peripheral origins of ALS pathology – the dying forward vs dying back hypotheses (Fischer et al. 2004). A downside of the approach developed here compared to work by (Uzel et al. 2016) is that it was not possible to directly measure force of muscle contraction ($N - 1\text{kg}\cdot\text{m}/\text{s}^2$), and instead velocity (m/s) was measured using particle image velocimetry (PIV) analysis. Previous work by Uzel and colleagues used muscle constructs suspended between cantilevers with defined tensile/mechanical properties. By measuring contraction induced deflection of the cantilevers it was possible for them to directly calculate force. In future the work described here could be further developed to directly measure contractile force by using atomic force microscopy and a defined hydrogel system (Norman et al. 2021).

The derivation of the different cell types used in this co-culture platform also provides several innovative features compared to other similar co-culture systems. By using magnetic-activated cell sorting (MACS) to enrich mESC-motor neurons and astrocytes it was possible to generate reproducible co-cultures of motor neurons and astrocytes with different genotypes at highly defined ratios (Figure. 3.1) (Machado et al. 2019). To achieve this the motor neuron

specific *HB9* promoter (*MNX1*) (Arber et al. 1999) and the astrocyte specific *GFAP* promoter (Brenner and Messing 2021) were used to drive the expression of a hCD14 cell surface antigen that could be used to MACS/FACS enrich specific populations from mixed starting populations. While GFAP expression can vary spatially, developmentally and depending on reactivity, antibodies against it are far superior to the more stably expressed ALDH1 astrocyte marker. This method is also further described in previous publications from the Lieberam lab (Machado et al. 2014, Bryson et al. 2014) and in chapter 4.

Using this co-culture platform, it was possible to probe developmental mechanisms relating to the activity-dependence of neuromuscular synapse formation. Synaptogenesis in both the central and peripheral nervous system has been shown to proceed in the absence of neuronal activity (Varoqueaux et al. 2002, Verhage et al. 2000), while neuronal activity has long been known to be crucial for the maintenance and refinement of mature synaptic connections (Barber and Lichtman 1999, Sanes and Lichtman 1999). However interestingly, emerging evidence does show that neural activity and pre-synaptic neurotransmitter release can influence synapse formation in the first place (Andreae and Burrone 2014). For example, mice lacking munc-18-1 a protein critical for pre-synaptic release show a dramatic reduction in the number of synapses in the cortex. In developing olfactory sensory neurons global silencing by overexpression of the inwardly rectifying potassium channel Kir2.1 (causing hyperpolarization and reduced firing) led to delayed axon outgrowth and disorganized target innervation. However other studies have again questioned whether this is a global or competitive effect (Burrone, O'Byrne and Murthy 2002). With regards to the neuromuscular junction, studies have shown that mice lacking ChAT, the enzyme responsible for the synthesis of acetyl choline, display a complete lack of neuromuscular transmission and have smaller motor nerve terminals and ultimately fewer synapses (Brandon et al. 2003). In Zebrafish expressing Kir2.1 motor neurons with abolished spontaneous Ca²⁺ spiking activity show substantial errors in axon pathfinding and rhythmic spontaneous activity has been shown to be important for axon outgrowth in the spinal cord (Hanson, Milner and Landmessey 2008). This matches with the findings outlined in this chapter, whereby optogenetic entrainment enhanced axon outgrowth, neuromuscular synapse formation, and myofiber contractility, while global application of TTX over the course of the co-culture led to significantly impaired neuromuscular transmission and myofiber contractility (Figure. 3.4, 3.5). However, since

these neuromuscular co-cultures were immature, with poly-innervated myofibers, we did not see activity-dependent elimination of synapses, which is required to generate mature single innervated myofibers during post-natal development. Creating stable neuromuscular co-cultures for longer than 2-weeks in this format was generally difficult as myofibers would collapse. If future studies could overcome this limitation, it would be possible to model longer-term activity dependent synapse elimination, refinement, and maintenance. It seems likely that longer term optogenetic entrainment or selectively increasing/decreasing activity in individual neurons would lead to the classically described activity-driven neuromuscular synapse elimination (Barber and Lichtman 1999, Sanes and Lichtman 1999). As part of this project work carried out by Carolina Barcellos-Machado (Machado et al. 2019) used the three compartment configuration of the co-culture platform to establish a competitive innervation assay, where one neural compartment was loaded with CHR2-YFP positive neurons and the other CHR2-YFP negative controls. Interestingly through this experiment it was found that CHR2-YFP positive neurons had a competitive advantage over CHR2-YFP negative neurons in the initial formation of synapses, in contrast to activity-dependent synapse elimination favoring inactive neurons described by Lichtman and colleagues (Barber and Lichtman 1999). This may point toward stage-specific effects of neural activity on initial synapse formation and subsequent synaptic elimination and refinement. It also highlights the way in which this co-culture platform could be reconfigured with different cell populations in each compartment to address different questions. An interesting future development would be to reconstruct an entire cortico-spinal motor tract by culturing cortical neurons, followed by spinal motor neurons and finally myofibers. It would then be possible to look at stage-specific and region-specific effects of different ALS-related mutations as well as studying dysfunction of different synaptic subtypes (cortical, cortico-motor, and neuromuscular).

Using the current co-culture platform, it was also possible to model the effects of ALS-related SOD1^{G93A} astrocytes on neuromuscular function. It has previously been well documented that ALS mutant SOD1 astrocytes can initiate ubiquitination and cell death in wildtype motor neurons in both animal (Papadeas et al. 2011) and ESC-derived cell culture models (Marchetto et al. 2008, Di Giorgio et al. 2008, Di Giorgio et al. 2007). In this chapter it was found that the deleterious non-cell autonomous effect of SOD1 astrocytes on motor neuron function extended to neuromuscular synapse dysfunction and impaired optogenetically evoked

myofiber contractility (Figure. 3.7, 3.8). It has previously been documented that neuromuscular junction defects are some of the earliest pathological events in the SOD1 mouse model of ALS (Fischer et al. 2004) and it is interesting that in the co-culture described here, similar defects are seen purely through a non-cell autonomous effect of the SOD1^{G93A} astrocytes. The data described in this chapter showed clear ubiquitination in the SOD1^{G93A} astrocytes and a deleterious effect of SOD1^{G93A} astrocytes on survival of wildtype motor neurons. This, along with other proposed toxic effects of SOD1 astrocytes on motor neuron function, such as impaired Ca²⁺ buffering, oxidative stress, impaired trophic support and release of toxic factors is likely to impact axon outgrowth and neuromuscular synapse function, leading to weaker optogenetically evoked myofiber contractions (Nagai et al. 2007). Furthermore, activation of astrocytes to become highly reactive has been widely observed in animal models of ALS as well as in other neurodegenerative and injury conditions and has been proposed as a key pathological component of ALS (Seifert, Schilling and Steinhauser 2006). Interestingly, recent work also demonstrated how astrocytes with ALS-related mutations can spontaneously become reactive *in vitro*, with distinct mutation specific profiles (Taha et al. 2022). It has been proposed that TGFβ1 is secreted by reactive SOD1 astrocytes, leading to activation of mTOR signaling in motor neurons causing impaired autophagy and degeneration (Endo et al. 2015, Tripathi et al. 2017). However, despite these results the SOD1^{G93A} astrocytes described in this chapter showed no clear upregulation of TGFβ1 or the reactive astrocyte marker *GFAP* (Figure. 3.6). As such the exact mechanism by which SOD1^{G93A} astrocytes exert a pathological effect on motor neuron survival, neuromuscular synapse function and neuromuscular transmission in this co-culture platform is unclear. In future work additional markers of astrocyte reactivity could be used, such as LCN2 and Serpina3n (Zamanian et al. 2012). Finally it would be interesting to artificially induce A1 reactive astrocytes using microglia associated cytokines such as TNF, IL1a and C1q to see how they compare with the SOD1^{G93A} astrocytes (Liddel et al. 2017).

Treatment with the RIPK1 inhibitor necrostatin did improve optogenetically evoked myofiber contractility, axon outgrowth and increased the total number of neuromuscular synapses, showing how this co-culture platform is amenable to drug screening purposes and indicating a possible role for necroptosis in the neuromuscular phenotypes observed (Re et al. 2014). This could hint at alternative inflammatory cytokines released by the SOD1^{G93A} astrocytes,

such as IFN and TNF- α that directly activate necroptotic pathways (Choi et al. 2019), however direct activation of necroptosis pathways by reactive A1 astrocytes is not clear cut (Liddel et al. 2017). As such it's possible that intrinsic motor neuron pathways that drive necroptosis, such as oxidative stress (Hanus, Anderson and Wang 2015) could be activated by the SOD1^{G93A} astrocytes indirectly. In future work other cell types such as oligodendrocytes and terminal Schwann cells should be incorporated into the co-culture platform to look at additional non-cell autonomous effects of ALS-related mutations on motor neuron survival. Interestingly work has shown that necroptosis of oligodendrocytes, mediated by RIPK1, causes demyelination and degeneration of motor axons, further highlighting RIPK1 and necroptosis as important mechanistic targets in ALS.

Finally, this chapter also describes the early development of a high-throughput 96-well neuromuscular co-culture format to model ALS using mouse ESC SOD1^{G93A} astrocytes, mouse ESC wildtype motor neurons and primary chick myoblasts. The 96-well format is further developed in chapter 6 and will be discussed in further detail there. Interestingly, the results here provide further mechanistic insight into the toxic effect of the SOD1^{G93A} astrocytes on neuromuscular function. BCR-Abl inhibition was found to significantly improve SOD1^{G93A} related neuromuscular phenotypes such as axon outgrowth, SV2 object number and neuromuscular junction morphology at lower doses (0.3 μ M and 0.1 μ M) (Figure. 3.9). SOD1^{G93A} astrocytes have been shown to activate c-Abl signalling in motor neurons via reactive oxygen species, leading to motor neuron death (Rojas et al. 2015). Furthermore, other studies have shown that Abl kinases are required at the neuromuscular junction (Finn, Feng and Pendergast 2003) and that c-Abl inhibition improves neuromuscular synapse reinnervation and delays motor neuron degeneration in the SOD1 mouse model of ALS (Katsumata et al. 2012) as well as in *in vitro* neuromuscular models of TDP-43 associated ALS (Osaki et al. 2018). It should be noted that the data in this chapter was not able to titrate out the effect of the BCR-Abl inhibitor and future experiments should seek to generate a complete dose-response. It is however encouraging that BCR-Abl inhibition seems to have a significant effect at very low concentrations. Taken together these results point toward c-Abl as a possible mechanistic target linking SOD1^{G93A} astrocytes to neuromuscular dysfunction. Future studies should seek to elucidate the exact mechanisms by which BCR-Abl and RIPK1 inhibition

improves motor neuron survival in this context and determine any potential off-target toxicity to other cell types.

4. Engineering human iPSC-derived neuromuscular co-cultures to model ALS

4.1 Hypotheses and aims

This chapter describes the establishment of human iPSC-derived neuromuscular co-cultures in compartmentalised microdevices. To achieve this, numerous stable human iPSC lines were engineered to perform a variety of functions, requiring the screening of hundreds of hiPSC clones, representing the majority of the work of this PhD. First CRISPR-Cas9 genome editing was used to correct a TDP-43^{G298S} mutation in a patient-derived hiPSC line. These lines, along with an additional wildtype line, were then separately downstream engineered to express a MACS sortable HB9::CD14 construct at the AAVS1 safe-harbour locus to enrich motor neuron populations, as well as express the optogenetic actuator, CHR2-YFP, to control the activity of these neurons. Initially the intention had also been to use CRISPR to induce the same TDP-43^{G298S} mutation in a wildtype line, however numerous failures at this and the sheer amount of time required meant this was not possible to complete before the end of the PhD. As such indicative statistics have been performed on these single lines, in line with similar studies characterising single ALS-related hiPSC lines in neuromuscular co-cultures (Osaki et al. 2018) and using electrophysiology (Devlin et al. 2015), despite the true biological N being 1. To make this clear, biological replicates (separate hiPSC lines) are denoted as (N), induction replicates (complete differentiations from hiPSCs) are denoted as (iN) and technical replicates, such as recordings from individual neurons, individual neuromuscular co-cultures or coverslips are denoted as (n).

By combining these cells with engineered forward programmable iPAX7 hiPSC-myoblasts in compartmentalised microdevices it was possible to generate functional human neuromuscular co-cultures. Using this platform the following aims were set:

1. Is human neuromuscular synapse formation activity dependent?
2. Does pathogenic TDP-43^{G298S} impact NMJ innervation?
3. Does pathogenic TDP-43^{G298S} impact muscle contraction strength?
4. Does pathogenic TDP-43^{G298S} impact spontaneous motor unit activity?

4.2 CRISPR–Cas9 mediated genome correction of ALS-related TDP-43^{G298S} mutation in a patient derived human iPSC line

Clustered regularly interspaced short palindromic repeat (CRISPR) – CRISPR associated protein 9 (Cas9) genome engineering was used to correct an endogenous ALS-related TDP-43^{G298S} mutation in exon 6 of the *TARDBP* gene. Initially two guide RNAs (sgRNAs) were designed with the cut site within 10bp of the A<G missense mutation to maximise homology directed repair (HDR) efficiency (Paquet et al. 2016), termed sgRNA-9 (ID: 901697809) and sgRNA-10 (ID: 901697810) (S Figure 4.10a). To compare sgRNA efficiency we performed TIDE analysis on bulk DNA derived from hiPSCs treated with Cas9 only or Cas9 +sgRNA (S Figure. 1a). It was found that sgRNA-10 had a moderately higher cutting efficiency (60.5%) than sgRNA-9 (56.7%) (S Figure 4.10c). However, since sgRNA-10 had more predicted off target sites with a mismatch of 2 (MM2), sgRNA-9 was chosen for genomic correction experiments in order to balance cutting efficiency with off-target activity (S Figure 4.10a).

For genomic correction experiments a donor template oligonucleotide was designed with the wildtype sequence in order to correct the TDP-43^{G298S} mutation, and with silent mutations in the Cas9 seed region (~5bp upstream of the PAM site) to prevent the Cas9 enzyme from cleaving template DNA that had already been integrated into the genome. Taking advantage of homology directed repair pathways in the cells to integrate the template sequence. Further to this, in order to improve clonal selection, a Xho1 restriction site was incorporated into the seed region as part of the silent mutagenesis (Figure 4.1a). Finally, codon usage bias was checked to confirm the new silently mutated codons had similar usage bias in human cells to those in the naïve sequence. Initial screening of the single-cell clones for integration of the Xho1 restriction site showed a 45% efficiency (9/20 clones). Subsequent sanger sequencing of exon 6 for these positive clones showed that 3 had normal sequences – an overall correction efficiency of 15% (3/20). A homozygous clone was chosen for further characterisation – as evidence by complete restriction digest and single peaks in the sequencing reads (Figure 4.1b,c). Subsequently 1000bp upstream and downstream of the Cas9 cut site were sequenced to check for larger genome deletions and the top 5 predicted off-target sites were sequenced to check for unintended off-target activity (S Figure 4.10d).

Pluripotency staining for OCT4, SOX2 and SSEA4 was carried out to confirm pluripotency of the lines (Figure 4.1d). G-banding was then used to confirm normal karyotype of the lines (Figure 4.1e). Western blot was used to confirm normal TDP-43 protein expression (Figure 4.1f). Finally, qRT-PCR was used to check alternative splicing of intron 5 and exon 6 of the *TARDBP* gene, since aberrant splicing can sometimes be an unintended effect of CRISPR-Cas9 mediated genome correction (Mou et al. 2017), (Figure 4.1g). It was found that intron 5 was equally excluded from mature transcripts in wildtype, corrected and G298S lines. While inclusion of exon 6 was moderately lower in the G298S line relative to the wildtype and corrected lines – an expected consequence of the mutation based on the autoregulatory properties of TDP-43 on its own splicing (Figure 4.1g).

Finally, we attempted to generate a knockdown clone of TDP-43 in a wildtype hiPSC line – since full knockout of TDP-43 is embryonic lethal. Using the same design approach as for the correction experiments, heterozygous Xho1 clones were selected with abnormal sequences. The intention of this was to select clones with one normal allele (the Xho1 positive allele that had integrated the donor template) and one allele that had been mutated by the Cas9 causing a frame-shift mutation and nonsense mediated decay of the mRNA. A clone was selected based on these criteria and was found via immunostaining to have a significantly lower expression of TDP-43 (S Figure 4.11a,b). However, the cell line grew so slowly, further experiments using it were not possible.

4.3 Directed differentiation of human iPSCs into motor neuron progenitors

A small molecule directed differentiation approach, based on developmental morphogen signalling and previously established protocols (Wichterle et al. 2002, Du et al. 2015) was adapted to generate motor neuron progenitors (MNPs) from hiPSCs. Initially dual SMAD inhibition using SB431542 and LDN193189 acts to inhibit BMP4 signalling, while GSK-3 inhibition using CHIR99021 activates Wnt signalling pathways. Together this induces confluent hiPSCs to form neuroectoderm (Figure 4.2a). Subsequently treatment with RA and the Shh agonist purmorphamine acts to pattern the rostro-caudal and dorso-ventral identity of spinal motor neurons. Based on (Du et al. 2015) it was possible to generate, expand and freeze spinal motor neuron progenitors (Figure 4.2b). Subsequently 1 week maturation with

RA and PurM led to mixed cultures of OLIG2+ MNPs and ISL1+ MNs. Efficiency varied a lot between cell lines and experiments with the percentage ISL1+ cells ranging anywhere from 10-80%, but an example from a typical differentiation yielded 28.2% ISL1+, 24.8% OLIG2+, 6.1% ISL1/OLIG2+ and 41% non-expressing cells for the wildtype line (n=3), 30.3% ISL1+, 47.5% OLIG2+, 17.4% ISL1/OLIG2+ and 4.7% non-expressing cells for the TDP-43^{G298S} CRISPR corrected cell line (n=3) and 38.2% ISL1+, 28.9% OLIG2+, 8.5% ISL1/OLIG2+ and 23.4% non-expressing cells for the TDP-43^{G298S} cell line and (n=3) (Figure 4.2c). Such variation in differentiation efficiencies between cell lines supports the need for robust MACS enrichment of post-mitotic motor neurons to ensure comparable neuronal cultures.

4.4 Stable integration of *HB9::CD14* construct into human iPSCs allows efficient magnetic activated cell sorting (MACS) enrichment of post-mitotic motor neurons

To improve the purity and reproducibility of the motor neuron cultures a motor neuron specific magnetic activated cell sortable (MACS) construct (generated by Carlolina Barcellos-Machado) was stably integrated into the hiPSC lines using TALENS based delivery into the AAVS1 safe-harbour locus (Hockemeyer et al. 2009). In this construct the expression of a cell surface (hCD14) antigen is driven by the motor neuron specific and post-mitotic *HB9* promoter. All lines were engineered to have homozygous integration of this construct (Figure 4.3a). By MACS sorting mixed MNP/MN cell populations engineered to express this construct it was possible to reliably generate 85-99% HB9/ISL1+ motor neuron cultures. Immunostaining for ISL1+ cells in pre-sort and eluate populations showed an enrichment of 63.89% (SE ± 1.92) to 88.72% (SE ± 3.24, T-test p=0.0028, n=3) in wildtype cells, 70.39% (SE ± 1.22) to 97% (SE ± 1.57, T-test p=0.0002, n=3) in TDP-43^{G298S} Corrected cells, and 71.34% (SE ± 1.07) to 95.42% (SE ± 1.61, T-test p=0.0002, n=3) in TDP-43^{G298S} cells (Figure 4.3b,c). Flow cytometry analysis from a separate differentiation showed similar levels of enrichment for hCD14+ motor neurons from 37.3% to 84.7% in wildtype cells, 12.8% to 84.6% in TDP-43^{G298S} corrected cells, and 75.3% to 90.2% in TDP-43^{G298S} cells (Figure 4.3d)

4.5 Stable integration of CAG::CHR2-YFP construct into human iPSCs facilitates optogenetic control of motor neurons

In order to control the activity of the hiPSC-derived motor neurons an optogenetic construct - Channelrhodopsin-2 YFP (CHR2-YFP) (Generated by Carolina Barcellos-Machado) – driven by the ubiquitous CAG promoter was stably expressed in the hiPSC lines using a piggybac integration system (Wang et al. 2008, Zhang et al. 2006). Subsequently polyclonal YFP+ lines were FACS sorted so that CHR2-YFP expression was comparable across all cell lines (Figure 4.4a). To further confirm comparable CHR2-YFP expression, hiPSCs were stained against YFP and fluorescence intensity measured. There was no significant difference in YFP intensity across the lines (Figure 4.4b). To confirm the functionality of the CHR2-YFP construct whole-cell patch clamp recordings were performed on YFP+ motor neurons differentiated and grown on GDNF expressing mouse ESC-derived astrocytes for 6 weeks (Figure 4.4d). Optogenetic stimulation of the motor neurons elicited robust firing of trains of action potentials for all cell lines (Figure 4.4e). The proportion of cells that fired at least one action potential in response to optogenetic stimulation was also comparable, 61.9% for wildtype, 80.6% for TDP-43^{G298S} corrected and 79.2% for TDP-43^{G298S} (Figure 4.4f).

4.6 Stable integration of doxycycline-inducible *iPAX7* construct into human iPSC lines facilitates forward programming into myoblast progenitors

To generate skeletal myoblasts from human iPSCs a forward programming approach was used, whereby the early myogenic gene, *PAX7*, was ectopically expressed using a doxycycline inducible Tet-on system to directly convert hiPSCs into myoblasts. *PAX7* was chosen over the more commonly used *MYOD* since *PAX7* is a myogenic progenitor transcription factor rather than a terminal myocyte transcription factor. This would facilitate multiple rounds of expansion of the myogenic progenitors prior to terminal differentiation and may also open up opportunities to generate *PAX7* positive satellite cells that are found in mature muscle for use in future studies. This tet-on *PAX7* construct – termed *iPAX7* (Cloned by Federica Riccio) – was stably integrated into the CLYBL safe-harbour locus using TALENS based delivery and homozygous clones were used (Figure. 5a). hiPSCs were first given a brief pulse of CHIR then treated with doxycycline for 18 days to generate *PAX7* and *MYOD* expressing myoblast progenitors (Figure 4.5b,c). These progenitors could be expanded for several passages and

frozen for future use. Subsequently after switching the media to myogenic differentiation media for 1 week, myoblast progenitors began to fuse and form myotubes, expressing myogenin and myosin (Figure 4.5c). After another week mature striated titin expressing myofibers began to form (Figure 4.5c).

Understanding how pathogenic TDP-43 might impact muscle function was another aim for this chapter. To this end, stable, homozygous TDP-43^{G298S} and TDP-43^{G298S} Corrected iPAX7 hiPSC lines were also generated at the same time as the wildtype iPAX7 line (S Figure 4.12a). When differentiated into myoblasts using the same protocol the TDP-43^{G298S} corrected line was able to form PAX7 and MYOD expressing progenitors comparable to the wildtype line, however the TDP-43^{G298S} line showed a considerable reduction in PAX7 positive cells – from 88% (SE ± 1.53) to 3% (SE ± 1.20, T-test p<0.0001, n=3) and MYOD positive cells – from 86% (SE ± 2.52) to 1% (SE ± 0.58, T-test p<0.0001, n=3) (S Figure 4.12c). After 1 week in myogenic differentiation medium the TDP-43^{G298S} Corrected line was able to form morphological myotubes, while the TDP-43^{G298S} line was unable to, with considerable cell death occurring (S Figure 4.12b). The reasons for this were never fully resolved, although possible explanations are discussed later in this chapter.

4.7 Generation of functional human iPSC-derived neuromuscular circuits in compartmentalized microdevices

Wildtype MACS enriched CHR2-YFP+ hiPSC-motor neurons were combined with GDNF expressing mESC-derived astrocytes into neural spheroids and co-cultured with wildtype iPAX7 hiPSC-myoblasts in compartmentalised microdevices like those described in chapter 2 but with minor modifications (Figure 4.6a). Following two weeks of co-culture myofiber contractions could be elicited through optogenetic stimulation of the motor neurons (Figure 4.6c,d). These contractions could be quantified using PIV analysis to generate a readout of contraction velocity. To validate that the myofiber contractions were occurring via transmission at neuromuscular synapses, co-cultures were treated with the AChR blocker d-tubocurarine (DTC), which completely abolished optogenetically evoked contractions from 30.01µm/s (SE ± 5.78, n=9) to 0.75µm/s (SE ± 0.10, n=4, T-test p=0.0072) (Figure 4.6e,d). Finally, to confirm the formation of neuromuscular synapses, immunostaining for pre-synaptic SV2 and

post-synaptic ACh receptors was carried out alongside staining for Titin and TUBB3. Clear colocalization of SV2 and AChR indicated the formation of neuromuscular synapses (Figure 4.6e). Associated supplementary movie QR codes available in supplementary figure 4.14.

In addition to using human iPSC-motor neurons and human iPSC-myofibers in the co-cultures, human iPSC-derived GDNF expressing astrocytes were also sought to be incorporated into the neural compartment of the co-culture platform in order to support the survival of the spinal motor neurons. To achieve this a CAG::GDNF+ construct was stably integrated into a background iAstro line using a piggybac integration system (S Figure 4.13a,b). Briefly this background iAstro line (generated by Federica Riccio) was based on a previously published approach to forward program human iPSCs into astrocytes by force expressing the astrocyte specific genes: SOX9 and NF1b (S Figure. 4a). This approach could reliably be used to generate GFAP and s100b expressing astrocytes (S Figure 4.13c – images generated by Federica Riccio). However, long-term motor neuron survival was significantly impaired when co-cultured with these astrocytes. At two-weeks there was 75.37% (SE \pm 5.26, n=8) motor neuron survival in cultures with no astrocytes, which dropped dramatically to 2.05% (SE \pm 0.38, n=8, One-way-ANOVA with Dunnet's test $p < 0.0001$) survival in co-cultures with wildtype iAstrocytes. This survival was moderately increased to 10.6% (SE \pm 3.61, n=6, One-way-ANOVA with Dunnet's test $p = 0.19$) in co-cultures with GDNF expressing iAstrocytes (S Figure 4.13d). Taken together however, the toxic nature of the iAstrocytes on motor neurons meant they were not taken forward into the neuromuscular co-cultures and any further experiments. Instead GDNF expressing mouse ESC astrocytes were used for all subsequent experiments.

4.8 Optogenetic entrainment enhances NMJ formation and myofiber contractility in human iPSC neuromuscular circuits

To ascertain whether neuromuscular synapse formation was dependent on neural activity, 1-hour 5Hz optogenetic entrainment was applied to the co-cultures every day for 5 days (Figure 4.7a). Optogenetic entrainment significantly improved optogenetically evoked myofiber contraction velocity from 11.99 $\mu\text{m/s}$ (SE \pm 4.37) without any entrainment to 28.46 $\mu\text{m/s}$ (SE \pm 4.16, n=6, T-test, $p = 0.02$) with entrainment (Figure 4.7b,c). Furthermore, optogenetic entrainment improved axon outgrowth from 9150 μm^2 (SE \pm 2142) to 41785 μm^2 (SE \pm 8069,

n=6, T-test p=0.0029) as well as improving neuromuscular synapse formation (number of colocalised SV2/AChR objects per field of view) from 23.67 (SE ± 4.44) to 87.83 (SE ± 9.67, n=6, T-test p=0.0001) (Figure 4.7d). Taken together this shows that neural activity improves neuromuscular synapse formation and myofiber contractility in human neuromuscular co-cultures. Associated supplementary movie QR codes available in supplementary figure 4.14

4.9 Human iPSC-derived neuromuscular circuits containing TDP-43^{G298S} motor neurons display increased spontaneous myofiber contractility, yet reduced optogenetically evoked maximal contractile output

To understand how the ALS-related pathogenic TDP-43^{G298S} mutation impacted neuromuscular function, neuromuscular co-cultures were generated with MACS enriched wildtype hiPSC-motor neurons, TDP-43^{G298S} corrected motor neurons, and TDP-43^{G298S} motor neurons and grown for 2-weeks with 5 days of optogenetic entrainment (Figure 4.7a). An observation made right away was an increase in spontaneous myofiber contractions in the TDP-43^{G298S} neuromuscular co-cultures – such spontaneous contractions were rarely observed in the wildtype and corrected conditions. To quantify this, three 5s video recordings were made at regular intervals over the course of 1 minute of the myofibers without any external stimulation and then quantified using particle image velocimetry (PIV) (Figure 4.8a,b). TDP-43^{G298S} co-cultures showed significantly stronger spontaneous contraction velocities 13.78µm/s (SE ± 2.36, n=10) than wildtype 2.66µm/s (SE ± 0.75, n=6, One-way-ANOVA with Dunnet's test p=0.0104) and corrected 5.36µm/s (SE ± 0.15, n=9, One-way-ANOVA with Dunnet's test p=0.037) co-cultures (Figure 4.8e). Furthermore, these spontaneous contractions were completely abolished by the addition of the AChR blocker d-tubocurarine to 0.523µm/s (SE ± 0.15, n=4, One-way-ANOVA with Dunnet's test p=0.0072) indicating that they were driven by neural activity as opposed to intrinsic contractility of the myofibers themselves (Figure 4.8e). Furthermore, spontaneous contraction frequency was also significantly higher in the TDP-43^{G298S} co-cultures at 0.25Hz (SE ± 0.03, n=10) compared to 0.04Hz (SE ± 0.05, n=6, One-way-ANOVA with Dunnet's test p=0.0007) in the wildtype and 0.05Hz (SE ± 0.02, n=9, One-way-ANOVA with Dunnet's test p=0.0002) in the corrected co-cultures (Figure 4.8f). As well as looking at spontaneous myofiber contractions, optogenetically evoked myofiber contractions were also quantified. Strikingly evoked

myofiber contraction velocity was significantly lower in the TDP-43^{G298S} co-cultures at 13.86 $\mu\text{m/s}$ (SE \pm 2.14, n=10) compared to 28.46 $\mu\text{m/s}$ (SE \pm 4.16, n=6, One-way-ANOVA with Dunnet's test p=0.049) in the wildtype and 30.01 $\mu\text{m/s}$ (SE \pm 5.78, n=9, One-way-ANOVA with Dunnet's test p=0.017) in the corrected co-cultures (Figure 4.8c,d,e). Taken together these results show that TDP-43^{G298S} neuromuscular co-cultures display increased spontaneous myofiber contractility yet a reduction in optogenetically evoked maximal contractile output. This result resembles the simultaneous occurrence of muscle fasciculations and muscle weakness observed in the early stages of ALS. Associated supplementary movie QR codes available in supplementary figure 4.14

4.10 Human iPSC-derived neuromuscular circuits containing TDP-43^{G298S} motor neurons display a reduction in axon outgrowth and neuromuscular synapses

To understand why the maximal optogenetically evoked contractions were weaker in the TDP-43^{G298S} neuromuscular co-cultures axon outgrowth and the number of neuromuscular synapses was compared across conditions. Initially, at D1 of the neuromuscular co-cultures axon maximum branch length outgrowth was comparable for all culture conditions: 261.7 μm (SE \pm 7.77, n=5) for wildtype, 306.7 μm (SE \pm 21.56, n=7) for corrected and 339.8 μm (SE \pm 27.62, n=6,) for TDP-43^{G298S} (One-way-ANOVA with Dunnet's test p=0.08), (Figure 4.9a). However, after two-weeks axon coverage was significantly lower in the TDP-43^{G298S} co-cultures at 11,076 μm^2 (SE \pm 3286, n=10) compared to 41,785 μm^2 (SE \pm 8069, n=6, One-way-ANOVA p=0.0002) for wildtype and 46,607 μm^2 (SE \pm 2755, n=9, One-way-ANOVA with Dunnet's test p<0.0001) for corrected co-cultures (Figure 4.9b,c). Furthermore, the number of neuromuscular synapses (SV2/AChR colocalised objects) was lower in the TDP-43^{G298S} co-cultures, at 40.10 (SE \pm 6.22, n=10) compared to 87.83 (SE \pm 9.69, n=6, One-way-ANOVA with Dunnet's test p=0.0083) in the wildtype and 77.11 (SE \pm 13.04, n=9, One-way-ANOVA with Dunnet's test p=0.021) in the corrected cultures (Figure 4.9b,c). Finally, the average size of the neuromuscular synapses was lower in the TDP-43^{G298S} co-cultures at 7.48 μm^3 (SE \pm 1.34, n=10) compared to 11.53 μm^3 (SE \pm 0.69, n=6, One-way-ANOVA with Dunnet's test p=0.068) in the wildtype and 12.42 μm^3 (SE \pm 1.17, n=9, One-way-ANOVA with Dunnet's test p=0.011) in the corrected co-cultures (Figure 4.9b,c). Taken together these results suggest that the reduction in maximal optogenetically evoked contractile output is lower due to a reduction

in axon outgrowth and the number neuromuscular synapses in the TDP-43^{G298S} neuromuscular co-cultures.

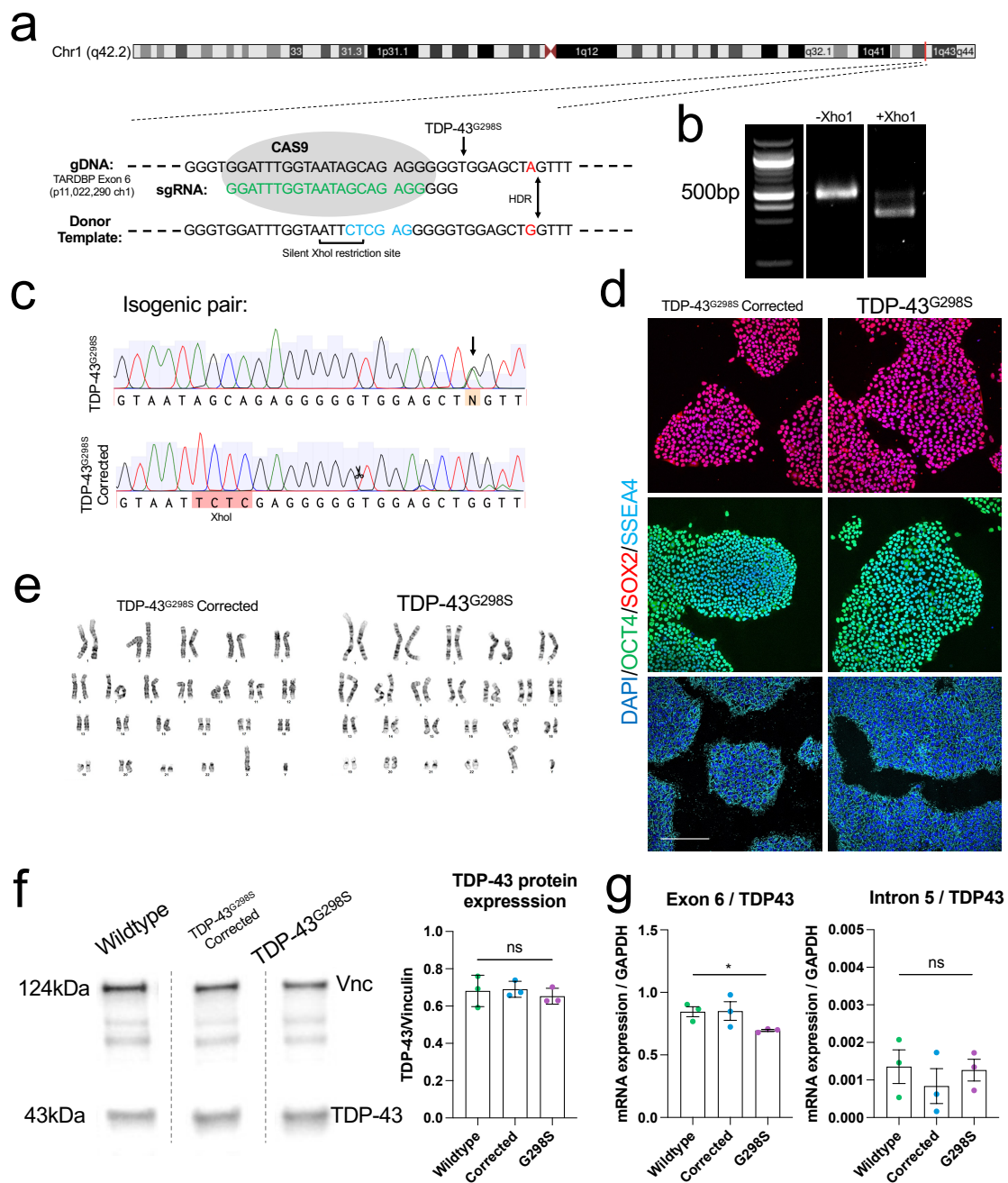


Figure 4.1. CRISPR–Cas9 mediated genome correction of ALS-related TDP-43^{G298S} mutation in a patient derived human iPSC line.

A, Schematic showing the CRISPR–Cas9 mediated genome editing strategy to correct the endogenous pathogenic ALS-related TDP-43^{G298S} mutation. **B**, Xho1 restriction digest of CRISPR–Cas9 edited hiPSC clone showing homozygous integration of the donor template harbouring the silent Xho1 restriction site. **C**, Sanger-sequencing of exon 6 of the *TARDBP* gene showing correction of the TDP-43^{G298S} mutation and homozygous integration of the donor template harbouring the silent Xho1 restriction site. **D**, Immunofluorescence staining of the pluripotency markers OCT4, SOX2 and SSEA4 counterstained for DAPI (Scale bar = 200µm). **E**, G-banding showing normal karyotype for parental TDP-43^{G298S} and TDP-43^{G298S}

CRISPR-Corrected hiPSC lines. **F**, Western blot analysis and quantification showing TDP-43 protein expression in wildtype (n=3), CRISPR corrected (n=3) and TDP-43^{G298S} (n=3) hiPSC lines relative to the housekeeper vinculin. **G**, qRT-PCR analysis of Exon 6 inclusion/intron 5 retention of the *TARDBP* gene to check for abnormal splicing of the *TARDBP* gene across hiPSC lines (n=3). Error bars represent the SEM, one-way-ANOVA used to determine statistical significance, *p<0.05.

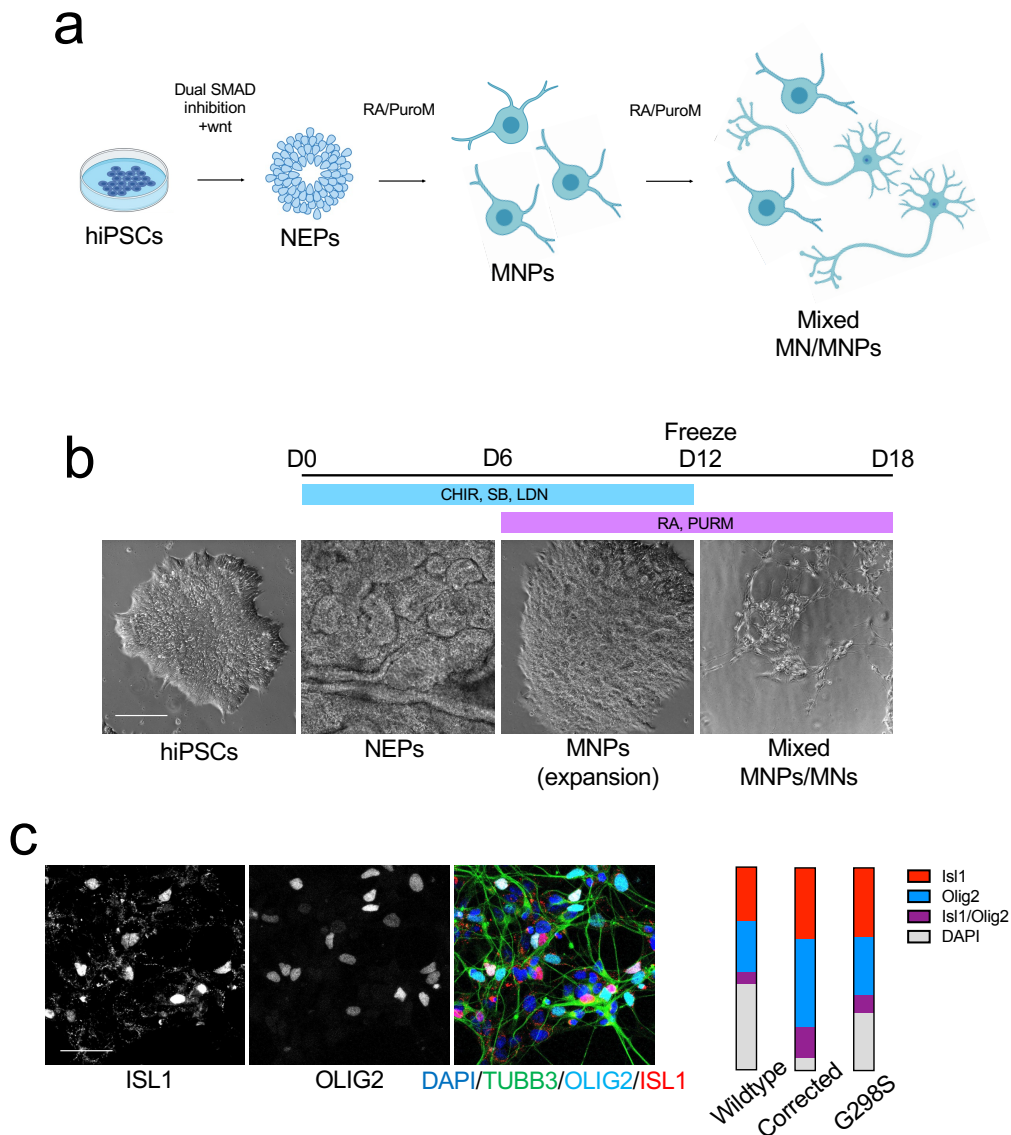


Figure 4.2. Directed differentiation of human iPSCs into motor neuron progenitors.

A, Schematic showing small-molecule protocol to direct the differentiation of hiPSCs into MNPs via a neuroectodermal progenitor state using dual smad inhibition (SB,LDN), Wnt activation (CHIR) and morphogen signalling (RA, PURM). **B**, Representative bright-field images taken at each stage of differentiation (Scale bar = 200µm). **C**, Immunofluorescence staining for the motor neuron marker ISL1 (red) and the motor neuron progenitor marker

OLIG2 (cyan), counterstained with DAPI (blue) and TUBB3 (green) (Scale bar = 50 μ m). Quantification of relative percentages of cells expressing ISL1, OLIG2, ISL1 and OLIG2 and neither marker for wildtype, corrected and TDP-43^{G298S} hiPSC lines (N=1, iN=1, n=3).

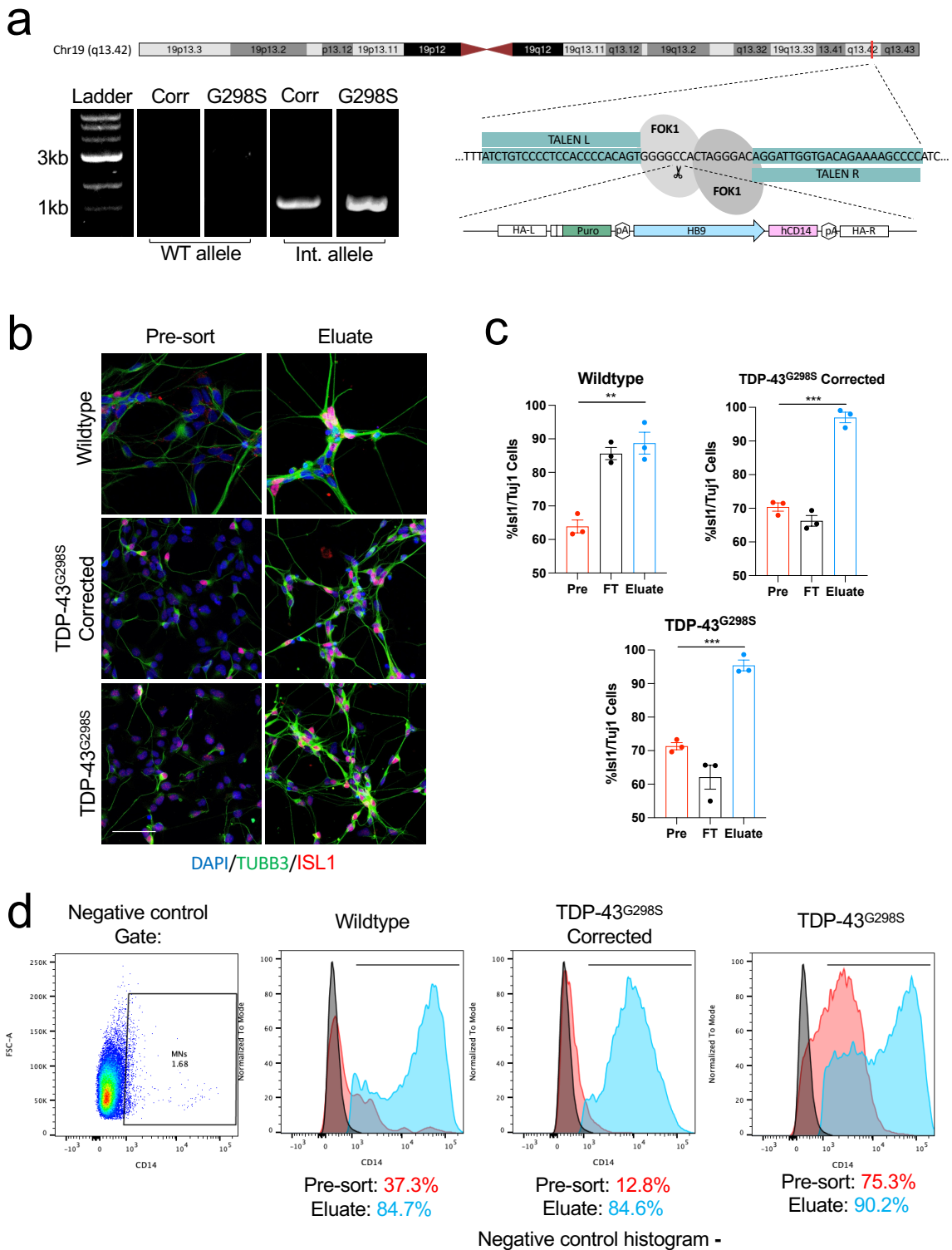


Figure 4.3. Stable integration of *HB9::CD14* construct into human iPSCs allows efficient magnetic activated cell sorting (MACS) enrichment of post-mitotic motor neurons.

A, Schematic showing TALENS based delivery of the MACS sortable *HB9::hCD14* construct into the AAVS1 safe-harbour locus in hiPSC lines. Homozygous integration can be determined by a negative PCR for the wildtype allele and a positive PCR for the integrated

allele. **B**, Immunofluorescence staining for ISL1 in pre-sort and eluate populations, counterstained for TUBB3 and DAPI (Scale bar = 50 μ m). **C**, Quantification of ISL1 positive cells in pre-sort, flow-through and eluate populations for wildtype, corrected, and TDP-43^{G298S} hiPSC lines, (N=1, iN=1, n=3). **D**, Flow cytometry analysis of pre-sort and eluate populations with negative control samples used to set the positive gates. Error bars represent the SEM. T-tests used to determine statistical significance. **p<0.01, ***p<0.001.

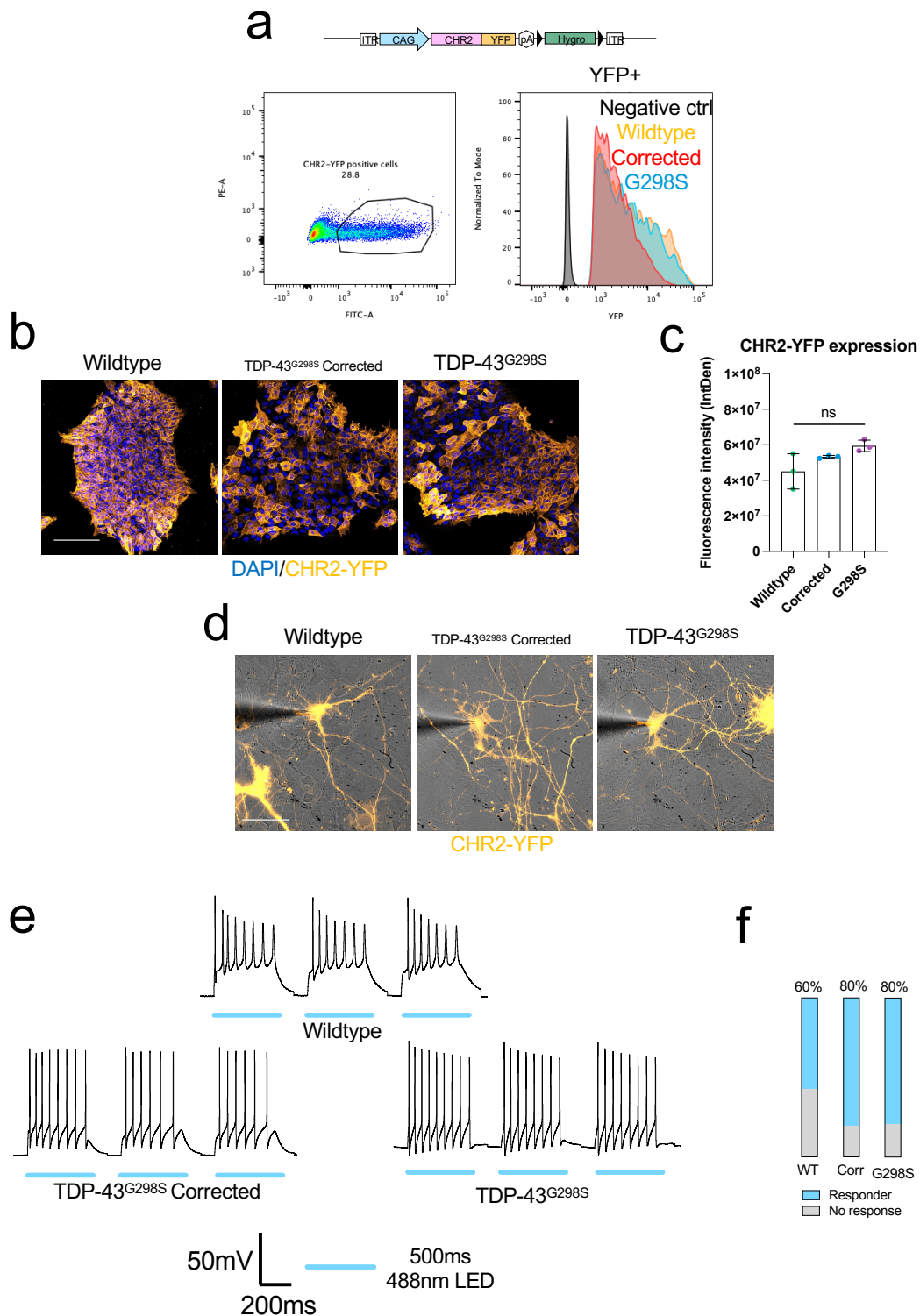


Figure 4.4. Stable integration of CAG::CHR2-YFP construct into human iPSCs facilitates optogenetic control of motor neurons.

A, Schematic of the CAG::CHR2-YFP construct and FACS gates used to select YFP+ polyclonal cell lines with comparable YFP expression. **B**, Immunofluorescence staining for CHR2-YFP in hiPSC lines, counterstained with DAPI (Scale bar = 50μm). **C**, Quantification of YFP

fluorescence intensity across cell lines. **D**, Whole-cell patch clamp recordings of CHR2-YFP+ MACS enriched hiPSC-motor neurons grown for 2-weeks on MACS enriched GDNF expressing mESC-astrocytes (Scale bar = 50 μ m). **E**, Optogenetic stimulation of hiPSC-motor neurons induces robust action potential firing across all cell lines (N=1, iN=3, n=20). **F**, Quantification of the proportion of motor neurons that fire action potentials in response to optogenetic stimulation. Error bars represent the SEM. One-way-ANOVA used to determine statistical significance.

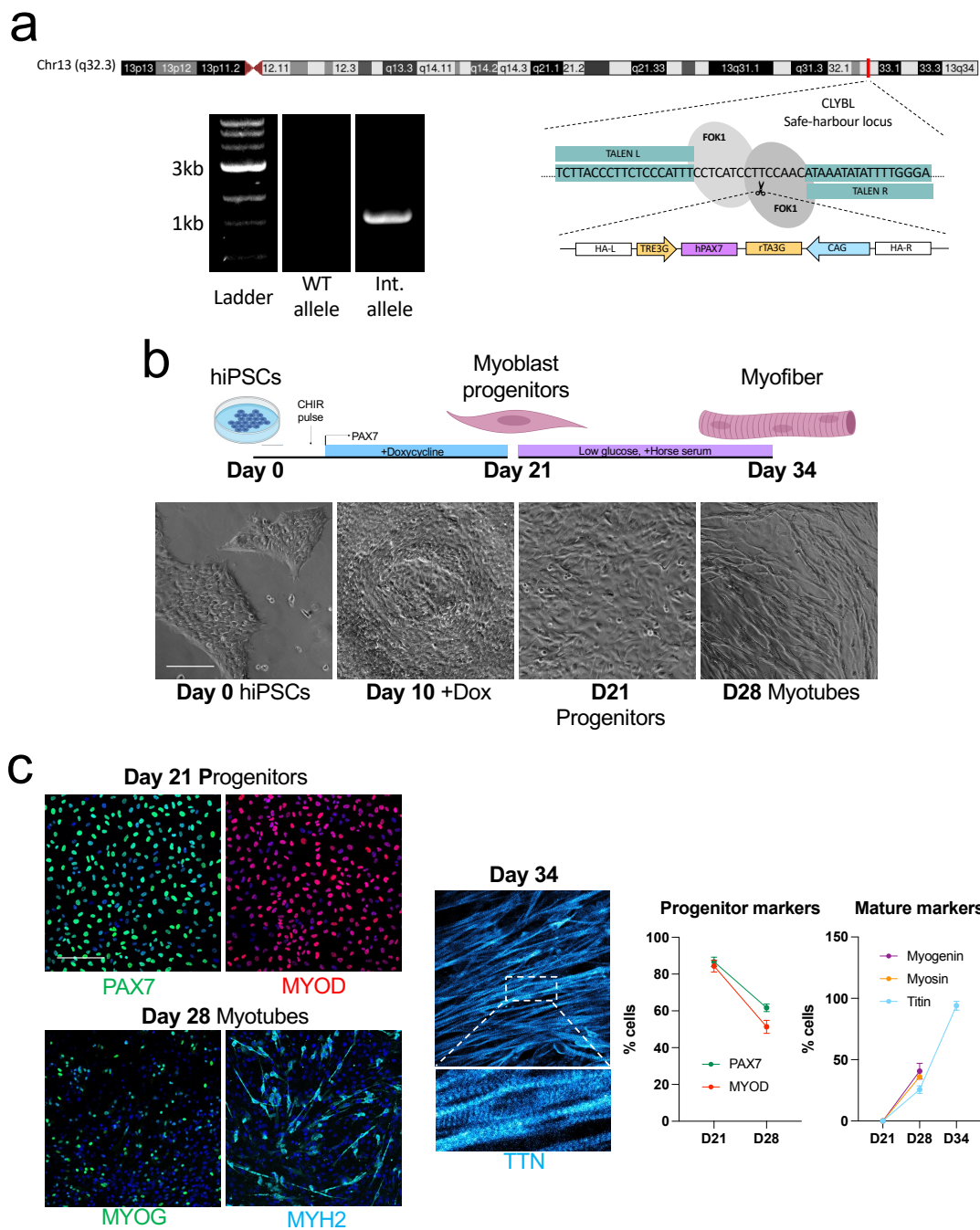


Figure 4.5. Stable integration of doxycycline-inducible iPAX7 construct into human iPSC lines facilitates forward programming into myoblast progenitors.

A, Schematic showing TALENS based delivery of the doxycycline-inducible iPAX7 construct into the CLYBL safe-harbour locus of hiPSC lines. Homozygous integration can be determined by a negative PCR for the wildtype allele and a positive PCR for the integrated allele. **B**, Schematic showing forward programming of iPAX7 lines from hiPSCs into PAX7 positive myoblast progenitors. Bright-field images show representative examples of each stage of the protocol (Scale bar = 200µm). **C**, Immunofluorescence staining of the progenitor markers PAX7 and MYOD at D21, the myotube markers myogenin and myosin

at D28 and the mature myofiber marker titin at D34. Counterstained with DAPI (Scale bar = 50 μ m). Quantification of the percentage cells expressing these markers at each stage of differentiation (N=1, iN=1, n=3). Error bars represent the SEM.

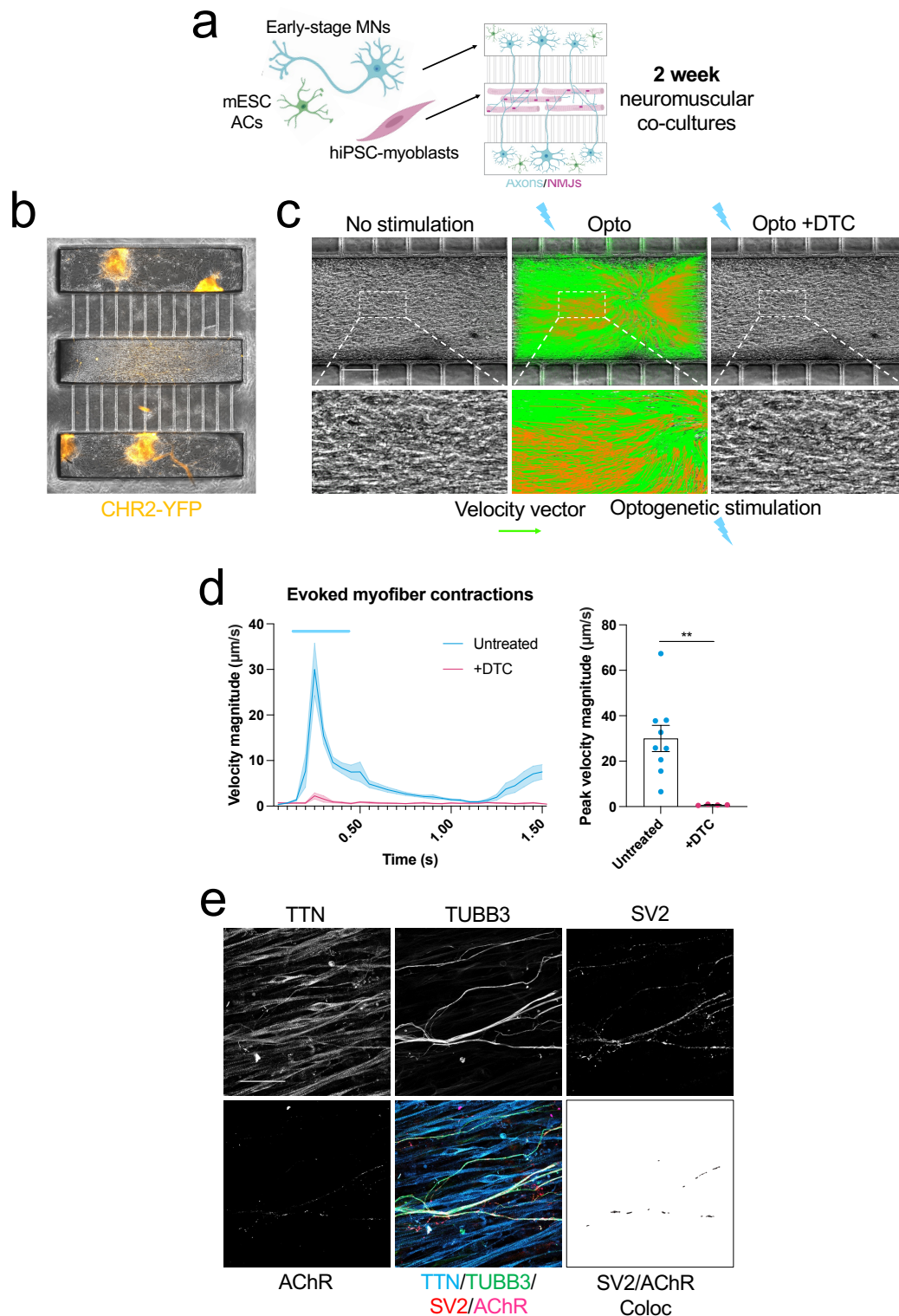


Figure 4.6. Generation of functional human iPSC-derived neuromuscular circuits in compartmentalized microdevices.

A, Schematic showing co-culture of hiPSC-derived motor neurons and myofibers in compartmentalized microdevices. **B**, Brightfield/CHR2-YFP image of a plated compartmentalized neuromuscular co-culture. **C**, Particle image velocimetry (PIV) analysis

of optogenetically evoked myofiber contractions before and after treatment with the AChR blocker d-Tubocurarine (DTC) (Scale bar = 200 μ m). **D**, Quantification of optogenetically evoked myofiber contractions before (N=1, iN=1, n=9) and after (N=1, iN=1, n=4) treatment with d-Tubocurarine (DTC). **E**, Immunofluorescence staining for Titin, TUBB3, SV2 and AChR alongside composite images and the colocalization channel for SV2 and AChR (Scale bar = 50 μ m). Error bars represent the SEM. T-test used to determine statistical significance. **p<0.01.

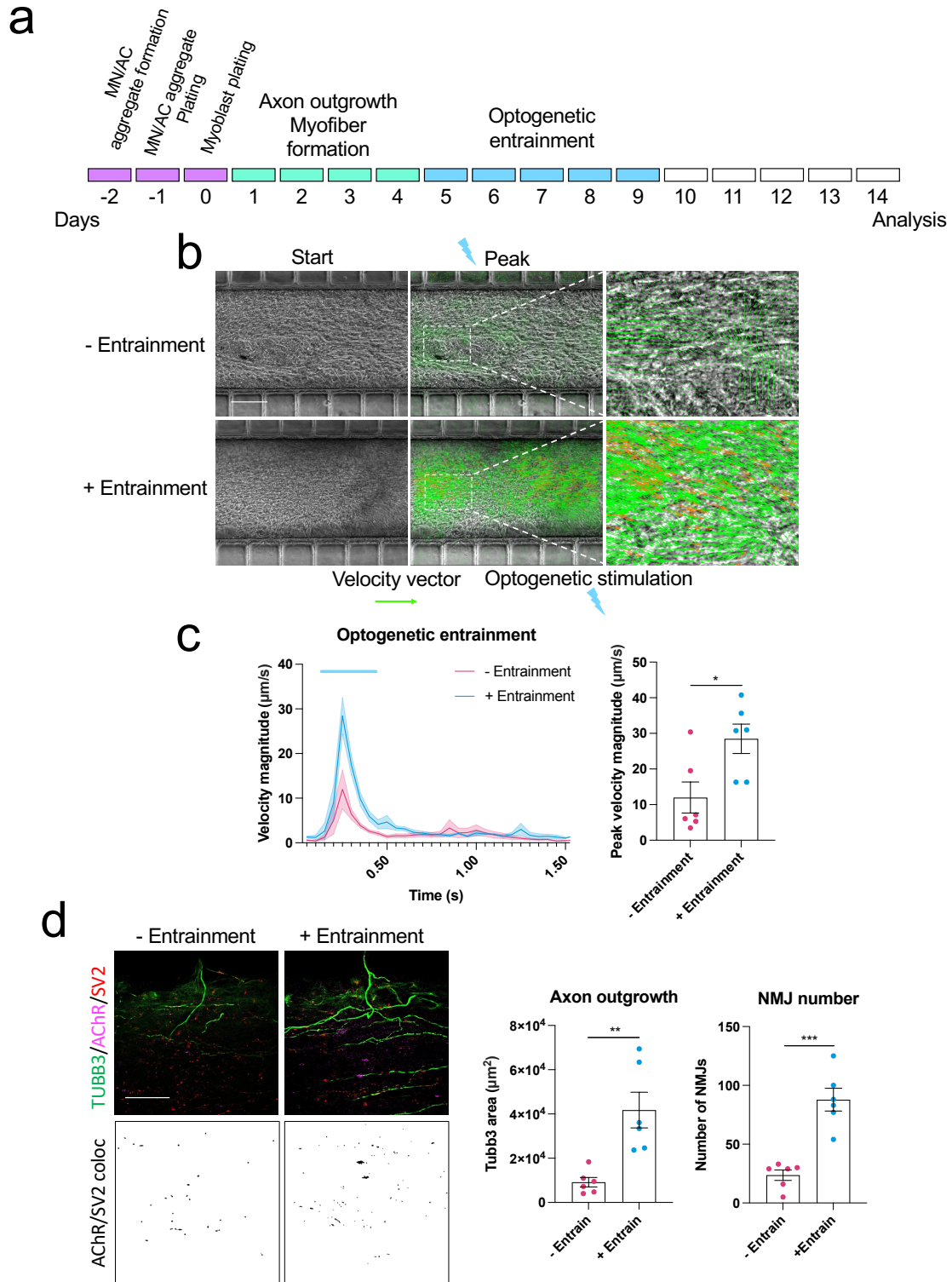


Figure 4.7. Optogenetic entrainment enhances NMJ formation and myofiber contractility in human iPSC neuromuscular circuits.

A, Schematic showing optogenetic entrainment of wildtype hiPSC-neuromuscular co-cultures. **B**, Particle image velocimetry (PIV) analysis of optogenetically evoked myofiber contractions in non entrained and entrained co-cultures (Scale bar = 200 μ m). **C**, Quantification of peak optogenetically evoked myofiber contraction velocity in non-

entrained and entrained co-cultures, n=6. **D**, Immunofluorescence staining for TUBB3, SV2 and AChR alongside SV2/AChR (NMJ) colocalization channels in non-entrained and entrained co-cultures (Scale bar = 50 μ m). Quantification of axon outgrowth and NMJ number in non-entrained and entrained conditions, (N=1, iN=1, n=6). Error bars represent the SEM, t-tests used to determine statistical significance. **p<0.01, ***p<0.001.

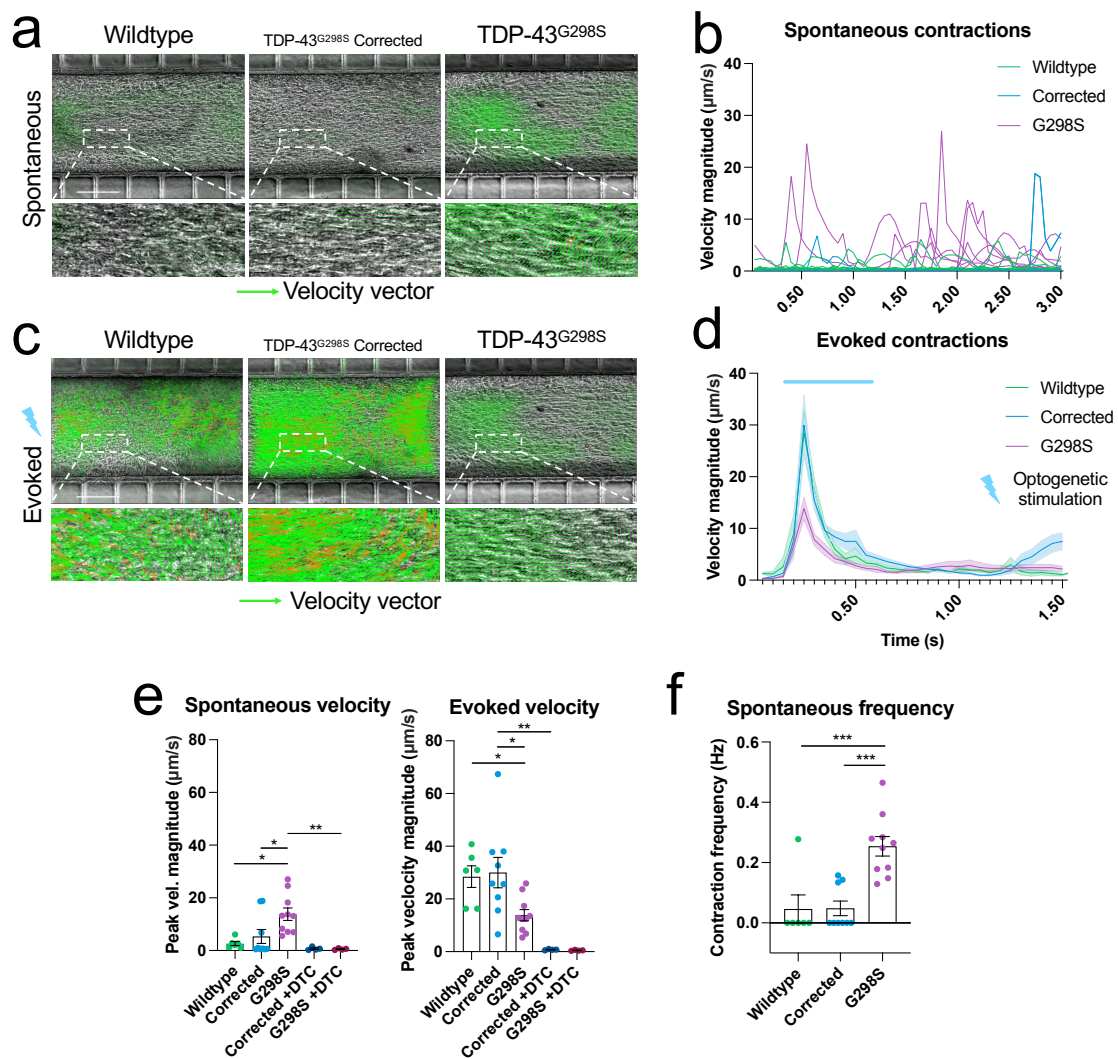


Figure 4.8. Human iPSC-derived neuromuscular circuits containing TDP-43^{G298S} motor neurons display increased spontaneous myofiber contractility, yet reduced optogenetically evoked maximal contractile output.

A, Particle image velocimetry (PIV) analysis of spontaneous myofiber contractions in wildtype (N=1, iN=3, n=6), corrected (N=1, iN=3, n=9) and TDP-43^{G298S} (N=1, iN=3, n=10) neuromuscular co-cultures (Scale bar = 200μm). **B**, Spontaneous myofiber contraction traces. **C**, Particle image velocimetry (PIV) analysis of optogenetically evoked myofiber contractions in wildtype, corrected, and TDP-43^{G298S} neuromuscular co-cultures (Scale bar = 200μm). **D**, Optogenetically evoked myofiber contraction traces. **E**, PIV quantification of peak spontaneous velocity and optogenetically evoked velocity in wildtype, corrected, TDP-43^{G298S} and corrected +DTC (N=1, iN=3, n=4) and TDP-43^{G298S} +DTC (N=1, iN=1, n=4) conditions. **F**, Quantification of spontaneous myofiber contraction frequency. Error bars represent the SEM. One-way-ANOVA used to determine statistical significance. *p<0.05, **p<0.01, ***p<0.001.

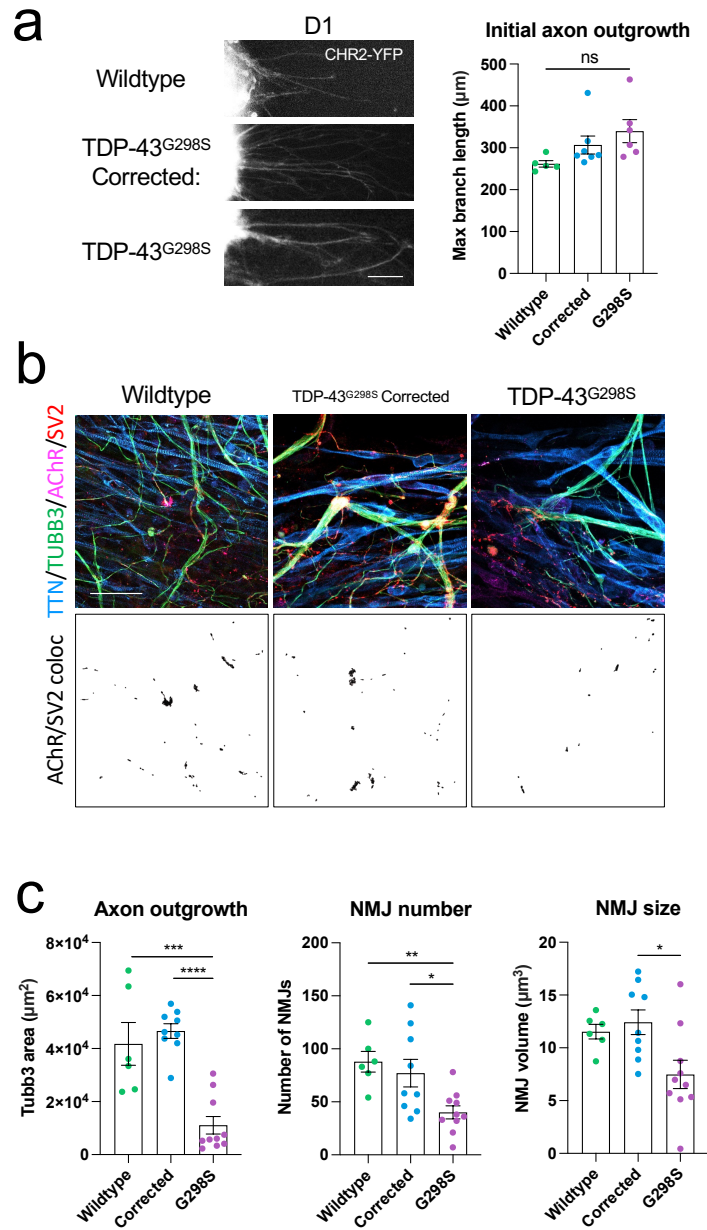


Figure 4.9. Human iPSC-derived neuromuscular circuits containing TDP-43^{G298S} motor neurons display a reduction in axon outgrowth and neuromuscular synapses.

A, Quantification of initial axon outgrowth based on CHR2-YFP at D1 of the neuromuscular co-cultures for wildtype (N=1, iN=3, n=6), corrected (N=1, iN=3, n=9) and TDP-43^{G298S} (N=1, iN=3, n=10) conditions (Scale bar = 50μm). **B**, Immunofluorescence staining of Titin, TUBB3, SV2, AChR and colocalization of SV2/AChR for wildtype, corrected and TDP-43^{G298S} 2-week neuromuscular co-cultures (Scale bar = 50μm). **C**, Quantification based on immunofluorescence staining of axon outgrowth, NMJ number and NMJ size. Error bars represent the SEM. One-way-ANOVA used to determine statistical significance. *p<0.05, **p<0.01, ***p<0.001, ****p<0.0001.

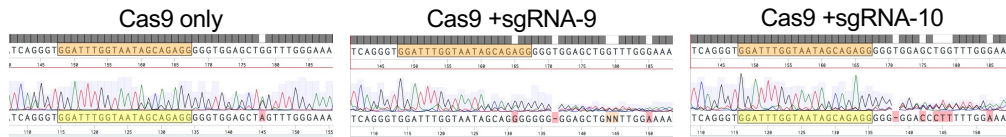
a

sgRNA-9: CRISPR ID: 901697809, Sequence: GGATTTGGTAATAGCAGAGG[^]GGG
(MM0: 0, MM1: 0, MM2: 1) Mismatch in the seed region.

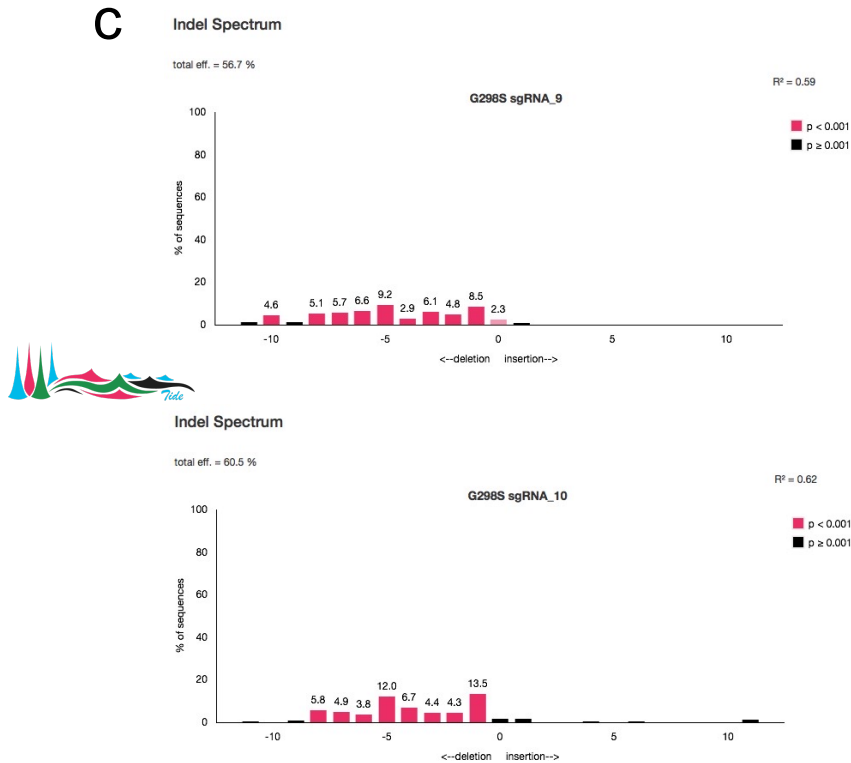
sgRNA-10: CRISPR ID: 901697810, Sequence: TTTGGTAATAGCAGAGGGGG[^]TGG
(MM0: 0, MM1:0, MM2:3)

*PAM, Seed region, ^ = cut site

b



c



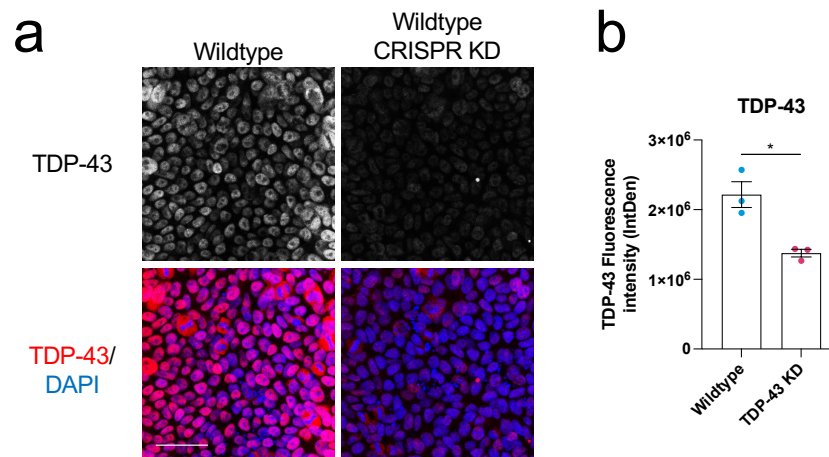
d

WGE ID	Location	Sequence	Mismatches	Strand	Type
901697809	Original CRISPR	GGATTTGGTAATAGCAGAGG GGG			Exonic
901697809	1:11022271-11022293	GGATTTGGTAATAGCAGAGG GGG	0	+	Exonic
948477943	2:238232583-238232605	GGATTTGGTAAGAGTAGAGG GGG	2	+	Intergenic
1041464290	8:58143403-58143425	GAAATTGGGAATAGCAGAGG AGG	3	+	Intronic
998316453	5:141187468-141187490	GGATCTGGGACTAGCAGAGG GGG	3	+	Exonic
998317072	5:141192702-141192724	GGATCTGGGACTAGCAGAGG GGG	3	+	Exonic
1075311287	10:121415882-121415904	GGAAGTGGTAATGCAGAGG TGG	3	+	Intergenic

Supplementary Figure 4.10. TIDE analysis of sgRNA-9 and sgRNA-10.

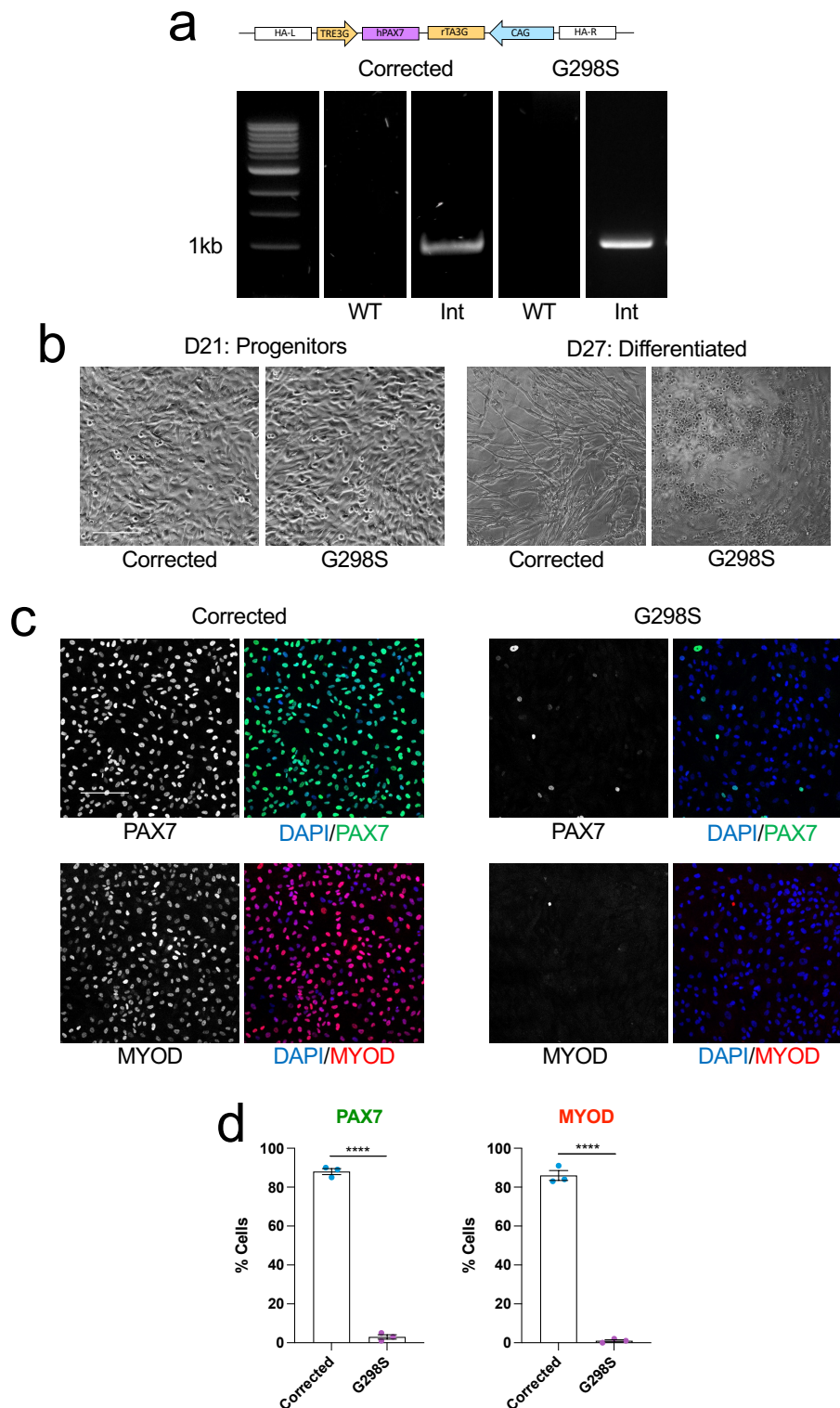
A, Details of both guide RNAs, including CRISPR ID, sequence and mis-match (MM) scores. PAM site in green, seed region in blue, ^ = cut site. **B**, Sanger sequencing showing sequence around the guide RNA target sites in CAS9 only conditions and CAS9 +sgRNA-9 and sgRNA-

10. **C**, TIDE analysis showing indel spectrum and estimated cutting efficiency for both guide RNAs. **D**, Top 5 predicted off-target loci for sgRNA-9.



Supplementary Figure 4.11. CRISPR-cas9 mediated knockdown of TDP-43 in wildtype hiPSCs.

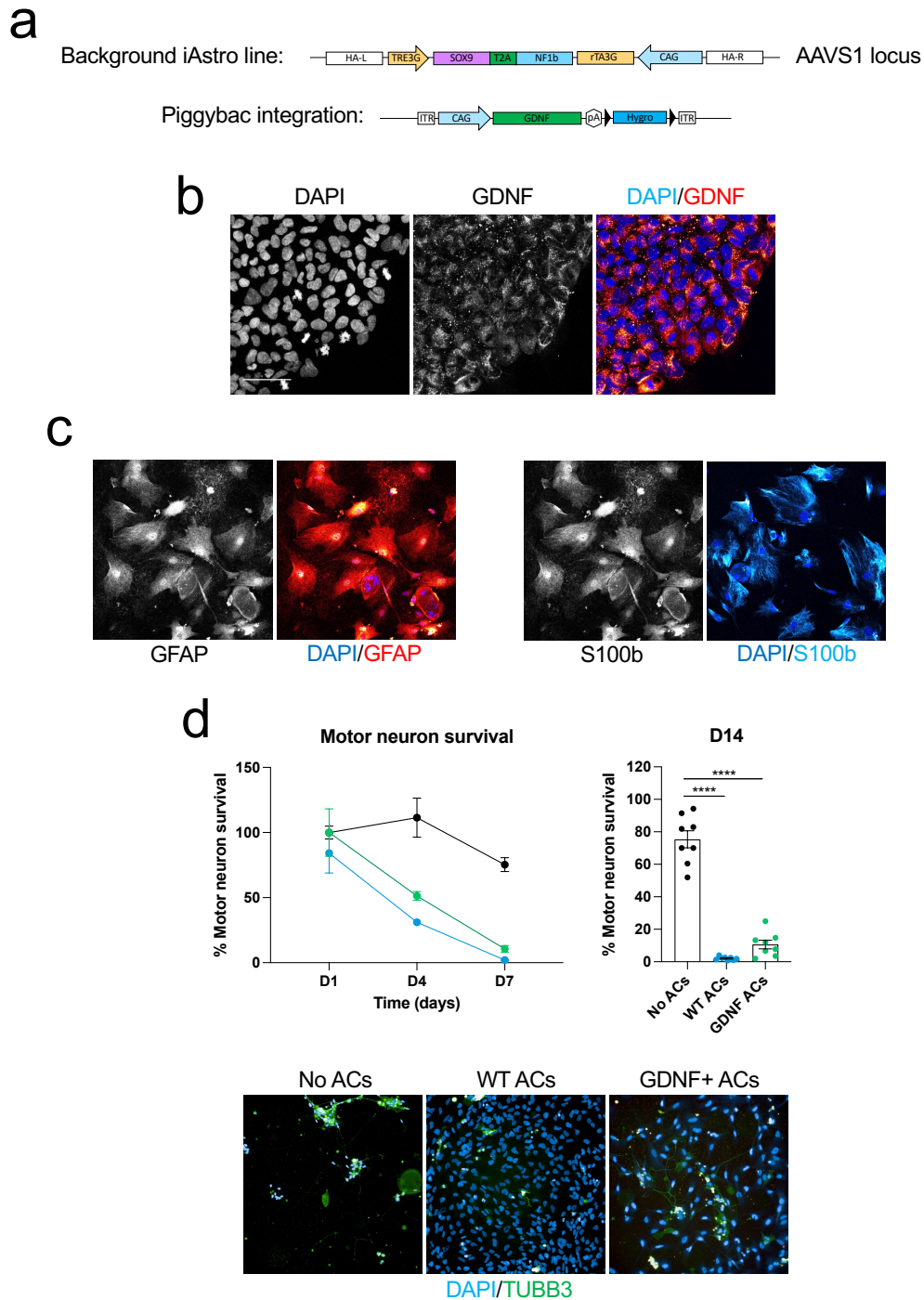
A, Immunofluorescence staining of TDP-43 in wildtype and CRISPR KD hiPSCs, counterstained with DAPI (Scale bar = 50 μ m). **B**, Quantification of TDP-43 fluorescence intensity in wildtype and CRISPR KD hiPSCs (N=1, iN=1, n=3). Error bars represent the SEM. Unpaired, t-test used to determine statistical significance. *p<0.05.



Supplementary Figure 4.12. Impaired differentiation of TDP-43^{G298S} iPAX7 hiPSCs into myoblasts.

A, Stable homozygous integration of the iPAX7 construct into the CLYBL safe-harbour loci of TDP-43^{G298S} corrected and TDP-43^{G298S} hiPSC lines. **B**, Brightfield images of D21 myoblast progenitors and D27 myotubes in TDP-43^{G298S} corrected and TDP-43^{G298S} lines (Scale bar =

200 μ m). **C**, Immunofluorescence staining of PAX7 and MYOD in D21 TDP-43^{G298S} corrected and TDP-43^{G298S} myoblast progenitors, counterstained with DAPI (Scale bar = 50 μ m). **D**, Quantification of the percentage cells expressing PAX7 and MYOD based on immunofluorescence staining (N=1, iN=1, n=3). Error bars represent the SEM. T-test used to determine statistical significance. ****p<0.0001.



Supplementary Figure 4.13. Generation and characterization of hiPSC-GDNF+ iAstrocytes.

A, Schematic of the iAstro construct already incorporated into the hiPSC line and the CAG::GDNF construct. **B**, Immunofluorescence staining for GDNF in hiPSCs stably engineered to express the CAG::GDNF construct using a piggybac integration system. Counter stained with DAPI (Scale bar = 50µm). **C**, Immunofluorescence staining for the

astrocyte markers GFAP and s100b in differentiated GDNF+ iAstrocytes, counterstained with DAPI (Scale bar = 50µm). **D**, Survival of wildtype hiPSC-motor neurons without iAstrocytes, with wildtype iAstrocytes and with GDNF+ iAstrocytes and representative images (N=1, iN=1, n=8). Error bars represent the SEM. One-way-ANOVA used to determine statistical significance. ****p<0.0001.

Figure 4.6. Supplementary Movies - QR Codes:



Figure 4.7. Supplementary Movies - QR Codes:



Figure 4.8. Supplementary Movies - QR Codes:



Supplementary Figure 4.14. QR codes for supplementary movies.

Supplementary Movie 4.1. Wildtype optogenetically evoked contraction (<https://youtu.be/-JT4KI4PHso>), **Supplementary Movie 4.2.** Wildtype ontogenetically evoked contraction +DTC (https://youtu.be/1b_0kZDZWIQ), **Supplementary Movie 4.3.**

Wildtype optogenetically evoked no entrainment (<https://youtu.be/Bmd6G0qpDpI>), **Supplementary Movie 4.4.** Wildtype optogenetically evoked entrained (<https://youtu.be/QufKWwN8aZM>), **Supplementary Movie 4.5.** TDP 43^{G298S} CRISPR Corrected optogenetically evoked contraction (https://youtu.be/vC_6pRqnozY), **Supplementary Movie 4.6.** TDP 43^{G298S} CRISPR Corrected spontaneous contractions (<https://youtu.be/3xFxy64RFmA>), **Supplementary Movie 4.7.** TDP 43^{G298S} optogenetically evoked contraction (<https://youtu.be/-n816knn0e8>), **Supplementary Movie 4.8.** TDP 43^{G298S} spontaneous contractions (<https://youtu.be/Z5rtHdiSLnY>).

4.11 Discussion

This chapter describes the development of a human iPSC-derived neuromuscular co-culture platform to model ALS. To achieve this hiPSCs were engineered to express a motor neuron specific MACS-sortable *HB9::hCD14* construct and the optogenetic actuator CHR2-YFP in order to generate highly enriched, optogenetically controllable human motor neurons (Figure 4.3, 4.4). Furthermore, a separate hiPSC clone was engineered to express a doxycycline inducible *iPAX7* construct, in order to forward program hiPSCs into skeletal myoblasts (Figure 4.5). hiPSC-motor neurons were then combined with mESC-astrocytes expressing GDNF (Chapter 3) into neural spheroids and co-cultured with hiPSC *iPAX7* myoblasts in compartmentalised microdevices (Figure 4.6). In order to model ALS, patient hiPSCs harbouring a TDP-43^{G298S} mutation were obtained from the Chandran group (University of Edinburgh) and CRISPR-Cas9 mediated genome engineering used to generate a gene-corrected isogenic control line (Figure 4.1). Using this co-culture platform, it was then possible to model developmental mechanisms and ALS-related neuromuscular phenotypes. It was found that human neuromuscular synapse formation was activity dependent (Figure 4.7). And, remarkably, neuromuscular co-cultures harbouring TDP-43^{G298S} motor neurons exhibited concomitant occurrence of increased spontaneous myofiber contractions and weaker optogenetically evoked maximal contractile output due to loss of neuromuscular junctions, mirroring the occurrence of myofiber fasciculations and muscle weakness seen in patients with ALS (Figure 4.8, 4.9) (Bashford et al. 2020).

In this chapter CRISPR Cas9 gene editing was employed to correct the endogenous TDP-43^{G298S} mutation in a patient derived hiPSC line (Figure 4.1). Pre-complexed recombinant Cas9 and chemically synthesised sgRNA ribonucleoprotein (RNP) based delivery was chosen rather than plasmid-based delivery of the Cas9 protein and the guide RNA. This was based on several

factors: first pre-complexed RNPs are much smaller than plasmids and as such the transfection efficiency would likely be much higher and toxicity lower (Kim et al. 2014). This was counter-balanced however by the fact that there would be no positive selection using FACS for GFP+ transfected cells as is normally carried out using a plasmid-based delivery system. Second, the RNP complex is pre-primed before transfection and as such is ready to cut straightaway. With a plasmid-based approach there is a delay between transfection and expression of the Cas9/sgRNA and formation of RNP complexes before cutting can begin, this is problematic since the donor template DNA is degraded relatively quickly – so timing optimal levels of RNP activity and donor template availability is crucial. Furthermore RNP complex formation may not occur correctly or efficiently and sgRNAs are degraded rapidly if not part of the RNP complex (Hendel et al. 2015). Finally, plasmid DNA remains in cells for a much longer period leading to increased likelihood of off target activity (Liang et al. 2015). Plasmid DNA has also been shown to directly integrate into the host genome, leading to further off-target effects (Kim et al. 2014). Using this approach, a high cutting efficiency of ~60% was achieved (S Figure 4.10). To facilitate the identification of recombinant clones, a silent Xho1 restriction site was incorporated into the donor template of the seed region of the sgRNA binding site. Mutating the seed region is common practice to prevent Cas9 cutting already integrated template DNA. Incorporation of the restriction site as part of this allowed a simple PCR and restriction digest screen to be carried out to determine which hiPSC clones had incorporated donor template DNA. From this it was found that donor template integration was very high at 45%. Sanger sequencing showed that 15% had normal sequences, while the rest typically showed abnormal sequences downstream of the sgRNA sequence. For the chosen clone there were no off-target effects in the top 5 predicted sites, the karyotype was normal, TDP-43 protein expression was normal, splicing of the intron 5/exon 6 boundary was normal and cells still expressed key pluripotency markers (Figure 4.1). A TDP-43 knockdown clone was also generated in a wildtype line (S Figure 4.11); however, the line grew so slow its use was discontinued – this is not too surprising as TDP-43 knockout is embryonic lethal after E3.5 (Kraemer et al. 2010). Future work to achieve TDP-43 knockdown in hiPSCs should use CRISPR interference (CRISPRi) or siRNA based approaches at later stages of the cultures (Mandegar et al. 2016).

The initial aim of this chapter was to generate fully human neuromuscular co-cultures using hiPSC-motor neurons, hiPSC-astrocytes and hiPSC-myofibers. Furthermore, it was also the intention to be able to generate each cell type from wildtype, TDP-43^{G298S} corrected and TDP-43^{G298S} backgrounds to be able to compare the contribution of the TDP-43^{G298S} mutation to ALS-related neuromuscular phenotypes in a cell type specific manner.

Generating human iPSC-motor neurons was relatively simple to establish. hiPSCs were differentiated using a 12-day small molecule approach into mixed motor neuron/motor neuron progenitor populations (Du et al. 2015) (Figure 4.2). The MACS sortable *HB9::hCD14* construct (used in chapter 3 – plasmid generated by Carolina Barcellos-Machado) was also stably integrated into the AAVS1 safe harbour locus (Hockemeyer et al. 2009) in hiPSCs using TALENS based delivery and could successfully be used to reliably enrich motor neurons to ~90% (Figure 4.3). The optogenetic actuator CHR2-YFP (used in chapter 3 – plasmid generated by Carolina Barcellos-Machado (Bryson et al. 2014)) was also incorporated into the hiPSCs and could be used to reliably induce trains of action potentials in hiPSC-motor neurons using blue light (Figure 4.4).

Generating human iPSC-myoblasts was more challenging. Other members of the lab (Aimee Cheesbrough, Lea R'Bbio) had repeatedly attempted a small-molecule approach to differentiate hiPSCs into myoblasts using the well-known protocol established by the Pourquie group (Chal et al. 2016), however had found it highly variable between cell lines and unreliable. Further discussions with our collaborators (Amaia Paredes, Yung-Yao Lin - QMUL) who regularly used this protocol revealed it only worked on a small number of hiPSC-lines and even then, was not 100% reliable. As such it was decided to take a different approach. Another member of the lab – Federica Riccio had had recent success using forward programming approaches to generate GABAergic and Glutamatergic cortical neurons from hiPSCs, and kindly agreed to clone the myogenic *PAX7* gene into the Dox-inducible construct for us to try (Rao et al. 2018). By stably integrating this construct into the CLYBL safe-harbour locus (Cerbini et al. 2015) of a wildtype hiPSC line it was then possible to reliably generate *PAX7*/*MYOD*+ myoblast progenitors within 21 days (Figure 4.5). Further differentiation for 1 week led to the formation of myosin/myogenin positive myotubes and a further week, the formation of striated titin+ myofibers (Figure 4.5). Interestingly this approach worked well for

the wildtype and TDP-43^{G298S} Corrected hiPSC lines, but completely failed for the TDP-43^{G298S} line, despite homozygous integration of the *iPAX7* construct (S Figure 4.12). This was found to be the case for multiple TDP-43^{G298S} *iPAX7* clones (data not shown). The reasons for this are unclear. It's possible that the *iPAX7* transgene had been silenced at the *CLYBL* locus specifically in the TDP-43^{G298S} clones by chance – indeed random silencing has been documented at the *AAVS1* safe-harbour locus (Ordovas et al. 2015) so similar silencing at the *CLYBL* locus is possible. However, the fact it only occurred in the TDP-43^{G298S} lines and not the wildtype or CRISPR corrected isogenic control lines, may mean that either the TDP-43^{G298S} mutation somehow increased gene silencing at the *CLYBL* safe-harbour loci or directly interfered with myogenic differentiation. Indeed a number of studies have shown that TDP-43 knockdown inhibits myogenic differentiation by inhibiting the expression of muscle genes such as *MYOD* (Militello et al. 2018), hinting at a possible mechanism behind these results. This opens interesting questions about the role of TDP-43 in muscle function, regeneration and possibly the origins of TDP-43 pathology in ALS – indeed several studies have shown TDP-43 forms aggregates in regenerating muscle (Vogler et al. 2018). Such aggregates have also been observed in skeletal muscle of patients with ALS (Soraru et al. 2010). It could be possible that the muscle damage and regeneration that occurs in ALS further contributes to the spread of or is even the original source of pathological TDP-43 aggregates in ALS. Indeed, such a co-culture platform as developed in this chapter would be a promising way to approach this question. It would be possible to artificially induce TDP-43 aggregation in the myofibers, by using an OptoTDP-43 system for example (Asakawa, Handa and Kawakami 2020) and then measure any retrograde prion like spreading of the TDP-43 aggregates into the motor neurons (Smethurst et al. 2016).

Generating hiPSC-astrocytes was possible using a forward programming approach. Specifically forced expression of the astrocyte genes *Sox9* and *NF1b* (Doxycycline inducible *AAVS1* knock in) in a line generated by Federica Riccio (Li et al. 2018). To make this amenable to motor neuron co-cultures a *GDNF* transgene (chapter 3) was incorporated using a piggybac integration system into this *iAstro* line. Using this approach, it was possible to generate GFAP and *S100b* positive astrocytes. However, when cultured with hiPSC-motor neurons it was found that both wildtype and *GDNF*+ astrocytes impeded motor neuron survival compared to culturing the motor neurons alone (S Figure 4.13). It's unclear why this was the case but

perhaps points toward a general drawback of forward programming approaches in how much the cells derived truly reflect their *in vivo* counterparts. While GFAP and S100b expression are widely used astrocyte markers, their expression alone does not mean they will behave exactly like *in vivo* astrocytes and perhaps other transcriptomic networks need to be activated – other than those activated by forced expression of Sox9 and NF1b - in order to truly recapitulate *in vivo* astrocytes. It's also possible that the astrocytes were still too immature (D21) and longer-term culture and maturation may improve their capacity to support motor neuron survival. Indeed, well-established small-molecule approaches to derive astrocytes from hiPSCs typically take longer at 45-60 days (Tyzack, Lakatos and Patani 2016, Taha et al. 2022). Or alternatively it's possible that the inducible astrocytes recapitulate a more reactive state that is less supportive of motor neuron survival. Finally the mismatch in regional identity of the dorsal forebrain astrocytes and spinal motor neurons may have resulted in impaired trophic support observed (Li et al. 2018).

Despite difficulties in generating hiPSC-derived astrocytes and hiPSC-derived myoblasts from TDP-43^{G298S} hiPSCs it was still possible to generate functional human iPSC-derived neuromuscular co-cultures. To achieve this, hiPSC-motor neurons and mESC-Astrocytes expressing GDNF (Machado et al. 2019) were cultured together in neural aggregates, which were then plated along with hiPSC-myoblasts into compartmentalised microdevices. Co-localisation of pre- and post-synaptic structures indicated the formation of neuromuscular junctions. Optogenetic stimulation of the motor neurons could elicit robust myofiber contractions that could be abolished by the AChR blocker d-Tubocurarine indicating that the neuromuscular junctions were functional (Figure 4.6). As in chapter 3, it was found that optogenetic entrainment could increase neuromuscular junction formation and optogenetically evoked myofiber contractility in an activity-dependent manner (Figure 4.7) – see discussion section for Chapter 3. However as was the case in Chapter 3, these neuromuscular co-cultures were generally immature, and poly innervated. This fact should be considered when interpreting age-related disease phenotypes – since comparable phenotypes in patients with ALS would occur in mature, mono-innervated motor units. Indeed, this is a broader implication for hiPSC research into age-related disorders since the maturity of hiPSC-derived neurons is often comparable to pre-natal stage neurons (Burke et al. 2020). However, this could also be interpreted as an advantage of using such a system,

allowing insights into very early pathological processes that may occur in cells and circuits years or decades before symptomatic onset of the disease.

Perhaps the most striking finding in this chapter was the occurrence of increased spontaneous myofiber contractions in the neuromuscular co-cultures containing TDP-43^{G298S} motor neurons (Figure 4.8, Supplementary Figure 4.14 - Supplementary Movie 4.8). Interestingly while spontaneous myofiber contractions were higher, maximal optogenetically evoked myofiber contractions were in fact weaker (Figure 4.8, Supplementary Figure 4.14 – Supplementary Movie 4.7). This finding was linked to a reduction axon outgrowth and the overall number of neuromuscular junctions (Figure 4.9). Taken together these findings indicate that the total number of functional motor units was lower in the TDP-43^{G298S} neuromuscular co-cultures, leading to weaker maximal contractile output. However, the remaining motor units were hyperexcitable, leading to increased spontaneous myofiber contractility. This finding mirrors the occurrence of muscle fasciculations (spontaneous twitching) and muscle weakness seen in patients with ALS (Liu et al. 2021, Bashford et al. 2020, de Carvalho et al. 2017), which forms a major diagnostic criteria for the disease (de Carvalho et al. 2017, Hardiman et al. 2017). Interestingly a recent longitudinal study of muscle fasciculations in patients with ALS showed that the highest fasciculation frequencies were found in bicep muscles that had recently become weak (Bashford et al. 2020). This finding was attributed to intrinsic hyperexcitability of the motor units and a “relentless shrinking of the motor unit pool”. Eventually the motor unit pool would shrink so much that fasciculation frequency would subsequently decline. Furthermore, this study suggested that fasciculations had a proximal origin at the soma/axon or possibly corticospinal inputs, rather than a distal origin at the terminal branches of the motor unit. This was evidenced by higher incidence of fasciculation doublets with an interval of 60-80ms as opposed to those with a 5-10ms interval that would be expected through a distal origin at the nerve terminal (Bashford et al. 2020). Other studies have shown that motor unit hyperexcitability is driven by altered Na⁺ and K⁺ conductances in peripheral axons (Vucic and Kiernan 2010, Kanai et al. 2006), possibly as a result of altered ion channel expression (Howells et al. 2018). It has also been shown that motor unit hyperexcitability is associated with increased disease severity and reduced survival time in patients with ALS (Shimizu et al. 2014). Furthermore, one of the few treatments to extend survival in ALS, riluzole, primarily acts to inhibit Na⁺ channels, glutamate release and

neuronal excitability (Doble 1996), suggesting that early motor unit hyperexcitability may play an active role in the progression of ALS. Indeed, aberrant hyperexcitability of the motor units may actively drive activity dependent elimination of the neuromuscular synapses - as occurs normally in development, where less active axons are favoured over highly active axons to promote efficacy, and prevent extreme metabolic demands of larger, more active synapses (Barber and Lichtman 1999). This would make sense in this neuromuscular co-culture model, which is already less mature owing to poly innervation of the myofibers, and increased motor unit excitability may help drive activity dependent synapse elimination. It's possible that similar mechanisms may occur aberrantly in mature, mono-innervated hyperexcitable motor units in patients with ALS and that extreme metabolic demands of hyperexcitable motor units may contribute to their eventual loss (Bashford et al. 2020).

Taken together these results show the establishment of a hiPSC-derived neuromuscular co-culture platform to model functional human motor units *in vitro*. Using this platform, it was possible to model ALS-related neuromuscular phenotypes by incorporating TDP-43^{G298S} hiPSC motor neurons and CRISPR-corrected isogenic controls. Key ALS-related neuromuscular phenotypes were recapitulated in the TDP-43^{G298S} neuromuscular co-cultures, relative to the wildtype and CRISPR corrected co-cultures. These included increased spontaneous myofiber contractility and weaker optogenetically evoked maximal contractile output, which was linked to a reduction in axon outgrowth and overall number of neuromuscular synapses. In summary this approach serves as a useful platform to model ALS-related human neuromuscular phenotypes in a simplified *in vitro* co-culture system.

5. Engineering high-throughput 96-well human iPSC-derived neuromuscular co-cultures

5.1 Aims & hypotheses

This chapter describes the development of a high-throughput 96-well hiPSC-neuromuscular co-culture platform and automated high content image analysis pipeline to automatically quantify human neuromuscular co-cultures. The impetus behind this was the low-throughput and time-consuming nature of establishing neuromuscular co-cultures in the compartmentalised microdevices. With these previous co-cultures the initial plating of the cells was time-consuming and fiddly, and the imaging and image analysis was all carried out manually. This was not only time-consuming but prone to sampling error and bias since it was not feasible to image the entire culture and only several representative fields of view were obtained for each culture. By establishing hiPSC-neuromuscular co-cultures in 96-well imaging plates it was then possible to develop an automated high content image analysis pipeline using an operetta CLS HCI system. Using this system the following aims were set:

1. Can functional human neuromuscular junctions be grown in 96-well plates
2. Can ALS-related phenotypes be automatically quantified using high content image analysis
3. Can DMD-related phenotypes be automatically quantified using high content image analysis
4. Can custom-built 96 well plates with suspended electrospun elastic nanofibers support long-term stability, alignment and maturation of contractile myofibers in hiPSC-neuromuscular co-cultures

As previously discussed indicative statistics have been performed on these single lines, in line with similar studies characterising single ALS-related hiPSC lines in neuromuscular co-cultures (Osaki et al. 2018) and using electrophysiology (Devlin et al. 2015), despite the true biological N being 1. To make this clear, biological replicates (separate hiPSC lines) are denoted as (N), induction replicates (complete differentiations from hiPSCs) are denoted as (iN) and technical replicates, such as recordings from individual neurons, neuromuscular co-cultures or coverslips are denoted as (n).

5.2 Automated high content image analysis of hiPSC-neuromuscular co-cultures in high-throughput 96-well plates

Since the plating, imaging and analysis of the compartmentalised neuromuscular co-cultures described in chapters 1 & 2 was time-consuming and not amenable to scalable drug-screening, a high throughput 96-well human iPSC-neuromuscular co-culture was developed. This format allowed far more conditions to be grown simultaneously and facilitated automated high content image (HCI) analysis of the co-cultures. Briefly, 40k human iPSC-myofibers were plated as a monolayer in each well of a 96-well plate. Subsequently neural aggregates consisting of 5k MACS enriched GDNF+ expressing mESC-astrocytes and 15k MACS enriched hiPSC-motor neurons were plated on top of the myofiber sheet, in the centre of each well. Neuromuscular co-cultures were then grown for between 5 and 7 days, then fixed and stained for the myofiber marker titin, the axonal marker TUBB3, the presynaptic marker SV2 and post-synaptic ACh receptors (Figure 5.1a,c). Following this, plates were automatically imaged using an Operetta CLS high content image (HCI) analysis system. The entire well was imaged in 20x tiles and as such was far more representative than the individual images taken of the compartmentalised neuromuscular co-cultures where it was not feasible to image the entire culture (Figure 5.2a). Using Harmony 4.9 HCI analysis software an automated image segmentation pipeline was built to create masks for: myofibers (based on the titin stain), axonal outgrowth (based on the TUBB3 stain), presynaptic structures (based on the SV2 stain), and post-synaptic structures (based on the AChR stain) (Figure 5.1d). Co-localisation of SV2 and AChR objects was then used to infer neuromuscular junction object numbers and morphological parameters (Figure 5.1d). Background noise and debris were also filtered out from the masks based on intensity and morphology – for example dead cells and debris in the cultures often showed up as bright spots/speckles in the image, which could be eliminated from the masks using a filter with a cut off above a certain fluorescence intensity and above a certain sphericity (S Figure 5.7). Similarly non-specific antibody staining often shows up as low-level background noise in the image, which can be filtered out by applying a cut-off below a certain fluorescence intensity. An example of a sub-optimal staining with segmentation filters applied is shown in S Figure 5.7.

5.3 Formation of functional neuromuscular junctions in 96-well plates

Aside from observing co-localisation of pre- and post-synaptic structures in the 96-well neuromuscular co-cultures (Figure 5.1d), functional neuromuscular transmission and myofiber contractility was also assessed. Optogenetic stimulation of the motor neurons elicited robust myofiber contractions, which could be quantified using particle image velocimetry (PIV) analysis. Treatment with the Na⁺ channel blocker tetrodotoxin (TTX) abolished optogenetically evoked myofiber contractions from 6.90 $\mu\text{m/s}$ (SE \pm 1.79) to 0.75 $\mu\text{m/s}$ (SE \pm 0.21, n=3, T-test p=0.027), showing that pre-synaptic action potentials are essential for optogenetically evoked myofiber contractions (Figure 5.2a). Furthermore, treatment with the AChR blocker d-tubocurarine (DTC) also abolished optogenetically evoked myofiber contractions from 6.05 $\mu\text{m/s}$ (SE \pm 1.40) to 0.66 $\mu\text{m/s}$ (SE \pm 0.11, n=3, T-test p=0.018), showing that optogenetically evoked myofiber contractions occur through neuromuscular transmission at ACh receptors (Figure 5.2b). Taken together this data shows that functional human neuromuscular junctions can form in 96-well hiPSC-neuromuscular co-cultures.

5.4 Automated HCI analysis of ALS-related phenotypes in high-throughput 96-well neuromuscular co-cultures

Clear ALS-related phenotypes had been observed in the compartmentalized neuromuscular co-cultures, so it was the next step to see if these phenotypes could also be recapitulated in the 96-well neuromuscular co-cultures and form the basis of a phenotypic small molecule screen. Initially for this, two other cell lines were used than those used in chapters 2 and 3. A wildtype line was used alongside an ALS patient derived hiPSC-line harboring a TDP-43^{M337V} mutation. Both lines had been engineered to express the MACS sortable *HB9::hCD14* construct and the optogenetic actuator CHR2-YFP as described in chapter 2 and differentiated and MACS enriched into motor neurons. First, functional neuromuscular transmission and myofiber contractility was assessed by optogenetically stimulating the motor neurons and quantifying myofiber contraction velocity. The pathogenic TDP-43^{M337V} mutation caused a significant decrease in optogenetically evoked peak myofiber contraction velocity 1.49 $\mu\text{m/s}$ (SE \pm 0.31) compared to 2.55 $\mu\text{m/s}$ (SE \pm 0.21, n=5, T-test p=0.023) in the wildtype conditions (Figure 5.3a). Next, automated high content image analysis (HCI) was carried out on wildtype, TDP-43^{M337V} and TDP-43^{M337V} + Necrostatin treated conditions as described in Figure 5.1. The

pathogenic TDP-43^{M337V} mutation caused a significant decrease in the total number of myofibers per well 40318 (SE ± 153.7) compared to 5060 (SE ± 187.9, n=8, One-way-ANOVA with Dunnet's test p=0.0059) in the wildtype conditions (Figure 5.3b,c). TDP-43^{M337V} also caused a significant reduction in total axon outgrowth 6.12E+06μm² (SE ± 2.04E+05) compared to 7.12E+06μm² (SE ± 2.25E+05, n=8, One-way-ANOVA with Dunnet's test p=0.035) in the wildtype condition. Necrostatin moderately improved axon outgrowth to 6.86E+06μm² (SE ± 3.79E+05, n=8, One-way-ANOVA with Dunnet's test p=0.1306) although this was not significant. TDP-43^{M337V} also caused a decrease in the number of pre-synaptic SV2 objects 19,518 (SE ± 930) compared to 24,269 (SE ± 681, n=8, One-way-ANOVA with Dunnet's test p=0.0003) in the wildtype condition. Necrostatin treatment significantly increased the number of SV2 objects to 22,422 (SE ± 535, n=8, One-way-ANOVA with Dunnet's test p=0.0201). TDP-43^{M337V} also caused a moderate but non-significant decrease in the total number of NMJs: 1388 (SE ± 94.59) compared to 1471 (SE ± 73.02, n=8, One-way-ANOVA with Dunnet's test p=0.72) in the wildtype. Necrostatin treatment significantly increased the total number of NMJs to 1874 (SE ± 88.41, n=8, One-way-ANOVA with Dunnet's test p=0.0013). Taken together these results show that ALS-related neuromuscular phenotypes can be effectively modelled in high-throughput 96-well hiPSC-neuromuscular co-cultures and high content image analysis can be used to quantify them in a rapid and automated manner. Furthermore, these results show that the RIPK1 inhibitor, necrostatin, can partially rescue ALS-related neuromuscular phenotypes.

5.5 Automated HCI analysis of DMD-related phenotypes in high-throughput 96-well neuromuscular co-cultures

In addition to modelling ALS disease phenotypes relating to motor neuron dysfunction it was also interesting to see if this high-throughput 96-well neuromuscular co-culture platform could be used to model other neuromuscular disease phenotypes relating to myofiber dysfunction as opposed to motor neuron dysfunction. Through a collaboration with Amaia Paredes and Yung-Yao Lin (QMUL) hiPSC-myofibers derived from patients with Duchenne muscular dystrophy (DMD) were co-cultured with wildtype motor neurons in the 96-well co-culture platform. These myofibers had a truncating dystrophin^{R3381X} mutation. First, functional neuromuscular transmission and myofiber contractility was assessed by optogenetically

stimulating the motor neurons and quantifying myofiber contraction velocity. The pathogenic dystrophin^{R3381X} mutation caused a significant decrease in optogenetically evoked peak myofiber contraction velocity 1.059 $\mu\text{m/s}$ (SE \pm 0.23, n=4) compared to 2.55 $\mu\text{m/s}$ (SE \pm 0.21, n=5, T-test p=0.0023) in wildtype conditions (Figure 5.4a). Next automated high content image analysis was carried out on wildtype, dystrophin^{R3381X} and dystrophin^{R3381X} + Necrostatin conditions as described in Figure 5.1. The pathogenic dystrophin^{R3381X} mutation caused a significant reduction in the total number of myofibers 2716 (SE \pm 93.19) compared to 5060 (SE \pm 197.9, n=8, One-way-ANOVA with Dunnet's test p<0.0001) in the wildtype conditions (Figure 5.4b,c). Dystrophin^{R3381X} also caused a significant reduction in myofiber size 407 μm^2 (SE \pm 13.9) compared to 651.8 μm^2 (SE \pm 20.83, n=8, One-way-ANOVA with Dunnet's test p<0.0001) in the wildtype conditions. Necrostatin treatment significantly increased myofiber size to 480.1 μm^2 (SE \pm 26.1, n=8, One-way-ANOVA with Dunnet's test p=0.04), although still not up to wildtype levels. It was found that the decrease in myofiber size was due to a reduction in myofiber length, while there was no change in myofiber width. Interestingly the dystrophin^{R3381X} myofibers had a significant impact on axon outgrowth, reducing axon outgrowth from 7.12E+06 μm^2 (SE \pm 2.25E+05) to 5.74E+06 μm^2 (SE \pm 2.67E+05, n=8, One-way-ANOVA with Dunnet's test p=0.0013). Necrostatin treatment rescued axon outgrowth back to wildtype levels 7.04E+06 μm^2 (SE \pm 2.44E+05, n=8, One-way-ANOVA with Dunnet's test p=0.0023). Finally, the pathogenic dystrophin^{R3381X} mutation significantly reduced the total number of neuromuscular junctions from 1471 (SE \pm 73.02) in the wildtype conditions to 691.5 (SE \pm 54.04, n=8, One-way-ANOVA with Dunnet's test p<0.0001). Necrostatin treatment significantly increased the number of neuromuscular junctions to 1159 (SE \pm 110.7, n=8, One-way-ANOVA with Dunnet's test p=0.0013). Taken together these results show that it is possible to model contrasting neuromuscular disease phenotypes relating to muscle dysfunction as opposed to motor neuron dysfunction. Specifically, Duchenne muscular dystrophy (DMD) phenotypes can be effectively modelled in high-throughput 96-well hiPSC-neuromuscular co-cultures and high content image analysis can be used to quantify them in a rapid and automated manner. Furthermore, these results show that the RIPK1 inhibitor necrostatin can partially rescue DMD-related neuromuscular phenotypes. In additional collaborative work it was shown that the TGF β inhibitor SB431542 could also rescue neuromuscular phenotypes, including myofiber morphology, NMJ morphology and axon outgrowth. The results are published in (Paredes-Redondo et al. 2021)

5.6 Manufacturing suspended biobased elastomer nanofiber scaffolds in 96-well imaging plates.

Long-term maintenance of 96-well neuromuscular co-cultures (past 5-7 days) proved challenging since contractile myofibers would collapse and detach from the 2D-tissue culture plastic. This was not so much of a problem in the compartmentalized microdevice cultures, since myofibers were embedded in a 3D hydrogel and could anchor to the PDMS chamber walls and the NOA coating. To overcome this limitation in the 96-well plate formats a collaboration with Aimee Cheesbrough (KCL/UCL) and Wenhui Song (UCL) was set up. Custom built 96-well plates with suspended elastomer nanofiber scaffolds were manufactured by Aimee Cheesbrough. Bottomless 96-well plates were placed between electrodes and well-aligned nanofibers were electrospun by a moving spinneret needle controlled by a step-motor across the plate between two collecting electrodes for 30 minutes (Figure. 5.5a,b). A glass base with the same dimensions as the 96-well plate was adhered to the plate using a custom laser-cut acrylic stamp and cured at 60°C overnight (Figure. 5.5a,c). Nanofibers were deposited uniformly across each well with minimal defects (Figure. 5.5d). In preparation for cell culture, plates were plasma-treated, UV sterilised and coated with GFR Matrigel overnight (Figure. 5.5a). In addition to this a 3D seeding mask was designed and printed to ensure uniform placement of neural aggregates in the centre of the wells (Figure 5.5e).

5.7 Electrospun suspended elastic nanofibers support long term stability, alignment and maturation of contractile myofibers in 96-well neuromuscular co-cultures

hiPSC-derived neuromuscular co-cultures were then grown on suspended biobased elastomer nanofiber scaffolds in custom built 96-well plates (Figure 5.6a). Elastomer nanofibers significantly improved myofiber alignment – a crucial step for myofiber maturation - as determined by fourier transformation analysis based on titin immunofluorescence labelling (Figure 5.6a). Furthermore, the direction of myofiber contractions was also aligned along the axis of the elastomer nanofibers (y-axis) and the predominant contribution to myofiber contraction force came from this axis (Figure 5.6b). Long term-stability of the neuromuscular co-cultures was also significantly improved by the elastomer nanofibers

compared to control plates. By D14 83.33% (SE \pm 4.17) of the control plate wells had shown significant myofiber detachment (defined as >30% detachment within the central field of view within the well – Figure 5.6c), while only 15.625% (SE \pm 7.86, n=4, T-test p=0.001) of the nanofiber wells had shown myofiber detachment (Figure 5.6c). This meant that by D14 there were significantly more myofibers still present in the nanofiber plates 5589 (SE \pm 410.1, n=5) compared to 2911 (SE \pm 114.4, n=7, T-test p<0.0001) in the control plates (Figure 5.6d). Furthermore, myofiber volume was also higher in the nanofiber plates 11,668 μm^3 (SE \pm 733.2, n=5) compared to 10,326 μm^3 (SE \pm 372, n=7, T-test p=0.041) in the control plates, indicating that the remaining myofibers were also more mature in the nanofiber plates (Figure 5.6c). Furthermore, axonal outgrowth was increased in the nanofiber plates from 6.6 $\times 10^6$ (SE \pm 1.5⁵ n=7) in the control plates to 14.7 $\times 10^6$ (SE \pm 8.8⁵, n=5, T-test p<0.0001) and NMJ size was also increased in the nanofiber plates from 27.06 (SE \pm 3.76, n=7) to 199.4 (SE \pm 11.49, n=5, T-test p<0.0001), indicating increased maturation of the neuromuscular co-cultures. Taken together these results show that custom nanofiber plates support long-term neuromuscular co-culture stability, maturation, and alignment in 96-well plates.

5.8 Necrostatin rescues ALS-related phenotypes in long-term neuromuscular co-cultures grown on 96-well nanofiber plates

Finally, to show that the 96-well neuromuscular co-cultures on nanofiber plates could be used as a phenotypic screen to test candidate ALS drugs, a small proof-of-principle screen was set up to look at the effect of the ALS-related TDP-43^{G298S} mutation and to carry out a dose response of the RIPK1 inhibitor necrostatin. The pathogenic TDP-43^{G298S} mutation caused a significant reduction in optogenetically evoked peak myofiber contraction velocity 4.34 $\mu\text{m}/\text{s}$ (SE \pm 0.44) relative to 8.97 $\mu\text{m}/\text{s}$ (SE \pm 0.57, n=8, One-way-ANOVA with Dunnet's test p<0.0001) in corrected conditions, and 7.33 $\mu\text{m}/\text{s}$ (SE \pm 0.38, n=8, One-way-ANOVA with Dunnet's test p=0.0007) in wildtype conditions (Figure 5.7a,b). Necrostatin treatment improved optogenetically evoked contractions to 6.98 $\mu\text{m}/\text{s}$ (SE \pm 0.27, n=10, One-way-ANOVA with Dunnet's test p=0.041) (Figure 5.7a,b). Automated high content image analysis also showed that the pathogenic TDP-43^{G298S} mutation caused a significant reduction in axon outgrowth 6.59⁷ μm^3 (1.09⁶) relative to wildtype 8.40⁷ μm^3 (SE \pm 2.28⁶, n=8, One-way-ANOVA with Dunnet's test p<0.0001) and corrected 7.61⁷ μm^3 (SE \pm 2.49⁶, n=8, One-way-ANOVA with

Dunnet's test $p=0.0043$) conditions (Figure 5.7c,d). Necrostatin treatment showed a dose-dependent increase on axon outgrowth, with $10\mu\text{M}$ significantly improving axon outgrowth to $7.727\mu\text{m}^3$ ($\text{SE} \pm 1.50^6$, $n=4$, One-way-ANOVA with Dunnet's test $p=0.0008$) (Figure 5.7c,d). TDP-43^{G298S} also caused a significant reduction in the number of pre-synaptic SV2 objects 169,979 ($\text{SE} \pm 2988$) relative to 212,470 ($\text{SE} \pm 8638$, $n=8$ One-way-ANOVA with Dunnet's test $p=0.0009$) in wildtype and 219,055 ($\text{SE} \pm 8848$, $n=8$, One-way-ANOVA with Dunnet's test $p=0.0018$) in corrected conditions. Again, $10\mu\text{M}$ necrostatin treatment significantly increased the number of presynaptic SV2 objects to 218,950 ($\text{SE} \pm 8333$, $n=4$, One-way-ANOVA with Dunnet's test $p=0.0019$) (Figure 5.7c,d). TDP-43^{G298S} caused a significant reduction in the number of NMJs from 912.1 ($\text{SE} \pm 112.1$) relative to corrected 1457 ($\text{SE} \pm 124.2$, $n=8$, One-way-ANOVA with Dunnet's test $p=0.022$) conditions. $10\mu\text{M}$ necrostatin treatment significantly increased the number of NMJs to 2104 ($\text{SE} \pm 230.4$, $n=4$, One-way-ANOVA with Dunnet's test $p<0.0001$) (Figure 5.7c,d). Finally, treatment with $10\mu\text{M}$ necrostatin also increased NMJ size from $247.5\mu\text{m}^3$ ($\text{SE} \pm 5.28$) in TDP-43^{G298S} conditions to $300.2\mu\text{m}^3$ ($\text{SE} \pm 15.74$, $n=4$, One-way-ANOVA with Dunnet's test $p=0.0074$) (Figure 5.7c,d). Taken together these results show that the 96-well neuromuscular co-culture platform with custom-built nanofiber plates can be used as a phenotypic assay to screen candidate ALS-drugs. PIV analysis revealed that the pathogenic TDP-43^{G298S} mutation caused a reduction in optogenetically evoked myofiber contraction velocity. Automated high content image analysis showed that TDP-43^{G298S} caused a reduction in axon outgrowth, presynaptic SV2 and total number of NMJs. Furthermore, a dose response of the RIPK1 inhibitor necrostatin showed that treatment with $10\mu\text{M}$ could significantly rescue these neuromuscular phenotypes. Supplementary movie QR codes can be found in supplementary figure 5.10.

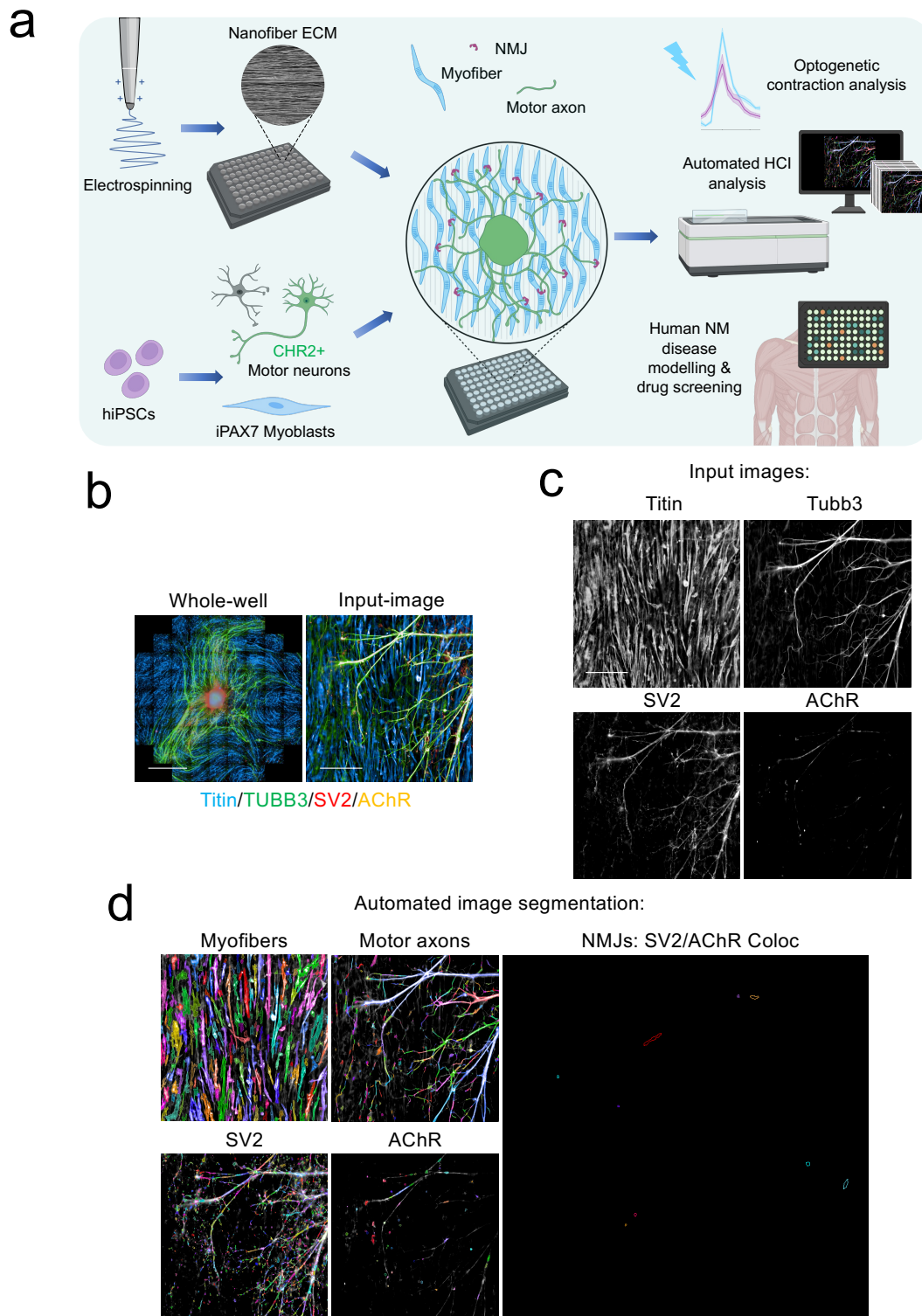


Figure 5.1. Automated high content image analysis of hiPSC-neuromuscular co-cultures in high-throughput 96-well plates.

A, Schematic showing co-culture of hiPSC-motor neurons and hiPSC-myoblasts in 96-well assay plates. **B**, shows an example of a whole-well composite image compiled of individual 20x tiles, taken on an operetta CLS high content imaging system (Scale bar = 2500 μ m) and

an individual 20x composite image (Scale bar = 200 μ m). **C**, example of the individual channels that make up a 20x composite image: Titin, TUBB3, SV2 and AChR (Scale bar = 200 μ m). **D**, automated high content image analysis of the individual channels. Automated segmentation generates masks for each channel, which are used to derive morphological and object number quantifications. Colocalisation of the SV2 and AChR objects is used to define NMJ objects.

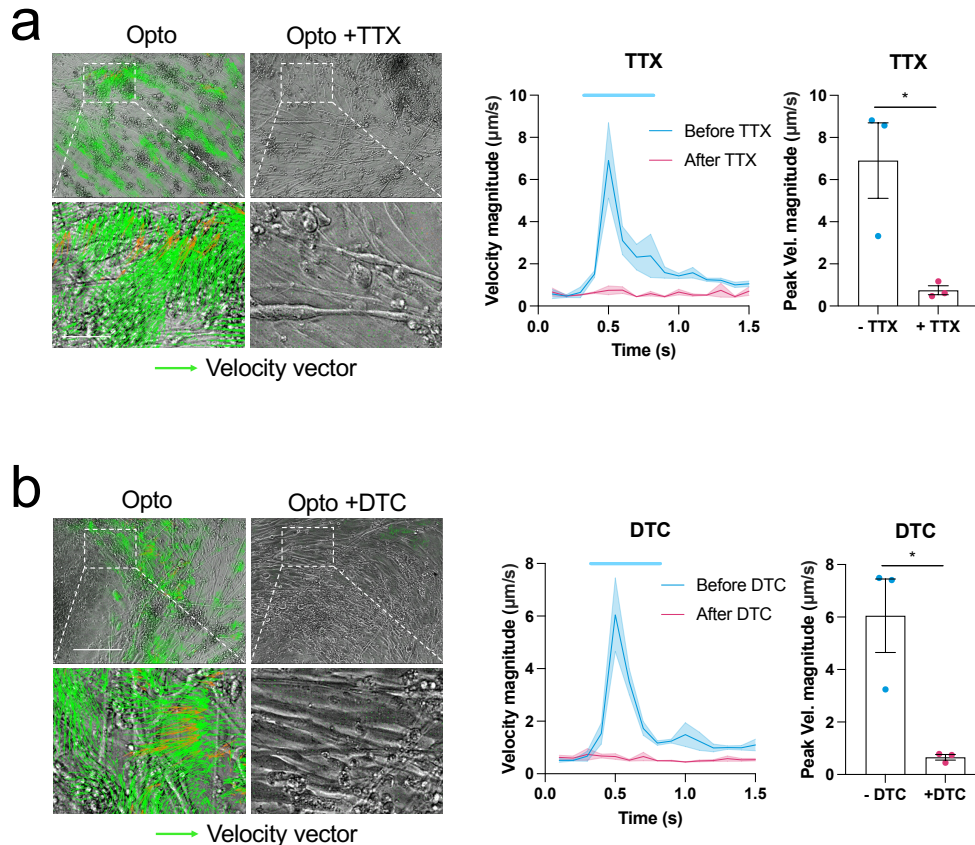


Figure 5.2. Formation of functional neuromuscular junctions in 96-well plates.

A, Particle image velocimetry (PIV) analysis of optogenetically evoked myofiber contractions in 96-well plates before and after treatment with the Na⁺ channel blocker tetrodotoxin (TTX), (N=1, iN=1, n=3) (Scale bar = 200 μ m). **B**, Particle image velocimetry (PIV) analysis of optogenetically evoked myofiber contractions in 96-well plates before and after treatment with the AChR blocker d-Tubocurarine (DTC), n=3 (Scale bar = 200 μ m). Error bars represent the SEM. Unpaired, non-parametric t-tests used to determine statistical significance. *p<0.05.

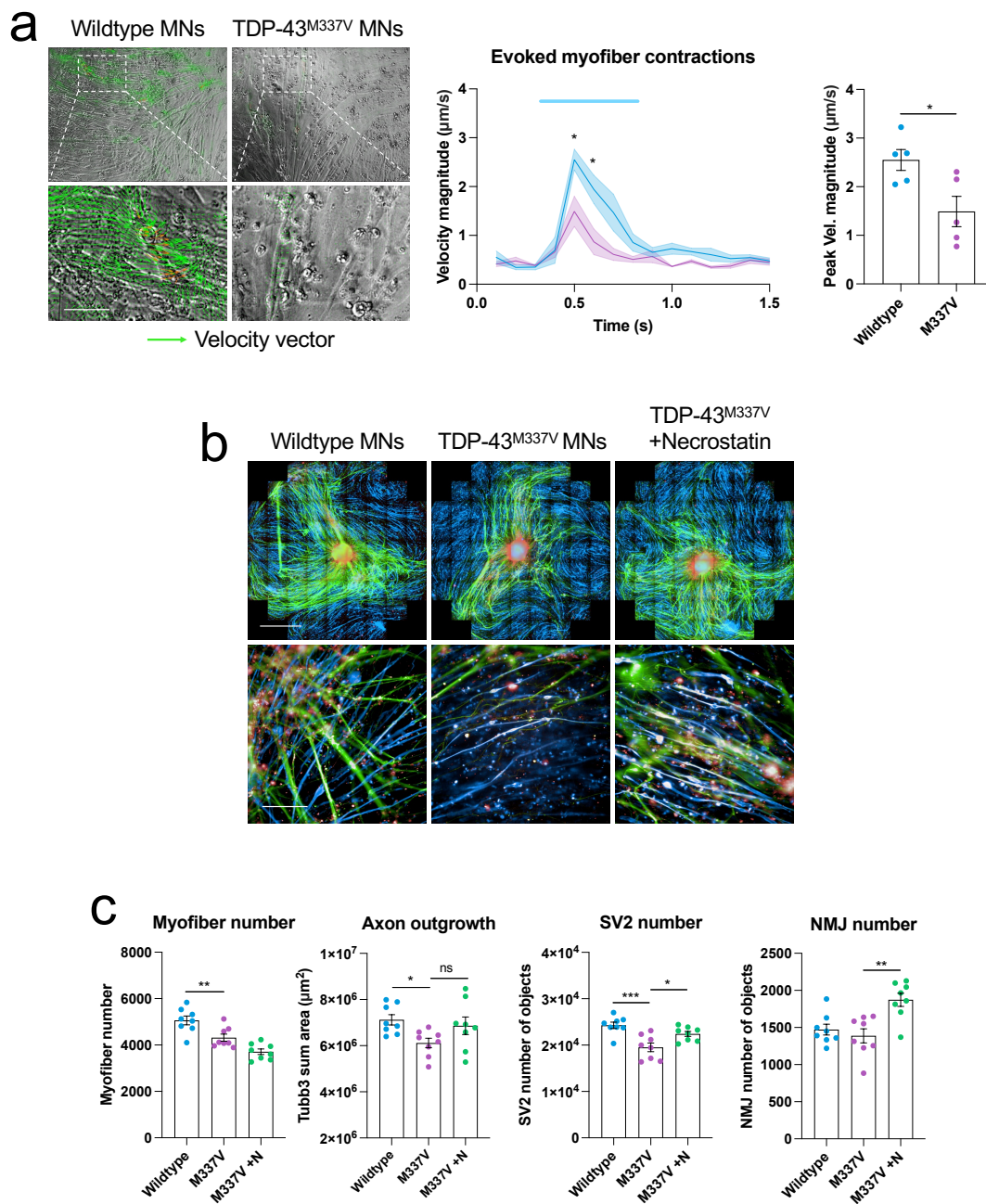


Figure 5.3. Automated HCI analysis of ALS-related phenotypes in high-throughput 96-well neuromuscular co-cultures.

A, Particle image velocimetry (PIV) analysis of optogenetically evoked myofiber contractions 96-well neuromuscular co-cultures containing in wildtype and TDP-43^{M337V} hiPSC-motor neurons, (N=1, iN=1 n=5) (Scale bar = 200 μm). **B**, Representative whole-well (Scale bar = 2500 μm) and individual field of view (Scale bar = 200 μm) composite images for wildtype, TDP-43^{M337V} and TDP-43^{M337V} +Necrostatin neuromuscular co-cultures. **C**, Automated high content image analysis quantification of myofiber number, total axon outgrowth, SV2 object number and NMJ object number across conditions. Error bars

represent the SEM. One-way-ANOVA with Dunnet's multiple comparison and unpaired, non-parametric t-tests used to determine statistical significance. * $p < 0.05$, ** $p < 0.01$, *** $p < 0.001$.

bar = 2500 μ m) and individual field of view composite images(Scale bar = 200 μ m) for wildtype, dystrophin^{R3381X} and dystrophin^{R3381X} +Necrostatin neuromuscular co-cultures. **C**, Automated high content image analysis quantification of myofiber number, myofiber area, myofiber length, myofiber width, total axon outgrowth, and NMJ object number across conditions. Error bars represent the SEM. One-way-ANOVA with Dunnet's multiple comparison and unpaired, non-parametric t-tests used to determine statistical significance. *p<0.05, **p<0.01, ****p<0.0001.

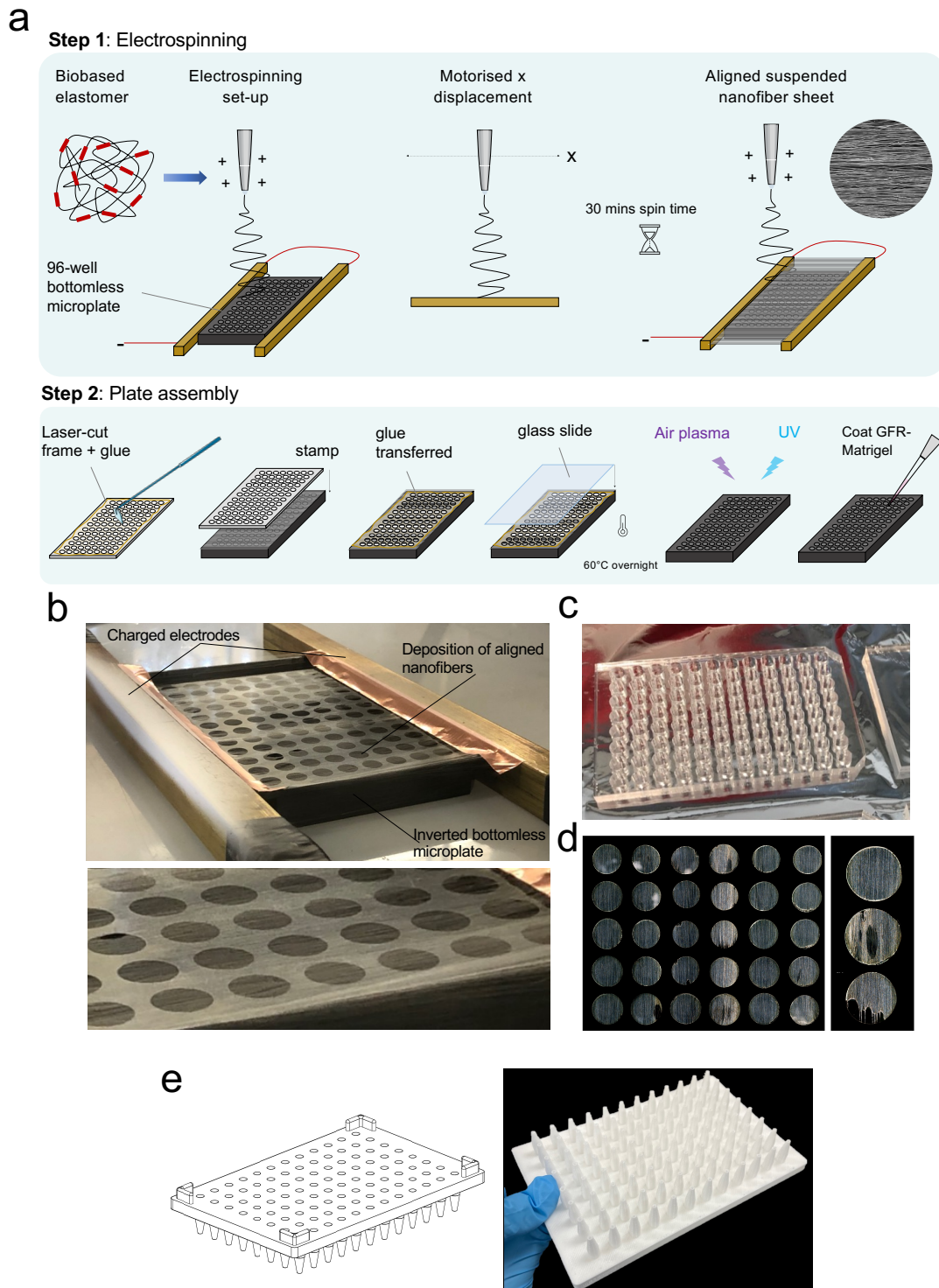


Figure 5.5. Manufacturing suspended biobased elastomer nanofiber scaffolds in 96-well imaging plates.

A, Schematic outlining the manufacturing process. In step 1 elastomer nanofibers are electrospun onto bottomless 96-well microplates. In step 2 glass bottoms are attached to the plates, plasma treated and coated with GFR-matrigel. **B**, Manufacture of custom built

96-well plates. Aligned nanofibers deposited on bottomless-96-well plate between two charged electrodes. **C**, Acrylic stamp used to glue glass base to plate. **D**, Examples of different nanofiber wells in a 96-well plate. The majority of wells had uniform alignment, whilst some, typically at the edges of the plate, had minor defects. Wells were inspected before use and only uniform wells were seeded with cells. **E**, CAD model and actual 3D printed seeding mask used to rapidly seed neural aggregates at the centre of each elastomer nanofiber well.

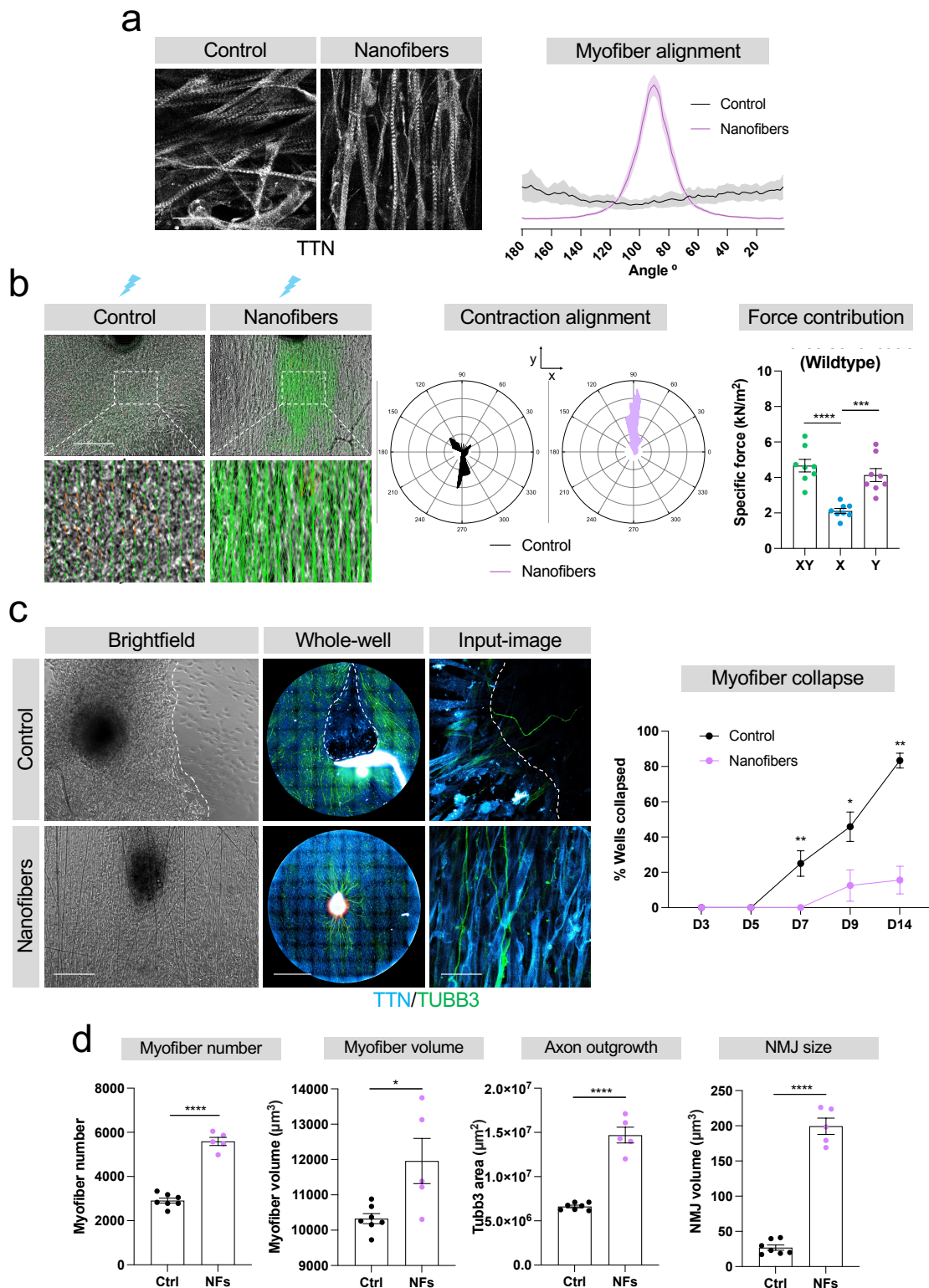


Figure 5.6. Electrospun suspended elastic nanofibers support long term stability, alignment and maturation of contractile myofibers in 96-well neuromuscular co-cultures.

A, Myofiber alignment on control and nanofiber plates (N=1, iN=1, n=8). Immunofluorescence images of TTN staining (Scale bar = 50μm). Alignment quantified using

Fourier transformation. **B**, Myofiber contraction direction based on PIV analysis. Compass plots show angle of contraction against velocity. Calculated peak XY, Y-specific and X-specific forces from PIV velocity values and comparison of XY, Y and X axis contribution to muscle contraction force. **C**, Brightfield, whole well and single field of view images showing examples of collapsed myofiber sheets on control plates vs intact sheets on nanofiber plates. Scale bars: 200 μ m, 2500 μ m, 50 μ m. Quantification of myofiber collapse overtime on control vs nanofiber plates. **D**, Quantification of neuromuscular parameters: myofiber number, myofiber volume, axon outgrowth and NMJ size on control vs nanofiber plates. Error bars represent the SEM, T-test used to ascertain statistical significance. * $p < 0.05$, ** $p < 0.01$, *** $p < 0.001$, **** $p < 0.0001$.

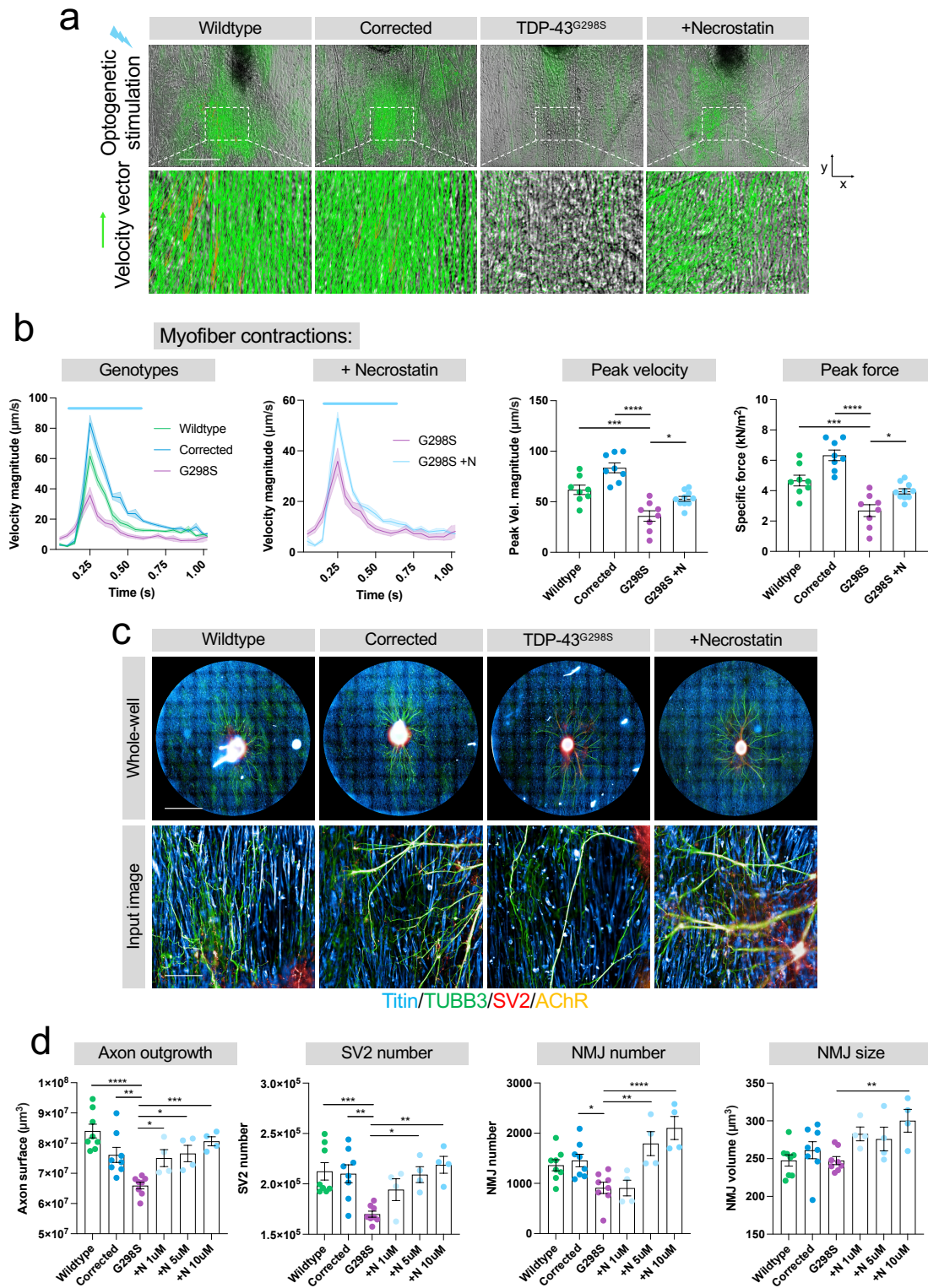
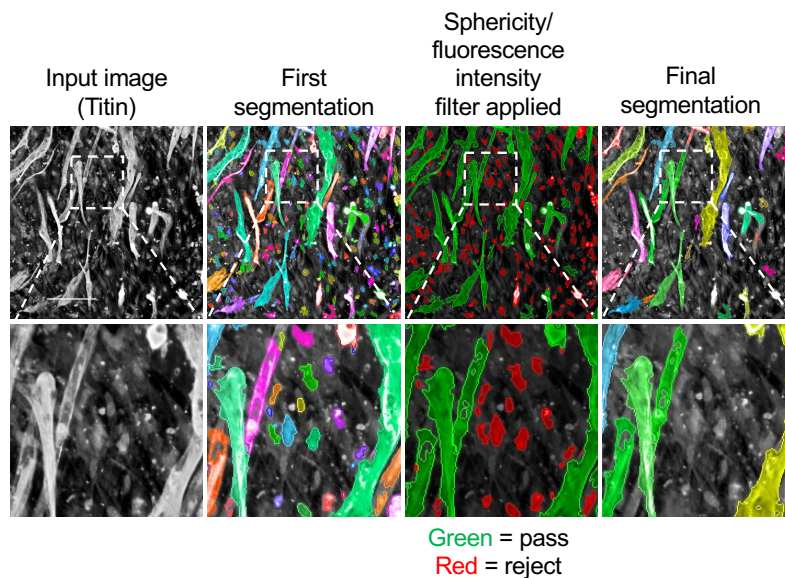


Figure 5.7. Necrostatin rescues ALS-related phenotypes in long-term neuromuscular co-cultures grown on 96-well nanofiber plates.

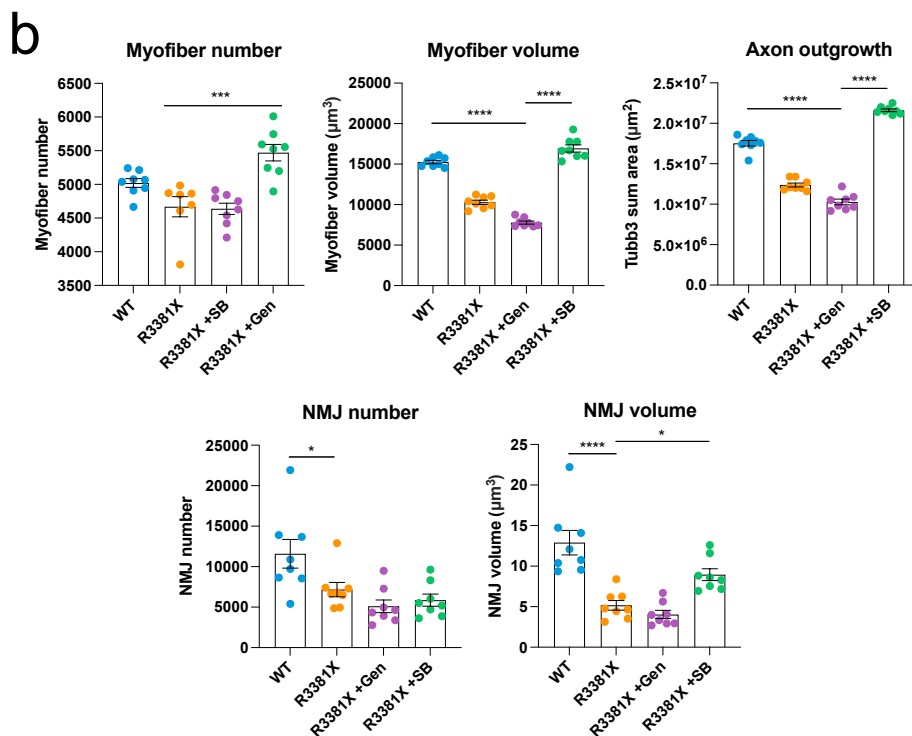
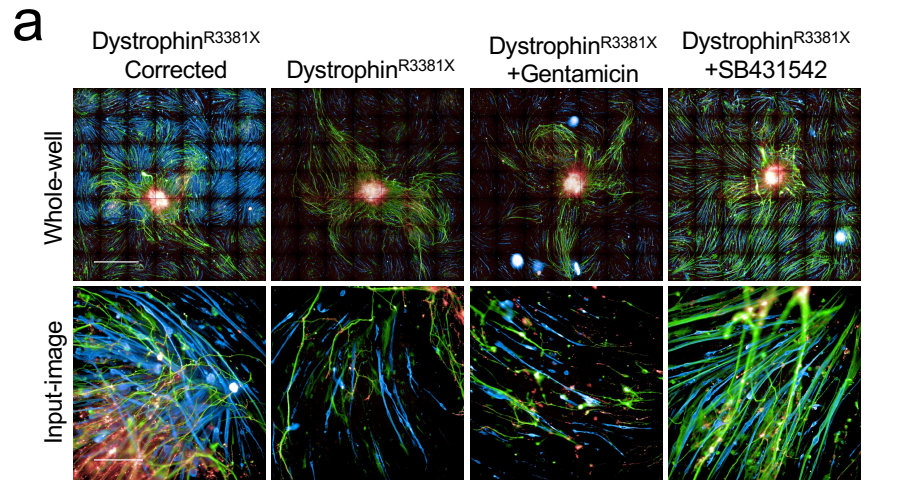
A, PIV analysis of optogenetically evoked myofiber contractions in 96-well neuromuscular co-cultures containing wildtype, TDP-43^{G298S} CRISPR corrected, TDP-43^{G298S} (N=1, iN=1, n=8) and TDP-43^{G298S} +Necrostatin (n=4) treated hiPSC-motor neurons. Scale bar = 200 μ m. **B**,

Quantification of myofiber contractions across different conditions. Contraction peaks for cultures containing wildtype, CRISPR corrected and TDP-43^{G298S} motor neurons. Contraction peaks comparing TDP-43^{G298S} cultures treated with and without necrostatin. Peak velocity values and peak force values. **C**, Whole-well and single field of view images taken using an automated operetta CLS HCI system. Scale bars = 2500 μ m, 200 μ m. **D**, Automated quantification of axon outgrowth, SV2 number, NMJ number and NMJ size across different conditions. Error bars represent the SEM, T-tests and one-way-ANOVA with Dunnet's multiple comparisons used to ascertain statistical significance. * $p < 0.05$, ** $p < 0.01$, *** $p < 0.001$, **** $p < 0.0001$.



Supplementary Figure 5.8. Example of filtering background noise in automated high content image analysis.

A, Input image of titin contains significant background noise. The first segmentation of the myofiber mask picks up this background noise. Subsequently a filter with a cut-off above a certain sphericity and below a certain fluorescence intensity rejects background objects (red) and keeps myofibers (green). The final segmentation mask only segments morphologically distinct myofibers and removes background noise (Scale bar = 200 μ m).



Supplementary Figure 5.9. The TGFβ inhibitor SB431542 partially rescues DMD-related neuromuscular phenotypes.

A, Representative whole-well (Scale bar = 2500μm) and individual 20x field of view (Scale bar = 200μm) images for neuromuscular co-cultures containing wildtype, dystrophin^{R3381X} myofibers and, dystrophin^{R3381X} +gentamicin, dystrophin^{R3381X} +SB431542 conditions (N=1, iN=1, n=8). **B**, Automated high content image analysis quantification of myofiber number, myofiber volume, axon outgrowth, NMJ number and NMJ volume across conditions. Error bars represent the SEM. One-way-ANOVA used to determine statistical significance. *p<0.05, ***p<0.001, ****p<0.0001.

Figure 6.5. Supplementary Movies - QR Codes:



SMovie 6.1.
Myofiber
detachment
control 96-well
plate



SMovie 6.1.
Myofiber stabilised
nanofiber 96-well
plate

Figure 6.6. Supplementary Movies - QR Codes:



SMovie 6.3.
TDP-43^{G298S}
Corrected evoked
contraction (96-well
nanofiber)



SMovie 6.4.
TDP-43^{G298S}
evoked contraction
(96-well nanofiber)



SMovie 6.5.
TDP-43^{G298S}
+Necrostatin
evoked contraction
(96-well nanofiber)

Supplementary Figure 5.10. QR codes for supplementary movies.

Supplementary Movie 6.1. Control plate myofiber collapse (<https://youtu.be/xk6Nylzhps0>). **Supplementary Movie 6.2.** Nanofiber plate no myofiber collapse (<https://youtu.be/vCA2uHpEcdc>). **Supplementary Movie 6.3.** TDP-43G298S Corrected evoked contraction (96well - nanofiber) (https://youtu.be/F8Xu8nANR_Q). **Supplementary Movie 6.4.** TDP-43G298S evoked contraction (96-well nanofiber) (<https://youtu.be/R1bzB00Cwvs>). **Supplementary Movie 6.5.** TDP-43G298S +Necrostatin evoked contraction (96-well nanofiber) (https://youtu.be/erynZ_hUy5s)

5.8 Discussion

This chapter describes the development of a high-throughput 96-well human iPSC-neuromuscular co-culture platform and automated high content image analysis pipeline to quantify human neuromuscular disease phenotypes. This represents a step toward a scalable drug screening assay that could be used to screen hundreds to thousands of small molecules

to identify novel treatments aimed at targeting peripheral pathological events in various neuromuscular diseases such as ALS or DMD.

The approach developed here is more scalable, rapid and amenable to automation than any human iPSC-derived neuromuscular co-culture platform previously developed, including our own compartmentalised microdevice (Chapter 3,4), (Machado et al. 2019, Osaki et al. 2018, Uzel et al. 2016, Abd Al Samid et al. 2018, Dittlau et al. 2021, Martins et al. 2020). Although some previous studies have developed 96-well myogenic only cultures for longitudinal study of muscle strength (Afshar et al. 2020). The fact that the neuromuscular co-cultures developed here were grown in 96-well imaging plates meant it was possible to use an Operetta CLS high content image analysis system to automatically image the entire plate and quantify neuromuscular parameters such as: myofiber number and morphology (based on Titin), axon outgrowth (based on TUBB3), pre- and post-synaptic structures (SV2 and AChR), and colocalization of these structures to infer neuromuscular synapse number and morphology (Figure 5.1). Typically, an entire 96-well plate took between 3-6 hours to image and would generate up to 100,000 images and 300Gb worth of data that could then be automatically analysed using a high content image analysis pipeline in Harmony in around 2 hours. This was substantially faster than the image acquisition and analysis of the compartmentalised neuromuscular co-culture in chapters 3 & 4, which would take a similar amount of time of manual confocal imaging and analysis in Imaris/ImageJ to analyse a mere fraction of the conditions. While the segmentation masks were not perfect a significant degree of care was taken to use fluorescence intensity and morphological classifiers to filter out background noise and non-specific staining (S Figure 5.8). Finally, owing to technical constraints, i.e. lack of specialist equipment, it was not possible to automate the myofiber contraction recordings and analysis – all of which were carried out manually as in chapters 3 & 4 (Figure 5.2). Despite this it would in theory be possible to do this using more recent high content image analysis systems by PerkinElmer that can carry out high-speed video recording. In future it may also be possible to combine PIV analysis matlab scripts into a custom pipeline within Harmony so that contraction analysis and NMJ high content image analysis could be combined. This would make it possible to correlate areas of high contractility with areas of high axon outgrowth or neuromuscular synapse formation and look for discrepancies between the two. Alternatively, Ca²⁺ imaging could be used to live image neuromuscular

transmission. For example, several genetically encoded acetylcholine indicators have recently been developed that could be used to achieve this (Jing et al. 2018, Xia et al. 2021).

Using this co-culture platform, it was possible to automatically quantify contrasting neuromuscular disease phenotypes by incorporating hiPSC-motor neurons from patients with ALS (Figure 5.3) and by incorporating hiPSC-myofibers from patients with Duchenne muscular dystrophy (DMD) (Figure 5.4). This highlights the versatility of this approach to model distinct neuromuscular diseases. Encouragingly similar ALS-related phenotypes were observed in this co-culture platform as those that had been observed in the compartmentalised microdevice platform (Chapter 4), and necrostatin was shown to improve neuromuscular phenotypes as demonstrated in Chapter 3. Furthermore necrostatin also improved DMD-related phenotypes (Figure 5.4), which is interesting since necroptosis has been implicated in muscle degeneration in various muscular dystrophies (Morgan et al. 2018). This possibly highlights RIPK1 as an even broader target for the treatment of contrasting neuromuscular diseases that differ in disease mechanism and cell types affected. Interestingly, the high content image analysis also revealed the occurrence of muscle-related phenotypes in the ALS co-cultures and axon outgrowth related phenotypes in the DMD co-cultures – highlighting how non-cell autonomous effects of diseased cell types can more broadly impact the neuromuscular circuit as a whole. This was evidenced quite nicely by the work carried out with our collaborators Amaia Paredes and Yung-Yao Lin on DMD (Paredes-Redondo et al. 2021). Here it was found that the dystrophin^{R3381X} mutation caused reduced expression of axon guidance genes such as Slit2, Slit3, Robo – possibly explaining the reduced axon outgrowth observed in the co-cultures. Furthermore it was found that TGF β inhibition could rescue expression of these genes and axon outgrowth (Paredes-Redondo et al. 2021) (S Figure 5.9). It's possible that similar mechanisms also account for the reduction in myofibers observed in the ALS-related co-cultures. Indeed, perturbed expression of axonal and synaptic genes was observed in the bulk RNA-sequencing data, which may impact axonal trophic support for the myofibers (Figure 5.4).

Finally, this chapter demonstrates a novel approach to stabilise contractile neuromuscular co-cultures in 96-well culture formats using suspended electrospun elastomer nanofibers previously developed in (Cheesbrough et al.). Stabilising contractile myofibers *in vitro* is a

major obstacle for *in vitro* disease modelling and drug screening for neuromuscular diseases. Without mechanical support myofibers will detach from 2D tissue culture surfaces following contraction (Figure 5.6) (Abd Al Samid et al. 2018), making longitudinal studies difficult as well as precluding contraction based phenotypic assays. A number of studies have used cantilevers to support bundles of contractile myofibers *in vitro* (Uzel et al. 2016, Osaki et al. 2018) and also in 96-well assay plates (Afshar et al. 2020). However suspended bundles of myofibers are difficult to image and require additional tissue processing to carry out immunofluorescence staining, precluding high content image analysis. A number of studies have developed electrospun aligned nanofiber scaffolds to support contractile cardiomyocytes in 2D (Ding et al. 2020). However previous systems have used rigid nanofibers, which have been shown to exhibit material stiffness (Sheets et al. 2013) and not necessarily support myofiber contractions in a dynamic way. The method developed here and initially in (Cheesbrough et al.) was to suspend the nanofibers across the well so that they could dynamically stretch and contract with the contracting myofibers owing to the elastic properties of the biobased elastomer. Using this approach 96-well neuromuscular co-cultures were stable for much longer periods and showed improved myofiber stability compared to control plates. Furthermore, the nanofibers supported alignment, contraction and maturation of the myofibers. In future work it would be interesting to see if this approach could be further miniaturised into 384-well plate formats to further increase the throughput. In theory this should be feasible although precise loading of the neural spheroids at this scale could be problematic and require robotic precision.

Taken together this chapter shows that human iPSC derived neuromuscular co-cultures can be grown in a high throughput 96-well plat format, allowing automated high content image analysis of distinct neuromuscular disease phenotypes. Furthermore, suspended aligned elastomer nanofibers can support long-term culture of contractile myofibers in this format. Future work should seek to carry out small molecule screens using this platform to identify novel compounds aimed at targeting peripheral neuromuscular phenotypes in ALS and DMD. Furthermore, future work should aim to incorporate muscle contraction readout into the automated analysis pipeline rather than having to be carried out manually.

6. Pathogenic TDP-43^{G298S} disrupts neuronal excitability and axon initial segment structure and plasticity

6.1 Hypothesis and aims

This chapter investigates the mechanisms contributing to abnormal excitability in TDP-43^{G298S} motor neurons. This follows from the increased spontaneous motor unit activity observed in chapter 4. Using a combination of confocal imaging and whole-cell patch clamp electrophysiology the effects of TDP-43^{G298S} mutations on neuronal excitability as well as AIS structure and plasticity were investigated. The following aims and hypotheses were set:

1. Does TDP-43^{G298S} impact intrinsic neuronal excitability?
2. Does TDP-43^{G298S} impact AIS structure?
3. Does TDP-43^{G298S} impact AIS plasticity?
4. What are the transcriptional changes associated with altered AIS structure, plasticity and neuronal excitability?
5. How do AIS and electrophysiological parameters change over the course of motor neuron maturation?

As previously discussed, indicative statistics have been performed on these single lines, in line with similar studies characterising single ALS-related hiPSC lines in neuromuscular co-cultures (Osaki et al. 2018) and using electrophysiology (Devlin et al. 2015), despite the true biological N being 1. To make this clear, biological replicates (separate hiPSC lines) are denoted as (N), induction replicates (complete differentiations from hiPSCs) are denoted as (iN) and technical replicates, such as recordings from individual neurons, neuromuscular co-cultures or coverslips are denoted as (n).

6.2 TDP-43^{G298S} causes hyperexcitability in early (6 week) motor neurons

Since the neuromuscular co-cultures harbouring TDP-43^{G298S} motor neurons displayed increased spontaneous activity, whole-cell patch clamp recordings were made of single motor neurons to characterise their intrinsic excitability. To do this, MACS enriched hiPSC-motor neurons were cultured on MACS enriched mESC-Astrocytes and grown for 2 weeks so they

were at an equivalent maturation stage as in the neuromuscular co-cultures. From the start of hiPSC-differentiation this meant they were 6-week-old motor neurons (Figure 6.1a). When carrying out whole-cell patch clamp recordings, motor neurons were distinguished from the supporting astrocytes by morphology and CHR2-YFP expression (Figure 6.1b). Current clamp recordings showed that the ALS-related pathogenic TDP-43^{G298S} mutation caused a significant reduction in the current threshold for AP-spiking with an average threshold of 44.29pA (SE ± 4.0, n=28) compared to 71.43pA (SE ± 10.47, n=21, One-way-ANOVA with Dunnet's test p=0.014) in the wildtype and 65.36pA (SE ± 6.14, One-way-ANOVA with Dunnet's test p=0.045) in the corrected conditions (Figure 6.1c). Furthermore TDP-43^{G298S} caused a significant upward shift in the relationship of injected current to AP firing (Figure 6.1d) (Repeated one-way-ANOVA with Dunnet's test: TDP-43^{G298S} n=28 vs. Wildtype n=21 p=0.026, TDP43^{G298S} vs. corrected n=25 p=0.083). This led to an overall increase in the maximum firing frequency at 10.65Hz (SE ± 1.62, n=28) compared to 3.25Hz (SE ± 0.56, n=21, One-way-ANOVA with Dunnet's test p=0.0003) in the wildtype and 4.52Hz (SE ± 1.13, n=28, One-way-ANOVA with Dunnet's test p=0.0012) in the corrected conditions (Figure 6.1d). Similarly, TDP-43^{G298S} also caused an increase in the spontaneous firing frequency at 1.03Hz (SE ± 0.43, n=8) compared to 0.1Hz (SE ± 0.05, n=4) in the wildtype and 0.07Hz (SE ± 0.01, n=4, Mann-Whitney U p=0.022) in the corrected conditions. In voltage clamp recordings it was found that TDP-43^{G298S} caused an increase in the minimum fast inward currents (putative Na⁺ currents – see Figure 6.7c) and a modest increase in the average steady state outward currents (putative K⁺ currents) (Figure 6.1f). Furthermore, current clamp recordings showed that TDP-43^{G298S} modified AP properties – increasing AP amplitude and rate of rise, while reducing the AP half-width. Other passive electrophysiological properties, such as membrane resistance, capacitance and resting voltage were comparable across culture conditions (S Table 6.1)

6.3 TDP-43^{G298S} causes increased AIS length in early (6 week) motor neurons

Morphological characteristics, including structural changes to the axon initial segment (AIS) have been shown to modulate intrinsic neuronal excitability. To this end, morphological features and structural changes to the AIS, based on Ankyrin-G staining, were measured in 6-week hiPSC-motor neurons grown on GDNF+ mESC-Astrocytes. Most notably TDP-43^{G298S} caused an increase in the length of the AIS – 56.29µm (SE ± 3.46, n=26) compared to 39.37µm

(SE \pm 2.10, n=21, One-way-ANOVA with Dunnett's test p=0.0002) in wildtype and 41.69 μ m (SE \pm 2.56, n=25, One-way-ANOVA with Dunnett's test p=0.0008) in corrected conditions (Figure 6.2b,c). 3D-reconstructions of Ankyrin-G showed that this increased length led to an increase in AIS volume and surface area and was associated with an overall increase in Ankyrin-G fluorescence intensity along the AIS (Figure 6.2d). AIS start position on the other hand was comparable across all culture conditions, as was AIS diameter (Figure 6.2d). Similarly, soma size and the number of dendrites was also comparable across culture conditions (Figure 6.2e). Taken together these results show that TDP-43^{G298S} causes an increase in the length of the AIS.

6.4 TDP-43^{G298S} impairs activity-dependent AIS plasticity and excitability homeostasis in early (6 week) motor neurons

Activity-dependent fine tuning of AIS position and/or length is a mechanism by which neurons modulate their intrinsic excitability. Numerous studies have reported shortening of the AIS in response to elevated activity is associated with a compensatory reduction in excitability (Evans et al. 2015, Sohn et al. 2019, Jamann et al. 2021, Pan-Vazquez et al. 2020, Kuba et al. 2010, Galliano et al. 2021), while other studies have shown a similar homeostatic modulation of excitability associated with a distal relocation of the AIS (Grubb and Burrone 2010a, Wefelmeyer et al. 2015, Lezmy et al. 2017, Hatch et al. 2017). To date, AIS plasticity in human spinal motor neurons has not been investigated, nor the effect of ALS-related pathogenic TDP-43 mutations.

AIS length was strongly reduced in response to short-term optogenetic stimulation in early 6-week hiPSC-motor neurons, while AIS position was unchanged (Figure 6.3a,b). However, although TDP-43^{G298S} motor neurons displayed a modest shortening of the AIS (No stimulation: 56.29 μ m SE \pm 3.46, n=26; Plus stimulation: 46.51 μ m SE \pm 3.136, n=21, Two-way-ANOVA with Tukey's test p=0.126), the mean change in length (Δ L) was less pronounced (Δ L - 9.776 μ m \pm 4.770) than in wildtype (No stimulation: 39.37 μ m SE \pm 2.09, n=21; Plus stimulation: 19.65 μ m SE \pm 2.12, n=21, Two-way-ANOVA with Tukey's test p<0.0001; Δ L -19.72 μ m \pm 2.974) and corrected conditions (No stimulation: 41.69 μ m SE \pm 2.56, n=25; Plus stim: 22.56 μ m SE \pm 2.69, n=21, Two-way-ANOVA with Tukey's test p<0.0001; Δ L -19.14 μ m \pm 3.726). As a result,

the mean difference in AIS length already present in baseline conditions ($14.60\mu\text{m} \pm 4.329$) was even more pronounced after stimulation ($23.96\mu\text{m} \pm 4.129$). Since paired measurements were not made owing to the lack of live AIS-labelling, statistics have not been performed on the ΔL measurements. In conjunction with this, the current threshold for AP spiking was significantly increased in the CRISPR-corrected motor neurons in agreement with a shortening of the AIS following optogenetic stimulation (No stimulation: $65.36\text{pA SE} \pm 6.14$, $n=28$; plus stimulation $94\text{pA SE} \pm 10.6$, $n=20$, Two-way-ANOVA with Tukey's test $p=0.0209$). Conversely, TDP-43^{G298S} motor neurons did not show a statistically significant increase in current threshold following optogenetic stimulation (No stimulation: $44.29\text{pA SE} \pm 3.9$ $n=28$; Plus stimulation: $59.41\text{pA SE} \pm 7.35$ $n=17$, Two-way-ANOVA with Tukey's test $p=0.4521$) (Figure 6.6c). Although changes in voltage threshold were not seen, diverging voltage thresholds across genotypes following optogenetic stimulation were observed; in this instance TDP-43^{G298S} motor neurons displayed a lower voltage threshold relative to CRISPR-corrected motor neurons, further contributing to neuronal hyperexcitability (TDP-43^{G298S} +Stim: $-29.4\text{mV SE} \pm 1.69$, $n=17$; TDP-43^{G298S} Corrected: $-23.47\text{mV SE} \pm 1.98$, $n=14$, T-test $p=0.029$) (Figure 6.3c). Finally, a significant downward shift in the relationship between injected current and AP spiking was observed in the corrected motor neurons but not in the TDP-43^{G298S} motor neurons (Figure 6.3d). Again, these differences in excitability could not be explained by changes in passive electrical properties (S Table 6.1). Taken together these results suggest AIS plasticity is reduced in TDP-43^{G298S} motor neurons, a feature that further contributes to dysregulation of neuronal excitability.

6.5 TDP-43^{G298S} causes differential expression of AIS and synaptic genes in early (6 week) motor neurons

To uncover potential molecular mechanisms by which TDP-43^{G298S} drives changes in AIS structure, plasticity and neuronal excitability, bulk RNA sequencing and differential gene expression analysis was performed on corrected and TDP-43^{G298S} samples taken at 6-weeks. Principle component analysis showed distinct clustering of the TDP-43^{G298S} and corrected samples (S Figure 6.1a). Overall, 469 genes were differentially expressed (Log2FoldChange >1.5 in either direction, adjusted p -value <0.05), of which 73% were expressed higher in the corrected condition (S Figure 6.1b). Top enriched GO terms upregulated in the TDP-43^{G298S}

conditions included calcium channel activity and ion channel activity, while top enriched GO terms upregulated in corrected conditions included muscle structure development and actin-myosin filament sliding.

TARDBP expression was lower in TDP-43^{G298S} motor neurons than in corrected neurons, and neurofilament heavy chain expression was higher in TDP-43^{G298S} motor neurons than corrected controls (Figure 6.4a). Both are expected molecular hallmarks of ALS. Differential expression of AIS genes (>1.3 Log2FoldChange in either direction) showed upregulation of the voltage gated sodium channel alpha subunit 1 – NAV1.1 (*SCN1A*) and voltage gated potassium alpha subunit – Kv1.1 (*KCNA1*) as well as upregulation of the neural cell adhesion molecule (NRCAM) enriched at the AIS (Figure 6.4b). Furthermore, there was downregulation of genes involved in AIS plasticity including the L-type calcium channel Cav1.1 (*CACNA1S*) and the Ca²⁺/calmodulin-dependent protein kinase II (*CAMK2*), (Figure 5.4b). Furthermore, there was significant differential expression for the GO terms “axon + synapse” and “motor neuron” (Figure 6.4c). Taken together these results show downregulation of *TARDBP* in the TDP-43^{G298S} motor neurons is associated with upregulation of voltage-gated sodium and potassium channels that are enriched at the AIS, and downregulation of genes involved in AIS plasticity – hinting at possible molecular mechanisms driving the altered AIS structure and plasticity previously observed. It should be noted however that the upregulation of muscle-related genes in the corrected samples (S Figure 6.9b) indicates a possible myogenic contamination in the cultures and as such these results are interpreted with caution.

6.6 TDP-43^{G298S} causes AIS shortening, hypoexcitability and impaired plasticity in late (10 week) motor neurons

Neuronal excitability has been shown to change over the course of ALS in both patient, animal and human iPSC studies. To this end AIS length and plasticity were measured alongside whole-cell patch clamp recordings of late (10-week) hiPSC-motor neurons cultured on GDNF+ mESC-astrocytes. At this later-stage TDP-43^{G298S} caused a relative shortening of the AIS - 32.35µm (SE ± 1.55, n=25) relative to 46.59µm (SE ± 3.10, n=25, T-test p=0.0002) in corrected controls (Figure 6.5a,b). Whole-cell patch clamp recordings also showed that TDP-43^{G298S} caused a corresponding downward shift in the relationship of injected current to AP firing, as well as a

reduction in maximum firing frequency from 20.4Hz (SE \pm 2.15, n=20) in corrected controls to 8.48Hz (SE \pm 1.79, n=21, T-test p=0.0001) in TDP-43^{G298S} conditions (Figure 6.5c,d). TDP-43^{G298S} also caused a significant reduction in putative Na⁺ and K⁺ currents at this later stage (Figure 6.5e). Furthermore, activity-dependent AIS length plasticity was now completely abolished in TDP-43^{G2398S} motor neurons at this later stage (No stimulation: 32.35 μ m SE \pm 1.55, n=25, Plus stim: 30.49 μ m SE \pm 1.61, n=25, Two-way-ANOVA with Tukey's test p=0.9328) (Figure 6.5f), while corrected control neurons were able to reduce the length of the AIS in response to short-term optogenetic stimulation (No stimulation: 46.59 μ m SE \pm 3.09, n=25; Plus stimulation 34.97 μ m SE \pm 2.2, n=25, Two-way-ANOVA with Tukey's test p=0.0018). Interestingly, at this later time-point all motor neurons showed a distal relocation of the AIS in response to optogenetic stimulation (Figure 6.5f). This occurred in both TDP-43^{G298S} and CRISPR-corrected neurons. Taken together this data shows that pathogenic TDP-43^{G298S} triggers an abnormal switch from hyper to hypoexcitability, which is accompanied by shortening and impaired plasticity of the AIS.

6.7 Changes in axon initial segment properties overtime

Since TDP-43^{G298S} had produced contrasting structural phenotypes at the AIS at different timepoints, the next objective was to track and compare how AIS and morphological characteristics of the motor neurons changed over the course of maturation. To do this MACS enriched hiPSC-motor neurons were cultured on MACS enriched GDNF+ mESC-astrocytes and samples fixed and stained for ankyrin-g at 6-, 8- and 10-week timepoints. Data was obtained from independent populations and not longitudinal analysis of the same cells. As previously described, TDP-43^{G298S} caused an increase in the length of the AIS at the early 6-week timepoint, and conversely a shortening of the AIS at the later 10-week timepoint. At the mid 8-week timepoint AIS length was comparable between TDP-43^{G298S} and corrected conditions (Figure 6.6a,b,c). In conjunction with this, AIS start position from the soma was reduced over the course of maturation from 27.68 μ m (SE \pm 3.32, n=25) at the 6-week timepoint to 8.11 μ m (SE \pm 2.04, n=25) at the 10-week timepoint in the corrected conditions. TDP-43^{G298S} had no effect on AIS start position at any timepoint. Conversely AIS diameter moderately increased over the course of maturation from 1.80 μ m (SE \pm 0.06, n=25) at the 6-week timepoint to 2.15 μ m (SE \pm 0.08, n=25) at the 10-week timepoint in the corrected conditions. Again TDP-

43^{G298S} had no effect on AIS diameter at any timepoint. Soma size more than doubled over the course of maturation from 648.32 μm^2 (SE \pm 52.17, n=25) at the 6-week timepoint to 1944.36 μm^2 (SE \pm 120.06, n=25) at the 10-week timepoint in the corrected conditions. TDP-43^{G298S} had no effect on soma size at any timepoint. Finally, the number of dendrites also dramatically increased over the course of maturation, from 13.72 (SE \pm 0.62, n=25) at the 6-week timepoint to 24.89 (SE \pm 1.35, n=25) at the 10-week timepoint. Again TDP-43^{G298S} had no effect on the number of dendrites at any timepoint. Taken together these results show that the ALS-related pathogenic TDP-43^{G298S} mutation has a specific effect on AIS length over the course of maturation. At the early 6-week timepoint TDP-43^{G298S} causes AIS extension, while conversely at the later 10-week timepoint TDP-43^{G298S} causes AIS shortening. All other AIS parameters including start position and diameter were comparable at all stages. Furthermore, other morphological parameters, including soma size and the number of dendrites were comparable at all stages. In general, the reduction in AIS start position, and the increase in AIS diameter, soma size and number of dendrites indicates comparable morphological maturation overtime for both TDP-43^{G298S} and corrected motor neurons.

6.8 Changes in electrophysiological properties overtime

Since TDP-43^{G298S} had produced contrasting electrophysiological phenotypes at different timepoints, the next objective was to track and compare how electrophysiological characteristics of the motor neurons changed over the course of maturation. Here, data was obtained from independent populations and not longitudinal analysis of the same cells. In general motor neurons from both TDP-43^{G298S} and corrected conditions exhibited electrophysiological maturation between the 6- and 10-week timepoints. Passive properties indicated maturation: for example, there was an increase in capacitance, roughly proportional to cell size (S Table 6.1,2) and a decrease in resistance (S Table 6.1,2), inversely proportional to the quantity of ion channels. Neurons also exhibited a robust transition to mature repetitive firing patterns. In corrected conditions only 3.23% of neurons were capable of repetitive firing at the 6-week timepoint. This increased to 60% at the 10-week timepoint. TDP-43^{G298S} motor neurons initially showed a similar trend, increasing from 9.68% at the 6-week timepoint to 34.48% at the 8-week timepoint, however this dropped down again at the later 10-week timepoint to 14.29% (Figure 6.7a). In the corrected conditions there was also a

linear increase in the amplitude of the minimum fast inward (putative Na⁺) currents and average steady state outward (putative K⁺) currents. Inward currents increased from 1519pA (SE ± 145.13) at the 6-week timepoint to 7442.47pA (SE ± 389.20) at the 10-week timepoint and K⁺ currents increased from 3984.28pA (SE ± 237.33) at the 6-week timepoint to 6647.52pA (SE ± 238.84) at the 10-week timepoint (Figure 6.7b,c). For the TDP-43^{G298S} conditions there was an initial increase in the inward and outward currents from 6- to 8-weeks, however both currents dropped at the later 10-week timepoint (Figure 6.7b,c). Action potential (AP) parameters also showed significant maturation between 6- and 10-weeks. In corrected conditions AP-amplitude increased from 43.07mV (SE ± 3.15) at the 6-week timepoint to 79.60mV (SE ± 2.83) at the 10-week timepoint. TDP-43^{G298S} motor neurons also showed an initial increase in AP amplitude from 58.07mV (SE ± 3.36) at the 6-week timepoint to 72.56mV (SE ± 3.23) at the 8-week timepoint, however this dropped at the 10-week timepoint to 59.28mV (SE ± 5.10) (Figure 6.7d,e). AP rate of change also increased in the corrected conditions from 0.39mV/ms (SE ± 0.06) at the 6-week timepoint to 2.30mV/ms (SE ± 0.29) at the 10-week timepoint. TDP-43^{G298S} motor neurons showed an initial increase in rate of change from 0.847mV/ms (SE ± 0.11) at the 6-week timepoint to 1.5mV/ms (SE ± 0.17) at the 8-week timepoint, however this again dropped at the 10-week timepoint to 1.13mV/ms (SE ± 0.20) (Figure 6.7d,e). AP half-width decreased in the corrected conditions from 6.12ms (SE ± 0.44) at the 6-week timepoint to 2.64ms (SE ± 0.28) at the 10-week timepoint, while the half-width in the TDP-43^{G298S} motor neurons remained relatively similar at 3.95ms (SE ± 0.37) at the 6-week timepoint and 3.77ms (SE ± 1.42) at the 10-week timepoint (Figure 6.7d,e). Taken together this data shows that corrected motor neurons show considerable electrophysiological maturation between 6- and 10 weeks, while TDP-43^{G298S} motor neurons show initially similar electrophysiological maturation between 6- and 8-weeks but an overall decline by 10-weeks.

6.9 TDP-43 pathology in early (6-week) and late (10-week) motor neurons

TDP-43 pathology, characterised by loss of nuclear TDP-43 and abnormal cytoplasmic aggregation, is seen in the vast majority of patients with ALS. To this end hiPSC-motor neurons were immunostained for TDP-43 and nuclear and cytoplasmic fluorescence intensities quantified. In the early 6-week motor neurons there was limited evidence of TDP-43

pathology, with TDP-43^{G298S} and corrected motor neurons displaying similar levels of nuclear and cytoplasmic TDP-43, while wildtype motor neurons did show slightly higher levels of both (Figure 6.8a,b). TDP-43^{G298S} neurons had an average nuclear intensity of 10547 (SE ± 604.9), corrected motor neurons 11029 (SE ± 605.2) and wildtype neurons 14044 (SE ± 1099). TDP-43^{G298S} neurons had an average cytoplasmic intensity of 10916 (SE ± 1311), corrected motor neurons 5910 (SE ± 506.9) and wildtype neurons 10916 (SE ± 1311). Cytoplasmic to nuclear ratio of TDP-43 was comparable for all cell lines, with TDP-43 predominantly residing in the nucleus for all lines. TDP-43^{G298S} motor neurons showed a cytoplasmic/nuclear ratio of 0.59 (SE ± 0.06), corrected motor neurons a ratio of 0.55 (SE ± 0.05) and wildtype neurons a ratio of 0.76 (SE ± 0.10).

Interestingly however there was evidence of TDP-43 pathology in the TDP-43^{G298S} motor neurons at the later 10-week timepoint (Figure 6.8c,d). TDP-43^{G298S} motor neurons showed a loss of nuclear TDP-43 15590 (SE ± 1923) compared to 23602 (SE ± 1688) in the corrected neurons and 23039 (SE ± 1992) in the wildtype neurons. Conversely TDP-43^{G298S} motor neurons showed a modest increase in cytoplasmic TDP-43 19348 (SE ± 3429) compared to 14197 (SE ± 1179) in the corrected neurons and 12442 (SE ± 2208) in the wildtype neurons. Furthermore, the ratio of cytoplasmic to nuclear TDP-43 had also shifted in the TDP-43^{G298S} neurons to a point where there was more cytoplasmic TDP-43 than nuclear TDP-43. TDP-43^{G298S} motor neurons showed a cytoplasmic to nuclear ratio of 1.22 (SE ± 0.18), while corrected neurons showed a ratio of 0.63 ± 0.06 and wildtype neurons a ratio of 0.55 (SE ± 0.09). However, no evidence of cytoplasmic aggregates was observed. Taken together these results suggest that overt TDP-43 protein pathology becomes evident in the TDP-43^{G298S} motor neurons at the later 10-week timepoint but not at the early 6-week timepoint.

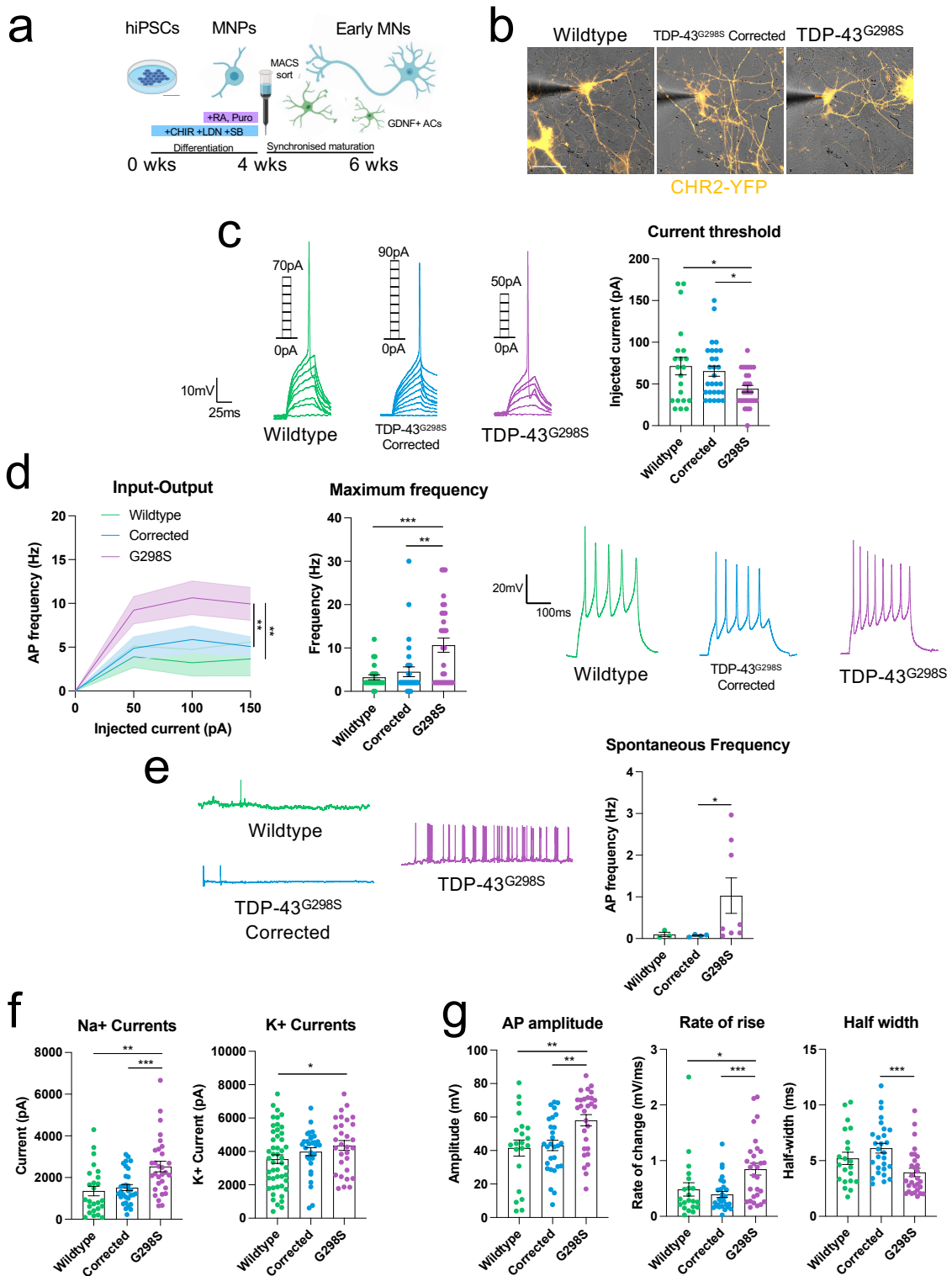


Figure 6.1. Pathogenic TDP-43^{G298S} causes hyperexcitability in early MNs.

A, Schematic of hiPSC-motor neuron differentiation, MACS enrichment and maturation on GDNF+ mESC-astrocytes. **B**, Brightfield images showing whole-cell patch clamp recordings of 6-week CHR2-YFP positive wildtype (N=1, iN=3, n=21), CRISPR corrected (N=1, iN=3, n=28) and TDP-43^{G298S} (N=1, iN=3, n=28) MNs. Scale bar = 50 μ m. **C**, Current threshold for

AP firing and representative single AP traces taken from current clamp recordings. **D**, Relationship between injected current and firing frequency and maximum evoked AP firing frequency taken from current clamp recordings. **E**, Spontaneous AP firing frequency taken from passive membrane recordings of all spontaneously firing neurons. **F**, Voltage clamp recordings of minimum fast inward (Na⁺ currents) and average steady state outward (K⁺) currents. **G**, Current clamp recordings showing single AP properties. Error bars represent the SEM. One-way ANOVA (+with repeated measures for D) test with Dunnett's comparison used to determine statistical significance, except 2d: Mann-Whitney test. * $p < 0.05$, ** $p < 0.01$, *** $p < 0.001$.

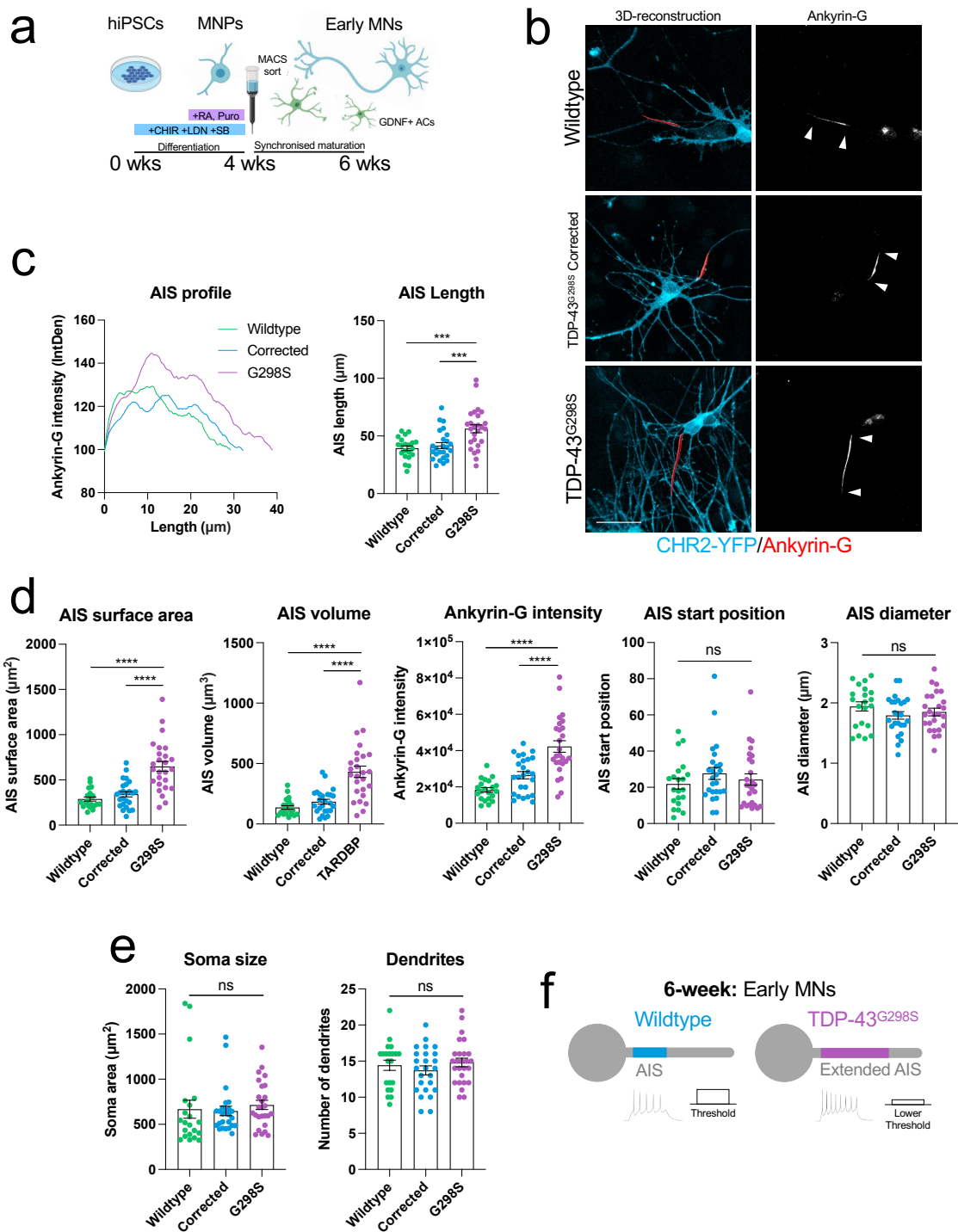


Figure 6.2. Pathogenic TDP-43^{G298S} causes increased AIS length in early MNs.

A, Schematic showing differentiation of hiPSCs into early MNs. **B**, Reconstructions of the AIS (red) in 6-week wildtype (N=1, iN=3, n=21), TDP-43^{G298S} CRISPR-corrected (N=1, iN=3, n=25), TDP-43^{G298S} (n=26) MNs based on ankyrin-G immunofluorescence staining. Counterstained against CHR2-YFP (Cyan). Scale bar = 50μm. **C**, Quantification of the average

ankyrin-G intensity profile along the AIS and total AIS length. **D**, Quantification of AIS surface area, volume, ankyrin-G intensity, AIS start position and AIS diameter across conditions. **E**, Quantification of soma size and number of dendrites across conditions. **F**, Schematic outlining main findings: TDP-43^{G298S} increases AIS length in 6-week early MN cultures. Error bars represent the SEM. One-way ANOVA with Dunnet's comparison used to determine statistical significance. *p<0.05, **p<0.01, ***p<0.001.

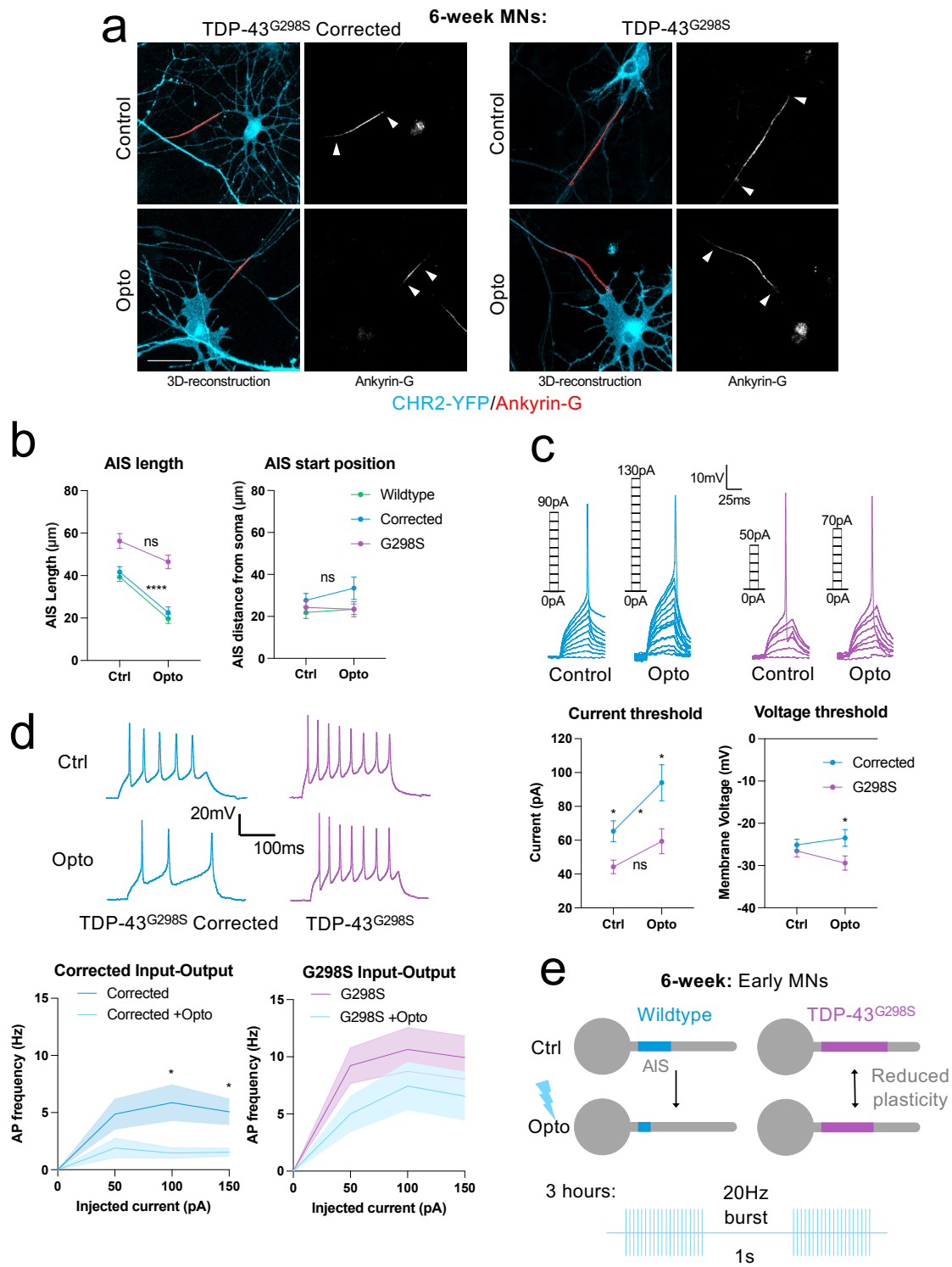


Figure 6.3. Pathogenic TDP-43^{G298S} reduces activity-dependent plasticity of the AIS in early MNs.

A, Reconstructions of the AIS (red) in 6-week wildtype (N=1, iN=3, n=21), TDP-43^{G298S} CRISPR corrected (N=1, iN=3, n=25), and TDP-43^{G298S} (N=1, iN=3, n=26) MNs and with 3 hours 5Hz 488nm optogenetic stimulation: wildtype (n=21), TDP-43^{G298S} CRISPR corrected

(n=21), and TDP-43^{G298S} (n=21) based on ankyrin-G immunofluorescence staining, counterstained against CHR2-YFP (cyan). Scale bar = 50µm. **B**, Quantification of AIS length change and start position in response to optogenetic stimulation. Two-way ANOVA: effect of genotype ****p<0.0001, effect of stimulation ****p<0.0001. Individual p-values from non-parametric, unpaired t-tests. **C**, Whole-cell current clamp recordings showing current and voltage thresholds for 6-week TDP-43^{G298S} CRISPR corrected (n=28), and TDP-43^{G298S} (n=28) MNs and with 3 hours 5Hz 488nm optogenetic stimulation: TDP-43^{G298S} CRISPR corrected (n=20), and TDP-43^{G298S} (n=17). Current threshold two-way ANOVA: effect of genotype **p=0.005, effect of stimulation **p=0.0046, voltage threshold two-way ANOVA: effect of genotype *p=0.025. Individual p-values from non-parametric, unpaired t-tests. Representative single AP traces and current steps. **D**, Relationship between injected current and firing frequency with and without optogenetic stimulation taken from current clamp recordings, representative AP firing traces at 100pA current injection. **E**, Schematic showing reduced activity-dependent length plasticity of the AIS in 6-week early TDP-43^{G298S} MNs and the optogenetic stimulation protocol used. Two-way-ANOVAs with Tukey's multiple comparisons and T-tests with multiple unpaired measures for D were used to ascertain statistical significance. Error bars represent the SEM. *p<0.05, **p<0.01, ***p<0.001, ****p<0.0001.

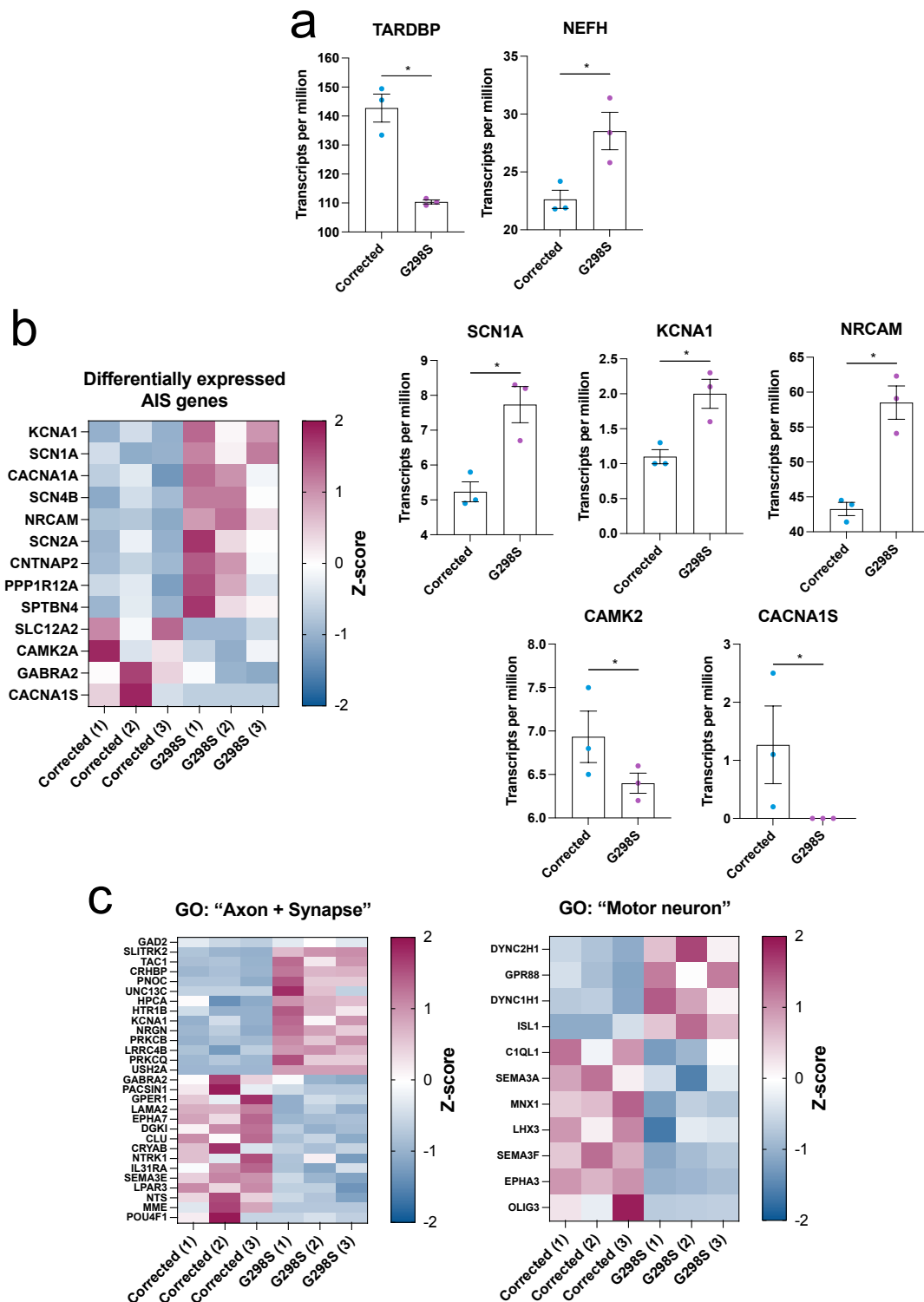


Figure 6.4. TDP-43^{G298S} causes differential expression of AIS and synaptic genes in early (6 week) motor neurons.

A, Differential expression analysis from bulk RNA sequencing of genes known to be differentially expressed in ALS – *TARDBP* and *NEFH*. **B**, Z-Scores showing differential expression of genes that encode proteins enriched at the axon initial segment. Higher

expression (red), lower expression (blue). Transcripts per million for AIS genes: *SCN1A*, *KCNA1*, *NRCAM*, *CAMK2*, and *CACNA1S*. **C**, Additional Z-score differential gene expression analysis for specific gene ontology (GO) search terms “axon + synapse” and “motor neuron”. Error bars represent the SEM, adjusted p-values from DGE analysis shown *p<0.05.

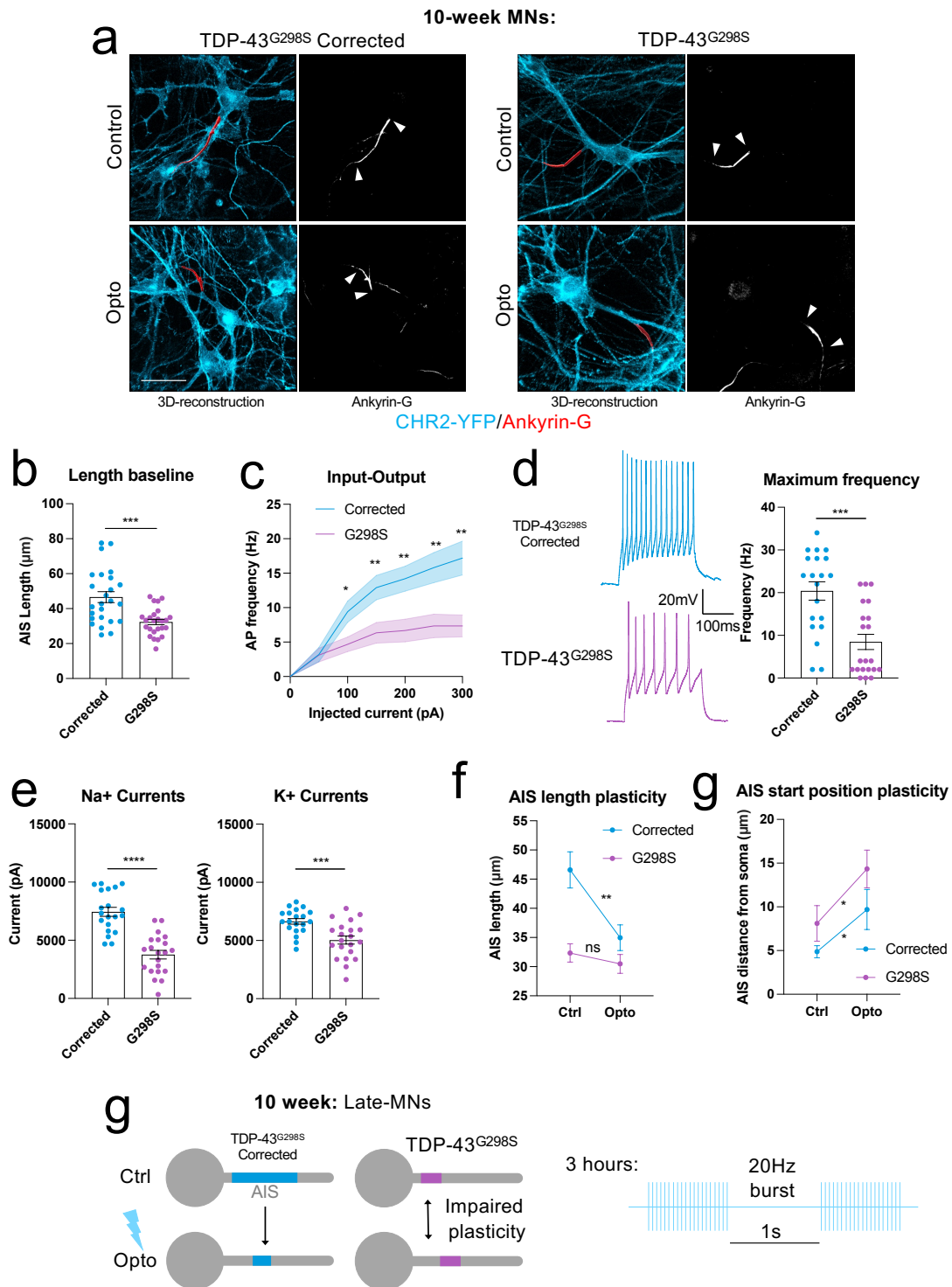


Figure 6.5. Pathogenic TDP-43^{G298S} causes AIS shortening, impaired plasticity, and hypoexcitability in late MNs.

A, Reconstructions of the AIS (red) in 10-week wildtype (N=1, iN=3, n=25), TDP-43^{G298S} CRISPR-corrected (N=1, iN=3, n=25), and TDP-43^{G298S} (N=1, iN=3, n=25) MNs with and without 3 hours 5Hz optogenetic stimulation. Based on ankyrin-G immunofluorescence

staining, counterstained against CHR2-YFP (cyan). Scale bar = 50 μ m. **B**, Quantification of AIS length based on ankyrin-G staining in baseline unstimulated conditions. **C**, Relationship between injected current and firing frequency taken from whole-cell current clamp recordings of 10-week TDP-43^{G298S} CRISPR-corrected (N=1, iN=3, n=20), and TDP-43^{G298S} (N=1, iN=3, n=21) MNs. **D**, Maximum evoked AP firing frequency (Hz) taken from current clamp recordings. **E**, Quantification of AIS length change in response to optogenetic stimulation. Two-way ANOVA: effect of genotype *p<0.04, effect of stimulation **p<0.004, interaction *p<0.029. **F**, Quantification of AIS start position change in response to optogenetic stimulation, measured as start position from the soma. **G**, Schematic showing shortening and impaired plasticity of the AIS in 10-week late TDP-43^{G298S} MNs and the optogenetic stimulation protocol used. T-tests (with multiple unpaired comparisons for C) and Two-way-ANOVAs with Tukey's test used to ascertain statistical significance. Error bars represent the SEM. p-values from non-parametric, unpaired t-tests: *p<0.05, **p<0.01, ***p<0.001.

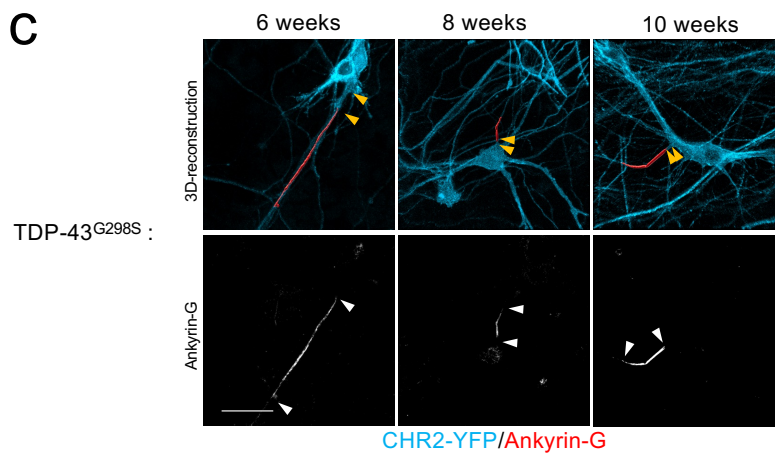
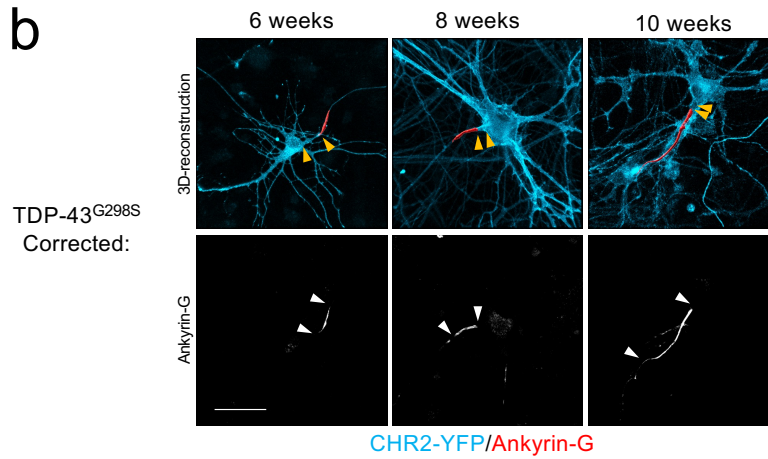
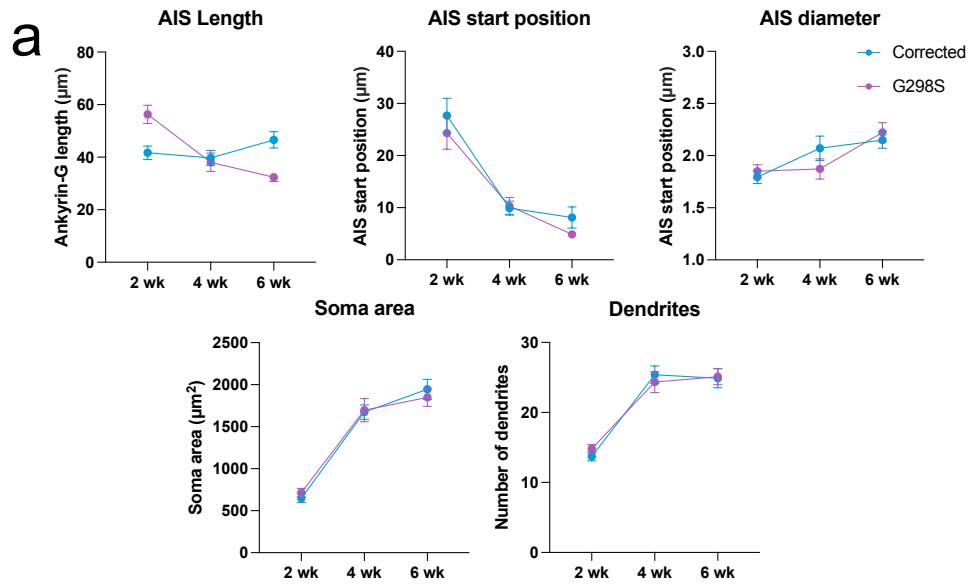


Figure 6.6. Changes in axon initial segment properties overtime.

A, Quantification of AIS length, start position and diameter at 6, 8 and 10 weeks maturation in TDP-43^{G298S} and TDP-43^{G298S} Corrected MNs. **B**, Immunofluorescence images and 3D-reconstructions of the AIS of TDP-43^{G298S} Corrected MNs, based on ankyrin-G staining at 6-, 8- and 10-weeks maturation. White arrows indicate AIS length, yellow arrows indicate AIS start position relative to the soma (Scale bar – 50µm). **C**, Immunofluorescence images and

3D-reconstructions of the AIS of TDP-43^{G298S} MNs, based on ankyrin-G staining at 6-, 8- and 10-weeks maturation. White arrows indicate AIS length, yellow arrows indicate AIS start position relative to the soma. Corrected: 6-weeks (N=1, iN=3, n=25), 8-weeks (N=1, iN=3, n=25), 10-weeks (N=1, iN=3, n=25). TDP=43^{G298S} 6-weeks (N=1, iN=3, n=26), 8-weeks (N=1, iN=3, n= 25), 10-weeks (N=1, iN=3, n=25). Data taken from independent populations and not longitudinal analysis of the same cells. ****p<0.0001 error bars represent the SEM.

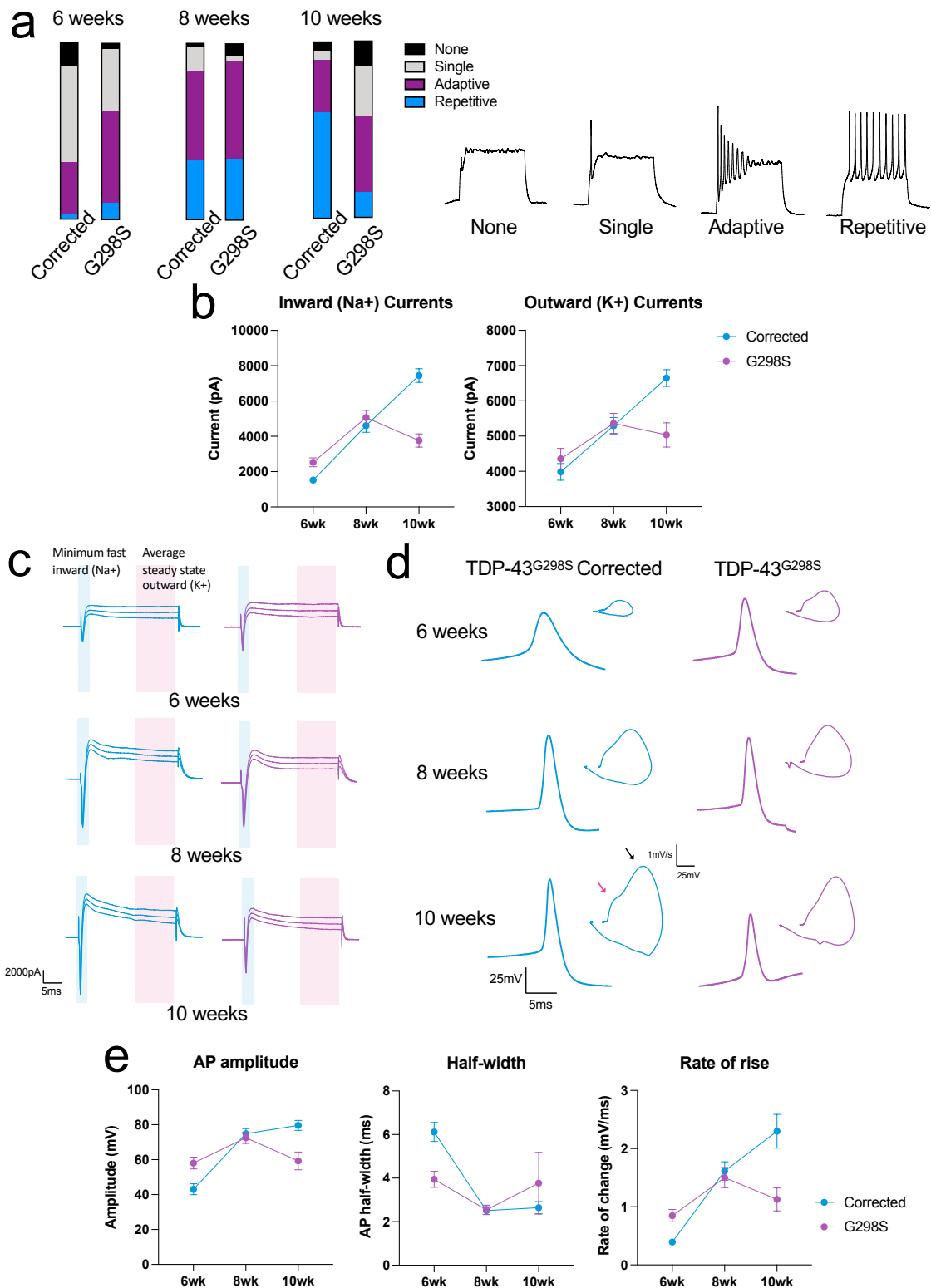


Figure 6.7. Changes in electrophysiological properties overtime.

A, Characterisation of firing patterns between TDP-43^{G298S} and CRISPR-corrected isogenic control lines taken at 6, 8 and 10 weeks maturation from whole cell patch clamp recordings. Firing types include: no AP, single AP, adaptive trains of APs and mature repetitive AP firing.

B, Quantification of inward (Na⁺), and outward (K⁺) currents 6-, 8- and 10-weeks

maturation. **C**, Representative inward (Na⁺) and outward (K⁺) current traces overtime taken at 0,10, and 20mV pulses. **D**, Representative single AP traces overtime and corresponding AP phase plots. The pink arrow indicates the AIS contribution to the rising phase of the action potential, while the black arrow indicates the somatodendritic contribution to the action potential. **E**, Quantification of AP amplitude, AP half-width and rate of change at 6-, 8- and 10-weeks maturation. Corrected: 6-weeks (N=1, iN=3, n=21), 8-weeks (N=1, iN=3, n=39), 10-weeks (N=1, iN=3, n=25). TDP=43^{G298S} 6-weeks (N=1, iN=3, n=28), 8-weeks (N=1, iN=3, n= 29), 10-weeks (N=1, iN=3, n=25). Data taken from independent populations and not longitudinal analysis of the same cells. Error bars represent the SEM. Non-parametric, unpaired t-tests used to determine statistical significance **p<0.01, ***p<0.001, ****p<0.0001.

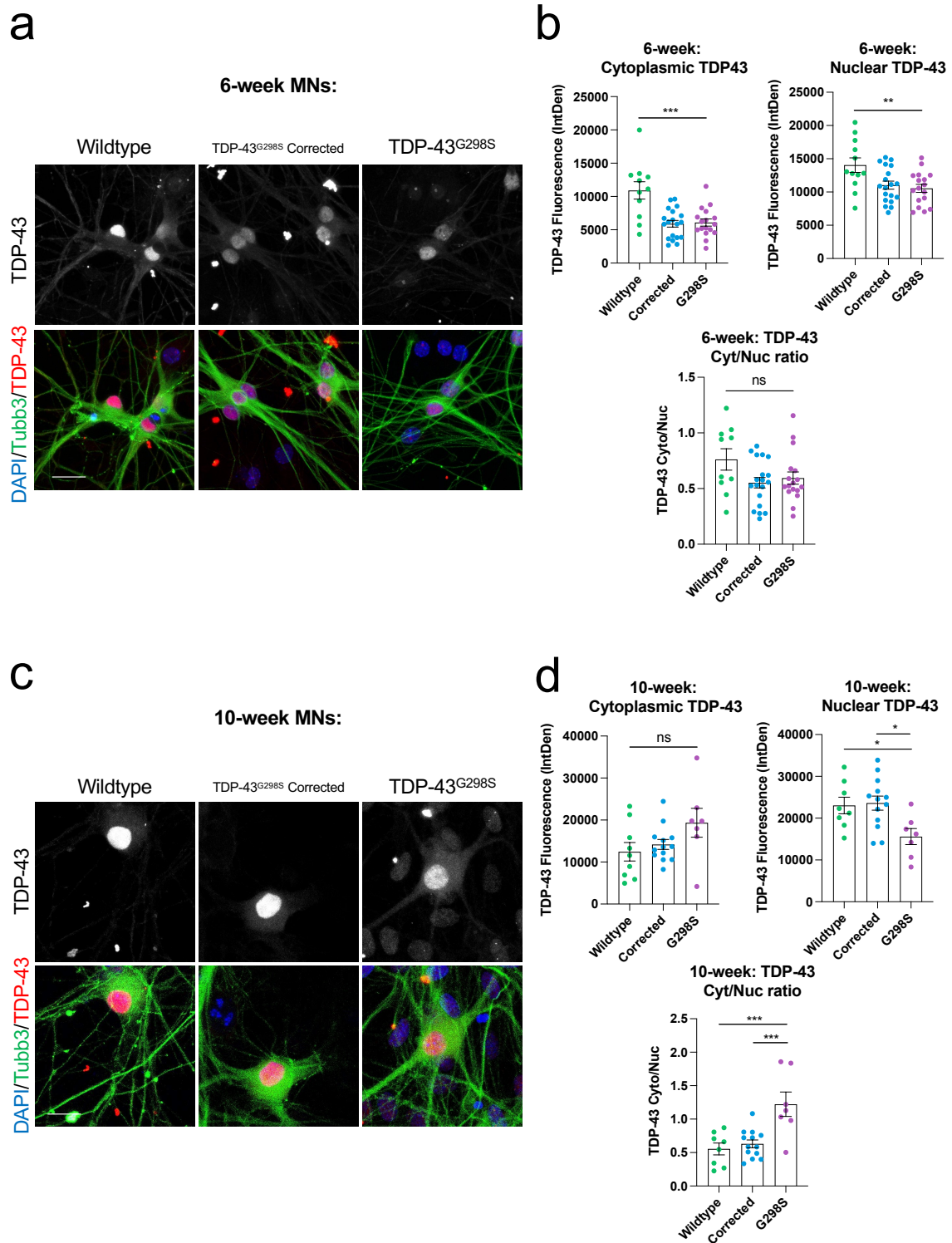


Figure 6.8. TDP-43 pathology in early (6-week) and late (10-week) motor neurons.

A, Immunofluorescence images of TDP-43 (red) counterstained with TUBB3 (green) and DAPI (blue) in early (6-week) MACS enriched hiPSC-derived wildtype (N=1, iN=1, n=10), corrected (N=1, iN=1, n=18) and TDP-43^{G298S} (N=1, iN=1, n=16) motor neurons (Scale bar = 25µm). **B**, Quantification of nuclear and cytoplasmic TDP-43 fluorescence intensity

(integrated density) and the ratio of cytoplasmic to nuclear fluorescence intensity in early (6-week) motor neurons. **C**, Immunofluorescence images of TDP-43 (red) counterstained with TUBB3 (green) and DAPI (blue) in late (10-week) MACS enriched hiPSC-derived wildtype, corrected and TDP-43^{G298S} motor neurons (Scale bar = 25µm). **B**, Quantification of nuclear and cytoplasmic TDP-43 fluorescence intensity (integrated density) and the ratio of cytoplasmic to nuclear fluorescence intensity in late (10-week) motor neurons. Error bars represent the SEM. One-way-ANOVA with Dunnet's multiple comparisons used to determine statistical significance. *p<0.05, **p<0.01, ***p<0.001.

2 weeks:	Wildtype	TDP-43^{G298S} Corrected	TDP-43^{G298S}	TDP-43^{G298S} Corrected +Opto	TDP-43^{G298S} +Opto	One-way ANOVA
RS	16.28 ± 1.67MΩ	16.70 ± 3.84MΩ	16.94 ± 1.48MΩ	14.58 ± 1.54MΩ	14.28 ± 2.07MΩ	p=0.87
RM	1063 ± 141MΩ	714 ± 69MΩ	786 ± 106MΩ	1207 ± 314MΩ	911 ± 176MΩ	p=0.09
CM	20.67 ± 2.49pF	23.49 ± 2.02pF	19.79 ± 3.51pF	25.96 ± 2.71pF	30.10 ±3.60pF	p=0.13
Resting voltage	-35.95 ± 2.85mV	-38.71 ± 1.20mV	-38.91 ± 2.84mV	-35.78 ± 2.25mV	-34.09 ± 2.90mV	p=0.64
Current Threshold	51.43 ± 10.47pA	45.36 ± 6.14pA	24.29 ± 3.20pA	74.00 ± 10.60pA	45.56 ± 9.26pA	*** p=0.0007
Voltage Threshold	-25.07 ± 2.12mV	-25.11 ± 1.32mV	-26.55 ± 1.40mV	23.47 ± 1.98mV	29.40 ± 1.69mV	p=0.20
Holding current	-33.68 ± 4.78pA	-32.14 ± 5.08pA	-29.03± 6.81pA	-37.71 ± 5.59pA	36.67 ± 6.29pA	P=0.77
Holding voltage	-59.77 ± 0.76mV	-60.43 ± 0.91mV	-60.69 ± 0.79mV	-60.27± 1.11mV	-60.90 ± 0.52mV	P=0.92

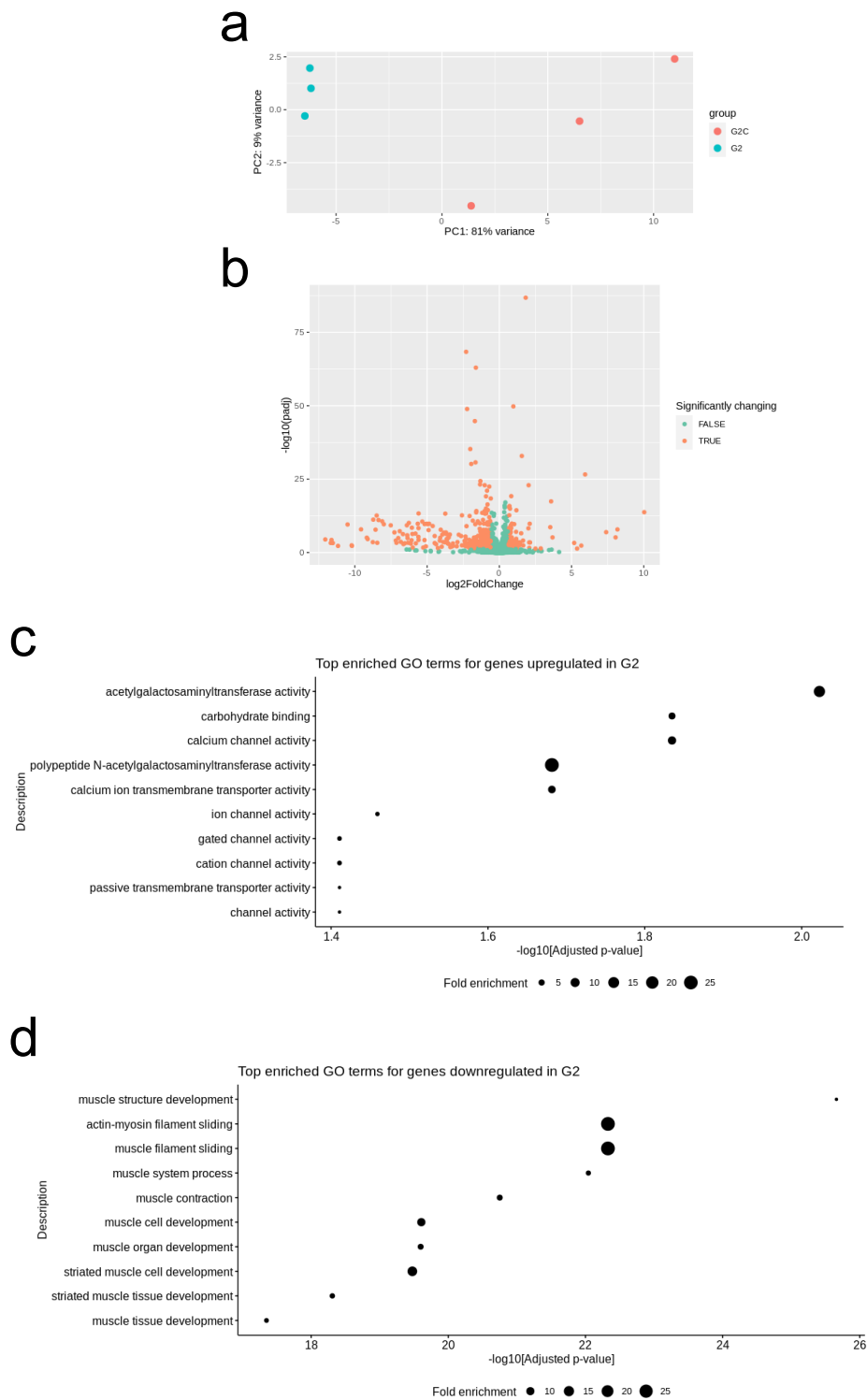
Supplementary Table 6.1. Passive membrane properties and other electrophysiological parameters.

Access resistance (RS), membrane resistance (RM), capacitance (CM), resting voltage, current threshold, voltage threshold, holding current and holding voltage in wildtype (N=1, iN=3, n=21), Corrected (N=1, iN=3, n=28) and TDP-43^{G298S} (N=1, iN=3, n=28) MNs at 6 weeks with and without optogenetic stimulation. P-values from one-way ANOVA. *p<0.05, **p<0.01, ***p<0.001.

4 weeks:	TDP-43^{G298S} Corrected	TDP-43^{G298S}	Unpaired T- test	6 weeks:	TDP-43^{G298S} Corrected	TDP-43^{G298S}	Unpaired T- test
RS	10.54 ± 0.47MΩ	9.80 ± 0.42MΩ	P=0.27	RS	9.06 ± 0.40MΩ	11.57 ± 0.78MΩ	**p=0.007
RM	497 ± 42MΩ	357 ± 28MΩ	*P=0.013	RM	320 ± 36MΩ	427 ± 72MΩ	p=0.20
CM	70.78 ± 5.73pF	84.8 ± 6.10pF	P=0.10	CM	88.67 ± 7.40pF	53.11 ± 6.43pF	**p=0.001
Resting voltage	-51.62 ± 1.58mV	-43.75 ± 2.91mV	*P=0.01	Resting voltage	-53.66 ± 2.30mV	-43.44 ± 3.96mV	**p=0.002
Current Threshold	57.57 ± 5.96pA	69.23 ± 7.19pA	P=0.22	Current Threshold	80.00 ± 9.67pA	54.71 ± 9.59pA	p=0.073
Voltage Threshold	-34.9 ± 1.40mV	-32.65 ± 1.37mV	P=0.27	Voltage Threshold	-31.95 ± 1.11mV	29.11 ± 2.3mV	p=0.248
Holding current	-31.41 ± 4.39pA	-51.07 ± 6.16pA	**P=0.0094	Holding current	-26.25 ± 7.36pA	-47.62 ± 9.28pA	p=0.08
Holding voltage	-60.77 ± 0.34mV	-60.42 ± 0.39mV	P=0.51	Holding voltage	-60.29 ± 1.17mV	-60.55 ± 1.10mV	p=0.87

Supplementary Table 6.2. Passive membrane properties and other electrophysiological parameters.

Access resistance (RS), membrane resistance (RM), capacitance (CM), resting voltage, current threshold, voltage threshold, holding current and holding voltage in wildtype, Corrected and TDP-43^{G298S} MNs at 8 and 10 weeks maturation. Corrected: 6-weeks (N=1, iN=3, n=21), 8-weeks (N=1, iN=3, n=39), 10-weeks (N=1, iN=3, n=25). TDP=43^{G298S} 6-weeks (N=1, iN=3, n=28), 8-weeks (N=1, iN=3, n= 29), 10-weeks (N=1, iN=3, n=25). P-values from unpaired nonparametric t-tests *p<0.05, **p<0.01, ***p<0.001.



Supplementary Figure 6.9. Additional bulk RNA-sequencing analysis.

A, Principal component analysis of TDP-43^{G298S} and TDP-43^{G298S} corrected sample clustering. **B**, differential gene expression analysis - Log2FoldChange >1.5 in either direction, adjusted p-value <0.05. **C**, Top enriched gene ontology (GO) terms for genes upregulated in the TDP-43^{G298S} samples. **D**, Top enriched gene ontology (GO) terms for genes upregulated in the TDP-43^{G298S} corrected samples.

6.10 Discussion

This chapter reports a previously unreported pathophysiological mechanism associated with excitability changes in human ALS-related motor neurons. Specifically, it was found that the pathogenic ALS-related TDP-43^{G298S} mutation altered the structure and activity-dependent plasticity of the axon initial segment in hiPSC motor neurons, which was linked to abnormal levels of neuronal excitability. Specifically, early (6-week) motor neurons showed an increase in the length of the axon initial segment and hyperexcitability (Figure 6.1, 6.2), while late (10-week) motor neurons showed a shortening of the axon initial segment and hypoexcitability (Figure 6.5). At both stages, activity-dependent plasticity of the axon initial segment was impaired, likely contributing to further dysregulated neuronal excitability (Figure 6.3, 6.5).

Altered neuronal excitability is a key pathological hallmark of ALS and has widely been reported in patient studies, as well as in animal and cell culture models. Patient studies have shown the occurrence of both cortical (Vucic et al. 2008, Van den Bos et al. 2018) and peripheral hyperexcitability affected lower motor neurons, with muscle fasciculations being one of the most obvious clinical signs of hyperexcitability in patients (Vucic and Kiernan 2006, Kanai et al. 2006, Bashford et al. 2020). With regards to cortical hyperexcitability in patients with ALS, there is evidence for both an increase in intrinsic excitability as demonstrated through transcranial magnetic stimulation studies looking at intracortical facilitation (ICF) (Vucic et al. 2008), and a decrease in inhibitory function as demonstrated through short interval intracortical inhibition (SICI) studies (Van den Bos et al. 2018). Studies into peripheral hyperexcitability have generally shown an imbalance of Na⁺ and K⁺ conductances (Kanai et al. 2006, Vucic and Kiernan 2010) likely due to altered ion channel expression (Howells et al. 2018). Other studies have also linked peripheral hyperactivity to increased drive from corticospinal inputs (Park et al. 2017). The SOD1 mouse model of ALS also shows clear evidence of hyperexcitability early on in the progression of the disease, characterised by increased persistent Na⁺ currents, reduced current and voltage thresholds, a shift in the relationship of injected current to AP firing, and an increase in the overall maximum firing frequency (Kuo et al. 2004, Kuo et al. 2005). Interestingly the SOD1 mouse model also shows evidence of a transition to hypoexcitability in the later stages of the disease (Martinez-Silva et al. 2018). Furthermore a mouse model of TDP-43 mis-localisation shows cortical hyperexcitability, characterised by reduced current thresholds and a shift in the relationship

of injected current to AP firing (Dyer et al. 2021). Human iPSC models of ALS have also shown evidence of both hyperexcitability (Devlin et al. 2015, Wainger et al. 2014) and hypoexcitability (Naujock et al. 2016, Sareen et al. 2013, Devlin et al. 2015). Interestingly one study looking at *TARDBP* and *C9orf72* mutations in patient hiPSCs showed early hyperexcitability and later hypoexcitability (Devlin et al. 2015), bringing apparently contradictory findings into agreement.

The whole-cell patch clamp recordings carried out on TDP-43^{G298S} hiPSC-motor neurons in this chapter seem to agree well with the wider literature (Devlin et al. 2015, Dyer et al. 2021). It was found that TDP-43^{G298S} caused early hyperexcitability, characterised by increased putative Na⁺ currents, reduced current thresholds, an upward shift in the relationship of injected current to AP spiking, increased maximum firing frequency and increased spontaneous firing frequency (Figure 6.1). It should also be noted that this early timepoint is the same as in the neuromuscular co-cultures from chapter 4, where increased motor unit excitability, as evidenced by increased spontaneous myofiber contraction frequency, was also observed (Figure 4.8). Subsequently it was found that TDP-43^{G298S} motor neurons declined in function at the later (10-week) timepoint (Figure 6.5). This was evidenced by reduced putative Na⁺ and K⁺ currents, reduced maximum firing frequency and a large downward shift in the relationship of injected current to AP spiking. Passive properties were also significantly different at this stage (Supplementary table 6.2). First the access resistance was slightly higher in the TDP-43^{G298S} neurons, although still well below the 25M Ω threshold for analysis and unlikely to have a major impact on the recordings, but potentially indicates reduced health of the neurons. Secondly capacitance was significantly lower, which could indicate a smaller soma size and possibly reduced maturation which could partially account for the reduction in Na⁺ and K⁺ currents. On the other hand, neurons with a lower capacitance should in theory respond faster to inputs leading to increased AP velocity, however conversely a reduction in AP rate of rise, firing rate, amplitude, and half-width was observed (Taylor 2012). Finally, the resting voltage was significantly higher in the TDP-43^{G298S} neurons suggesting that they would be more excitable however no change in current and voltage threshold was observed and in contrast the neurons exhibited a large reduction in the relationship of injected current to AP spiking and maximum firing frequency. Alternatively, the higher membrane potential could be explained by the neurons being less mature.

The experimental set up in this chapter has several advantages compared to previous electrophysiology studies on ALS-related hiPSC motor neurons. First, this is the first study of its kind to incorporate CRISPR Cas9 gene corrected isogenic control lines – providing a much higher degree of confidence that this phenotype is specific to the TDP-43^{G298S} mutation and not due to variation between individual hiPSC lines. Secondly, this is the first study to use highly MACS enriched populations of hiPSC-motor neurons and as such the likelihood of recording other contaminating neuronal cell types such as interneurons or immature progenitors is much lower. Indeed, this was a potential issue identified by Devlin and colleagues (Devlin et al. 2015). A major future improvement would be to accurately record specific Na⁺ and K⁺ currents by treating the cultures with specific Na⁺ channel blockers (TTX), K⁺ channel blockers (TEA) during the voltage clamp recordings. In the present study putative Na⁺ currents based on the minimum fast inward current and putative K⁺ currents based on the average steady state output were estimated from voltage clamp recordings. Furthermore, additional electrophysiological measures such as rheobase current threshold should be determined. It would also be interesting to quantify synaptic activity by measuring excitatory and inhibitory post synaptic potentials (EPSP/IPSPs) in response to glutamate, GABA and glycine treatment – indeed a similar experimental approach carried out by Devlin and colleagues (Devlin et al. 2015) found evidence for reduced synaptic activity in hiPSC-motor neurons harbouring ALS related TDP-43 and *C9orf72* mutations. In a more complex experimental set up it would be intriguing to carry out paired recordings of pre- and post-synaptic neurons/or myofibers to precisely measure synaptic transmission at different classes of synapse (cortical, corticomotor, neuromuscular). Recent studies have identified abnormal splicing of presynaptic proteins, most notably UNC13a, upon knockdown of TDP-43 (Ma et al. 2022, Brown et al. 2022) and it would be interesting to see if restoring normal splicing of these synaptic proteins could rescue normal synaptic transmission.

Previous studies have implicated the axon initial segment as a possible target in ALS. Significant swelling of the axon initial segment has been reported in early electron microscopy studies of post-mortem ALS lumbar spinal motor neurons (Sasaki and Maruyama 1992). In this study neurofilament accumulations were associated with increased axon initial segment diameter, while the soma, axon hillock and dendrites remained normal. Later work also

demonstrated neurofilament accumulation and impaired axon transport at the axon initial segment in the SOD1 mouse model of ALS (Sasaki et al. 2005). Other studies in the SOD1 mouse model have demonstrated altered axon initial segment length in pre-symptomatic and symptomatic stages of the disease (Bonnievie et al. 2020, Jorgensen et al. 2021). Interestingly (Jorgensen et al. 2021) observed extension of the AIS at symptom onset in SOD1 mice was associated with increased Na⁺ conductance, the first study to link changes at the AIS with changes in neuronal excitability in a model of ALS. However, since patients with *SOD1* mutations do not exhibit TDP-43 pathology (Mackenzie et al. 2007), a feature seen in the majority of ALS patients (Neumann et al. 2006), the aim of this chapter was to investigate how pathogenic TDP-43 mutations would impact both AIS structure and homeostatic plasticity in a representative human model of the disease.

The results described in this chapter are the first to characterize structural and functional changes at the axon initial segment in a human iPSC model of ALS and the first to explore a possible link between pathogenic TDP-43 mutations, changes to the AIS, and abnormal neuronal excitability in ALS motor neurons. It was found that the pathogenic TDP-43^{G298S} mutation caused an increase in the length of the AIS in early (6-week) motor neurons (Figure 6.2), which was associated with a corresponding increase in neuronal excitability characterized by lower current thresholds, a shift in the relationship of injected current to AP spiking, increased maximum firing frequency and increased spontaneous firing frequency (Figure 6.1). Furthermore, putative Na⁺ currents were also higher as well as AP amplitude and rate of rise, while AP half-width was lower. Taken together these results suggest that increased AIS length may be a contributing factor for early hyperexcitability in motor neurons harbouring ALS-related pathogenic TDP-43 mutations. Indeed, many experimental and computational studies have shown that modulation of AIS length greatly influences neuronal excitability primarily by increasing sodium channel density and conductance (Kole et al. 2008, Evans et al. 2015, Galliano et al. 2021, Jamann et al. 2021, Pan-Vazquez et al. 2020, Sohn et al. 2019, Gullledge and Bravo 2016, Goethals and Brette 2020). Computational studies predict that increasing AIS length would primarily decrease current and voltage thresholds (Goethals and Brette 2020, Gullledge and Bravo 2016), although current threshold is a less direct measure as it can be influenced by other factors such as neuronal morphology (Goethals and Brette 2020). The results in this chapter showed that increased AIS length was associated

strongly with reduced current threshold, however voltage threshold was only moderately reduced – a result that was not significant. It's possible that this was due to inaccuracies and large variation in the measurements of voltage threshold, particularly in the immature neurons where the inflection point was typically much broader. At the later 10-week timepoint it was found that the pathogenic TDP-43^{G298S} mutation caused a shortening of the AIS and a decline in electrophysiological function characterized by reduced putative Na⁺ and K⁺ currents, a downward shift in the relationship of injected current to AP firing and reduced maximum firing frequency. This decline in electrophysiological function was also observed by Devlin and colleagues in hiPSC-motor neurons harbouring pathogenic TDP-43 mutations (Devlin et al. 2015). It should be noted that the link between AIS shortening and neuronal hypoexcitability is less clear at this later timepoint since no significant changes in current or voltage threshold were observed. It's possible that the reduction in putative Na⁺/K⁺ currents, firing frequency and AIS shortening reflect a broader decline in neuronal function at this stage. It should be noted that the TDP-43^{G298S} motor neurons were much harder to patch than the isogenic controls at this later stage, perhaps reflecting increased vulnerability.

The results described in this chapter also showed that activity-dependent structural plasticity of the AIS in response to short term optogenetic stimulation was impaired in both early (6-week) and late (10-week) motor neurons (Figure 6.3, 6.5). Indeed, AIS shortening in response to increased activity or extension in response to sensory deprivation has been documented as a homeostatic mechanism to maintain neuronal excitability within a set range. The results here showed that AIS length was strongly reduced in response to short-term optogenetic stimulation in early 6-week hiPSC-motor neurons, while AIS position was unchanged. TDP-43^{G298S} motor neurons did display significant shortening of the AIS, however the change in length (ΔL) was less pronounced ($\Delta L -9.776\mu\text{m} \pm 4.770$) compared to wildtype ($\Delta L -19.72\mu\text{m} \pm 2.974$) and corrected ($\Delta L -19.14\mu\text{m} \pm 3.726$) conditions. As a result, the difference in AIS length already present in baseline conditions ($14.60\mu\text{m} \pm 4.329$) was even more pronounced after stimulation ($23.96\mu\text{m} \pm 4.129$). Theoretically this would contribute even further to hyperexcitability. Indeed, it was found that the current threshold was significantly increased following optogenetic stimulation in the corrected neurons but not in the TDP-43^{G298S} neurons. Furthermore, a significant downward shift in the relationship of injected current to AP spiking was observed in the corrected neurons but not in the TDP-43^{G298S} motor neurons.

Finally diverging current thresholds following optogenetic stimulation meant that the voltage threshold was significantly lower in the TDP-43^{G298S} motor neurons relative to the CRISPR corrected motor neurons following stimulation. Taken together these results suggest that impaired AIS plasticity contributes further to dysregulated excitability homeostasis in TDP-43^{G298S} motor neurons. At the later 10-week timepoint AIS shortening in response to optogenetic stimulation was completely abolished in the TDP-43^{G298S} motor neurons but not in the corrected neurons. Interestingly however at this stage the AIS showed a distal relocation in response to optogenetic stimulation in both corrected and TDP-43^{G298S} motor neurons – possibly indicating different forms of AIS plasticity at different stages of electrophysiological maturation. Finally, while we did see impaired AIS plasticity in response to optogenetic stimulation, it is possible that this response could be specific to this experimental model and stimulation approach. As such future studies should seek to stimulate ALS-related motor neurons in a more physiological manner by specifically driving pre-synaptic neurons and measuring AIS changes in post-synaptic neurons. This could be achieved by selectively expressing CHR2 in mixed neuronal populations and only measuring AIS changes in CHR2 negative neurons. Alternatively, for longer time scales DREADDs could be used to specifically activate pre-synaptic neurons over days-weeks (Roth 2016).

How TDP-43 modulates axon initial segment structure and plasticity is unclear. To elucidate possible molecular mechanisms, bulk RNA sequencing was performed on early (6-week) TDP-43^{G298S} and CRISPR corrected neuronal cultures. Interestingly it was found that several AIS genes were differentially expressed (Figure 6.4). Most notably *SCNA1*, which encodes the voltage-gated sodium channel, Nav1.1, was upregulated, which could possibly account for more ankyrin-g being trafficked to the AIS, leading to an overall increase in AIS length as well as the increase in putative Na⁺ currents observed. Similarly, *KCN1A* encoding the voltage-gated potassium channel KV1.1 was upregulated as was the neuronal adhesion molecule – *NRCAM*. Conversely *CAMK2* encoding the Ca²⁺/calmodulin-dependent protein kinase II was downregulated, and the *CACNA1S* encoding the Cav1.1 L-type calcium channel - both of which are important for AIS plasticity - possibly explaining impaired activity-dependent plasticity of the AIS (Evans et al. 2013, Grubb and Burrone 2010a). Despite these interesting molecular clues, the RNA-sequencing showed large upregulation of myogenic genes in the corrected samples (Supplementary figure 6.9) – indicating a possible myogenic contamination in the

cultures as has previously been documented in hiPSC neuronal differentiations (Quadrato et al. 2017). Despite the MACS enrichment, there are still a small percentage of contaminating cells present in the cultures, which likely contributed to this contamination. As such the data here is interpreted with a significant degree of caution. Other studies, however, have shown that TDP-43 can bind and modulate the splicing of numerous AIS genes, including *ANK3* and *SCNA1* (Narayanan et al. 2013, Lagier-Tourenne et al. 2012). Two very recent studies both identified alternative splicing of *ANK3* (Ankyrin-G), *SCN1A* (Nav1.1), *SCN2A* (Nav1.2), *SCN8A* (Nav1.8) and several other key AIS genes following TDP-43 depletion in hiPSCs and ALS patient samples (Brown et al. 2022, Ma et al. 2022). One of these studies found alternative splicing of exon 41 in the *ANK3* gene (Brown et al. 2022), which is differentially spliced in the short 190kDa, 270kDa and long 480kDa isoforms of Ankyrin-G. Since the long 480kDa isoform is found at the AIS, while the shorter isoforms are found at the dendrites and nodes of Ranvier (Nelson and Jenkins 2016) it's possible that differential splicing of these isoforms leads to increased accumulation of Ankyrin-g at the AIS in the 6-week TDP-43^{G298S} motor neurons and possibly depletion of the other isoforms at the dendrites and nodes of ranvier, which could partly account for defects seen at the dendrites and nodes of ranvier in other studies of TDP-43 associated ALS (Chang et al. 2021, Herzog et al. 2017). Non-conserved cryptic exons have also been discovered in the AIS-specific *KCNQ2* channel following TDP-43 depletion. This channel generates an M-type potassium current that alters the membrane potential and voltage threshold at the AIS. The cryptic exon in this gene would predict loss of one of the transmembrane domains, which could impair *KCNQ2* localisation to the AIS and lead to hyperexcitability by repression of the M-current. Indeed *KCNQ2* mutations are a common cause of infantile epilepsy (Lee et al. 2019) and a possible link between TDP-43 pathology, *KCNQ2* splicing, *KCNQ2* localisation to the AIS and hyperexcitability should be explored in future studies. Indeed, the results here show evidence of TDP-43 depletion in both RNA expression at the early timepoint (Figure 5.4) and reduced nuclear/cytoplasmic ratio at the later timepoint (Figure 6.8). Taken together these may indicate a possible link between TDP-43 depletion, altered splicing of AIS genes, and abnormal AIS structure and plasticity. It's also possible that neurofilament accumulation mitochondrial accumulation and impaired axon transport could cause increased accumulation of structural proteins at the AIS. Indeed, impaired axon transport and neurofilament accumulation have been observed at the AIS in the *SOD1* mouse model of ALS (Sasaki et al. 2005) and impaired axon transport has been

documented in TDP-43 mutant hiPSC-motor neurons (Alami et al. 2014). Finally, it's possible that reduced synaptic input may contribute to plasticity of the axon initial segment as a homeostatic response to lower levels of network activity, which could explain the initially increased length. Indeed, previous studies have shown evidence of reduced synaptic activity in TDP-43 mutant hiPSC-motor neurons (Devlin et al. 2015), and future work should seek to also address this by performing paired-recordings of pre- and post-synaptic neurons.

7. Conclusions and future perspectives

The compartmentalised neuromuscular co-cultures developed in chapters 3 and 4 open a great deal of opportunities for future experiments on the function and dysfunction of nerve-muscle connectivity. First, the three-compartment design allows for the co-cultures to be reconfigured. For instance, it would be possible to generate cortico-spinal neuromuscular co-cultures, with cortical neurons plated in the first compartment, spinal motor neurons in the central compartment and muscle in the third compartment. Such a reconfiguration would make it possible to assess regional specific ALS-related phenotypes and help contribute to answering the 'dying forward vs dying back' hypotheses of motor neuron degeneration in ALS. Such an experiment would be relatively straightforward to set up by generating cortical neurons using a forward programming approach via forced expression of hNGN2 (Pawlowski et al. 2017). Furthermore, it would also be interesting to incorporate other cell types from patient-derived hiPSCs, including astrocytes, microglia, myofibers and terminal Schwann cells. Deriving these different cell types from patient hiPSC with different ALS-related mutations such as *SOD1*, *FUS*, *C9orf72* and *VCP* would also help uncover new mutation specific and non-cell autonomous disease processes. Another interesting line of experiments would be to try and develop fast vs. slow motor units in the neuromuscular co-cultures. This would be particularly interesting since patients with ALS show differential degeneration of fast and slow motor neurons, with motor neurons innervating fast-twitch myofibers degenerating first. It was recently shown that DLK1 is required for fast motor neuron biophysical signature so modulation of notch signalling during hiPSC-motor neuron differentiation may be a potential route to generating fast and slow circuits (Muller et al. 2014). Looking at muscle specific expression of fast MHC IIa,b and slow MHC I fibers could be used along with contractile properties to assess the generation of fast vs slow motor units.

It would also be possible to set up new assays in the compartmentalised neuromuscular co-cultures. For instance, the long micro-channels containing the motor axons would be ideally suited to axon transport assays to measure anterograde and retrograde axon transport defects caused by ALS-related or indeed other disease related mutations (Alami et al. 2014). This could be achieved by using genetically encoded photoconvertible reporters such as dendra2 fused to cargo proteins of interest. For example, a TDP-43-dendra2 construct could be used to directly measure axonal transport of TDP-43. This could also link with the axon initial segment phenotypes detailed in chapter 6 since the axon initial segment acts as a diffusion barrier between somatodendritic and axonal compartments, it would be interesting to see if structural changes at the AIS are associated with impaired transport of cargo proteins or whether impaired transport of AIS cargo proteins leads to the accumulation of ankyrin-g at the AIS in the first instance (Li et al. 2011, Sasaki et al. 2005). Furthermore, using the compartmentalised neuromuscular co-cultures would make it possible to carry out regional specific transcriptomic and proteomic analysis of somatodendritic and axonal compartments. Since TDP-43 plays a critical role in mRNA splicing it would be interesting to compare how splicing of proximal and distal genes is affected and how translation is affected at different neuronal compartments. Indeed recent evidence suggests that synaptic mRNAs are actively translated at synapses (Biever et al. 2020).

With regards to the high-throughput 96-well neuromuscular co-culture platform developed in chapter 5, there are several key experiments and future improvements that could be made. First a proof of principle drug screen could be carried out to identify novel targets that improve peripheral ALS-related neuromuscular phenotypes. Indeed, this was the original intention for the PhD project, and a list of 137 annotated AstraZeneca compounds had been finalised based on our own RNAseq dataset, previous publicly available RNAseq datasets (Klim et al. 2019, Melamed et al. 2019) and ALS-related gene ontology terms, including “Synapse assembly”, “Neuromuscular junction”, “Axon guidance”, “Autophagy”, “Reactive oxygen species”, “Action potential” and “Motor neuron”, with hits appearing in multiple datasets and those with at least 10 available compounds with a potency above 1 μ M being prioritised (See appendix). Carrying out this initial screen at a single dose would be entirely feasible with the 96-well co-culture platform and the Operetta CLS available at KCL. Another set of

improvements that could be made to the 96-well co-culture platform would be to incorporate piezoelectric materials, such as polyvinylidene difluoride (PVDF) into the nanofiber sheets using co-axial electrospinning (Dang et al. 2015). Piezoelectric materials produce an electric current when they experience mechanical stress and as such could be used to directly calculate the mechanical force of the contracting myofibers (Jarkov et al.). In theory a custom-built 96-well plate could be engineered with microelectrodes to directly measure these changes in voltage, negating the need for high throughput video recordings of muscle contractions and PIV analysis that requires extensive amounts of data storage. Piezoelectric nanofibers would also be able to directly produce voltage and as such could also be used to stimulate/entrain the neuromuscular co-cultures – providing a constant feedback loop to generate electrically mature co-cultures (Ribeiro et al. 2018). Combining this with live synaptic/axonal reporters would greatly increase the potential throughput of the assay.

Finally, with regards to the axon initial segment and excitability phenotypes detailed in chapter 6 there are several key experiments that could be carried out to further understand this interesting ALS-related phenotype. First it would be crucial to determine whether the structural and plasticity phenotypes are conserved across a range of different ALS-related mutant hiPSC-lines such as *SOD1*, *C9orf72*, *VCP* and *FUS*. Second it would be interesting to confirm the phenotypes in other model systems such as TDP-43 knockdown cell culture models, TDP-43 mouse models and post-mortem ALS samples. Indeed, previous work has shown AIS related phenotypes in patient samples, however this work was done prior to the establishment of AIS specific antibodies such as ankyrin-g and so repeating this work with these antibodies would be incredibly informative. In addition to this, uncovering molecular mechanisms linking pathogenic ALS-related mutations to the AIS phenotypes would be important. Repeating bulk RNA sequencing on samples without myogenic contamination would be a starting point to identify key molecular targets. Furthermore, carrying out de-novo alternative splicing analysis alongside differential expression analysis could help uncover whether TDP-43 dependent alternative splicing of AIS genes is occurring. Indeed, two recent papers both showed TDP-43 knockdown leads to aberrant splicing of Ankyrin-G and various voltage gated sodium channels enriched at the AIS, including Nav1.1, Nav1.2, and Nav1.6 (Brown et al. 2022, Ma et al. 2022). Indeed, alternative splicing has been shown to play a critical role in AIS function (Zheng 2020). It would also be interesting to see how neuronal

activity impacts alternative splicing of AIS genes and whether this might be important for activity-dependent plasticity of the AIS. Furthermore, super-resolution imaging such as STORM could be employed to uncover how pathogenic ALS-related mutations impact the nanoscale structure of the AIS. Other interesting experiments would be to live-label the AIS while carrying out whole-cell patch clamp recordings using neurofascin-186 antibodies or genetically encoded reporters such as CHR2-YFP NavII-III (Grubb and Burrone 2010b, Dumitrescu, Evans and Grubb 2016). This way activity-dependent AIS plasticity and whole cell patch clamp recordings could be measured at the same cell before and after stimulation and precise measurements of the fold change in length individual AIS's could be determined to accurately quantify aberrant changes in plasticity. Finally It would also be interesting to carry out super-resolution imaging such as STORM, to determine if nanoscale organization of the AIS is also abnormal, as was found in a hiPSC-model of Tau-FTD (Sohn et al. 2019).

Taken together the work here provides new insights into pathological processes that occur in ALS-related TDP-43^{G298S} motor neurons. Most notably, structural changes to the axon initial segment, combined with impaired activity-dependent plasticity of the AIS are linked with aberrant hyperexcitability of TDP-43^{G298S} motor neurons as well as increased spontaneous activity of TDP-43^{G298S} hiPSC-derived motor units, mirroring changes in excitability and muscle fasciculations seen in patients with ALS (Bashford et al. 2020). An aberrant increase in AIS length and impaired ability to reduce intrinsic excitability in response to increased activity would have serious consequences on homeostatic maintenance of normal network excitability. An inability to maintain normal network homeostasis could lead to increased metabolic demands and excitotoxicity of motor neurons and neuromuscular synapses. This hyperexcitability-driven excitotoxicity could be a key driver of neuromuscular synapse loss and weaker evoked contractions observed in this model and in patients with ALS (Bashford et al. 2020). Furthermore, loss of neuromuscular transmission has been shown to trigger an increase in AIS length, suggesting that loss of NMJs could feedback to further dysregulate AIS function and excitability (Jensen et al. 2020), which could further exacerbate this pathological process. Hyperexcitability has also been shown to directly exacerbate TDP-43 pathology (Weskamp et al. 2020), which would lead to dysregulation of TDP-43-dependent processes in RNA processing and metabolism, as well as TDP-43-dependent dysregulation of neuronal excitability. This could lead to a vicious cycle of TDP-43 driving hyperexcitability, which in turn

further drives TDP-43 pathology, which further drives hyperexcitability. Indeed, Riluzole, which targets neuronal hyperexcitability is one of the only available treatments for ALS that can extend life. As such a clearer understanding of the molecular, cell-intrinsic and circuit-level mechanisms leading to abnormal neuronal excitability in ALS could lead to better and more precise treatments for patients with ALS, with reduced adverse side-effects (Inoue-Shibui et al. 2019). The 96-well neuromuscular co-culture platform developed in chapter 5 could be used to screen drugs that restore normal levels of neuronal excitability and spontaneous activity. It would be interesting to see if such compounds could also rescue the loss of neuromuscular synapses and evoked contractile output observed, providing a causal link between these pathological processes. Overall, the neuromuscular co-culture models developed in this thesis will hopefully serve as a useful human *in vitro* platform to disentangle the mechanisms driving and interlinking complex peripheral neuromuscular phenotypes observed in patients with ALS.

References:

- Abd Al Samid, M., J. S. McPhee, J. Saini, T. R. McKay, L. M. Fitzpatrick, K. Mamchaoui, A. Bigot, V. Mouly, G. Butler-Browne & N. Al-Shanti (2018) A functional human motor unit platform engineered from human embryonic stem cells and immortalized skeletal myoblasts. *Stem Cells and Cloning-Advances and Applications*, 11, 85-93.
- Ackerley, S., A. J. Grierson, S. Banner, M. S. Perkinson, J. Brownlee, H. L. Byers, M. Ward, P. Thornhill, K. Hussain, J. S. Waby, B. H. Anderton, J. D. Cooper, C. Dingwall, P. N. Leigh, C. E. Shaw & C. C. J. Miller (2004) p38 alpha stress-activated protein kinase phosphorylates neurofilaments and is associated with neurofilament pathology in amyotrophic lateral sclerosis. *Molecular and Cellular Neuroscience*, 26, 354-364.
- Afshar, M. E., H. Y. Abraha, M. A. Bakooshli, S. Davoudi, N. Thavandiran, K. Tung, H. Ahn, H. J. Ginsberg, P. W. Zandstra & P. M. Gilbert (2020) A 96-well culture platform enables longitudinal analyses of engineered human skeletal muscle microtissue strength. *Scientific Reports*, 10.
- Ahmed, N. Y., R. Knowles & N. Dehorter (2019) New Insights Into Cholinergic Neuron Diversity. *Frontiers in Molecular Neuroscience*, 12.
- Alami, N. H., R. B. Smith, M. A. Carrasco, L. A. Williams, C. S. Winborn, S. S. W. Han, E. Kiskinis, B. Winborn, B. D. Freibaum, A. Kanagaraj, A. J. Clare, N. M. Badders, B. Bilican, E. Chaum, S. Chandran, C. E. Shaw, K. C. Eggan, T. Maniatis & J. P. Taylor (2014) Axonal Transport of TDP-43 mRNA Granules Is Impaired by ALS-Causing Mutations. *Neuron*, 81, 536-543.
- Altman, T., A. Ionescu, A. Ibraheem, D. Priesmann, T. Gradus-Pery, L. Farberov, G. Alexandra, N. Shelestovich, R. Dafinca, N. Shomron, F. Rage, K. Talbot, M. E. Ward, A. Dori, M. Kruger & E. Perlson (2021) Axonal TDP-43 condensates drive neuromuscular junction disruption through inhibition of local synthesis of nuclear encoded mitochondrial proteins. *Nature Communications*, 12.
- Andreae, L. C. & J. Burrone (2014) The role of neuronal activity and transmitter release on synapse formation. *Current Opinion in Neurobiology*, 27, 47-52.
- Arber, S., B. Han, M. Mendelsohn, M. Smith, T. M. Jessell & S. Sockanathan (1999) Requirement for the homeobox gene Hb9 in the consolidation of motor neuron identity. *Neuron*, 23, 659-674.
- Arnold, E. S., S. C. Ling, S. C. Huelga, C. Lagier-Tourenne, M. Polymenidou, D. Ditsworth, H. B. Kordasiewicz, M. McAlonis-Downes, O. Platoshyn, P. A. Parone, S. Da Cruz, K. M. Clutario, D. Swing, L. Tessarollo, M. Marsala, C. E. Shaw, G. W. Yeo & D. W. Cleveland (2013) ALS-linked TDP-43 mutations produce aberrant RNA splicing and adult-onset motor neuron disease without aggregation or loss of nuclear TDP-43. *Proceedings of the National Academy of Sciences of the United States of America*, 110, E736-E745.
- Asakawa, K., H. Handa & K. Kawakami (2020) Optogenetic modulation of TDP-43 oligomerization accelerates ALS-related pathologies in the spinal motor neurons. *Nature Communications*, 11.
- Babinchak, W. M., R. Haider, B. K. Dumm, P. Sarkar, K. Surewicz, J. K. Choi & W. K. Surewicz (2019) The role of liquid-liquid phase separation in aggregation of the TDP-43 low-complexity domain. *Journal of Biological Chemistry*, 294, 6306-6317.
- Bakooshli, M. A., E. S. Lippmann, B. Mulcahy, N. Iyer, C. T. Nguyen, K. Tung, B. A. Stewart, H. van den Dorpel, T. Fuehrmann, M. Shoichet, A. Bigot, E. Pegoraro, H. Ahn, H. Ginsberg,

- M. Zhen, R. S. Ashton & P. M. Gilbert (2019) A 3D culture model of innervated human skeletal muscle enables studies of the adult neuromuscular junction. *Elife*, 8.
- Banerjee, A., R. S. Larsen, B. D. Philpot & O. Paulsen (2016) Roles of Presynaptic NMDA Receptors in Neurotransmission and Plasticity. *Trends in Neurosciences*, 39, 26-39.
- Barber, M. J. & J. W. Lichtman (1999) Activity-driven synapse elimination leads paradoxically to domination by inactive neurons. *Journal of Neuroscience*, 19, 9975-9985.
- Barber, S. C. & P. J. Shaw (2010) Oxidative stress in ALS: Key role in motor neuron injury and therapeutic target. *Free Radical Biology and Medicine*, 48, 629-641.
- Barik, A., L. Li, A. Sathyamurthy, W. C. Xiong & L. Mei (2016) Schwann Cells in Neuromuscular Junction Formation and Maintenance. *Journal of Neuroscience*, 36, 9770-9781.
- Barker, A. T. & R. Jalinous (1985) NON-INVASIVE MAGNETIC STIMULATION OF HUMAN MOTOR CORTEX. *Lancet*, 1, 1106-1107.
- Barton, S. K., M. Dario, O. G. James, M. R. Livesey, B. T. Selvaraj, O. T. James, E. M. Perkins, J. M. Gregory, E. C. Cleary, Rosanne M Ausems, Roderick N Carter Carter, Navneet A Vasistha, C. Zhao, K. Burr, D. Story, A. Cardinali, N. M. Morton, G. E. Hardingham, D. J. A. Wyllie & S. Chandran. 2021. Transactive response DNA-binding protein-43 proteinopathy in oligodendrocytes revealed using an induced pluripotent stem cell model. . *Brain Communications: Brain Communications*.
- Bashford, J. A., A. Wickham, R. Iniesta, E. M. Drakakis, M. G. Boutelle, K. R. Mills & C. E. Shaw (2020) The rise and fall of fasciculations in amyotrophic lateral sclerosis. *Brain Communications*, 2.
- Bayraktar, O. A., L. C. Fuentealba, A. Alvarez-Buylla & D. H. Rowitch (2015) Astrocyte Development and Heterogeneity. *Cold Spring Harbor Perspectives in Biology*, 7.
- Bentzinger, C. F., Y. X. Wang & M. A. Rudnicki (2012) Building Muscle: Molecular Regulation of Myogenesis. *Cold Spring Harbor Perspectives in Biology*, 4.
- Benusa, S. D., N. M. George, B. A. Sword, G. H. DeVries & J. L. Dupree (2017) Acute neuroinflammation induces AIS structural plasticity in a NOX2-dependent manner. *Journal of Neuroinflammation*, 14.
- Berger, S. L., A. Leo-Macias, S. Yuen, L. Khatri, S. Pfennig, Y. Q. Zhang, E. Agullo-Pascual, G. Caillol, M. S. Zhu, E. Rothenberg, C. V. Melendez-Vasquez, M. Delmar, C. Leterrier & J. L. Salzer (2018) Localized Myosin II Activity Regulates Assembly and Plasticity of the Axon Initial Segment. *Neuron*, 97, 555-+.
- Biever, A., C. Glock, G. Tushev, E. Ciirdaeva, T. Dalmay, J. D. Langer & E. M. Schuman (2020) Monosomes actively translate synaptic mRNAs in neuronal processes. *Science*, 367, 526-+.
- Bonnevie, V. S., K. P. Dimintiyanova, A. Hedegaard, J. Lehnhoff, L. Grondahl, M. Moldovan & C. F. Meehan (2020) Shorter axon initial segments do not cause repetitive firing impairments in the adult presymptomatic G127X SOD-1 Amyotrophic Lateral Sclerosis mouse. *Scientific Reports*, 10.
- Borthwick, G. M., M. A. Johnson, P. G. Ince, P. J. Shaw & D. M. Turnbull (1999) Mitochondrial enzyme activity in amyotrophic lateral sclerosis: Implications for the role of mitochondria in neuronal cell death. *Annals of Neurology*, 46, 787-790.
- Brandon, E. P., W. C. Lin, K. A. D'Amour, D. P. Pizzo, B. Dominguez, Y. Sugiura, S. Thode, C. P. Ko, L. J. Thal, F. H. Gage & K. F. Lee (2003) Aberrant Patterning of neuromuscular synapses in choline acetyltransferase-deficient mice. *Journal of Neuroscience*, 23, 539-549.
- Brenner, M. & A. Messing (2021) Regulation of GFAP Expression. *Asn Neuro*, 13.

- Brown, A.-L., O. G. Wilkins, M. J. Keuss, S. E. Hill, M. Zanovello, W. C. Lee, A. Bampton, F. C. Y. Lee, L. Masino, Y. A. Qi, S. Bryce-Smith, A. Gatt, M. Hallegger, D. Fagegaltier, H. Phatnani, J. Kwan, D. Sareen, J. R. Broach, Z. Simmons, X. Arcila-Londono, E. B. Lee, V. M. Van Deerlin, N. A. Shneider, E. Fraenkel, L. W. Ostrow, F. Baas, N. Zaitlen, J. D. Berry, A. Malaspina, P. Fratta, G. A. Cox, L. M. Thompson, S. Finkbeiner, E. Dardiotis, T. M. Miller, S. Chandran, S. Pal, E. Hornstein, D. J. MacGowan, T. Heiman-Patterson, M. G. Hammell, N. A. Patsopoulos, O. Butovsky, J. Dubnau, A. Nath, R. Bowser, M. Harms, E. Aronica, M. Poss, J. Phillips-Cremins, J. Cray, N. Atassi, D. J. Lange, D. J. Adams, L. Stefanis, M. Gotkine, R. H. Baloh, S. Babu, T. Raj, S. Paganoni, O. Shalem, C. Smith, B. Zhang, B. Harris, I. Broce, V. Drory, J. Ravits, C. McMillan, V. Menon, L. Wu, S. Altschuler, Y. Lerner, R. Sattler, K. Van Keuren-Jensen, O. Rozenblatt-Rosen, K. Lindblad-Toh, K. Nicholson, P. Gregersen, J.-H. Lee, S. Kokos, S. Muljo, J. Newcombe, E. K. Gustavsson, S. Seddighi, J. F. Reyes, S. L. Coon, D. Ramos, G. Schiavo, E. M. C. Fisher, M. Secrier, T. Lashley, J. Ule, E. Buratti, J. Humphrey, M. E. Ward & N. A. Consortium (2022) TDP-43 loss and ALS-risk SNPs drive mis-splicing and depletion of UNC13A. *Nature*, 603, 131-137.
- Bruneteau, G., T. Simonet, S. Bauche, N. Mandjee, E. Malfatti, E. Girard, M. L. Tanguy, A. Behin, F. Khiami, E. Sariali, C. Hell-Remy, F. Salachas, P. F. Pradat, E. Fournier, L. Lacomblez, J. Koenig, N. B. Romero, B. Fontaine, V. Meininger, L. Schaeffer & D. Hantai (2013) Muscle histone deacetylase 4 upregulation in amyotrophic lateral sclerosis: potential role in reinnervation ability and disease progression. *Brain*, 136, 2359-2368.
- Bryson, J. B., C. B. Machado, M. Crossley, D. Stevenson, V. Bros-Facer, J. Burrone, L. Greensmith & I. Lieberam (2014) Optical Control of Muscle Function by Transplantation of Stem Cell-Derived Motor Neurons in Mice. *Science*, 344, 94-97.
- Bulow, P., T. J. Murphy, G. J. Bassell & P. Wenner (2019) Homeostatic Intrinsic Plasticity Is Functionally Altered in Fmr1 KO Cortical Neurons. *Cell Reports*, 26, 1378-+.
- Burke, E. E., J. G. Chenoweth, J. H. Shin, L. Collado-Torres, S. K. Kim, N. Micali, Y. H. Wang, C. Colantuoni, R. E. Straub, D. J. Hoepfner, H. Y. Chen, A. Sellers, K. Shibbani, G. R. Hamersky, M. D. Bustamante, B. N. Phan, W. S. Ulrich, C. Valencia, A. Jaishankar, A. J. Price, A. Rajpurohit, S. A. Semick, R. W. Burli, J. C. Barrow, D. J. Hiler, S. C. Page, K. Martinowich, T. M. Hyde, J. E. Kleinman, K. F. Berman, J. A. Apud, A. J. Cross, N. J. Brandon, D. R. Weinberger, B. J. Maher, R. D. G. McKay & A. E. Jaffe (2020) Dissecting transcriptomic signatures of neuronal differentiation and maturation using iPSCs. *Nature Communications*, 11.
- Burrone, J., M. O'Byrne & V. N. Murthy (2002) Multiple forms of synaptic plasticity triggered by selective suppression of activity in individual neurons. *Nature*, 420, 414-418.
- Canals, I., A. Ginisty, E. Quist, R. Timmerman, J. Fritze, G. Miskinyte, E. Monni, M. G. Hansen, I. Hidalgo, D. Bryder, J. Bengzon & H. Ahlenius (2018) Rapid and efficient induction of functional astrocytes from human pluripotent stem cells. *Nature Methods*, 15, 693-+.
- Cantor, S., W. Zhang, N. Delestree, L. Remedio, G. Z. Mentis & S. J. Burden (2018) Preserving neuromuscular synapses in ALS by stimulating MuSK with a therapeutic agonist antibody. *Elife*, 7, 19.
- Caroni, P., F. Donato & D. Muller (2012) Structural plasticity upon learning: regulation and functions. *Nature Reviews Neuroscience*, 13, 478-490.
- Cerbini, T., R. Funahashi, Y. Q. Luo, C. Y. Liu, K. Park, M. Rao, N. Malik & J. H. Zou (2015) Transcription Activator-Like Effector Nuclease (TALEN)-Mediated CRYBL Targeting Enables Enhanced Transgene Expression and One-Step Generation of Dual Reporter

- Human Induced Pluripotent Stem Cell (iPSC) and Neural Stem Cell (NSC) Lines. *Plos One*, 10.
- Chal, J., Z. Al Tanoury, M. Hestin, B. Gobert, S. Aivio, A. Hick, T. Cherrier, A. P. Nesmith, K. K. Parker & O. Pourquie (2016) Generation of human muscle fibers and satellite-like cells from human pluripotent stem cells in vitro. *Nature Protocols*, 11, 1833-1850.
- Chal, J. & O. Pourquie (2017) Making muscle: skeletal myogenesis in vivo and in vitro. *Development*, 144, 2104-2122.
- Chand, K. K., K. M. Lee, J. D. Lee, H. Qiu, E. F. Willis, N. A. Lavidis, M. A. Hilliard & P. G. Noakes (2018) Defects in synaptic transmission at the neuromuscular junction precede motor deficits in a TDP-43(Q331K) transgenic mouse model of amyotrophic lateral sclerosis. *Faseb Journal*, 32, 2676-2689.
- Chang, K. J., I. Agrawal, A. Vainshtein, W. Y. Ho, W. Xin, G. Tucker-Kellogg, K. Susuki, E. Peles, S. C. Ling & J. R. Chan (2021) TDP-43 maximizes nerve conduction velocity by repressing a cryptic exon for paranodal junction assembly in Schwann cells. *Elife*, 10.
- Cheesbrough, A., F. Sciscione, F. Riccio, P. Harley, L. R'Bibo, G. Ziakas, A. Darbyshire, I. Lieberam & W. Song Biobased Elastomer Nanofibers Guide Light-controlled Human iPSC-derived Skeletal Myofibers. *Advanced Materials*, n/a, 2110441.
- Choi, M. E., D. R. Price, S. W. Ryter & A. M. K. Choi (2019) Necroptosis: a crucial pathogenic mediator of human disease. *Jci Insight*, 4.
- Colombrita, C., E. Zennaro, C. Fallini, M. Weber, A. Sommacal, E. Buratti, V. Silani & A. Ratti (2009) TDP-43 is recruited to stress granules in conditions of oxidative insult. *Journal of Neurochemistry*, 111, 1051-1061.
- Conforti, L., J. Gilley & M. P. Coleman (2014) Wallerian degeneration: an emerging axon death pathway linking injury and disease. *Nature Reviews Neuroscience*, 15, 394-409.
- Cooke, R. (2004) Milestone in physiology - The sliding filament model: 1972-2004. *Journal of General Physiology*, 123, 643-656.
- Costa, R. P., B. E. P. Mizusaki, P. J. Sjostrom & M. C. W. van Rossum (2017) Functional consequences of pre- and postsynaptic expression of synaptic plasticity. *Philosophical Transactions of the Royal Society B-Biological Sciences*, 372.
- Cruz, P. M. R., J. Cossins, D. Beeson & A. Vincent (2020) The Neuromuscular Junction in Health and Disease: Molecular Mechanisms Governing Synaptic Formation and Homeostasis. *Frontiers in Molecular Neuroscience*, 13.
- Dang, T. T., T. T. T. Nguyen, O. H. Chung & J. S. Park (2015) Fabrication of form-stable poly(ethylene glycol)-loaded poly(vinylidene fluoride) nanofibers via single and coaxial electrospinning. *Macromolecular Research*, 23, 819-829.
- Davis-Dusenbery, B. N., L. A. Williams, J. R. Klim & K. Eggan (2014) How to make spinal motor neurons. *Development*, 141, 491-501.
- de Carvalho, M., M. C. Kiernan & M. Swash (2017) Fasciculation in amyotrophic lateral sclerosis: origin and pathophysiological relevance. *Journal of Neurology Neurosurgery and Psychiatry*, 88, 773-779.
- De Winter, F., T. Vo, F. J. Stam, L. A. B. Wisman, P. R. Bar, S. P. Niclou, F. L. van Muiswinkel & J. Verhaagen (2006) The expression of the chemorepellent Semaphorin 3A is selectively induced in terminal Schwann cells of a subset of neuromuscular synapses that display limited anatomical plasticity and enhanced vulnerability in motor neuron disease. *Molecular and Cellular Neuroscience*, 32, 102-117.
- Debanne, D., Y. Inglebert & M. Russier (2019) Plasticity of intrinsic neuronal excitability. *Current Opinion in Neurobiology*, 54, 73-82.

- Deisseroth, K., G. P. Feng, A. K. Majewska, G. Miesenbock, A. Ting & M. J. Schnitzer (2006) Next-generation optical technologies for illuminating genetically targeted brain circuits. *Journal of Neuroscience*, 26, 10380-10386.
- Devlin, A. C., K. Burr, S. Borooah, J. D. Foster, E. M. Cleary, I. Geti, L. Vallier, C. E. Shaw, S. Chandran & G. B. Miles (2015) Human iPSC-derived motoneurons harbouring TARDBP or C9ORF72 ALS mutations are dysfunctional despite maintaining viability. *Nature Communications*, 6, 12.
- Di Giorgio, F. P., G. L. Boulting, S. Bobrowicz & K. C. Eggan (2008) Human Embryonic Stem Cell-Derived Motor Neurons Are Sensitive to the Toxic Effect of Glial Cells Carrying an ALS-Causing Mutation. *Cell Stem Cell*, 3, 637-648.
- Di Giorgio, F. P., M. A. Carrasco, M. C. Siao, T. Maniatis & K. Eggan (2007) Non-cell autonomous effect of glia on motor neurons in an embryonic stem cell-based ALS model. *Nature Neuroscience*, 10, 608-614.
- Dimos, J. T., K. T. Rodolfa, K. K. Niakan, L. M. Weisenthal, H. Mitsumoto, W. Chung, G. F. Croft, G. Saphier, R. Leibel, R. Goland, H. Wichterle, C. E. Henderson & K. Eggan (2008) Induced pluripotent stem cells generated from patients with ALS can be differentiated into motor neurons. *Science*, 321, 1218-1221.
- Ding, M., H. Andersson, S. Martinsson, A. Sabirsh, A. Jonebring, Q. D. Wang, A. T. Plowright & L. Drowley (2020) Aligned nanofiber scaffolds improve functionality of cardiomyocytes differentiated from human induced pluripotent stem cell-derived cardiac progenitor cells. *Scientific Reports*, 10.
- Dittlau, K. S., E. N. Krasnow, L. Fumagalli, T. Vandoorne, P. Baatsen, A. Kerstens, G. Giacomazzi, B. Pavie, E. Rossaert, J. Beckers, M. Sampaolesi, P. Van Damme & L. Van den Bosch (2021) Human motor units in microfluidic devices are impaired by FUS mutations and improved by HDAC6 inhibition. *Stem Cell Reports*, 16, 2213-2227.
- Doble, A. (1996) The pharmacology and mechanism of action of riluzole. *Neurology*, 47, S233-S241.
- Dong, H. L., L. Chen & Z. Y. Wu (2021) A novel de novo SPTAN1 nonsense variant causes hereditary motor neuropathy in a Chinese family. *Brain*, 144.
- Du, Z. W., H. Chen, H. S. Liu, J. F. Lu, K. Qian, C. L. Huang, X. F. Zhong, F. Fan & S. C. Zhang (2015) Generation and expansion of highly pure motor neuron progenitors from human pluripotent stem cells. *Nature Communications*, 6, 9.
- Dudek, S. M. & M. F. Bear (1992) HOMOSYNAPTIC LONG-TERM DEPRESSION IN AREA CA1 OF HIPPOCAMPUS AND EFFECTS OF N-METHYL-D-ASPARTATE RECEPTOR BLOCKADE. *Proceedings of the National Academy of Sciences of the United States of America*, 89, 4363-4367.
- Dumitrescu, A. S., M. D. Evans & M. S. Grubb (2016) Evaluating Tools for Live Imaging of Structural Plasticity at the Axon Initial Segment. *Frontiers in Cellular Neuroscience*, 10.
- Dyer, M. S., L. A. Reale, K. E. Lewis, A. K. Walker, T. C. Dickson, A. Woodhouse & C. A. Blizzard (2021) Mislocalisation of TDP-43 to the cytoplasm causes cortical hyperexcitability and reduced excitatory neurotransmission in the motor cortex. *Journal of Neurochemistry*, 157, 1300-1315.
- Egorov, A. V., B. N. Hamam, E. Franssen, M. E. Hasselmo & A. A. Alonso (2002) Graded persistent activity in entorhinal cortex neurons. *Nature*, 420, 173-178.
- Endo, F., O. Komine, N. Fujimori-Tonou, M. Katsuno, S. Jin, S. Watanabe, G. Sobue, M. Dezawa, T. Wyss-Coray & K. Yamanaka (2015) Astrocyte-Derived TGF-beta 1 Accelerates

- Disease Progression in ALS Mice by Interfering with the Neuroprotective Functions of Microglia and T Cells. *Cell Reports*, 11, 592-604.
- Escartin, C., E. Galea, A. Lakatos, J. P. O'Callaghan, G. C. Petzold, A. Serrano-Pozo, C. Steinhauser, A. Volterra, G. Carmignoto, A. Agarwal, N. J. Allen, A. Araque, L. Barbeito, A. Barzilai, D. E. Bergles, G. Bonvento, A. M. Butt, W. T. Chen, M. Cohen-Salmon, C. Cunningham, B. Deneen, B. De Strooper, B. Diaz-Castro, C. Farina, M. Freeman, V. Gallo, J. E. Goldman, S. A. Goldman, M. Gotz, A. Gutierrez, P. G. Haydon, D. H. Heiland, E. M. Hol, M. G. Holt, M. Iino, K. V. Kastanenka, H. Kettenmann, B. S. Khakh, S. Koizumi, C. J. Lee, S. A. Liddelow, B. A. MacVicar, P. Magistretti, A. Messing, A. Mishra, A. V. Molofsky, K. K. Murai, C. M. Norris, S. Okada, S. H. R. Oliet, J. F. Oliveira, A. Panatier, V. Parpura, M. Pekna, M. Pekny, L. Pellerin, G. Perea, B. G. Perez-Nievas, F. W. Pfrieger, K. E. Poskanzer, F. J. Quintana, R. M. Ransohoff, M. Riquelme-Perez, S. Robel, C. R. Rose, J. D. Rothstein, N. Rouach, D. H. Rowitch, A. Semyanov, S. Sirko, H. Sontheimer, R. A. Swanson, J. Vitorica, I. B. Wanner, L. B. Wood, J. Q. Wu, B. H. Zheng, E. R. Zimmer, R. Zorec, M. V. Sofroniew & A. Verkhratsky (2021) Reactive astrocyte nomenclature, definitions, and future directions. *Nature Neuroscience*, 24, 312-325.
- Evans, M. D., A. S. Dumitrescu, D. L. H. Kruijssen, S. E. Taylor & M. S. Grubb (2015) Rapid Modulation of Axon Initial Segment Length Influences Repetitive Spike Firing. *Cell Reports*, 13, 1233-1245.
- Evans, M. D., R. P. Sammons, S. Lebron, A. S. Dumitrescu, T. B. K. Watkins, V. N. Uebele, J. J. Renger & M. S. Grubb (2013) Calcineurin Signaling Mediates Activity-Dependent Relocation of the Axon Initial Segment. *Journal of Neuroscience*, 33, 6950-6963.
- Favero, M., G. Busetto & A. Cangiano (2012) Spike timing plays a key role in synapse elimination at the neuromuscular junction. *Proceedings of the National Academy of Sciences of the United States of America*, 109, E1667-E1675.
- Feiler, M. S., B. Strobel, A. Freischmidt, A. M. Hefnerich, J. Kappel, B. M. Brewer, D. Li, D. R. Thal, P. Walther, A. C. Ludolph, K. M. Danzer & J. H. Weishaupt (2015) TDP-43 is intercellularly transmitted across axon terminals. *Journal of Cell Biology*, 211, 897-911.
- Felice, K. J. (1997) A longitudinal study comparing thenar motor unit number estimates to other quantitative tests in patients with amyotrophic lateral sclerosis. *Muscle & Nerve*, 20, 179-185.
- Finn, A. J., G. P. Feng & A. M. Pendergast (2003) Postsynaptic requirement for Abl kinases in assembly of the neuromuscular junction. *Nature Neuroscience*, 6, 717-723.
- Fischer, L. R., D. G. Culver, A. A. Davis, P. Tennant, M. S. Wang, M. Coleman, S. Asress, R. Adalbert, G. M. Alexander & J. D. Glass (2005) The Wld(s) gene modestly prolongs survival in the SOD1(G93A). *Neurobiology of Disease*, 19, 293-300.
- Fischer, L. R., D. G. Culver, P. Tennant, A. A. Davis, M. S. Wang, A. Castellano-Sanchez, J. Khan, M. A. Polak & J. D. Glass (2004) Amyotrophic lateral sclerosis is a distal axonopathy: evidence in mice and man. *Experimental Neurology*, 185, 232-240.
- Fourcaudot, E., F. Gambino, Y. Humeau, G. Casassus, H. Shaban, B. Poulain & A. Luthi (2008) cAMP/PKA signaling and RIM1 alpha mediate presynaptic LTP in the lateral amygdala. *Proceedings of the National Academy of Sciences of the United States of America*, 105, 15130-15135.
- Fox, K. & M. Stryker (2017) Integrating Hebbian and homeostatic plasticity: introduction. *Philosophical Transactions of the Royal Society B-Biological Sciences*, 372.
- Fujitani, M., Y. Otani & H. Miyajima (2021) Pathophysiological Roles of Abnormal Axon Initial Segments in Neurodevelopmental Disorders. *Cells*, 10.

- Galanis, C. & A. Vlachos (2020) Hebbian and Homeostatic Synaptic Plasticity-Do Alterations of One Reflect Enhancement of the Other? *Frontiers in Cellular Neuroscience*, 14.
- Galliano, E., C. Hahn, L. P. Browne, P. R. Villamayor, C. Tufo, A. Crespo & M. S. Grubb (2021) Brief Sensory Deprivation Triggers Cell Type-Specific Structural and Functional Plasticity in Olfactory Bulb Neurons. *Journal of Neuroscience*, 41, 2135-2151.
- Gasset-Rosa, F., S. Lu, H. Y. Yu, C. Chen, Z. Melamed, L. Guo, J. Shorter, S. Da Cruz & D. W. Cleveland (2019) Cytoplasmic TDP-43 De-mixing Independent of Stress Granules Drives Inhibition of Nuclear Import, Loss of Nuclear TDP-43, and Cell Death. *Neuron*, 102, 339-+.
- Gibb, S. L., W. Boston-Howes, Z. S. Lavina, S. Gustincich, R. H. Brown, P. Pasinelli & D. Trotti (2007) A caspase-3-cleaved fragment of the glial glutamate transporter EAAT2 is sumoylated and targeted to promyelocytic leukemia nuclear bodies in mutant SOD1-linked amyotrophic lateral sclerosis. *Journal of Biological Chemistry*, 282, 32480-32490.
- Goethals, S. & R. Brette (2020) Theoretical relation between axon initial segment geometry and excitability. *Elife*, 9.
- Gregory, R. I., K. P. Yan, G. Amuthan, T. Chendrimada, B. Doratotaj, N. Cooch & R. Shiekhattar (2004) The Microprocessor complex mediates the genesis of microRNAs. *Nature*, 432, 235-240.
- Grubb, M. S. & J. Burrone (2010a) Activity-dependent relocation of the axon initial segment fine-tunes neuronal excitability. *Nature*, 465, 1070-U131.
- (2010b) Channelrhodopsin-2 Localised to the Axon Initial Segment. *Plos One*, 5.
- Gulledge, A. T. & J. J. Bravo. 2016. Neuron Morphology Influences Axon Initial Segment Plasticity. *eNeuro: eNeuro*.
- Gunes, Z. I., V. W. Y. Kan, X. Q. Ye & S. Liebscher (2020) Exciting Complexity: The Role of Motor Circuit Elements in ALS Pathophysiology. *Frontiers in Neuroscience*, 14.
- Hanson, M. G., L. D. Milner & L. T. Landmesser (2008) Spontaneous rhythmic activity in early chick spinal cord influences distinct motor axon pathfinding decisions. *Brain Research Reviews*, 57, 77-85.
- Hanus, J., C. Anderson & S. S. Wang (2015) RPE necroptosis in response to oxidative stress and in AMD. *Ageing Research Reviews*, 24, 286-298.
- Hanyu, N., K. Oguchi, N. Yanagisawa & H. Tsukagoshi (1982) DEGENERATION AND REGENERATION OF VENTRAL ROOT MOTOR FIBERS IN AMYOTROPHIC LATERAL SCLEROSIS - MORPHOMETRIC STUDIES OF CERVICAL VENTRAL ROOTS. *Journal of the Neurological Sciences*, 55, 99-115.
- Hardiman, O., A. Al-Chalabi, A. Chio, E. M. Corr, G. Logroscino, W. Robberecht, P. J. Shaw, Z. Simmons & L. H. van den Berg (2017) Amyotrophic lateral sclerosis. *Nature Reviews Disease Primers*, 3.
- Hardiman, O., L. H. van den Berg & M. C. Kiernan (2011) Clinical diagnosis and management of amyotrophic lateral sclerosis. *Nature Reviews Neurology*, 7, 639-649.
- Harty, R. C., T. H. Kim, E. A. Thomas, L. Cardamone, N. C. Jones, S. Petrou & V. C. Wimmer (2013) Axon initial segment structural plasticity in animal models of genetic and acquired epilepsy. *Epilepsy Research*, 105, 272-279.
- Hasegawa, M., T. Ara, T. Nonaka, F. Kametani, M. Yoshida, Y. Hashizume, T. G. Beach, E. Buratti, F. Baralle, M. Morita, I. Nakano, T. Oda, K. Tsuchiya & H. Akiyama (2008) Phosphorylated TDP-43 in frontotemporal lobar degeneration and amyotrophic lateral sclerosis. *Annals of Neurology*, 64, 60-70.

- Hatch, R. J., Y. Wei, D. Xia & J. Gotz (2017) Hyperphosphorylated tau causes reduced hippocampal CA1 excitability by relocating the axon initial segment. *Acta Neuropathologica*, 133, 717-730.
- Hebb, D. O., J. L. Martinez & S. E. Glickman (1994) THE ORGANIZATION OF BEHAVIOR - A NEUROPSYCHOLOGICAL THEORY - HEBB, DO. *Contemporary Psychology*, 39, 1018-1020.
- Hendel, A., R. O. Bak, J. T. Clark, A. B. Kennedy, D. E. Ryan, S. Roy, I. Steinfeld, B. D. Lunstad, R. J. Kaiser, A. B. Wilkens, R. Bacchetta, A. Tsalenko, D. Dellinger, L. Bruhn & M. H. Porteus (2015) Chemically modified guide RNAs enhance CRISPR-Cas genome editing in human primary cells. *Nature Biotechnology*, 33, 985-U232.
- Herzog, J. J., M. Deshpande, L. Shapiro, A. A. Rodal & S. Paradis (2017) TDP-43 misexpression causes defects in dendritic growth. *Scientific Reports*, 7.
- Hinman, J. D., M. N. Rasband & S. T. Carmichael (2013) Remodeling of the Axon Initial Segment After Focal Cortical and White Matter Stroke. *Stroke*, 44, 182-189.
- Hirabayashi, Y., N. Suzki, M. Tsuboi, T. A. Endo, T. Toyoda, J. Shinga, H. Koseki, M. Vidal & Y. Gotoh (2009) Polycomb Limits the Neurogenic Competence of Neural Precursor Cells to Promote Astrogenic Fate Transition. *Neuron*, 63, 600-613.
- Hockemeyer, D., F. Soldner, C. Beard, Q. Gao, M. Mitalipova, R. C. DeKever, G. E. Katibah, R. Amora, E. A. Boydston, B. Zeitler, X. D. Meng, J. C. Miller, L. Zhang, E. J. Rebar, P. D. Gregory, F. D. Urnov & R. Jaenisch (2009) Efficient targeting of expressed and silent genes in human ESCs and iPSCs using zinc-finger nucleases. *Nature Biotechnology*, 27, 851-U110.
- Howells, J., J. M. Matamala, S. B. Park, N. Garg, S. Vucic, H. Bostock, D. Burke & M. C. Kiernan (2018) In vivo evidence for reduced ion channel expression in motor axons of patients with amyotrophic lateral sclerosis. *Journal of Physiology-London*, 596, 5379-5396.
- Iijima, T. & T. Yoshimura (2019) A Perspective on the Role of Dynamic Alternative RNA Splicing in the Development, Specification, and Function of Axon Initial Segment. *Frontiers in Molecular Neuroscience*, 12.
- Inoue-Shibui, A., M. Kato, N. Suzuki, J. Kobayashi, Y. Takai, R. Izumi, Y. Kawauchi, H. Kuroda, H. Warita & M. Aoki (2019) Interstitial pneumonia and other adverse events in riluzole-administered amyotrophic lateral sclerosis patients: a retrospective observational study. *Bmc Neurology*, 19.
- Ito, Y., D. Ofengeim, A. Najafov, S. Das, S. Saberi, Y. Li, J. Hitomi, H. Zhu, H. B. Chen, L. Mayo, J. F. Geng, P. Amin, J. P. DeWitt, A. K. Mookhtiar, M. Florez, A. T. Ouchida, J. B. Fan, M. Pasparakis, M. A. Kelliher, J. Ravits & J. Y. Yuan (2016) RIPK1 mediates axonal degeneration by promoting inflammation and necroptosis in ALS. *Science*, 353, 603-608.
- Jamann, N., D. Dannehl, N. Lehmann, R. Wagener, C. Thielemann, C. Schultz, J. Staiger, M. H. P. Kole & M. Engelhardt (2021) Sensory input drives rapid homeostatic scaling of the axon initial segment in mouse barrel cortex. *Nature Communications*, 12.
- Jarkov, V., S. J. Allan, C. Bowen & H. Khanbarez Piezoelectric materials and systems for tissue engineering and implantable energy harvesting devices for biomedical applications. *International Materials Reviews*.
- Jensen, D. B., S. Klingenberg, K. P. Dimintyanova, J. Wienecke & C. F. Meehan (2020) Intramuscular Botulinum toxin A injections induce central changes to axon initial segments and cholinergic boutons on spinal motoneurons in rats. *Scientific Reports*, 10.

- Jessell, T. M. (2000) Neuronal specification in the spinal cord: Inductive signals and transcriptional codes. *Nature Reviews Genetics*, 1, 20-29.
- Jing, M., P. Zhang, G. F. Wang, J. S. Feng, L. Mesik, J. Z. Zeng, H. Q. Jiang, S. H. Wang, J. C. Looby, N. A. Guagliardo, L. W. Langma, J. Lu, Y. Zuo, D. A. Talmage, L. W. Role, P. Q. Barrett, L. I. Zhang, M. M. Luo, Y. Song, J. J. Zhu & Y. L. Li (2018) A genetically encoded fluorescent acetylcholine indicator for in vitro and in vivo studies. *Nature Biotechnology*, 36, 726-+.
- Johnston, C. A., B. R. Stanton, M. R. Turner, R. Gray, A. H. M. Blunt, D. Butt, M. A. Ampong, C. E. Shaw, P. N. Leigh & A. Al-Chalabi (2006) Amyotrophic lateral sclerosis in an urban setting - A population based study of inner city London. *Journal of Neurology*, 253, 1642-1643.
- Jones, R. A., C. Harrison, S. L. Eaton, M. L. Hurtado, L. C. Graham, L. Alkhamash, O. A. Oladiran, A. Gale, D. J. Lamont, H. Simpson, M. W. Simmen, C. Soeller, T. M. Wishart & T. H. Gillingwater (2017) Cellular and Molecular Anatomy of the Human Neuromuscular Junction. *Cell Reports*, 21, 2348-2356.
- Jorgensen, H. S., D. B. Jensen, K. P. Dimintyanova, V. S. Bonnevie, A. Hedegaard, J. Lehnhoff, M. Moldovan, L. Grondahl & C. F. Meehan (2021) Increased Axon Initial Segment Length Results in Increased Na⁺ Currents in Spinal Motoneurons at Symptom Onset in the G127X SOD1 Mouse Model of Amyotrophic Lateral Sclerosis. *Neuroscience*, 468, 247-264.
- Julian, T. H., N. Glasgow, A. D. F. Barry, T. Moll, C. Harvey, Y. C. Klimentidis, M. Newell, S. Zhang, M. P. Snyder, J. Cooper-Knock & P. J. Shaw (2021) Physical exercise is a risk factor for amyotrophic lateral sclerosis: Convergent evidence from Mendelian randomisation, transcriptomics and risk genotypes. *Ebiomedicine*, 68.
- Kanai, K., S. Kuwabara, S. Misawa, N. Tamura, K. Ogawara, M. Nakata, S. Sawai, T. Hattori & H. Bostock (2006) Altered axonal excitability properties in amyotrophic lateral sclerosis: impaired potassium channel function related to disease stage. *Brain*, 129, 953-962.
- Kanning, K. C., A. Kaplan & C. E. Henderson (2010) Motor Neuron Diversity in Development and Disease. *Annual Review of Neuroscience*, Vol 33, 33, 409-440.
- Katsumata, R., S. Ishigaki, M. Katsuno, K. Kawai, J. Sone, Z. Huang, H. Adachi, F. Tanaka, F. Urano & G. Sobue (2012) c-Abl Inhibition Delays Motor Neuron Degeneration in the G93A Mouse, an Animal Model of Amyotrophic Lateral Sclerosis. *Plos One*, 7.
- Keck, T., T. Toyozumi, L. Chen, B. Doiron, D. E. Feldman, K. Fox, W. Gerstner, P. G. Haydon, M. Hubener, H. K. Lee, J. E. Lisman, T. Rose, F. Sengpiel, D. Stellwagen, M. P. Stryker, G. G. Turrigiano & M. C. van Rossum (2017) Integrating Hebbian and homeostatic plasticity: the current state of the field and future research directions. *Philosophical Transactions of the Royal Society B-Biological Sciences*, 372.
- Kim, N. & S. J. Burden (2008) MuSK controls where motor axons grow and form synapses. *Nature Neuroscience*, 11, 19-27.
- Kim, S., D. Kim, S. W. Cho, J. Kim & J. S. Kim (2014) Highly efficient RNA-guided genome editing in human cells via delivery of purified Cas9 ribonucleoproteins. *Genome Research*, 24, 1012-1019.
- Klim, J. R., L. A. Williams, F. Limone, I. G. San Juan, B. N. Davis-Dusenbery, D. A. Mordes, A. Burberry, M. J. Steinbaugh, K. K. Gamage, R. Kirchner, R. Moccia, S. H. Casse, K. C. Chen, B. J. Wainger, C. J. Woolf & K. Eggan (2019) ALS-implicated protein TDP-43

- sustains levels of STMN2, a mediator of motor neuron growth and repair. *Nature Neuroscience*, 22, 167-+.
- Kole, M. H. P., S. U. IIschner, B. M. Kampa, S. R. Williams, P. C. Ruben & G. J. Stuart (2008) Action potential generation requires a high sodium channel density in the axon initial segment. *Nature Neuroscience*, 11, 178-186.
- Kraemer, B. C., T. Schuck, J. M. Wheeler, L. C. Robinson, J. Q. Trojanowski, V. M. Y. Lee & G. D. Schellenberg (2010) Loss of murine TDP-43 disrupts motor function and plays an essential role in embryogenesis. *Acta Neuropathologica*, 119, 409-419.
- Kuba, H., Y. Oichi & H. Ohmori (2010) Presynaptic activity regulates Na⁺ channel distribution at the axon initial segment. *Nature*, 465, 1075-U136.
- Kuo, J. J., M. Schonewille, T. Siddique, A. N. A. Schults, R. G. Fu, P. R. Bar, R. Anelli, C. J. Heckman & A. B. A. Kroese (2004) Hyperexcitability of cultured spinal motoneurons from presymptomatic ALS mice. *Journal of Neurophysiology*, 91, 571-575.
- Kuo, J. J., T. Siddique, R. Fu & C. J. Heckman (2005) Increased persistent Na⁺ current and its effect on excitability in motoneurons cultured from mutant SOD1 mice. *Journal of Physiology-London*, 563, 843-854.
- Lagier-Tourenne, C., M. Polymenidou, K. R. Hutt, A. Q. Vu, M. Baughn, S. C. Huelga, K. M. Clutario, S. C. Ling, T. Y. Liang, C. Mazur, E. Wancewicz, A. S. Kim, A. Watt, S. Freier, G. G. Hicks, J. P. Donohue, L. Shiue, C. F. Bennett, J. Ravits, D. W. Cleveland & G. W. Yeo (2012) Divergent roles of ALS-linked proteins FUS/TLS and TDP-43 intersect in processing long pre-mRNAs. *Nature Neuroscience*, 15, 1488-1497.
- Lee, I. C., T. M. Chang, J. S. Liang & S. Y. Li (2019) KCNQ2 mutations in childhood nonlesional epilepsy: Variable phenotypes and a novel mutation in a case series. *Molecular Genetics & Genomic Medicine*, 7.
- Lee, K. J., P. Dietrich & T. M. Jessell (2000) Genetic ablation reveals that the roof plate is essential for dorsal interneuron specification. *Nature*, 403, 734-740.
- Lee, K. J., M. Mendelsohn & T. M. Jessell (1998) Neuronal patterning by BMPs: a requirement for GDF7 in the generation of a discrete class of commissural interneurons in the mouse spinal cord. *Genes & Development*, 12, 3394-3407.
- Leterrier, C. (2018) The Axon Initial Segment: An Updated Viewpoint. *Journal of Neuroscience*, 38, 2135-2145.
- Lezmy, J., M. Lipinsky, Y. Khrapunsky, E. Patrich, L. Shalom, A. Peretz, I. A. Fleidervish & B. Attali (2017) M-current inhibition rapidly induces a unique CK2-dependent plasticity of the axon initial segment. *Proceedings of the National Academy of Sciences of the United States of America*, 114, E10234-E10243.
- Li, B. S., J. P. Virtanen, A. Oeltermann, C. Schwarz, M. A. Giese, U. Ziemann & A. Benali (2017) Lifting the veil on the dynamics of neuronal activities evoked by transcranial magnetic stimulation. *Elife*, 6.
- Li, X., Y. Z. Tao, R. Bradley, Z. W. Du, Y. L. Tao, L. H. Kong, Y. Dong, J. Jones, Y. W. Yan, C. R. K. Harder, L. M. Friedman, M. Bilal, B. Hoffmann & S. C. Zhang (2018) Fast Generation of Functional Subtype Astrocytes from Human Pluripotent Stem Cells. *Stem Cell Reports*, 11, 998-1008.
- Li, X. Y., Y. Kumar, H. Zempel, E. M. Mandelkow, J. Biernat & E. Mandelkow (2011) Novel diffusion barrier for axonal retention of Tau in neurons and its failure in neurodegeneration. *Embo Journal*, 30, 4825-4837.
- Liang, X. Q., J. Potter, S. Kumar, Y. F. Zou, R. Quintanilla, M. Sridharan, J. Carte, W. Chen, N. Roark, S. Ranganathan, N. Ravinder & J. D. Chesnut (2015) Rapid and highly efficient

- mammalian cell engineering via Cas9 protein transfection. *Journal of Biotechnology*, 208, 44-53.
- Liddel, S. A., K. A. Guttenplan, L. E. C. Larke, F. C. Bennett, C. J. Bohlen, L. Schirmer, M. L. Bennett, A. E. Munch, W. S. Chung, T. C. Peterson, D. K. Wilton, A. Frouin, B. A. Napier, N. Panicker, M. Kumar, M. S. Buckwalter, D. H. Rowitch, V. L. Dawson, T. M. Dawson, B. Stevens & B. Barres (2017) Neurotoxic reactive astrocytes are induced by activated microglia. *Nature*, 541, 481-487.
- Lin, C. Y., C. L. Wu, K. Z. Lee, Y. J. Chen, P. H. Zhang, C. Y. Chang, H. J. Han, S. Z. Lin & H. J. Tsai (2019) Extracellular Pdgfra enhances neurite outgrowth of motoneurons through Nogo66/NgR-independent targeting of NogoA. *Elife*, 8.
- Lindhout, F. W., R. Kooistra, S. Portegies, L. J. Herstel, R. Stucchi, B. L. Snoek, A. Altelaar, H. D. MacGillavry, C. J. Wierenga & C. C. Hoogenraad (2020) Quantitative mapping of transcriptome and proteome dynamics during polarization of human iPSC-derived neurons. *Elife*, 9.
- Liu, J. P., E. Laufer & T. M. Jessell (2001) Assigning the positional identity of spinal motor neurons: Rostrocaudal patterning of Hox-c expression by FGFs, Gdf11, and retinoids. *Neuron*, 32, 997-1012.
- Liu, J. W., Y. Li, J. W. Niu, L. Zhang, J. Fan, Y. Z. Guan, L. Y. Cui & M. S. Liu (2021) Fasciculation differences between ALS and non-ALS patients: an ultrasound study. *Bmc Neurology*, 21.
- Logroscino, G., B. J. Traynor, O. Hardiman, A. Chio, D. Mitchell, R. J. Swingler, A. Millul, E. Benn, E. Beghi & Eurals (2010) Incidence of amyotrophic lateral sclerosis in Europe. *Journal of Neurology Neurosurgery and Psychiatry*, 81, 385-390.
- Lomo, T. (2003) The discovery of long-term potentiation. *Philosophical Transactions of the Royal Society B-Biological Sciences*, 358, 617-620.
- Ma, X. R., M. Prudencio, Y. Koike, S. C. Vatsavayai, G. Kim, F. Harbinski, A. Briner, C. M. Rodriguez, C. Guo, T. Akiyama, H. B. Schmidt, B. B. Cummings, D. W. Wyatt, K. Kurylo, G. Miller, S. Mekhoubad, N. Sallee, G. Mekonnen, L. Ganser, J. D. Rubien, K. Jansen-West, C. N. Cook, S. Pickles, B. Oskarsson, N. R. Graff-Radford, B. F. Boeve, D. S. Knopman, R. C. Petersen, D. W. Dickson, J. Shorter, S. Myong, E. M. Green, W. W. Seeley, L. Petrucelli & A. D. Gitler (2022) TDP-43 represses cryptic exon inclusion in the FTD-ALS gene UNC13A. *Nature*, 603, 124-130.
- Machado, C. B., K. C. Kanning, P. Kreis, D. Stevenson, M. Crossley, M. Nowak, M. Iacovino, M. Kyba, D. Chambers, E. Blanc & I. Lieberam (2014) Reconstruction of phrenic neuron identity in embryonic stem cell-derived motor neurons. *Development*, 141, 784-794.
- Machado, C. B., P. Pluchon, P. Harley, M. Rigby, V. G. Sabater, D. C. Stevenson, S. Hynes, A. Lowe, J. Burrone, V. Viasnoff & I. Lieberam (2019) In Vitro Modeling of Nerve-Muscle Connectivity in a Compartmentalized Tissue Culture Device. *Advanced Biosystems*, 3.
- Mack, T. G. A., M. Reiner, B. Beirowski, W. Q. Mi, M. Emanuelli, D. Wagner, D. Thomson, T. Gillingwater, F. Court, L. Conforti, F. S. Fernando, A. Tarlton, C. Andressen, K. Addicks, G. Magni, R. R. Ribchester, V. H. Perry & M. P. Coleman (2001) Wallerian degeneration of injured axons and synapses is delayed by a Ube4b/Nmnat chimeric gene. *Nature Neuroscience*, 4, 1199-1206.
- Mackenzie, I. R. A., E. H. Bigio, P. G. Ince, F. Geser, M. Neumann, N. J. Cairns, L. K. Kwong, M. S. Forman, J. Ravits, H. Stewart, A. Eisen, L. McClusky, H. A. Kretschmar, C. M. Monoranu, J. R. Highley, J. Kirby, T. Siddique, P. J. Shaw, V. M. Y. Lee & J. Q. Trojanowski (2007) Pathological TDP-43 distinguishes sporadic amyotrophic lateral

- sclerosis from amyotrophic lateral sclerosis with SOD1 mutations. *Annals of Neurology*, 61, 427-434.
- Mandegar, M. A., N. Huebsch, E. B. Frolov, E. Shin, A. Truong, M. P. Olvera, A. H. Chan, Y. Miyaoka, K. Holmes, C. I. Spencer, L. M. Judge, D. E. Gordon, T. V. Eskildsen, J. E. Villalta, M. A. Horlbeck, L. A. Gilbert, N. J. Krogan, S. P. Sheikh, J. S. Weissman, L. S. Qi, P. L. So & B. R. Conklin (2016) CRISPR Interference Efficiently Induces Specific and Reversible Gene Silencing in Human iPSCs. *Cell Stem Cell*, 18, 541-553.
- Marchetto, M. C. N., A. R. Muotri, Y. L. Mu, A. M. Smith, G. G. Cezar & F. H. Gage (2008) Non-Cell-Autonomous Effect of Human SOD1(G37R) Astrocytes on Motor Neurons Derived from Human Embryonic Stem Cells. *Cell Stem Cell*, 3, 649-657.
- Martinez-Silva, M. D., R. D. Imhoff-Manuel, A. Sharma, C. J. Heckman, N. A. Shneider, F. Roselli, D. Zytynicki & M. Manuel (2018) Hypoexcitability precedes denervation in the large fast-contracting motor units in two unrelated mouse models of ALS. *Elife*, 7.
- Martins, J. M. F., C. Fischer, A. Urzi, R. Vidal, S. Kunz, P. L. Ruffault, L. Kabuss, I. Hube, E. Gazzero, C. Birchmeier, S. Spuler, S. Sauer & M. Gouti (2020) Self-Organizing 3D Human Trunk Neuromuscular Organoids. *Cell Stem Cell*, 26, 172-+.
- Mehta, P. R., A. R. Jones, S. Opie-Martin, A. Shatunov, A. Iacoangeli, A. Al Khleifat, B. N. Smith, S. Topp, K. E. Morrison, P. J. Shaw, C. E. Shaw, S. Morgan, A. Pittman & A. Al-Chalabi (2019) Younger age of onset in familial amyotrophic lateral sclerosis is a result of pathogenic gene variants, rather than ascertainment bias. *Journal of Neurology Neurosurgery and Psychiatry*, 90, 268-271.
- Mejzini, R., L. L. Flynn, L. L. Pitout, S. Fletcher, S. D. Wilton & P. A. Akkari (2019) ALS Genetics, Mechanisms, and Therapeutics: Where Are We Now? *Frontiers in Neuroscience*, 13.
- Melamed, Z., J. Lopez-Erauskin, M. W. Baughn, O. Zhang, K. Drenner, YingSun, F. Freyermuth, M. A. McMahan, M. S. Beccari, J. W. Artates, T. Ohkubo, M. Rodriguez, N. W. Lin, D. M. Wu, C. F. Bennetts, F. Rigos, S. Da Cruz, J. Ravits, C. Lagier-Tourenne & D. W. Cleveland (2019) Premature polyadenylation-mediated loss of stathmin-2 is a hallmark of TDP-43-dependent neurodegeneration. *Nature Neuroscience*, 22, 180-+.
- Militello, G., M. R. Hosen, Y. Ponomareva, P. Gellert, T. Weirick, D. John, S. M. Hindi, K. Mamchaoui, V. Mouly, C. Doring, L. D. Zhang, M. Nakamura, A. Kumar, S. Fukada, S. Dimmeler & S. Uchida (2018) A novel long non-coding RNA Myolinc regulates myogenesis through TDP-43 and Filip1. *Journal of Molecular Cell Biology*, 10, 102-117.
- Mills, K. R. (2010) Characteristics of fasciculations in amyotrophic lateral sclerosis and the benign fasciculation syndrome. *Brain*, 133, 3458-3469.
- Moloney, E. B., F. de Winter & J. Verhaagen (2014) ALS as a distal axonopathy: molecular mechanisms affecting neuromuscular junction stability in the presymptomatic stages of the disease. *Frontiers in Neuroscience*, 8.
- Morgan, J. E., A. Prola, V. Mariot, V. Pini, J. H. Meng, C. Hourde, J. Dumonceaux, F. Conti, F. Relaix, F. J. Authier, L. Tiret, F. Muntoni & M. Bencze (2018) Necroptosis mediates myofibre death in dystrophin-deficient mice. *Nature Communications*, 9.
- Morgan, P. J., R. Bourboulou, C. Filippi, J. Koenig-Gambini & J. Epsztein (2019) Kv1.1 contributes to a rapid homeostatic plasticity of intrinsic excitability in CA1 pyramidal neurons in vivo. *Elife*, 8.
- Mori, F., M. Tada, T. Kon, Y. Miki, K. Tanji, H. Kurotaki, M. Tomiyama, T. Ishihara, O. Onodera, A. Kakita & K. Wakabayashi (2019) Phosphorylated TDP-43 aggregates in skeletal and cardiac muscle are a marker of myogenic degeneration in amyotrophic lateral sclerosis and various conditions. *Acta Neuropathologica Communications*, 7.

- Mou, H. W., J. L. Smith, L. T. Peng, H. Yin, J. Moore, X. O. Zhang, C. Q. Song, A. Sheel, Q. Q. Wu, D. M. Ozata, Y. X. Li, D. G. Anderson, C. P. Emerson, E. J. Sontheimer, M. J. Moore, Z. P. Weng & W. Xue (2017) CRISPR/Cas9-mediated genome editing induces exon skipping by alternative splicing or exon deletion. *Genome Biology*, 18.
- Muller, D., P. Cherukuri, K. Henningfeld, C. H. Poh, L. Wittler, P. Grote, O. Schluter, J. Schmidt, J. Laborda, S. R. Bauer, R. M. Brownstone & T. Marquardt (2014) Dlk1 Promotes a Fast Motor Neuron Biophysical Signature Required for Peak Force Execution. *Science*, 343, 1264-1266.
- Nagai, M., D. B. Re, T. Nagata, A. Chalazonitis, T. M. Jessell, H. Wichterle & S. Przedborski (2007) Astrocytes expressing ALS-linked mutated SOD1 release factors selectively toxic to motor neurons. *Nature Neuroscience*, 10, 615-622.
- Nakata, M., S. Kuwabara, K. Kanai, S. Misawa, N. Tamura, S. Sawai, T. Hattori & H. Bostock (2006) Distal excitability changes in motor axons in amyotrophic lateral sclerosis. *Clinical Neurophysiology*, 117, 1444-1448.
- Narayanan, R. K., M. Mangelsdorf, A. Panwar, T. J. Butler, P. G. Noakes & R. H. Wallace (2013) Identification of RNA bound to the TDP-43 ribonucleoprotein complex in the adult mouse brain. *Amyotrophic Lateral Sclerosis and Frontotemporal Degeneration*, 14, 252-260.
- Naujock, M., N. Stanslowsky, S. Bufler, M. Naumann, P. Reinhardt, J. Sternecker, E. Kefalakes, C. Kassebaum, F. Bursch, X. Lojewski, A. Storch, M. Frickenhaus, T. M. Boeckers, S. Putz, M. Demestre, S. Liebau, M. Klingenstein, A. C. Ludolph, R. Dengler, K. S. Kim, A. Hermann, F. Wegner & S. Petri (2016) 4-Aminopyridine Induced Activity Rescues Hypoexcitable Motor Neurons from Amyotrophic Lateral Sclerosis Patient-Derived Induced Pluripotent Stem Cells. *Stem Cells*, 34, 1563-1575.
- Nelson, A. D. & P. M. Jenkins (2016) The Splice Is Right: ANK3 and the Control of Cortical Circuits. *Biological Psychiatry*, 80, 263-265.
- Neumann, M., D. M. Sampathu, L. K. Kwong, A. C. Truax, M. C. Micsenyi, T. T. Chou, J. Bruce, T. Schuck, M. Grossman, C. M. Clark, L. F. McCluskey, B. L. Miller, E. Masliah, I. R. Mackenzie, H. Feldman, W. Feiden, H. A. Kretschmar, J. Q. Trojanowski & V. M. Y. Lee (2006) Ubiquitinated TDP-43 in frontotemporal lobar degeneration and amyotrophic lateral sclerosis. *Science*, 314, 130-133.
- Nonaka, T., M. Masuda-Suzukake, T. Arai, Y. Hasegawa, H. Akatsu, T. Obi, M. Yoshida, S. Murayama, D. M. A. Mann, H. Akiyama & M. Hasegawa (2013) Prion-like Properties of Pathological TDP-43 Aggregates from Diseased Brains. *Cell Reports*, 4, 124-134.
- Norman, M. D. A., S. A. Ferreira, G. M. Jowett, L. Bozec & E. Gentleman (2021) Measuring the elastic modulus of soft culture surfaces and three-dimensional hydrogels using atomic force microscopy. *Nature Protocols*, 16.
- O'Leary, T., M. C. W. van Rossum & D. J. A. Wyllie (2010) Homeostasis of intrinsic excitability in hippocampal neurones: dynamics and mechanism of the response to chronic depolarization. *Journal of Physiology-London*, 588, 157-170.
- Ogiwara, I., H. Miyamoto, N. Morita, N. Atapour, E. Mazaki, I. Inoue, T. Takeuchi, S. Itoharu, Y. Yanagawa, K. Obata, T. Furuichi, T. K. Hensch & K. Yamakawa (2007) Na(v)1.1 localizes to axons of parvalbumin-positive inhibitory interneurons: A circuit basis for epileptic seizures in mice carrying an Scn1a gene mutation. *Journal of Neuroscience*, 27, 5903-5914.
- Oliveri, M., C. Caltagirone, M. M. Filippi, R. Traversa, P. Cicinelli, P. Pasqualetti & P. M. Rossini (2000) Paired transcranial magnetic stimulation protocols reveal a pattern of

- inhibition and facilitation in the human parietal cortex. *Journal of Physiology-London*, 529, 461-468.
- Ordovas, L., R. Boon, M. Pistoni, Y. M. Chen, E. Wolfs, W. T. Guo, R. Sambathkumar, S. Bobis-Wozowicz, N. Helsen, J. Vanhove, P. Berckmans, Q. Cai, K. Vanuytsel, K. Eggermont, V. Vanslembrouck, B. Z. Schmidt, S. Raitano, L. Van Den Bosch, Y. Nahmias, T. Cathomen, T. Struys & C. M. Verfaillie (2015) Efficient Recombinase-Mediated Cassette Exchange in hPSCs to Study the Hepatocyte Lineage Reveals AAVS1 Locus-Mediated Transgene Inhibition. *Stem Cell Reports*, 5, 918-931.
- Osaki, T., S. G. M. Uzel & R. D. Kamm (2018) Microphysiological 3D model of amyotrophic lateral sclerosis (ALS) from human iPSC-derived muscle cells and optogenetic motor neurons. *Science Advances*, 4, 15.
- Oskarsson, B., D. K. Horton & H. Mitsumoto (2015) Potential Environmental Factors in Amyotrophic Lateral Sclerosis. *Neurologic Clinics*, 33, 877-+.
- Pan-Vazquez, A., W. Wefelmeyer, V. G. Sabater, G. Neves & J. Burrone (2020) Activity-Dependent Plasticity of Axo-axonic Synapses at the Axon Initial Segment. *Neuron*, 106, 265-+.
- Papadeas, S. T., S. E. Kraig, C. O'Banion, A. C. Lepore & N. J. Maragakis (2011) Astrocytes carrying the superoxide dismutase 1 (SOD1(G93A)) mutation induce wild-type motor neuron degeneration in vivo. *Proceedings of the National Academy of Sciences of the United States of America*, 108, 17803-17808.
- Paquet, D., D. Kwart, A. Chen, A. Sproul, S. Jacob, S. Teo, K. M. Olsen, A. Gregg, S. Noggle & M. Tessier-Lavigne (2016) Efficient introduction of specific homozygous and heterozygous mutations using CRISPR/Cas9. *Nature*, 533, 125-+.
- Pardo, A. C., V. Wong, L. M. Benson, M. Dykes, K. Tanaka, J. D. Rothstein & N. J. Maragakis (2006) Loss of the astrocyte glutamate transporter GLT1 modifies disease in SOD1(G93A) mice. *Experimental Neurology*, 201, 120-130.
- Paredes-Redondo, A., P. Harley, E. Maniati, D. Ryan, S. Louzada, J. H. Meng, A. Kowala, B. Y. Fu, F. T. Yang, P. T. Liu, S. Marino, O. Pourquie, F. Muntoni, J. Wang, I. Lieberam & Y. Y. Lin (2021) Optogenetic modeling of human neuromuscular circuits in Duchenne muscular dystrophy with CRISPR and pharmacological corrections. *Science Advances*, 7.
- Park, S. B., M. C. Kiernan & S. Vucic (2017) Axonal Excitability in Amyotrophic Lateral Sclerosis. *Neurotherapeutics*, 14, 78-90.
- Parkhouse, W. S., L. Cunningham, I. McFee, J. M. L. Miller, D. Whitney, S. L. Pelech & C. Krieger (2008) Neuromuscular dysfunction in the mutant superoxide dismutase mouse model of amyotrophic lateral sclerosis. *Amyotrophic Lateral Sclerosis*, 9, 24-34.
- Pawlowski, M., D. Ortmann, A. Bertero, J. M. Tavares, R. A. Pedersen, L. Vallier & M. R. N. Kotter (2017) Inducible and Deterministic Forward Programming of Human Pluripotent Stem Cells into Neurons, Skeletal Myocytes, and Oligodendrocytes. *Stem Cell Reports*, 8, 803-812.
- Phukan, J., M. Elamin, P. Bede, N. Jordan, L. Gallagher, S. Byrne, C. Lynch, N. Pender & O. Hardiman (2012) The syndrome of cognitive impairment in amyotrophic lateral sclerosis: a population-based study. *Journal of Neurology Neurosurgery and Psychiatry*, 83, 102-108.
- Piotrkiewicz, M., L. Kudina, J. Mierzejewska & I. Hausmanowa-Petrusewicz (2008) Analysis of double discharges in amyotrophic lateral sclerosis. *Muscle & Nerve*, 38, 845-854.

- Poesen, K. & P. Van Damme (2019) Diagnostic and Prognostic Performance of Neurofilaments in ALS. *Frontiers in Neurology*, 9.
- Pollari, E., G. Goldsteins, G. Bart, J. Koistinaho & R. Giniatullin (2014) The role of oxidative stress in degeneration of the neuromuscular junction in amyotrophic lateral sclerosis. *Frontiers in Cellular Neuroscience*, 8.
- Pozo, K. & Y. Goda (2010) Unraveling Mechanisms of Homeostatic Synaptic Plasticity. *Neuron*, 66, 337-351.
- Prasad, A., V. Bharathi, V. Sivalingam, A. Girdhar & B. K. Patel (2019) Molecular Mechanisms of TDP-43 Misfolding and Pathology in Amyotrophic Lateral Sclerosis. *Frontiers in Molecular Neuroscience*, 12.
- Quadrato, G., T. Nguyen, E. Z. Macosko, J. L. Sherwood, S. M. Yang, D. R. Berger, N. Maria, J. Scholvin, M. Goldman, J. P. Kinney, E. S. Boyden, J. W. Lichtman, Z. M. Williams, S. A. McCarroll & P. Arlotta (2017) Cell diversity and network dynamics in photosensitive human brain organoids. *Nature*, 545, 48-+.
- Rao, L. J., Y. Qian, A. Khodabukus, T. Ribar & N. Bursac (2018) Engineering human pluripotent stem cells into a functional skeletal muscle tissue. *Nature Communications*, 9.
- Re, D. B., V. Le Verche, C. H. Yu, M. W. Amoroso, K. A. Politi, S. Phani, B. Ikiz, L. Hoffmann, M. Koolen, T. Nagata, D. Papadimitriou, P. Nagy, H. Mitsumoto, S. Kariya, H. Wichterle, C. E. Henderson & S. Przedborski (2014) Necroptosis Drives Motor Neuron Death in Models of Both Sporadic and Familial ALS. *Neuron*, 81, 1001-1008.
- Ribeiro, S., A. C. Gomes, I. Etxebarria, S. Lanceros-Mendez & C. Ribeiro (2018) Electroactive biomaterial surface engineering effects on muscle cells differentiation. *Materials Science & Engineering C-Materials for Biological Applications*, 92, 868-874.
- Rojas, F., D. Gonzalez, N. Cortes, E. Ampuero, D. E. Hernandez, E. Fritz, S. Abarzua, A. Martinez, A. A. Elorza, A. Alvarez, F. Court & B. van Zundert (2015) Reactive oxygen species trigger motoneuron death in non-cell-autonomous models of ALS through activation of c-Abl signaling. *Frontiers in Cellular Neuroscience*, 9.
- Rosen, D. R., T. Siddique, D. Patterson, D. A. Figlewicz, P. Sapp, A. Hentati, D. Donaldson, J. Goto, J. P. Oregan, H. X. Deng, Z. Rahmani, A. Krizus, D. McKenneyasek, A. Cayabyab, S. M. Gaston, R. Berger, R. E. Tanzi, J. J. Halperin, B. Herzfeldt, R. Vandenberg, W. Y. Hung, T. Bird, G. Deng, D. W. Mulder, C. Smyth, N. G. Laing, E. Soriano, M. A. Pericakvance, J. Haines, G. A. Rouleau, J. S. Gusella, H. R. Horvitz & R. H. Brown (1993) MUTATIONS IN CU/ZN SUPEROXIDE-DISMUTASE GENE ARE ASSOCIATED WITH FAMILIAL AMYOTROPHIC-LATERAL-SCLEROSIS. *Nature*, 362, 59-62.
- Rosenberg, T., S. Gal-Ben-Ari, D. C. Dieterich, M. R. Kreutz, N. E. Ziv, E. Gundelfinger & K. Rosenblum (2014) The roles of protein expression in synaptic plasticity and memory consolidation. *Frontiers in Molecular Neuroscience*, 7.
- Rossor, A. M., B. Kalmar, L. Greensmith & M. M. Reilly (2012) The distal hereditary motor neuropathies. *Journal of Neurology Neurosurgery and Psychiatry*, 83, 6-14.
- Roth, B. L. (2016) DREADDs for Neuroscientists. *Neuron*, 89, 683-694.
- Rothstein, J. D., M. DykesHoberg, C. A. Pardo, L. A. Bristol, L. Jin, R. W. Kuncl, Y. Kanai, M. A. Hediger, Y. F. Wang, J. P. Schielke & D. F. Welty (1996) Knockout of glutamate transporters reveals a major role for astroglial transport in excitotoxicity and clearance of glutamate. *Neuron*, 16, 675-686.
- Sando, R., E. Bushong, Y. C. Zhu, M. Huang, C. Considine, S. Phan, S. Y. Ju, M. Uytiepo, M. Ellisman & A. Maximov (2017) Assembly of Excitatory Synapses in the Absence of Glutamatergic Neurotransmission. *Neuron*, 94, 312-+.

- Sanes, J. R. & J. W. Lichtman (1999) Development of the vertebrate neuromuscular junction. *Annual Review of Neuroscience*, 22, 389-442.
- Sareen, D., J. G. O'Rourke, P. Meera, A. Muhammad, S. Grant, M. Simpkinson, S. Bell, S. Carmona, L. Ornelas, A. Sahabian, T. Gendron, L. Petrucelli, M. Baughn, J. Ravits, M. B. Harms, F. Rigo, C. F. Bennett, T. S. Otis, C. N. Svendsen & R. H. Baloh (2013) Targeting RNA Foci in iPSC-Derived Motor Neurons from ALS Patients with a C9ORF72 Repeat Expansion. *Science Translational Medicine*, 5.
- Sasaki, S. & S. Maruyama (1992) INCREASE IN DIAMETER OF THE AXONAL INITIAL SEGMENT IS AN EARLY CHANGE IN AMYOTROPHIC-LATERAL-SCLEROSIS. *Journal of the Neurological Sciences*, 110, 114-120.
- (1994) SYNAPSE LOSS IN ANTERIOR HORN NEURONS IN AMYOTROPHIC-LATERAL-SCLEROSIS. *Acta Neuropathologica*, 88, 222-227.
- Sasaki, S., H. Warita, K. Abe & M. Iwata (2005) Impairment of axonal transport in the axon hillock and the initial segment of anterior horn neurons in transgenic mice with a G93A mutant SOD1 gene. *Acta Neuropathologica*, 110, 48-56.
- Scanziani, M. & M. Hausser (2009) Electrophysiology in the age of light. *Nature*, 461, 930-939.
- Scotter, E. L., H. J. Chen & C. E. Shaw (2015) TDP-43 Proteinopathy and ALS: Insights into Disease Mechanisms and Therapeutic Targets. *Neurotherapeutics*, 12, 352-363.
- Scotter, E. L., C. Vance, A. L. Nishimura, Y. B. Lee, H. J. Chen, H. Urwin, V. Sardone, J. C. Mitchell, B. Rogelj, D. C. Rubinsztein & C. E. Shaw (2014) Differential roles of the ubiquitin proteasome system and autophagy in the clearance of soluble and aggregated TDP-43 species. *Journal of Cell Science*, 127, 1263-1278.
- Seifert, G., K. Schilling & C. Steinhauser (2006) Astrocyte dysfunction in neurological disorders: a molecular perspective. *Nature Reviews Neuroscience*, 7, 194-206.
- Sheets, K., J. Wang, S. Meehan, P. Sharma, C. Ng, M. Khan, B. Koons, B. Behkam & A. S. Nain (2013) Cell-Fiber Interactions on Aligned and Suspended Nanofiber Scaffolds. *Journal of Biomaterials and Tissue Engineering*, 3, 355-368.
- Shepherd, J. D., G. Rumbaugh, J. Wu, S. Chowdhury, N. Plath, D. Kuhl, R. L. Haganir & P. F. Worley (2006) Arc/Arg3.1 mediates homeostatic synaptic scaling of AMPA receptors. *Neuron*, 52, 475-484.
- Shimizu, T., Y. Fujimaki, S. Nakatani-Enomoto, S. Matsubara, K. Watabe, P. M. Rossini & Y. Ugawa (2014) Complex fasciculation potentials and survival in amyotrophic lateral sclerosis. *Clinical Neurophysiology*, 125, 1059-1064.
- Shin, J. E., B. R. Miller, E. Babetto, Y. Cho, Y. Sasaki, S. Qayum, E. V. Russler, V. Cavalli, J. Milbrandt & A. DiAntonio (2012) SCG10 is a JNK target in the axonal degeneration pathway. *Proceedings of the National Academy of Sciences of the United States of America*, 109, E3696-E3705.
- Sigler, A., W. C. Oh, C. Imig, B. Altas, H. Kawabe, B. H. Cooper, H. B. Kwon, J. S. Rhee & N. Brose (2017) Formation and Maintenance of Functional Spines in the Absence of Presynaptic Glutamate Release. *Neuron*, 94, 304-+.
- Siklos, L., J. Engelhardt, Y. Harati, R. G. Smith, F. Joo & S. H. Appel (1996) Ultrastructural evidence for altered calcium in motor nerve terminals in amyotrophic lateral sclerosis. *Annals of Neurology*, 39, 203-216.
- Smethurst, P., J. Newcombe, C. Troakes, R. Simone, Y. R. Chen, R. Patani & K. Sidle (2016) In vitro prion-like behaviour of TDP-43 in ALS. *Neurobiology of Disease*, 96, 236-247.
- Sofroniew, M. V. & H. V. Vinters (2010) Astrocytes: biology and pathology. *Acta Neuropathologica*, 119, 7-35.

- Sohn, P. D., C. T. L. Huang, R. Yan, L. Fan, T. E. Tracy, C. M. Camargo, K. M. Montgomery, T. Arhar, S. A. Mok, R. Freilich, J. Baik, M. N. He, S. C. Gong, E. D. Roberson, C. M. Karch, J. E. Gestwicki, K. Xu, K. S. Kosik & L. Gan (2019) Pathogenic Tau Impairs Axon Initial Segment Plasticity and Excitability Homeostasis. *Neuron*, 104, 458-+.
- Song, J. H., C. S. Huang, K. Nagata, J. Z. Yeh & T. Narahashi (1997) Differential action of riluzole on tetrodotoxin-sensitive and tetrodotoxin-resistant sodium channels. *Journal of Pharmacology and Experimental Therapeutics*, 282, 707-714.
- Soraru, G., V. Orsetti, E. Buratti, F. Baralle, V. Cima, M. Volpe, C. D'Ascenzo, A. Palmieri, K. Koutsikos, E. Pegoraro & C. Angelini (2010) TDP-43 in skeletal muscle of patients affected with amyotrophic lateral sclerosis. *Amyotrophic Lateral Sclerosis*, 11, 240-U35.
- Sreedharan, J., I. P. Blair, V. B. Tripathi, X. Hu, C. Vance, B. Rogelj, S. Ackerley, J. C. Durnall, K. L. Williams, E. Buratti, F. Baralle, J. de Belleruche, J. D. Mitchell, P. N. Leigh, A. Al-Chalabi, C. C. Miller, G. Nicholson & C. E. Shaw (2008) TDP-43 mutations in familial and sporadic amyotrophic lateral sclerosis. *Science*, 319, 1668-1672.
- Stifani, N. (2014) Motor neurons and the generation of spinal motor neuron diversity. *Frontiers in Cellular Neuroscience*, 8, 1-22.
- Sudhof, T. C. (2012) The Presynaptic Active Zone. *Neuron*, 75, 11-25.
- Taha, D. M., B. E. Clarke, C. E. Hall, G. E. Tyzack, O. J. Ziff, L. Greensmith, B. Kalmar, M. Ahmed, A. Alam, E. P. Thelin, N. M. Garcia, A. Helmy, C. R. Sibley & R. Patani (2022) Astrocytes display cell autonomous and diverse early reactive states in familial amyotrophic lateral sclerosis. *Brain*.
- Takahashi, K., K. Tanabe, M. Ohnuki, M. Narita, T. Ichisaka, K. Tomoda & S. Yamanaka (2007) Induction of pluripotent stem cells from adult human fibroblasts by defined factors. *Cell*, 131, 861-872.
- Takahashi, K. & S. Yamanaka (2006) Induction of pluripotent stem cells from mouse embryonic and adult fibroblast cultures by defined factors. *Cell*, 126, 663-676.
- Taylor, A. L. (2012) What we talk about when we talk about capacitance measured with the voltage-clamp step method. *Journal of Computational Neuroscience*, 32, 167-175.
- Taylor, J. P., R. H. Brown & D. W. Cleveland (2016) Decoding ALS: from genes to mechanism. *Nature*, 539, 197-206.
- Thiagarajan, T. C., E. S. Piedras-Renteria & R. W. Tsien (2002) alpha- and beta CaMKII: Inverse regulation by neuronal activity and opposing effects on synaptic strength. *Neuron*, 36, 1103-1114.
- Tiwari, N., A. Pataskar, S. Peron, S. Thakurela, S. K. Sahu, M. Figueres-Onate, N. Marichal, L. Lopez-Mascaraque, V. K. Tiwari & B. Berninger (2018) Stage-Specific Transcription Factors Drive Astroglialogenesis by Remodeling Gene Regulatory Landscapes. *Cell Stem Cell*, 23, 557-+.
- Tovar-y-Romo, L. B., U. N. Ramirez-Jarquín, R. Lazo-Gomez & R. Tapia (2014) Trophic factors as modulators of motor neuron physiology and survival: implications for ALS therapy. *Frontiers in Cellular Neuroscience*, 8.
- Tripathi, P., N. Rodriguez-Muela, J. R. Klim, A. S. de Boer, S. Agrawal, J. Sandoe, C. S. Lopes, K. S. Ogliari, L. A. Williams, M. Shear, L. L. Rubin, K. Eggan & Q. Zhou (2017) Reactive Astrocytes Promote ALS-like Degeneration and Intracellular Protein Aggregation in Human Motor Neurons by Disrupting Autophagy through TGF-beta 1. *Stem Cell Reports*, 9, 667-680.

- Tyzack, G., A. Lakatos & R. Patani (2016) Human Stem Cell-Derived Astrocytes: Specification and Relevance for Neurological Disorders. *Current Stem Cell Reports*, 2, 236-247.
- Uzel, S. G. M., R. J. Platt, V. Subramanian, T. M. Pearl, C. J. Rowlands, V. Chan, L. A. Boyer, P. T. C. So & R. D. Kamm (2016) Microfluidic device for the formation of optically excitable, three-dimensional, compartmentalized motor units. *Science Advances*, 2, 13.
- Valko, M., C. J. Rhodes, J. Moncol, M. Izakovic & M. Mazur (2006) Free radicals, metals and antioxidants in oxidative stress-induced cancer. *Chemico-Biological Interactions*, 160, 1-40.
- Van den Bos, M. A. J., M. Higashihara, N. Geevasinga, P. Menon, M. C. Kiernan & S. Vucic (2018) Imbalance of cortical facilitatory and inhibitory circuits underlies hyperexcitability in ALS. *Neurology*, 91, E1669-E1676.
- van Rheenen, W., R. A. A. van der Spek, M. K. Bakker, J. van Vugt, P. J. Hop, R. A. J. Zwamborn, N. de Klein, H. J. Westra, O. B. Bakker, P. Deelen, G. Shireby, E. Hannon, M. Moisse, D. Baird, R. Restuadi, E. Dolzhenko, A. M. Dekker, K. Gawor, H. J. Westeneng, G. H. P. Tazelaar, K. R. van Eijk, M. Kooyman, R. P. Byrne, M. Doherty, M. Heverin, A. Al Khleifat, A. Iacoangeli, A. Shatunov, N. Ticozzi, J. Cooper-Knock, B. N. Smith, M. Gromicho, S. Chandran, S. Pal, K. E. Morrison, P. J. Shaw, J. Hardy, R. W. Orrell, M. Sendtner, T. Meyer, N. Basak, A. J. van der Kooi, A. Ratti, I. Fogh, C. Gellera, G. Lauria, S. Corti, C. Cereda, D. Sproviero, S. D'Alfonso, G. Soraru, G. Siciliano, M. Filosto, A. Padovani, A. Chio, A. Calvo, C. Moglia, M. Brunetti, A. Canosa, M. Grassano, E. Beghi, E. Pupillo, G. Logroscino, B. Nefussy, A. Osmanovic, A. Nordin, Y. Lerner, M. Zabari, M. Gotkine, R. H. Baloh, S. Bell, P. Vourc'h, P. Corcia, P. Couratier, S. Millecamps, V. Meininger, F. Salachas, J. M. S. Pardina, A. Assialioui, R. Rojas-Garcia, P. A. Dion, J. P. Ross, A. C. Ludolph, J. H. Weishaupt, D. Brenner, A. Freischmidt, G. Bensimon, A. Brice, A. Durr, C. A. M. Payan, S. Saker-Delye, N. W. Wood, S. Topp, R. Rademakers, L. Tittmann, W. Lieb, A. Franke, S. Ripke, A. Braun, J. Kraft, et al. (2021) Common and rare variant association analyses in amyotrophic lateral sclerosis identify 15 risk loci with distinct genetic architectures and neuron-specific biology. *Nature Genetics*, 53, 1636-+.
- Varoqueaux, F., A. Sigler, J. S. Rhee, N. Brose, C. Enk, K. Reim & C. Rosenmund (2002) Total arrest of spontaneous and evoked synaptic transmission but normal synaptogenesis in the absence of Munc13-mediated vesicle priming. *Proceedings of the National Academy of Sciences of the United States of America*, 99, 9037-9042.
- Vascak, M., J. L. Sun, M. Baer, K. M. Jacobs & J. T. Povlishock (2017) Mild Traumatic Brain Injury Evokes Pyramidal Neuron Axon Initial Segment Plasticity and Diffuse Presynaptic Inhibitory Terminal Loss. *Frontiers in Cellular Neuroscience*, 11.
- Verhage, M., A. S. Maia, J. J. Plomp, A. B. Brussaard, J. H. Heeroma, H. Vermeer, R. F. Toonen, R. E. Hammer, T. K. van den Berg, M. Missler, H. J. Geuze & T. C. Sudhof (2000) Synaptic assembly of the brain in the absence of neurotransmitter secretion. *Science*, 287, 864-869.
- Vogler, T. O., J. R. Wheeler, E. D. Nguyen, M. P. Hughes, K. A. Britson, E. Lester, B. Rao, N. Dalla Betta, O. N. Whitney, T. E. Ewachiw, E. Gomes, J. Shorter, T. E. Lloyd, D. S. Eisenberg, J. P. Taylor, A. M. Johnson, B. B. Olwin & R. Parker (2018) TDP-43 and RNA form amyloid-like myo-granules in regenerating muscle. *Nature*, 563, 508-+.
- Vucic, S. & M. C. Kiernan (2006) Axonal excitability properties in amyotrophic lateral sclerosis. *Clinical Neurophysiology*, 117, 1458-1466.

- (2010) Upregulation of persistent sodium conductances in familial ALS. *Journal of Neurology Neurosurgery and Psychiatry*, 81, 222-227.
- Vucic, S., G. A. Nicholson & M. C. Kiernan (2008) Cortical hyperexcitability may precede the onset of familial amyotrophic lateral sclerosis. *Brain*, 131, 1540-1550.
- Wainger, B. J., E. Kiskinis, C. Mellin, O. Wiskow, S. S. W. Han, J. Sandoe, N. P. Perez, L. A. Williams, S. Lee, G. Boulting, J. D. Berry, R. H. Brown, M. E. Cudkowicz, B. P. Bean, K. Eggan & C. J. Woolf (2014) Intrinsic Membrane Hyperexcitability of Amyotrophic Lateral Sclerosis Patient-Derived Motor Neurons. *Cell Reports*, 7, 1-11.
- Wang, W., C. Y. Lin, D. Lu, Z. M. Ning, T. Cox, D. Melvin, X. Z. Wang, A. Bradley & P. T. Liu (2008) Chromosomal transposition of PiggyBac in mouse embryonic stem cells. *Proceedings of the National Academy of Sciences of the United States of America*, 105, 9290-9295.
- Wefelmeyer, W., D. Cattaert & J. Burrone (2015) Activity-dependent mismatch between axo-axonic synapses and the axon initial segment controls neuronal output. *Proceedings of the National Academy of Sciences of the United States of America*, 112, 9757-9762.
- Weskamp, K., E. M. Tank, R. Miguez, J. P. McBride, N. B. Gomez, M. White, Z. Q. Lin, C. M. Gonzalez, A. Serio, J. Sreedharan & S. J. Barmada (2020) Shortened TDP43 isoforms upregulated by neuronal hyperactivity drive TDP43 pathology in ALS. *Journal of Clinical Investigation*, 130, 1139-1155.
- Wichterle, H., I. Lieberam, J. A. Porter & T. M. Jessell (2002) Directed differentiation of embryonic stem cells into motor neurons. *Cell*, 110, 385-397.
- Wilhelm, J. C., M. M. Rich & P. Wenner (2009) Compensatory changes in cellular excitability, not synaptic scaling, contribute to homeostatic recovery of embryonic network activity. *Proceedings of the National Academy of Sciences of the United States of America*, 106, 6760-6765.
- Xia, J. F., H. R. Yang, M. Mu, N. Micovic, K. E. Poskanzer, J. R. Monaghan & H. A. Clark (2021) Imaging in vivo acetylcholine release in the peripheral nervous system with a fluorescent nanosensor. *Proceedings of the National Academy of Sciences of the United States of America*, 118.
- Yermakov, L. M., D. E. Drouet, R. B. Griggs, K. M. Elased & K. Susuki (2018) Type 2 Diabetes Leads to Axon Initial Segment Shortening in db/db Mice. *Frontiers in Cellular Neuroscience*, 12.
- Yin, H., F. Price & M. A. Rudnicki (2013) SATELLITE CELLS AND THE MUSCLE STEM CELL NICHE. *Physiological Reviews*, 93, 23-67.
- Yoshida, M., S. Kitaoka, N. Egawa, M. Yamane, R. Ikeda, K. Tsukita, N. Amano, A. Watanabe, M. Morimoto, J. Takahashi, H. Hosoi, T. Nakahata, H. Inoue & M. K. Saito (2015) Modeling the Early Phenotype at the Neuromuscular Junction of Spinal Muscular Atrophy Using Patient-Derived iPSCs. *Stem Cell Reports*, 4, 561-568.
- Zamanian, J. L., L. J. Xu, L. C. Foo, N. Nouri, L. Zhou, R. G. Giffard & B. A. Barres (2012) Genomic Analysis of Reactive Astroglia. *Journal of Neuroscience*, 32, 6391-6410.
- Zhang, F., L. P. Wang, E. S. Boyden & K. Deisseroth (2006) Channelrhodopsin-2 and optical control of excitable cells. *Nature Methods*, 3, 785-792.
- Zhang, S. Y., M. Xu, Q. L. Miao, M. M. Poo & X. H. Zhang (2009) Endocannabinoid-Dependent Homeostatic Regulation of Inhibitory Synapses by Miniature Excitatory Synaptic Activities. *Journal of Neuroscience*, 29, 13222-13231.
- Zhang, W. & D. J. Linden (2003) The other side of the engram: Experience-driven changes in neuronal intrinsic excitability. *Nature Reviews Neuroscience*, 4, 885-900.

- Zheng, S. K. (2020) Alternative splicing programming of axon formation. *Wiley Interdisciplinary Reviews-Rna*, 11.
- Zong, Y. N. & R. S. Jin (2013) Structural mechanisms of the agrin-LRP4-MuSK signaling pathway in neuromuscular junction differentiation. *Cellular and Molecular Life Sciences*, 70, 3077-3088.
- Zucker, R. S. & W. G. Regehr (2002) Short-term synaptic plasticity. *Annual Review of Physiology*, 64, 355-405.

FULL PAPER

Modelling Neuromuscular Connectivity

**ADVANCED
BIOSYSTEMS**
www.adv-biosys.com

In Vitro Modeling of Nerve–Muscle Connectivity in a Compartmentalized Tissue Culture Device

Carolina Barcellos Machado,* Perrine Pluchon, Peter Harley, Mark Rigby, Victoria Gonzalez Sabater, Danielle C. Stevenson, Stephanie Hynes, Andrew Lowe, Juan Burrone, Virgile Viasnoff, and Ivo Lieberam*

Motor neurons project axons from the hindbrain and spinal cord to muscle, where they induce myofibre contractions through neurotransmitter release at neuromuscular junctions. Studies of neuromuscular junction formation and homeostasis have been largely confined to in vivo models. In this study, three powerful tools have been merged—pluripotent stem cells, optogenetics, and microfabrication—and an open microdevice is designed in which motor axons grow from a neural compartment containing embryonic stem cell-derived motor neurons and astrocytes through microchannels to form functional neuromuscular junctions with contractile myofibres in a separate compartment. Optogenetic entrainment of motor neurons in this reductionist neuromuscular circuit enhances neuromuscular junction formation more than twofold, mirroring the activity-dependence of synapse development in vivo. An established motor neuron disease model is incorporated into the system and it is found that coculture of motor neurons with *SOD1*^{G93A} astrocytes results in denervation of the central compartment and diminishes myofibre contractions, a phenotype which is rescued by the receptor interacting serine/threonine kinase 1 inhibitor necrostatin. This coculture system replicates key aspects of nerve–muscle connectivity in vivo and represents a rapid and scalable alternative to animal models of neuromuscular function and disease.

1. Introduction

The central nervous system (CNS) relays motor commands to skeletal muscle through motor neurons (MNs), specialized nerve cells located in the brainstem, and spinal cord. The degeneration of MNs and their synaptic connections with muscle underlies several paralyzing and often fatal neuromuscular diseases. Consequently, understanding nerve–muscle connectivity is key to developing medical interventions which preserve or restore vital motor functions in humans.

During embryonic development in vertebrates, MNs emerge from ventral progenitor domains in the caudal neural tube^[1] and project axons into the surrounding mesenchyme.^[2] Motor axon growth cones then navigate toward their specific target muscle in a series of binary pathway choices, guided by local positional cues.^[3] As they approach their synaptic targets, the release of agrin and acetylcholine from motor axons induces a redistribution of nicotinic acetylcholine receptors (AChRs) on myofibres through interactions that involve the activation of the Lrp4/Musk/Rapsyn receptor complex on the postsynaptic side.^[4] This leads to an alignment of postsynaptic AChR clusters with presynaptic sites, the exclusion of AChRs from areas not occupied by axonal contacts, and the formation of the postsynaptic specialization at the neuromuscular junction (NMJ).^[5] As NMJs mature, they stabilize and increase in size, a process that is dependent on neural activity and cholinergic neurotransmission between motor axon and myofibre.^[6] The outgrowth of peripheral motor axons and the establishment of NMJs are crucial steps in connecting the CNS to muscles throughout the body and are essential for motor functions such as locomotion, posture, and breathing.


Loss of NMJ stability is an early pathological feature of amyotrophic lateral sclerosis (ALS), a fatal adult-onset neurodegenerative disease caused by the selective degeneration of MNs. About 15–20% of all ALS cases are familial, and some of the most common genetic defects associated with ALS are point mutations in the superoxide dismutase-1 (*SOD1*) gene.^[7]

Dr. C. B. Machado, Dr. P. Pluchon, P. Harley, S. Hynes, Dr. I. Lieberam
Centre for Stem Cells and Regenerative Medicine
King's College London
London SE1 9RT, UK

E-mail: carolina.barcellos_machado@kcl.ac.uk; ivo.lieberam@kcl.ac.uk
Dr. C. B. Machado, Dr. P. Pluchon, P. Harley, Dr. M. Rigby, V. G. Sabater,
Dr. D. C. Stevenson, S. Hynes, Dr. A. Lowe, Prof. J. Burrone,
Dr. I. Lieberam

Centre for Developmental Neurobiology/MRC Centre
for Neurodevelopmental Disorders
King's College London
London SE1 1UL, UK

Dr. P. Pluchon, Prof. V. Viasnoff
Mechanobiology Institute
National University of Singapore
Singapore 117411, Singapore

 The ORCID identification number(s) for the author(s) of this article can be found under <https://doi.org/10.1002/adbi.201800307>.

© 2019 The Authors. Published by WILEY-VCH Verlag GmbH & Co. KGaA, Weinheim. This is an open access article under the terms of the Creative Commons Attribution License, which permits use, distribution and reproduction in any medium, provided the original work is properly cited.

DOI: 10.1002/adbi.201800307

HEALTH AND MEDICINE

Optogenetic modeling of human neuromuscular circuits in Duchenne muscular dystrophy with CRISPR and pharmacological corrections

Amaia Paredes-Redondo^{1,2,3}, Peter Harley⁴, Eleni Maniati⁵, David Ryan⁶, Sandra Louzada^{6†}, Jinhong Meng⁷, Anna Kowala^{1,2,3}, Beiyuan Fu⁶, Fengtang Yang⁶, Pentao Liu⁸, Silvia Marino¹, Olivier Pourquié⁹, Francesco Muntoni^{7,10}, Jun Wang⁵, Ivo Lieberam^{4*}, Yung-Yao Lin^{1,2,3,*‡}

Duchenne muscular dystrophy (DMD) is caused by *dystrophin* gene mutations leading to skeletal muscle weakness and wasting. Dystrophin is enriched at the neuromuscular junction (NMJ), but how NMJ abnormalities contribute to DMD pathogenesis remains unclear. Here, we combine transcriptome analysis and modeling of DMD patient-derived neuromuscular circuits with CRISPR-corrected isogenic controls in compartmentalized microdevices. We show that NMJ volumes and optogenetic motor neuron-stimulated myofiber contraction are compromised in DMD neuromuscular circuits, which can be rescued by pharmacological inhibition of TGFβ signaling, an observation validated in a 96-well human neuromuscular circuit coculture assay. These beneficial effects are associated with normalization of dysregulated gene expression in DMD myogenic transcriptomes affecting NMJ assembly (e.g., *MUSK*) and axon guidance (e.g., *SLIT2* and *SLIT3*). Our study provides a new human microphysiological model for investigating NMJ defects in DMD and assessing candidate drugs and suggests that enhancing neuromuscular connectivity may be an effective therapeutic strategy.

INTRODUCTION

Duchenne muscular dystrophy (DMD), caused by mutations in the gene encoding dystrophin (*DMD*) on the X chromosome, is a fatal and the most common inherited neuromuscular disorder in childhood, affecting 1 in 3500 to 5000 live male births (1). The dystrophin-glycoprotein complex (DGC) maintains the integrity of skeletal muscle by linking the intracellular cytoskeleton to the extracellular matrix and participates in cellular signaling processes (2). Patients with DMD suffer from progressive skeletal muscle weakness and wasting that lead to eventual loss of ambulation with reduced life expectancy (3). Current standard of care for DMD is based on the palliative effect of corticosteroids, which increase muscle mass and strength while reducing inflammation and necrosis. Nevertheless, prolonged corticosteroid treatment is associated with side effects, including weight gain, osteoporosis, and cataracts (4). To date, only

two types of curative medicines have received approval for treating DMD. Ataluren is a compound that induces ribosomal readthrough of premature termination codons to restore dystrophin protein expression, suitable for approximately 13% of patients with DMD, and approved by European Medicines Agency (5). Eteplirsen, golodirsen, viltolarsen, and casimersen are antisense oligonucleotides that mediate pre-mRNA exon skipping to restore the open reading frame in patients with DMD with eligible mutations (6, 7), cumulatively allowing targeting approximately 30% of patients with DMD. Despite these existing drugs, there is still no cure or effective treatment for DMD.

The formation of neuromuscular circuits is critical for generating voluntary movement, in which skeletal muscle contraction is induced by motor neurons (MNs) through neurotransmitter release at neuromuscular junctions (NMJs), where motor axons form synaptic contacts with myofibers. The DGC is enriched at the plasma membrane of myofibers and NMJs (8). While research in DMD primarily focused on muscle wasting, studies have shown that both patients with DMD and dystrophin-deficient *mdx* mice have structural alterations at the NMJs and aberrant electrophysiological changes (9–12), suggesting that NMJ abnormalities may contribute to pathophysiology of DMD. Although dystrophin-deficient mice have been extensively used as an animal model to investigate mechanisms underlying DMD, the genetic and physiological differences between rodents and humans highlight the need to improve translatability of preclinical studies using the *mdx* mice for evaluating potential therapeutics. For example, in contrast to patients with DMD, the *mdx* mice have relatively mild muscle pathology, possibly due to compensatory or species-specific mechanisms in mice (13). Furthermore, human and mouse NMJs differ substantially in their cellular anatomy and synaptic proteomes (14). To reduce the use of animals and facilitate the selection of the most promising therapies for DMD clinical trials, it is important to develop human-specific and physiologically relevant models for preclinical studies of neuromuscular circuits in health and disease, as well as for assessing the efficacy of therapeutic strategies.

¹Centre for Genomics and Child Health, Blizard Institute, Barts and the London School of Medicine and Dentistry, Queen Mary University of London, 4 Newark Street, London E1 2AT, UK. ²Stem Cell Laboratory, National Bowel Research Centre, Blizard Institute, Barts and the London School of Medicine and Dentistry, Queen Mary University of London, 2 Newark Street, London E1 2AT, UK. ³Centre for Predictive in vitro Model, Queen Mary University of London, Mile End Road, London E1 4NS, UK. ⁴Centre for Stem Cells and Regenerative Medicine, MRC Centre for Neurodevelopmental Disorders, and Centre for Developmental Neurobiology, King's College London, London, UK. ⁵Centre for Cancer Genomics and Computational Biology, Barts Cancer Institute, Queen Mary University of London, London, UK. ⁶Wellcome Sanger Institute, Wellcome Genome Campus, Hinxton, Cambridge CB10 1SA, UK. ⁷UCL Great Ormond Street Institute of Child Health, 30 Guilford Street, London WC1N 1EH, UK. ⁸School of Biomedical Sciences, Stem Cell and Regenerative Medicine Consortium, Li Ka Shing Faculty of Medicine, The University of Hong Kong, Hong Kong, China. ⁹Department of Genetics and Department of Pathology, Brigham and Women's Hospital, Harvard Medical School, 60 Fenwood Road, Boston, MA, USA. ¹⁰NIHR Biomedical Research Centre, Great Ormond Street Hospital, Great Ormond Street, London, UK.

*Corresponding author. Email: yy.lin@qmul.ac.uk

†Present addresses: Laboratory of Cytogenomics and Animal Genomics, Department of Genetics and Biotechnology, University of Trás-os-Montes and Alto Douro, Vila Real, Portugal; BioSystems and Integrative Sciences Institute, Faculty of Sciences, University of Lisbon, Lisbon, Portugal.

‡These authors contributed equally as co-senior authors.

Copyright © 2021 The Authors, some rights reserved; exclusive licensee American Association for the Advancement of Science. No claim to original U.S. Government Works. Distributed under a Creative Commons Attribution License 4.0 (CC BY).

Downloaded from <https://www.science.org> on March 30, 2022

Biobased Elastomer Nanofibers Guide Light-Controlled Human-iPSC-Derived Skeletal Myofibers

Aimee Cheesbrough, Fabiola Sciscione, Federica Riccio, Peter Harley, Lea R'Bibo, Georgios Ziakas, Arnold Darbyshire, Ivo Lieberam,* and Wenhui Song*

Generating skeletal muscle tissue that mimics the cellular alignment, maturation, and function of native skeletal muscle is an ongoing challenge in disease modeling and regenerative therapies. Skeletal muscle cultures require extracellular guidance and mechanical support to stabilize contractile myofibers. Existing microfabrication-based solutions are limited by complex fabrication steps, low throughput, and challenges in measuring dynamic contractile function. Here, the synthesis and characterization of a new biobased nanohybrid elastomer, which is electrospun into aligned nanofiber sheets to mimic the skeletal muscle extracellular matrix, is presented. The polymer exhibits remarkable hyperelasticity well-matched to that of native skeletal muscle ($\approx 11\text{--}50$ kPa), with ultimate strain $\approx 1000\%$, and elastic modulus ≈ 25 kPa. Uniaxially aligned nanofibers guide myoblast alignment, enhance sarcomere formation, and promote a $\approx 32\%$ increase in myotube fusion and $\approx 50\%$ increase in myofiber maturation. The elastomer nanofibers stabilize optogenetically controlled human induced pluripotent stem cell derived skeletal myofibers. When activated by blue light, the myofiber–nanofiber hybrid constructs maintain a significantly higher ($>200\%$) contraction velocity and specific force ($>280\%$) compared to conventional culture methods. The engineered myofibers exhibit a power density of ≈ 35 W m $^{-3}$. This system is a promising new skeletal muscle tissue model for applications in muscular disease modeling, drug discovery, and muscle regeneration.

1. Introduction


Advances in the field of skeletal muscle tissue engineering depend on generating stable and life-like skeletal muscle micro-tissues in vitro. This requires an interdisciplinary approach, whereby cells are incorporated into a biological or synthetic mechanical microenvironment. Such work enables accurate modeling of skeletal muscle function and disease, and progress in the generation of transplantable tissues to treat muscle trauma and degeneration. Skeletal muscle is a highly organized complex organ composed of connective tissue, blood vessels, and aligned contractile myofiber bundles, which are innervated by motor neurons (MNs); the output layer of the central nervous system. This complex network of different cell types and extracellular structures work in synergy to contribute to muscle force generation, transmission, maintenance, and repair.^[1]

Scalable nanostructured biomaterial substrates are required to mimic the native skeletal muscle extracellular matrix (ECM) in vitro. These have the potential to interact with tissues on a cellular and

molecular level by imitating mechanical and biochemical cues. Typically, they guide myotube alignment, provide anchorage to contractile myotubes,^[2] and enhance cellular maturity. In the absence of a supporting scaffold, developing myofibers cultured on rigid tissue culture (TC) surfaces are unstable and detach from their substrate as they contract.^[3] Both natural and synthetic polymers have been used to fabricate substrates for skeletal muscle tissue engineering. These include encapsulating myofibers in biopolymer hydrogels such as collagen,^[4,5] fibrin,^[6,7] gelatin,^[8,9] and biopolymer mixtures or nanocomposites.^[10–12] Synthetic polymers such as poly(vinyl alcohol), poly(lactic acid), and poly(caprolactone)^[13] have been fabricated into sheets, porous sponges, and fibers^[14,15] to guide skeletal muscle organization. Thermoset silicones such as polydimethylsiloxane (PDMS) have been used to cast flexible tendon-like microstructures, which provide structural supports, such as uniaxial tension across attachment sites.^[2] These are often used in neuromuscular biosystem applications.^[16–18] Unlike synthetic polymers, most natural biopolymer hydrogels are prone to rapid degradation by the proteases secreted by cells.^[16] As a

A. Cheesbrough, F. Sciscione, G. Ziakas, A. Darbyshire, W. Song
UCL Centre for Biomaterials in Surgical Reconstruction
and Regeneration
Department of Surgical Biotechnology
Division of Surgery and Interventional Science
University College London
London NW3 2PF, UK
E-mail: w.song@ucl.ac.uk

A. Cheesbrough, F. Riccio, P. Harley, L. R'Bibo, I. Lieberam
Centre for Gene Therapy and Regenerative Medicine
MRC Centre for Neurodevelopmental Disorders
Centre for Developmental Neurobiology
Kings College London
London SE1 9RT, UK
E-mail: ivo.lieberam@kcl.ac.uk

 The ORCID identification number(s) for the author(s) of this article can be found under <https://doi.org/10.1002/adma.202110441>.

© 2022 The Authors. Advanced Materials published by Wiley-VCH GmbH. This is an open access article under the terms of the Creative Commons Attribution License, which permits use, distribution and reproduction in any medium, provided the original work is properly cited.

DOI: 10.1002/adma.202110441



bioRxiv posts many COVID19-related papers. A reminder: they have not been formally peer-reviewed and should not guide health-related behavior or be reported in the press as conclusive.

New Results

[Follow this preprint](#)

Pathogenic TDP-43 Disrupts Axon Initial Segment Structure and Neuronal Excitability in a Human iPSC Model of ALS

Peter Harley, Guilherme Neves, Federica Riccio, Carolina Barcellos Machado, Aimee Cheesbrough, Lea R'Bibo, Juan Burrone, Ivo Lieberam

doi: <https://doi.org/10.1101/2022.05.16.492186>

This article is a preprint and has not been certified by peer review [what does this mean?].



Abstract

Full Text

Info/History

Metrics

[Preview PDF](#)

Abstract

Dysregulated neuronal excitability is a hallmark of amyotrophic lateral sclerosis (ALS). We sought to investigate how functional changes to the axon initial segment (AIS), the site of action potential generation, could impact neuronal excitability in a human iPSC model of ALS. We found that early (6-week) ALS-related TDP-43^{G298S} motor neurons showed an increase in the length of the AIS, relative to CRISPR-corrected controls. This was linked to neuronal

1

2 **3D Compartmentalised Human Pluripotent Stem Cell-derived Neuromuscular Co-cultures**3 Peter Harley^{1,2}, Amaia Paredes-Redondo^{3,4}, Gianluca Greci⁵, Virgile Viasnoff⁵, Yung-Yao Lin^{3,4,#,*}
4 and Ivo Lieberam^{1,2,#,*}

5

6 ¹Centre for Gene Therapy & Regenerative Medicine, Kings College London, London SE1 9RT, UK7 ²Centre for Developmental Neurobiology and MRC Centre for Neurodevelopmental Disorders, Institute
8 of Psychiatry, Psychology and Neuroscience, Kings College London, London SE1 1UL, UK9 ³Centre for Genomics and Child Health, Blizard Institute, Barts and the London School of Medicine and
10 Dentistry, Queen Mary University of London, 4 Newark Street, London E1 2AT, UK11 ⁴Centre for Predictive in vitro Model, Queen Mary University of London, Mile End Road, London E1 4NS,
12 UK13 ⁵Mechanobiology Institute, National University of Singapore, 5a Engineering Drive 1, 117411 Singapore

14 #Contributed equally to this work

15 *For correspondence: yy.lin@qmul.ac.uk and ivo.lieberam@kcl.ac.uk

16

17 **[Abstract]** Human neuromuscular diseases represent a diverse group of disorders with unmet clinical
18 need, ranging from muscular dystrophies such as Duchenne muscular dystrophy (DMD) to
19 neurodegenerative disorders such as amyotrophic lateral sclerosis (ALS). In many of these conditions,
20 axonal and neuromuscular synapse dysfunction have been implicated as crucial pathological events,
21 highlighting a need for *in vitro* disease models that accurately recapitulate these aspects of human
22 neuromuscular physiology. The protocol reported here describes the co-culture of neural spheroids
23 composed of human pluripotent stem cell (PSC)-derived motor neurons and astrocytes, and human
24 PSC-derived myofibers in 3D compartmentalised microdevices to generate functional human
25 neuromuscular circuits *in vitro*. In this microphysiological model, motor axons project from a central
26 nervous system (CNS)-like compartment along microchannels to innervate skeletal myofibers plated in

Small molecule screen – AstraZeneca compound list

Data set source	IDENTIFIER	GENE_NAME	OFFICIAL_SYMBOL	OFFICIAL_NAME	Total_Annots_with_Protated_Cpds	Total_Annots_at_least_1uM
Lieberam data Melamed et al. data GO Reactive oxygen species	ENSG00000146648 P00533	EGFR	EGFR	epidermal growth factor receptor	2286	752
Lieberam data GO Neuromuscular junction GO Synapse assembly GO Autophagy	ENSG00000149295 P14416	DRD2	DRD2	dopamine receptor D2	1699	566
Lieberam data Melamed et al. data GO Autophagy	ENSG00000135914 P41595	HTR2B	HTR2B	5-hydroxytryptamine receptor 2B	1881	528
Lieberam data GO Reactive oxygen species	ENSG00000100030 P28482	MAPK1	MAPK1	mitogen-activated protein kinase 1	1944	496
Lieberam data GO axon guidance	ENSG00000165731 P07949	RET	RET	ret proto-oncogene	1720	475
Positive controls GO Synapse assembly GO Autophagy	P49841	GSK3B	GSK3B	glycogen synthase kinase 3 beta	2068	447
Klim et al. data GO Synapse assembly GO Reactive oxygen species GO Autophagy	ENSG00000197122 P12931	SRC	SRC	SRC proto-oncogene, non-receptor tyrosine kinase	1738	435
Lieberam data GO Synapse assembly GO Reactive oxygen species	ENSG00000096968 O60674	JAK2	JAK2	Janus kinase 2	1068	412
Lieberam data Melamed et al. data GO Synapse assembly GO axon guidance	ENSG00000198400 P04629	NTRK1	NTRK1	neurotrophic receptor tyrosine kinase 1	1273	411
GO Synapse assembly GO Reactive oxygen species	Q99720	SIGMAR1	SIGMAR1	sigma non-opioid intracellular receptor 1	1188	328
Lieberam data GO Neuromuscular junction GO Synapse assembly GO Reactive oxygen species GO Autophagy	ENSG00000097007 P00519	ABL1	ABL1	ABL proto-oncogene 1, non-receptor tyrosine kinase	818	311
Lieberam data Melamed et al. data	ENSG00000181072	CHRM2	CHRM2	cholinergic receptor muscarinic 2	1500	282
Lieberam data GO Synapse assembly GO axon guidance	ENSG00000169398 Q05397	PTK2	PTK2	protein tyrosine kinase 2	1044	253
Positive controls Lieberam data GO Autophagy	P49840 ENSG00000105723	GSK3A	GSK3A	glycogen synthase kinase 3 alpha	823	253
Klim et al. data GO action potential	ENSG00000145349 Q13557	CAMK2D	CAMK2D	calcium/calmodulin dependent protein kinase II delta	656	247
Lieberam data GO Reactive oxygen species GO Autophagy	ENSG00000107643 P45983	MAPK8	MAPK8	mitogen-activated protein kinase 8	1214	222
Lieberam data Klim et al. data	ENSG00000082556	OPRK1	OPRK1	opioid receptor kappa 1	1717	218
Klim et al. data GO axon guidance GO Reactive oxygen species	ENSG00000010810 P06241	FYN	FYN	FYN proto-oncogene, Src family tyrosine kinase	1156	216
Melamed et al. data GO action potential	ENSG00000055118 Q12809	KCNH2	KCNH2	potassium voltage-gated channel subfamily H member 2	3433	212
GO Reactive oxygen species GO Autophagy	P08581	MET	MET	MET proto-oncogene, receptor tyrosine kinase	1407	208
Lieberam data GO Reactive oxygen species GO Autophagy	ENSG00000102882 P27361	MAPK3	MAPK3	mitogen-activated protein kinase 3	725	205
Lieberam data GO axon guidance	ENSG00000196411 P54760	EPHB4	EPHB4	EPH receptor B4	931	202
Lieberam data GO Motor neuron GO Reactive oxygen species GO Autophagy	ENSG00000132356 Q13131	PRKAA1	PRKAA1	protein kinase AMP-activated catalytic subunit alpha 1	771	200
GO Neuromuscular junction GO axon guidance GO Motor neuron	P04626	ERBB2	ERBB2	erb-b2 receptor tyrosine kinase 2	692	198
Melamed et al. data GO Synapse assembly GO action potential	ENSG00000148053 Q16620	NTRK2	NTRK2	neurotrophic receptor tyrosine kinase 2	678	182
GO Neuromuscular junction GO Synapse assembly GO Reactive oxygen species GO Autophagy	Q55007	LRRK2	LRRK2	leucine rich repeat kinase 2	370	176
Lieberam data Melamed et al. data Klim et al. data	ENSG00000170145	SIK2	SIK2	salt inducible kinase 2	337	176
Lieberam data Klim et al. data	ENSG00000058404	CAMK2B	CAMK2B	calcium/calmodulin dependent protein kinase II beta	930	170
GO Neuromuscular junction GO Synapse assembly GO Reactive oxygen species GO Autophagy	P42345	MTOR	MTOR	mechanistic target of rapamycin kinase	889	164
GO Neuromuscular junction GO Synapse assembly GO Autophagy	P17612	PRKACA	PRKACA	protein kinase cAMP-activated catalytic subunit alpha	1304	161
GO Synapse assembly GO axon guidance	P54762	EPHB1	EPHB1	EPH receptor B1	741	153
Lieberam data Klim et al. data GO Synapse assembly	ENSG00000151834 P47869	GABRA2	GABRA2	gamma-aminobutyric acid type A receptor alpha2 subunit	725	144
Melamed et al. data Klim et al. data GO Autophagy	ENSG00000145632 Q9NYY3	PLK2	PLK2	polo like kinase 2	540	140
GO Neuromuscular junction GO Synapse assembly GO axon guidance GO Motor neuron GO Autophagy	Q00535	CDK5	CDK5	cyclin dependent kinase 5	504	135
Klim et al. data GO axon guidance	ENSG00000142627 P29317	EPHA2	EPHA2	EPH receptor A2	613	138
Lieberam data GO Reactive oxygen species	ENSG00000163932 Q05655	PRKCD	PRKCD	protein kinase C delta	540	138
Lieberam data GO Synapse assembly	ENSG00000113327 P18507	GABRG2	GABRG2	gamma-aminobutyric acid type A receptor gamma2 subunit	671	134
Lieberam data GO Synapse assembly	ENSG00000273079 Q13224	GRIN2B	GRIN2B	glutamate ionotropic receptor NMDA type subunit 2B	295	134
Lieberam data GO Synapse assembly	ENSG00000166206 P28472	GABRB3	GABRB3	gamma-aminobutyric acid type A receptor beta3 subunit	684	133

Data set source	IDENTIFIER	GENE_NAME	OFFICIAL_SYMBOL	OFFICIAL_NAME	Total_Annotated_Cpds	Total_Annotated_at_least_1_uM
Lieberam data Melamed et al. data	ENSG00000027644	INSRR	INSRR	insulin receptor related receptor	746	128
Lieberam data Klim et al. data	ENSG00000168067	MAP4K2	MAP4K2	mitogen-activated protein kinase kinase kinase 2	472	128
Lieberam data GO Synapse assembly GO Reactive oxygen species	ENSG00000176884 Q05586	GRIN1	GRIN1	glutamate ionotropic receptor NMDA type subunit 1	360	124
Lieberam data GO action potential	ENSG00000151067 Q13936	CACNA1C	CACNA1C	calcium voltage-gated channel subunit alpha1 C	1720	118
Lieberam data GO Neuromuscular junction GO Synapse assembly	ENSG00000030304 O15146	MUSK	MUSK	muscle associated receptor tyrosine kinase	366	117
Lieberam data GO Phase separation GO Autophagy	ENSG00000181085 Q8TD08	MAPK15	MAPK15	mitogen-activated protein kinase 15	475	117
Lieberam data Klim et al. data	ENSG00000163349	HIPK1	HIPK1	homeodomain interacting protein kinase 1	297	116
Lieberam data Klim et al. data	ENSG00000186297	GABRA5	GABRA5	gamma-aminobutyric acid type A receptor alpha5 subunit	651	114
Lieberam data GO Reactive oxygen species	ENSG00000134853 P16234	PDGFRA	PDGFRA	platelet derived growth factor receptor alpha	220	103
GO Neuromuscular junction GO Synapse assembly	P22303	ACHE	ACHE	acetylcholinesterase (Cartwright blood group)	1237	103
Lieberam data Klim et al. data	ENSG00000171132	PRKCE	PRKCE	protein kinase C epsilon	690	99
Klim et al. data GO Synapse assembly	ENSG00000145864 P47870	GABRB2	GABRB2	gamma-aminobutyric acid type A receptor beta2 subunit	664	97
Lieberam data GO Synapse assembly GO axon guidance	ENSG00000133216 P29323	EPHB2	EPHB2	EPH receptor B2	360	93
Lieberam data GO Neuromuscular junction GO Synapse assembly GO axon guidance	ENSG00000135333 Q15375	EPHA7	EPHA7	EPH receptor A7	334	93
Lieberam data Klim et al. data	ENSG00000137843	PAK6	PAK6	p21 (RAC1) activated kinase 6	510	87
Lieberam data Klim et al. data	ENSG00000142875	PRKACB	PRKACB	protein kinase cAMP-activated catalytic subunit beta	294	85
Lieberam data Klim et al. data GO Motor neuron	ENSG00000065559 P45985	MAP2K4	MAP2K4	mitogen-activated protein kinase kinase 4	246	84
Lieberam data GO Reactive oxygen species	ENSG00000102572 Q9Y6E0	STK24	STK24	serine/threonine kinase 24	352	84
Klim et al. data GO Reactive oxygen species	ENSG00000100985 P14780	MMP9	MMP9	matrix metalloproteinase 9	192	80
GO Neuromuscular junction GO axon guidance GO Motor neuron	P54764	EPHA4	EPHA4	EPH receptor A4	361	78
Lieberam data Melamed et al. data GO action potential	ENSG00000183873 Q14524	SCN5A	SCN5A	sodium voltage-gated channel alpha subunit 5	777	75
Melamed et al. data GO Reactive oxygen species	ENSG00000087245 P08253	MMP2	MMP2	matrix metalloproteinase 2	601	74
Lieberam data Klim et al. data GO Autophagy	ENSG00000140474 Q6PHR2	ULK3	ULK3	unc-51 like kinase 3	312	72
Klim et al. data GO Motor neuron	ENSG00000205571 Q16637	SMN2 SMN1	SMN2	survival of motor neuron 2, centromeric	462	72
Klim et al. data GO Motor neuron	ENSG00000172062 Q16637	SMN1	SMN1	survival of motor neuron 1, telomeric	462	71
GO Reactive oxygen species GO Autophagy	Q16665	HIF1A	HIF1A	hypoxia inducible factor 1 subunit alpha	285	70
Lieberam data GO action potential	ENSG00000136531 Q99250	SCN2A	SCN2A	sodium voltage-gated channel alpha subunit 2	637	67
Lieberam data Klim et al. data GO axon guidance	ENSG00000070886 P29322	EPHA8	EPHA8	EPH receptor A8	340	67
Klim et al. data GO action potential	ENSG00000053918 P51787	KCNQ1	KCNQ1	potassium voltage-gated channel subfamily Q member 1	102	66
Klim et al. data GO Neuromuscular junction	ENSG00000101306 Q9H1R3	MYLK2	MYLK2	myosin light chain kinase 2	208	63
Klim et al. data GO Synapse assembly GO Reactive oxygen species GO Autophagy	ENSG00000186868 P10636	MAPT	MAPT	microtubule associated protein tau	697	61
Lieberam data GO action potential	ENSG00000153253 Q9NY46	SCN3A	SCN3A	sodium voltage-gated channel alpha subunit 3	402	61
Klim et al. data GO Neuromuscular junction GO Synapse assembly GO axon guidance GO Reactive oxygen species GO Autophagy	ENSG00000142192 P05067	APP	APP	amyloid beta precursor protein	161	57
Lieberam data Klim et al. data GO Reactive oxygen species	ENSG00000115694 O00506	STK25	STK25	serine/threonine kinase 25	243	56
Klim et al. data GO Synapse assembly GO Reactive oxygen species GO Autophagy	ENSG00000094631 Q9UBN7	HDAC6	HDAC6	histone deacetylase 6	121	56
Lieberam data GO axon guidance GO Motor neuron	ENSG00000044524 P29320	EPHA3	EPHA3	EPH receptor A3	297	56
GO Neuromuscular junction GO Synapse assembly GO axon guidance GO Autophagy	Q15078	CDK5R1	CDK5R1	cyclin dependent kinase 5 regulatory subunit 1	140	54
Klim et al. data GO Autophagy	ENSG00000167657 O43293	DAPK3	DAPK3	death associated protein kinase 3	333	54
Lieberam data GO Reactive oxygen species GO Autophagy	ENSG00000141510 P04637	TP53	TP53	tumor protein p53	420	53

Excel_Source_Tab	IDENTIFIER	GENE_NAME	OFFICIAL_SYMBOL	OFFICIAL_NAME	Total_Annots_with_potency_atleast_1uM	Total_Annots
Klim et al. data GO Synapse assembly GO axon guidance	ENSG00000182580 P54753	EPHB3	EPHB3	EPH receptor B3	457	53
Lieberam data Melamed et al. data Klim et al. data GO Reactive oxygen species	ENSG00000144891 P30556	AGTR1	AGTR1	angiotensin II receptor type 1	817	49
Lieberam data Klim et al. data GO action potential	ENSG00000144285 P35498	SCN1A	SCN1A	sodium voltage-gated channel alpha subunit 1	383	49
GO Synapse assembly GO Reactive oxygen species	Q8NER1	TRPV1	TRPV1	transient receptor potential cation channel subfamily V member 1	347	49
Klim et al. data GO Reactive oxygen species	ENSG00000149968 P08254	MMP3	MMP3	matrix metalloproteinase 3	90	48
GO Neuromuscular junction GO Synapse assembly GO action potential	P17787	CHRN2	CHRN2	cholinergic receptor nicotinic beta 2 subunit	76	47
Lieberam data GO Motor neuron	ENSG00000071909 Q8WXR4	MYO3B	MYO3B	myosin IIIB	194	44
Lieberam data Klim et al. data	ENSG00000148408	CACNA1B	CACNA1B	calcium voltage-gated channel subunit alpha1 B	512	44
Lieberam data Melamed et al. data Klim et al. data	ENSG00000120948	TARDBP	TARDBP	TAR DNA binding protein	288	42
Lieberam data GO Reactive oxygen species	ENSG00000089250 P29475	NOS1	NOS1	nitric oxide synthase 1	180	40
Lieberam data GO Neuromuscular junction GO Synapse assembly GO Reactive oxygen species	ENSG00000068024 P56524	HDAC4	HDAC4	histone deacetylase 4	60	37
Lieberam data GO Reactive oxygen species GO Autophagy	ENSG00000080824 P07900	HSP90AA1	HSP90AA1	heat shock protein 90 alpha family class A member 1	102	36
Lieberam data Klim et al. data	ENSG00000124507	PACIN1	PACIN1	protein kinase C and casein kinase substrate in neurons 1	236	36
GO Neuromuscular junction GO Synapse assembly GO Autophagy	P49768	PSEN1	PSEN1	presenilin 1	240	34
GO Synapse assembly GO Reactive oxygen species	P01375	TNF	TNF	tumor necrosis factor	65	34
GO Neuromuscular junction GO action potential	P23415	GLRA1	GLRA1	glycine receptor alpha 1	601	33
Lieberam data Melamed et al. data GO Reactive oxygen species	ENSG00000163513 P37173	TGFBR2	TGFBR2	transforming growth factor beta receptor 2	59	31
Klim et al. data GO Reactive oxygen species GO Autophagy	ENSG00000164305 P42574	CASP3	CASP3	caspase 3	245	29
GO axon guidance GO Motor neuron	Q15465	SHH	SHH	sonic hedgehog signaling molecule	32	29
Lieberam data GO action potential	ENSG00000177098 Q8IWT1	SCN4B	SCN4B	sodium voltage-gated channel beta subunit 4	260	27
GO action potential GO Reactive oxygen species	P22460	KCNA5	KCNA5	potassium voltage-gated channel subfamily A member 5	162	27
Melamed et al. data Klim et al. data GO axon guidance GO action potential	ENSG00000105711 Q07699	SCN1B	SCN1B	sodium voltage-gated channel beta subunit 1	261	27
Lieberam data Melamed et al. data	ENSG00000111199	TRPV4	TRPV4	transient receptor potential cation channel subfamily V member 4	148	26
Lieberam data Klim et al. data GO axon guidance	ENSG00000137285 Q9BVA1	TUBB2B	TUBB2B	tubulin beta 2B class IIb	38	25
GO Neuromuscular junction GO Synapse assembly	P32297	CHRNA3	CHRNA3	cholinergic receptor nicotinic alpha 3 subunit	48	22
Klim et al. data GO Autophagy	ENSG00000139112 Q9H0R8	GABARAPL1	GABARAPL1	GABA type A receptor associated protein like 1	447	22
Lieberam data GO Autophagy	ENSG00000034713 P60520	GABARAPL2	GABARAPL2	GABA type A receptor associated protein like 2	447	22
GO Synapse assembly GO Autophagy	O95166	GABARAP	GABARAP	GABA type A receptor-associated protein	447	22
Lieberam data GO Neuromuscular junction GO action potential	ENSG00000138435 P02708	CHRNA1	CHRNA1	cholinergic receptor nicotinic alpha 1 subunit	725	21
Lieberam data Klim et al. data GO axon guidance	ENSG00000258947 Q13509	TUBB3	TUBB3	tubulin beta 3 class III	34	20
Lieberam data Melamed et al. data Klim et al. data	ENSG00000141526	SLC16A3	SLC16A3	solute carrier family 16 member 3	138	19
Klim et al. data GO action potential GO Motor neuron GO Autophagy	ENSG00000177628 P04062	GBA	GBA	glucosylceramidase beta	218	19
Lieberam data Klim et al. data GO Neuromuscular junction	ENSG00000167552 Q71U36	TUBA1A	TUBA1A	tubulin alpha 1a	25	19
Lieberam data Klim et al. data	ENSG00000159216	RUNX1	RUNX1	RUNX family transcription factor 1	220	19
Lieberam data Klim et al. data GO action potential	ENSG00000153956 P54289	CACNA2D1	CACNA2D1	calcium voltage-gated channel auxiliary subunit alpha2delta 1	42	17
Lieberam data Melamed et al. data	ENSG00000163873	GRIK3	GRIK3	glutamate ionotropic receptor kainate type subunit 3	57	17
Lieberam data Klim et al. data	ENSG00000172572	PDE3A	PDE3A	phosphodiesterase 3A	58	17
Lieberam data GO Reactive oxygen species GO Autophagy	ENSG00000171791 P10415	BCL2	BCL2	BCL2 apoptosis regulator	79	16

Excel_Source_Tab	IDENTIFIER	GENE_NAME	OFFICIAL_SYMBOL	OFFICIAL_NAME	Total_Annnotated_Cpds	Total_Annnotated_Cpds_with_potency_at_least_1uM
Lieberam data Melamed et al. data	ENSG00000186642	PDE2A	PDE2A	phosphodiesterase 2A	167	15
Lieberam data Klim et al. data GO Synapse assembly	ENSG00000196230 P07437	TUBB	TUBB	tubulin beta class I	21	14
Lieberam data Klim et al. data GO Reactive oxygen species	ENSG00000164251 P55085	F2RL1	F2RL1	F2R like trypsin receptor 1	61	13
Lieberam data Klim et al. data GO Reactive oxygen species	ENSG00000136869 O00206	TLR4	TLR4	toll like receptor 4	240	13
Melamed et al. data GO Neuromuscular junction	ENSG00000109738 P48167	GLRB	GLRB	glycine receptor beta	371	13
Lieberam data Melamed et al. data	ENSG00000138448	ITGAV	ITGAV	integrin subunit alpha V	33	13
Klim et al. data GO action potential	ENSG00000121361 Q15842	KCNJ8	KCNJ8	potassium voltage-gated channel subfamily J member 8	21	12
Lieberam data Melamed et al. data	ENSG00000196277	GRM7	GRM7	glutamate metabotropic receptor 7	201	12
Lieberam data Klim et al. data GO action potential	ENSG00000100346 Q9P0X4	CACNA1I	CACNA1I	calcium voltage-gated channel subunit alpha1 I	28	12
Lieberam data Melamed et al. data	ENSG00000196482	ESRRG	ESRRG	estrogen related receptor gamma	49	12
Melamed et al. data GO action potential	ENSG00000006283 O43497	CACNA1G	CACNA1G	calcium voltage-gated channel subunit alpha1 G	32	11
Lieberam data Melamed et al. data	ENSG00000185149	NPY2R	NPY2R	neuropeptide Y receptor Y2	102	11
Lieberam data Klim et al. data	ENSG00000115232	ITGA4	ITGA4	integrin subunit alpha 4	16	11
Lieberam data Klim et al. data GO action potential	ENSG00000163399 P05023	ATP1A1	ATP1A1	ATPase Na+/K+ transporting subunit alpha 1	101	10
Lieberam data GO Reactive oxygen species GO Autophagy	ENSG00000100300 P30536	TSPO	TSPO	translocator protein	18	10
Lieberam data Klim et al. data GO action potential	ENSG00000090020 P19634	SLC9A1	SLC9A1	solute carrier family 9 member A1	12	10
Lieberam data Klim et al. data	ENSG00000122861	PLAU	PLAU	plasminogen activator, urokinase	32	10
Melamed et al. data GO action potential	ENSG00000143153 P05026	ATP1B1	ATP1B1	ATPase Na+/K+ transporting subunit beta 1	18	10
Lieberam data GO Synapse assembly	ENSG00000137845 O14672	ADAM10	ADAM10	ADAM metallopeptidase domain 10	15	10
Positive controls Klim et al. data GO Reactive oxygen species	Q13546 ENSG00000137275	RIPK1	RIPK1	receptor interacting serine/threonine kinase 1	51	25